



Universiteit
Leiden
The Netherlands

Aria of the Dutch North Sea

Sertlek, H.O.; Sertlek H.O.

Citation

Sertlek, H. O. (2016, June 9). *Aria of the Dutch North Sea*. Retrieved from <https://hdl.handle.net/1887/40158>

Version: Not Applicable (or Unknown)

License: [Licence agreement concerning inclusion of doctoral thesis in the Institutional Repository of the University of Leiden](#)

Downloaded from: <https://hdl.handle.net/1887/40158>

Note: To cite this publication please use the final published version (if applicable).

Cover Page



Universiteit Leiden



The handle <http://hdl.handle.net/1887/40158> holds various files of this Leiden University dissertation

Author: Sertlek, Hüseyin Özkan

Title: Aria of the Dutch North Sea

Issue Date: 2016-06-09

ARIA OF THE DUTCH NORTH SEA

Hüseyin Özkan Sertlek

Cover art and design: Lisanne Brouwer

Copyright © by Hüseyin Özkan Sertlek. All rights are reserved. No part of this book may be reproduced, stored in a retrieval system or transmitted in any form or by any means, without the prior permission of the author.

ARIA OF THE DUTCH NORTH SEA

Propagation, source and sound mapping
simulations for the Dutch North Sea

PROEFSCHRIFT

ter verkrijging van

de graad van Doctor aan de Universiteit Leiden,

op gezag van Rector Magnificus Prof. Mr. C.J.J.M. Stolker

volgens besluit van het College voor Promoties

te verdedigen op donderdag 9 June 2016

klokke 13.45 uur

door

Hüseyin Özkan Sertlek

Geboren te Karabük, Turkey in 1985

Promotiecommissie

Promotores:

Prof. Dr. C. J. ten Cate

Prof. Dr. M. A. Ainslie (TNO, The Netherlands and ISVR, University of Southampton, UK)

Co-promotor:

Dr. Hans W. Slabbekoorn

Overige leden

Prof. Dr. H. P. Spaink

Prof. Dr. N.R. Chapman (School of Earth and Ocean Sciences, University of Victoria, Canada)

Dr. C.A.F. de Jong (TNO, The Netherlands)

Prof. Dr. A. Doelman

This PhD project was supported by NWO-ZKO (grant 839.10.521) as part of the larger programme: 'Effects of underwater noise on fish and marine mammals in the North Sea'.

CONTENTS

CHAPTER 1 INTRODUCTION	7
CHAPTER 2 MODELING THE UNDERWATER ACOUSTIC PROPAGATION IN THE DUTCH NORTH SEA	9
2.1.OVERVIEW OF PROPAGATION METHODS AND THEIR PERFORMANCE: PROPAGATION LOSS MODEL COMPARISONS ON SELECTED SCENARIOS FROM THE WESTON MEMORIAL WORKSHOP	11
2.2. DERIVATIONS FOR RANGE INDEPENDENT WAVEGUIDES: A DEPTH-DEPENDENT FORMULA FOR SHALLOW WATER PROPAGATION	21
2.3. SOPRANO HYBRID PROPAGATION MODEL: RANGE-DEPENDENT PROPAGATION EQUATIONS AND RESULTS FOR THE SHALLOW WATER WAVEGUIDES	47
CHAPTER 3 SOURCE MODELS AND SOUND MAPS	75
3.1. EFFECT ON SOUND SPEED PROFILE ON SHIPPING SOUND MAPS	77
3.2. VALIDATION STUDY: COMPARISON OF SHIPPING SOUND MAP WITH THE MEASUREMENTS	85
3.3. AGORA: AIRGUN SOURCE SIGNATURE MODEL	99
3.4. SOURCE SPECIFIC SOUND MAPPING: SPATIAL, TEMPORAL AND SPECTRAL DISTRIBUTION OF SOUND IN A HEAVILY EXPLOITED SEA	111
CHAPTER 4 BIOLOGICAL RELEVANCE OF SOUND MAPS	137
4.1. BIOLOGICAL RELEVANCE FOR MARINE MAMMALS: ASSESSING THE IMPACT OF UNDERWATER CLEARANCE OF UNEXPLODED ORDNANCE ON HARBOUR PORPOISES (PHOCOENA PHOCOENA) IN THE SOUTHERN NORTH SEA	139
4.2. MOVEMENT BEHAVIOUR INFLUENCES POPULATION LEVEL EXPOSURE TO UNDERWATER SOUND: IMPACT OF EXPLOSIONS ON HARBOUR POPOISES	169
CHAPTER 5 DISCUSSION AND SUMMARY	193
DUTCH SUMMARY	197
REFERENCES	201
ACKNOWLEDGEMENTS	223

Chapter 1 INTRODUCTION

Underwater sound is a critical tool for aquatic animals that communicate acoustically or exploit environmental sounds to find prey, avoid predators, or for orientation [Slabbekoorn et al. 2010; Fay 2009]. The interference of various anthropogenic and natural sound sources can make it difficult to distinguish biologically relevant sounds and can even cause physical damage to these animals. This has given rise to international concern about possible effects of anthropogenic sound sources on marine life due to increasing shipping traffic, exploitation of oil and gas reserves and the development of new offshore energy sources. For instance, the European Union's Marine Strategy Framework Directive (MSFD) [EU 2008] requires EU Member States to achieve or maintain Good Environmental Status (GES) by the year 2020. Specifically, GES Descriptor 11 requires underwater noise to be "at levels that do not adversely affect the marine environment". Calculating the sound distribution and estimating the associated environmental risk requires a multidisciplinary collaboration between acousticians, biologists and decision-makers. Understanding the spatial, spectral and temporal distribution of various sound sources and the characterisation of the acoustic environment are critical components to estimate the possible impact of sound on the marine life.

The MSFD requirement to investigate the potential impact of sound on marine life in the Dutch North Sea provided the background and motivation for a large scale project on "The effects of underwater noise on fish and marine mammals in the North Sea", funded by the NWO-ZKO programme. Within this project, three subprojects dealt with complementary topics including behavioural impact of sound on fish and sound exposure estimates for marine mammals. The aim of my project was to understand the distribution and composition of the sound in the North Sea. This aim is achieved by generating sound maps and calculating total acoustic energies for the various sound sources in the North Sea. The output of this project can serve in the impact assessment of underwater sound on environmental status.

In this thesis, the spatial, temporal and spectral distributions of sound generated by anthropogenic and natural sources in the Dutch North Sea are investigated. In order to achieve this aim, the acoustic propagation is calculated; source characteristics are modelled; and the resulting sound distribution is mapped for each source type. An aria is a piece of music sung by one person, normally as part of a larger performance. The sound maps for each type of source are created by

INTRODUCTION

assuming all other sources are quiet during the activities of the selected source. For example, the sound maps for shipping only contain the voice of ships. The title of my thesis “Aria of the Dutch North Sea” is chosen to indicate that each sound map is for a chosen type of source. In Chapter 2, I start with multi-model propagation loss comparisons to investigate the accuracy of well-known propagation models [Chapter 2.1]. The insight obtained from these comparisons was used for the derivation of a fast and accurate propagation model (SOPRANO) for shallow water test cases based on scenarios specified by the Weston Memorial Workshop, held at the University of Cambridge in 2010 [Chapter 2.2 and 2.3]. This propagation model can calculate propagation loss without requiring a large computational load and complicated algorithms.

Chapter 3 starts with the effect of the sound speed profile on shipping sound maps [Chapter 3.1], compares the shipping sound maps with actual measurements [Chapter 3.2]; and describes the airgun source model AGORA [Chapter 3.3]. Finally, combining source and propagation models as a tool for predicting sound fields, sound maps are generated for the Dutch North Sea and the total acoustic energies are calculated for weekly and yearly periods [Chapter 3.4]. In Chapter 4, some examples of studies are provided to illustrate the use of the simulated sound maps for understanding the biological impact. These maps are used to investigate the potential impact of sound on the marine life. The source models and sound maps which are included in this thesis are listed in Table I. Chapter 5 summarizes the findings and insights from all chapters and involves a general discussion based on the results of my thesis.

Table I. Sound sources, source models and sound maps included in this thesis

Source	Sound Maps	Source Model
Ship	+	+
Underwater Explosions	+	+
Airguns	+	+
Pile Driving	-	-
Wind	+	+
Rain	-	+
Lightning	-	-
Biological sounds (i.e. marine mammals, fish and invertebrates)	-	-

Chapter 2 MODELING THE UNDERWATER ACOUSTIC PROPAGATION IN THE DUTCH NORTH SEA

This chapter explains the propagation model developed to generate shallow water sound maps. In Chapter 2.1, well-known propagation methods are compared for the selected test cases. It is shown that

- mode theory can generate accurate results
- flux theory can provide fast analytical solutions.

These advantages are merged in the proposed hybrid propagation approach. First, this approach is derived for the range independent shallow water waveguides [Chapter 2.2]. Then, it is extended to range dependent waveguides and obtained results are investigated with multimodel comparisons [Chapter 2.3].

2.1 OVERVIEW OF PROPAGATION METHODS AND THEIR PERFORMANCE: PROPAGATION LOSS MODEL COMPARISONS ON SELECTED SCENARIOS FROM THE WESTON MEMORIAL WORKSHOP

This section is a modified version of “H.Ö. Sertlek and M.A. Ainslie, Propagation loss model comparisons on selected scenarios from the Weston Memorial Workshop, Proc. 1st International Conference on Underwater Acoustic (UAC), 441-448, Corfu, Greece, 2013”

Abstract: *The accurate and stable calculation of underwater acoustic propagation is needed for applications such as sonar performance prediction, noise mapping and acoustic communication. In this work, some widely used acoustic propagation models, based on different methods such as normal mode, ray tracing, parabolic equation and flux theory are tested on the scenarios specified for the Weston Memorial Workshop, held at the University of Cambridge in 2010. Incoherent, coherent and depth-averaged propagation losses are generated for range independent and range-dependent scenarios. The effects of each method's characteristic parameters (such as number of rays, stair-step size, Weston's approximations, range and depth resolution etc.) on propagation loss are investigated. Propagation loss results and run times of each model are compared at the different frequencies, ranges and receiver depths. An automated script has been developed to carry out systematic convergence tests from a single input file. Using this script, comparisons are made of propagation loss results generated by different methods. These comparisons provide insight to the optimal choice of running parameters and performance of each model.*

2.1.1 Introduction

Accurate estimation of propagation loss (PL) plays an important role in underwater acoustic simulations. An unstable and inaccurate propagation loss result may lead to undesirable errors in sonar performance simulations, environmental risk assessments etc. The propagation loss calculations should therefore be compared with available benchmark results. Test problems from the 2010 Weston Memorial workshop [Ainslie,2010b; Zampolli et al,2010] are considered. These are based on the test problems for the 2006 and 2008 Reverberation Modelling Workshops at the University of Texas at Austin [Thorsos and Perkins,2007]. In this section, some of these test cases are solved with different methods for different bathymetries, smooth sea surface and uniform sound speed. The detailed descriptions of each available algorithm have been investigated. The critical characteristic parameters of the methods used (such as number of rays, stair-step sizes, spatial resolution etc.) are analysed systematically by using convergence tests. Then, an automatic comparison script has been used in order to minimize user errors for the comparisons and estimate running parameters for an arbitrary problem. This program compares the propagation loss (PL) versus range, depth and frequency which is calculated by various methods such as Normal Mode, Ray Tracing, Parabolic Equation and Weston's approach for the calculation of average intensity. The different running parameters are used and the sensitivity and stability of each method is tested. Well-known propagation models that are available in the Ocean Acoustic Library (OALIB) are used [oalib.hlsresearch.com]. The details of these test cases will be given in the next sections. the scenario naming convention follows [Ainslie et al,2013].

2.1.2 Used Methods

There is no single standard method to estimate PL. Different methods can be preferred depending on the frequency range, problem size or calculation time. One may even need to develop a new propagation algorithm to solve the specific problem. In order to investigate the accuracy of any PL model, some benchmark tests can be done for the calibration of the model. In this section, the PL calculations with different methods such as normal modes, ray tracing, parabolic equation and Weston's approximations are investigated. The use of the model with the inappropriate options may lead to errors. The possible effect of these options on PL accuracy is investigated in the following sections.

Normal Mode Theory

The normal mode method can provide a full wave solution which may be used as a benchmark test. It is based on the solution of the Helmholtz equation by the separation of variables technique. A stair-step approximation of bathymetry is used for range-dependent problems. Selection of step size can affect the accuracy [de Groot-Hedlin,2004; Jensen and Ferla,1990]. In Figure 1, a comparison of incoherent PL with different step sizes is shown for Case 4 (see Fig. 5). These figures were generated with the adiabatic approximation option of Krakenc. It can be seen from this comparison that the effect of stair step size also depends on frequency and on other environmental changes. For high frequencies, the selection of stair-steps size can be more critical. The fluctuations in Figure 1 are related to the different mode cut-off frequencies for different water depths. In this section, minimum step length is selected as 20 m (after convergence tests) for all normal mode calculations. Normal mode comparisons are achieved by the well-known normal mode algorithm Kraken[Porter,1990] and another normal mode solution based on an analytical estimation of eigenvalues [Sertlek and Aksoy, 2010].

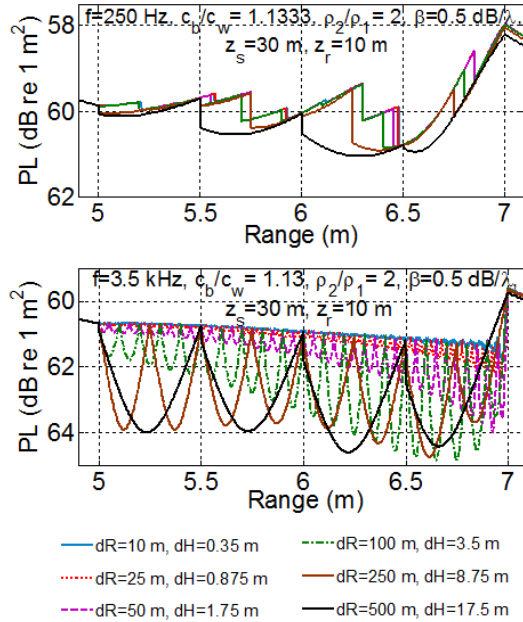


Figure 1. Propagation loss vs range for Case 4
(Effect of stair-step sizes on PL for 250 Hz and 3.5 kHz)

Ray Theory

Ray based models are widely used in many underwater acoustic applications. A ray tracing algorithm traces a sound ray for each launch angle by using physical concepts. It is based on a high frequency approximation. For this reason, ray theory results may be inaccurate in shallow water and especially near the cut-off frequency of the waveguide. However, it can be a useful method where the running times are critical. Bellhop is a well-known ray tracing program [oalib.hlsresearch.com]. It can provide propagation loss, ray paths, arrival times, eigenrays etc. Different tracing options can be selected in Bellhop. In this work, the geometric ray option is used. The required number of rays depends on the range and geometry. A sufficient number of rays can be selected by convergence testing. Especially for long range problems, a large number of rays may be required. The effect of rays on the accuracy of incoherent PL for Case 9 (see Figure 7) is shown in Figure 2.

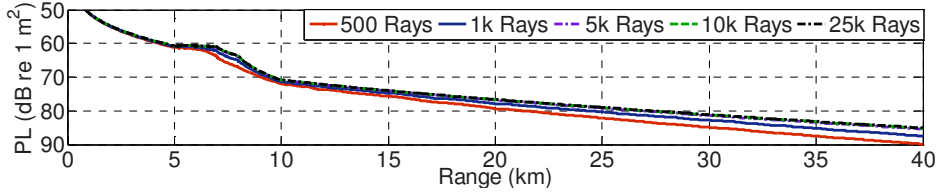


Figure 2. Propagation loss vs range for Case 9:
Effect of number of rays for depth-averaged PL ($f=3.5$ kHz)

Parabolic Equation Method

The parabolic equation (PE) method is used in many different fields of wave propagation such as electromagnetism, optics, seismology and underwater acoustics. RAM is a well-known PE program [Collins,1999]. It can solve range-dependent ocean acoustics problems with the split-step Padé algorithm [Collins,1993]. It is based on the paraxial approximation for the wave equation, providing a one-way solution to the wave-equation. It is especially used for range-dependent propagation problems. The accuracy of a parabolic equation solution depends on its starter field, number of Padé terms, false bottom, the grid size (the choice of which depends on frequency). Selection of range and depth step sampling size is important in PE calculations. Using smaller steps may reduce the fluctuations in the calculated fields, but increases the computation

time [Robertson,1999]. In Figure 3, the effect of depth sampling size is shown for coherent PL. An optimum value of grid size should be selected. Beside the selection of grid sampling size, selection of the sediment layer thickness (which must be artificially truncated at a user-specified depth [Jensen et al,1994]) can be important for low frequencies.

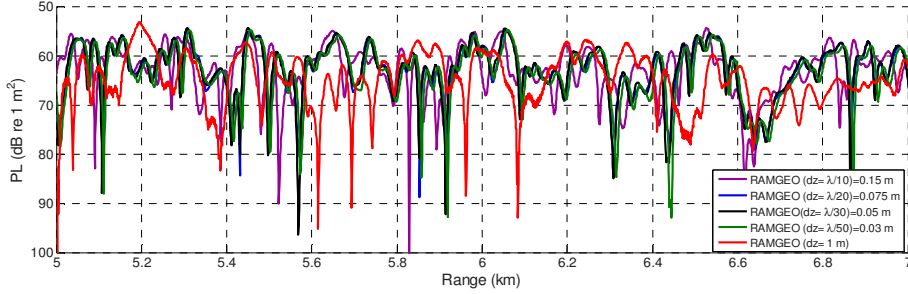


Figure 3. PL vs range for Case 1: effect of depth sampling sizes for 1 kHz at 1 m above sea bottom

Weston's Approximations

According to Weston's paper, propagation loss for range dependent media can be calculated using the effective depth concept [Weston,1971 ; Weston,1976]. For an arbitrary bathymetry, the depth profile can be divided into small segments. Then, variation of depth for each segment can be simplified in order to calculate the effective depth integral analytically. It can provide an analytical estimation of PL for range-dependent and lossy waveguides. The estimated PL is depth-averaged.

2.1.3 Comparisons

PL versus range (up to 40 km) comparisons are obtained for coherent, incoherent and depth-averaged (averaged over receiver depth) calculation of PL. However, only depth averaged results are shown for sake of simplicity. The depth averaged PL was computed over incoherent field except RAM's results. This exception was made because RAM only generates coherent field. The characteristic parameters of each method (such as depth and range sampling size, number of rays etc.) are obtained by convergence tests. In all test cases, the sound speed in water is 1500

m/s. The sound speed in sediment is 1700 m/s and bottom absorption loss is 0.5 dB/wavelength [0.294 dB/ (m kHz)]. The Thorp model [Jensen et al,1994] is used for the volume absorption. The first scenario ("Case 1" [Ainslie et al,2013]) is a flat waveguide with 100 m depth. The model is run for 250 Hz, 1 kHz and 3.5 kHz for a fixed source depth at 30 m. PL versus range comparisons are shown for Case 1 in Figure 4. There is a good agreement between the solutions until 20 km. However, the RAM solution is different at longer ranges. This difference depends on the choice of spatial resolution. The RAM version used in these tests is based on single precision. Although the choice of small spatial sampling size increases the agreement with normal mode results until around 20 km, floating point errors may arise at longer ranges.

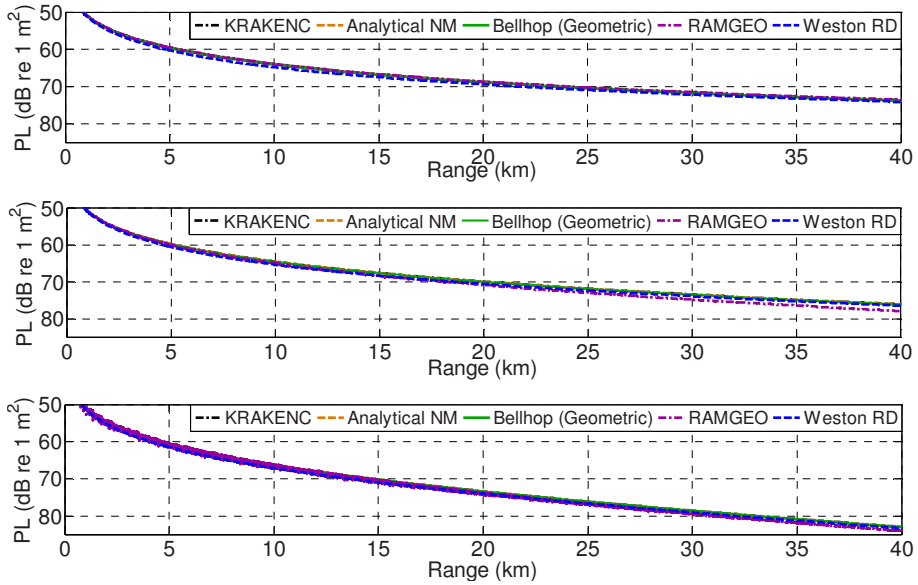


Figure 4. Depth-averaged (over receiver depth) PL vs range for Case 1 ($f=250$ Hz (top), $f=1$ kHz (middle), $f=3.5$ kHz (bottom)). Source depth = 30 m.

The second scenario is "Case 4" [Ainslie et al,2013]. It has 100 m water depth up to 5 km. Then, it features an upslope from 5 km to 7 km up to water depth 30 m (see Figure 5). The bathymetry and depth-averaged (over receiver depth) PL comparisons are shown for Case 4 in Figure 6.

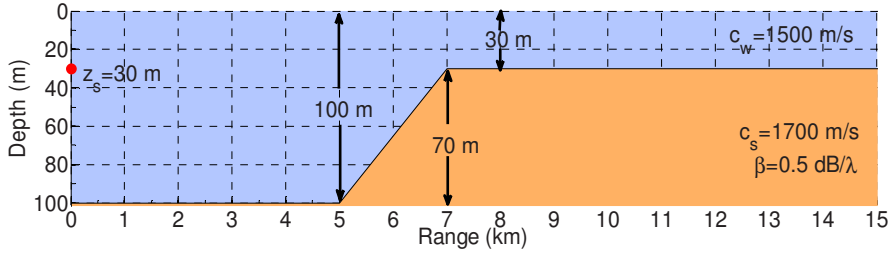
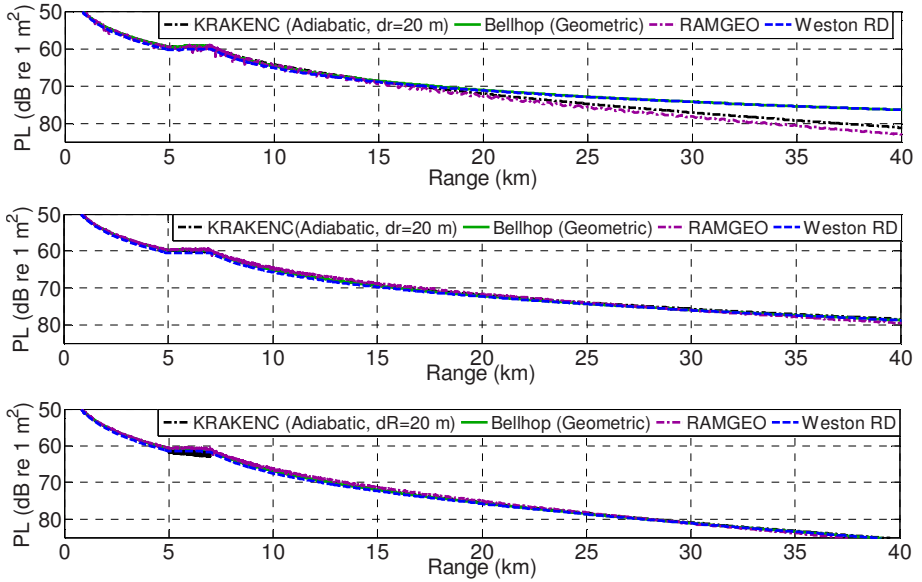


Figure 5. The bathymetry of Case 4


 Figure 6. Depth-averaged (over receiver depth) PL vs range for Case 4. ($f=250$ Hz (top), $f=1$ kHz (middle), $f=3.5$ kHz (bottom)). Source depth = 30 m.

For 250 Hz, Weston approximations and Bellhop result seem different after 20 km. This difference is related to propagation in the single mode region [Weston,1971; Weston,1976]. This error can be addressed by replacing the flux integral with a discrete mode sum in this region at long ranges.

The last scenario, “Case 9”, has 100 m water depth up to 5 km, followed by an upslope region from 5 km to 7 km up to water depth 30 m comparable to “Case 4”. A shallow water region (depth 30 m) is then followed by a downslope region from 8 km to 10 km down to water depth 100 m, and uniform depth thereafter (see Figure 7).

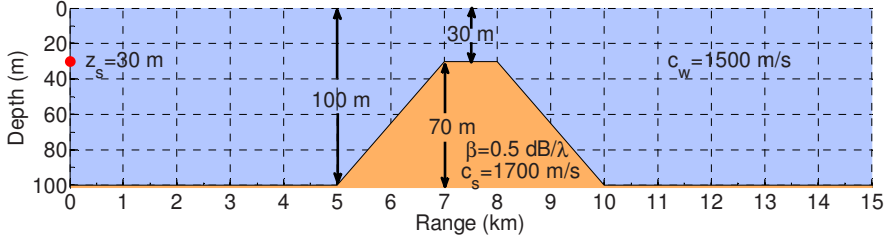


Figure 7. The bathymetry of Case 9

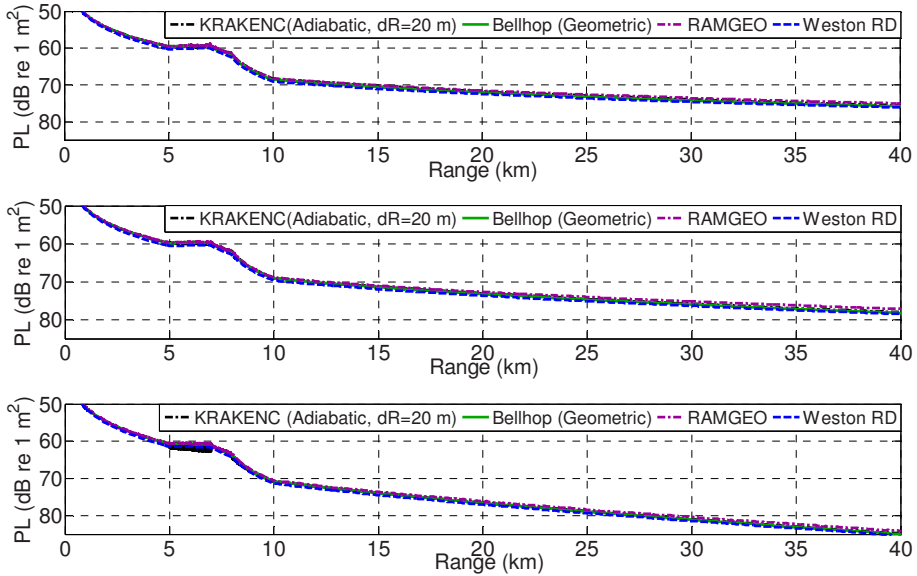


Figure 8. Depth-averaged (over receiver depth) PL vs range for Case9. ($f=250$ Hz (top), $f=1$ kHz (middle), $f=3.5$ kHz (bottom)). Source depth = 30 m.

Weston’s range dependent approach has a good agreement with other models. All models have a good agreement between depth-averaged PL results. However, coherent PL comparisons might

be different due to the sensitivity of environmental parameters and used different approaches for range dependency.

2.1.4 Conclusion

An automated script has been used to make the comparisons between selected methods with provided bathymetry, frequency, receiver and source depths with incoherent, coherent and depth-averaged options. Each method is based on different assumptions and numerical algorithms. Thus, the characteristic parameters of these methods should be selected with convenient convergence tests or comparisons with other models in the validity range of each model. Otherwise, it may lead inaccurate results especially for long range problems and range-dependent bathymetries. The comparison results can provide an insight into the possible differences between these methods.

2.2 DERIVATIONS FOR RANGE INDEPENDENT WAVEGUIDES: A DEPTH-DEPENDENT FORMULA FOR SHALLOW WATER PROPAGATION

This section is modified version of “H.Ö. Sertlek and M.A. Ainslie, A depth-dependent formula for shallow water propagation, J. Acoust. Soc. Am. 136(2), 573-582, 2014”.

Abstract: *In shallow water propagation, the sound field depends on the proximity of the receiver to the sea surface, the seabed, the source depth and the complementary source depth. While normal mode theory can predict this depth dependence, it can be computationally intensive. In this work, an analytical solution is derived in terms of the Faddeeva function by converting a normal mode sum into an integral based on a hypothetical continuum of modes. For a Pekeris waveguide, this approach provides accurate depth dependent propagation results (especially for the surface decoupling) without requiring complex calculation methods for eigenvalues and corresponding eigenfunctions.*

2.2.1. Introduction

The accurate calculation of propagation loss (PL) is needed for many acoustic problems such as sonar performance modeling, underwater acoustic communication, environmental risk assessment and oceanography. These applications can require the simulation of propagation characteristics at different ranges and depths. Propagation loss can be defined as

$$PL = 10 \log_{10} \frac{F^{-1}}{r_{ref}^2} \text{ dB re } 1 \text{ m}^2 \quad (1)$$

where F is known as the “transmission factor” [Weston,1980] or “propagation factor” [Ainslie,2010a] and r_{ref} is the reference distance, equal to 1 m. Propagation loss can be estimated with different methods such as normal modes, ray theory, parabolic equation, and flux theory. Variation of PL with range, water depth, frequency, source depth and receiver depth can be critical for determining detection ranges, isoclines for environmental risk assessment, etc. Weston introduced an energy flux approach for the calculation of depth-averaged propagation loss without tracing rays or summing normal modes, and thus applicable to large scale problems [Weston,1971]. Weston’s flux equation can be derived from ray and mode theories [Weston,1980]. In Weston’s approach, four propagation regions are described as the spherical, cylindrical spreading, mode-stripping and single mode regions. While permitting an analytical solution even for a range dependent environment [Weston,1976], Weston’s flux formulation may not provide satisfactory simulation results when the source or receiver depths are located close to each other, to the seabed or (especially) to the sea surface. [Weston,1980] addressed this weakness by deriving depth dependence using wave theory concepts, applying these to a selection of predetermined functional forms for the distribution of energy with angle, making an implicit assumption that the frequency is sufficiently high for the various depth-dependent corrections not to overlap with one another. [Harrison,2013] derived a range- and depth-correction to Weston’s flux theory that includes ray convergence terms, while neglecting the depth dependence close to source depth, complementary depth and boundaries. In the present section, a method is developed to calculate the depth dependence by deriving a generalisation of Weston’s approach that does not rely on prior knowledge of the angular energy distribution, and

is valid even when the correction terms overlap. The solution, in terms of the Faddeeva function, is derived from an incoherent normal mode sum by using some trigonometric transformations, and is valid for any angular distribution compatible with propagation from a point source in a Pekeris waveguide, and for any source-receiver depth combination. Results computed in this way for different frequencies and receiver depths are compared with results using the normal mode program KrakenC⁸. For the comparisons, a range independent test case (Scenario A2.I) from the Weston Memorial Workshop [Ainslie,2010b; Zampolli et al,2010] is used. The detailed description of this test case is given in the comparisons section.

2.2.2. Depth Dependence of Propagation Loss

The depth dependence of PL can have different characteristics due to the depth of the receiver relative to the sea surface, seabed, source depth and complementary source depth [Weston,1980]. The complementary source (z_{cs}) or receiver depth (z_{cr}) can be defined for source depth z_s (or receiver depth z_r) as

$$z_{cs,cr} = D - z_{s,r} \quad (2)$$

where

$$D = h + \Delta_W \quad (3)$$

and $\Delta_W = \frac{\rho_2/\rho_1}{k_1 \sin \theta_c}$ is the vertical wave shift and described by [Weston,1960; Weston,1994], h is water depth, ρ_2 is the density of sediment, ρ_1 is the density of sea water, k_1 is the wavenumber in the water layer and θ_c is the sediment critical angle. When PL is plotted vs z_s for a constant receiver depth, similar depth dependent properties is observed around the true receiver depth z_r as the complementary receiver depth $D - z_r$.

2.2.2.1. Derivation

By using the incoherent mode sum, the propagation factor F for an isovelocity and isodensity waveguide can be written as

$$F(z_r, z_s) = \frac{2\pi}{r} \sum_{n=1}^{\infty} \frac{\psi_n^2(z_s) \psi_n^2(z_r)}{\kappa_n} \exp(-2\delta_n r) \quad (4)$$

Here $\psi_n(z)$ is the eigenfunction

$$\psi_n(z) = A_n \sin(\gamma_n z) \quad (5)$$

where A_n is the amplitude of n th eigenfunction, γ_n is vertical wavenumber, and κ_n the horizontal wavenumber. Defining the quantity of $L_n = \int \frac{1}{\sqrt{k_1^2(z) - \kappa_n^2}} dz = \frac{r_{\text{CM}}}{2\kappa_n}$, the normalisation constant A_n^2 can be written [Tindle and Weston, 1980]

$$A_n^2 = \frac{2}{L_n} (k_1^2 - \kappa_n^2)^{-1/2} = \frac{4 \cot \theta_n}{r_{\text{CM}}} \quad (6)$$

where r_{CM} is the modal cycle distance, and θ_n is the n th mode grazing angle given by

$$\theta_n = \arcsin\left(\frac{n\lambda}{2D}\right), n = 1, 2, 3, \dots \quad (7)$$

The relation between the modal cycle distance and geometric ray cycle distance (r_{cG}) is [Tindle and Weston,1980]

$$r_{cM} = r_{cG} + 2\Delta_B \cot\theta, \quad (8)$$

where $\Delta_B = \frac{(\gamma_{1n}^2 + \gamma_{2n}^2)}{\gamma_{1n}\gamma_{2n}^2 \left(\frac{\rho_1\gamma_{2n}}{\rho_2\gamma_{1n}} + \frac{\rho_2\gamma_{1n}}{\rho_1\gamma_{2n}} \right)}$ is the vertical *beam* shift [Weston,1994] (converted from the corresponding horizontal shift stated by [Weston and Tindle,1979]) This relation can be written for isovelocity case by substituting for $r_{cG} = 2h \cot(\theta)$

$$r_{cM} = 2(h + \Delta_B) \cot\theta. \quad (9)$$

If one uses the relations of $\gamma_{1n}^2 = k_1^2 \sin^2 \theta$ and $\gamma_{2n}^2 = k_1^2 - \gamma_{1n}^2 - k_2^2$, the beam shift takes the form

$$\Delta_B = \frac{\rho_1 \rho_2 (k_1^2 - k_2^2)}{\sqrt{k_1^2 \cos^2 \theta - k_2^2} (\rho_2^2 k_1^2 \sin^2 \theta + \rho_1^2 k_1^2 \cos^2 \theta - \rho_1^2 k_2^2)} \quad (10)$$

where $k_2 = \omega/c_2$. The attenuation term in the horizontal direction is added by a perturbation approach with the contribution of a small imaginary part δ_n to κ_n [Tindle,1979]. This small imaginary part leads to an exponential attenuation with range as $\exp(-2\delta_n r)$, where δ_n can be related to the reflection coefficient of sea bottom $V(\theta)$ according to

$$\delta_n = \text{Im}\{k_1 \cos(\theta_n)\} = -\frac{\ln(|V(\theta_n)|)}{r_{cM}} \quad (11)$$

The following relations can be obtained with the relation of $\gamma_{1n} = \frac{n\pi}{D}$ in Eq.(A4) and Eq.(A5) as shown in Appendix A.

$$F(D - z_r, z_s) = F(z_r, z_s) = F(z_r, D - z_s) \quad (12)$$

This property is useful because if $F(z_r, z_s)$ is known for $0 < z_r, z_s < D/2$, Eq.(30) permits straightforward evaluation of $F(z_r, z_s)$ for $D/2 < z_r, z_s < h$. The discrete mode sum (F) can be approximated by the following integral which is denoted by F_0 ,

$$F_0(z_r, z_s) = \frac{2\pi}{r} \int_0^\infty \frac{\psi_n^2(z_s) \psi_n^2(z_r)}{\kappa_n} |V|^{\frac{2r}{r_{cM}}} dn \quad (13)$$

By this integral representation, the integer n is replaced by a continuous function of the grazing angle θ as $n \approx n(\theta)$. The variation of $n(\theta)$ versus θ can be written as

$$\frac{dn(\theta)}{d\theta} = \frac{r_{cM}}{2\pi} k_1 \sin(\theta) \quad (14)$$

However, the integrand is defined only at the discrete eigenvalues. In the following steps, this integrand will be interpolated between the eigenvalues as a continuous function of θ , thus permitting evaluation of the integral

$$F_0(z_r, z_s) = \frac{1}{r} \int_0^{\frac{\pi}{2}} A_n^4 \sin^2(\gamma_{1n} z_s) \sin^2(\gamma_{1n} z_r) r_{cM} \tan(\theta) |V|^{\frac{2r}{r_{cM}}} d\theta \quad (15)$$

where A_n and r_{cM} are given by Eq.(6) and Eq.(9). The integral can be written in the different forms by using trigonometric identities. First, using the trigonometric identity $\sin^2(\gamma_{1n} z) \equiv \frac{1}{2} - \frac{1}{2} \cos(2\gamma_{1n} z)$ for eigenfunctions, this integral becomes

$$F_0(z_r, z_s) = \frac{4}{r} \int_0^{\frac{\pi}{2}} \frac{(1 - \cos(2\gamma_{1n} z_s))(1 - \cos(2\gamma_{1n} z_r))}{r_{cM} \tan(\theta)} |V|^{\frac{2r}{r_{cM}}} d\theta \quad (16)$$

Then, changing the variable of integration to continuous grazing angle and using the trigonometric identity

$$\cos(2k_1 z_s \sin \theta) \cos(2k_1 z_r \sin \theta) = \frac{\cos(2k_1 (z_s - z_r) \sin \theta) + \cos(2k_1 (z_s + z_r) \sin \theta)}{2} \quad (17)$$

results in the following integral form for the propagation factor,

$$F_0(z_r, z_s) = \frac{4}{r} \int_0^{\frac{\pi}{2}} \frac{(1 - W(z_r, z_s, \theta))}{r_{cM} \tan \theta} |V|^{\frac{2r}{r_{cM}}} d\theta \quad (18)$$

where the term involving source and receiver depths can be written

$$W(z_r, z_s, \theta) = \cos(2k_1 z_s \sin \theta) + \cos(2k_1 z_r \sin \theta) - \frac{\cos(2k_1 \sin \theta (z_s - z_r)) + \cos(2k_1 \sin \theta (z_s + z_r))}{2} \quad (19)$$

If $W(z_r, z_s, \theta)$ were sufficiently close to zero on average, Eq. (18) would have the same form as the flux integral, which has an analytical solution in the form of an error function if the reflection loss increases linearly with angle [Ainslie, 2010a; Macpherson and Daintith, 1967]. This gives the depth-averaged propagation factor.

2.2.2.2. Reflections from the seabed

Eq.(18) can be evaluated numerically for any given seabed reflection coefficients. The possibility of analytical evaluation for special forms of the reflection coefficient is explored next.

A. *Exponential reflection coefficient*

One reflection coefficient assumption that permits an analytical evaluation of the integral is exponential reflection coefficient in the form

$$|V| = \exp(-\eta \theta^2 / \tan \theta) \quad (20)$$

where η is the rate of increase with grazing angle of the sediment reflection loss [Ainslie, 2010], in nepers per radian (Np/rad). This form of reflection coefficient simplifies the derivation without requiring small angle approximation. Specifically, the propagation factor becomes

$$F_0(z_r, z_s) = \frac{4}{r} \int_0^{\theta_c} \frac{(1 - W(z_r, z_s, \theta))}{r_{\text{CM}} \tan \theta} \exp\left(-\frac{2\eta r}{r_{\text{CM}} \tan \theta} \theta^2\right) d\theta \quad (21)$$

This integral can be solved analytically for the isovelocity and isodensity case. For the isovelocity case, ray cycle distance is $r_{\text{CM}} = 2(h + \Delta_B) \cot \theta$. Then, the propagation factor becomes

$$F_0(z_r, z_s) = \frac{2}{r} \int_0^{\theta_c} \frac{(1 - W(z_r, z_s, \theta))}{h + \Delta_B} \exp\left(-\frac{\eta r}{(h + \Delta_B)} \theta^2\right) d\theta \quad (22)$$

The vertical beam shift is important for low frequencies and is itself a function of angle [Weston,1994]. Eq. (22) can be used for low frequencies by evaluating the integral numerically. The beam shift can be ignored for higher frequencies, in which case the following equation results

$$F_0(z_r, z_s) = \frac{2}{rh} \int_0^{\theta_c} (1 - W(z_r, z_s, \theta)) \exp\left(-\frac{\eta r}{h} \theta^2\right) d\theta, \quad (23)$$

where $W(z_r, z_s, \theta)$ is the sum of cosine functions from Eq.(19). Thus, the analytical solution for the following type of integral leads an analytical solution for the propagation factor:

$$\begin{aligned}
 \Phi[Z, R, \theta_c] &= \int_0^{\theta_c} \cos(Z\theta) \exp(-R\theta^2) d\theta \\
 &= \sqrt{\frac{\pi}{R}} \frac{\exp\left(-\frac{Z^2}{4R}\right)}{4} \left(w\left(\frac{Z}{2\sqrt{R}} - i\sqrt{R}\theta_c\right) \exp\left(\left(\frac{Z}{2\sqrt{R}} - i\sqrt{R}\theta_c\right)^2\right) \right. \\
 &\quad \left. - w\left(\frac{Z}{2\sqrt{R}} + i\sqrt{R}\theta_c\right) \exp\left(\left(\frac{Z}{2\sqrt{R}} + i\sqrt{R}\theta_c\right)^2\right) \right) \quad (24)
 \end{aligned}$$

where $w(x + iy)$ is the Faddeeva function [Poppe and Wijers, 1967; Abramowitz and Stegun, 1972] which is defined as

$$w(x + iy) = \exp(-(x + iy)^2) \left(1 + \frac{2i}{\sqrt{\pi}} \int_0^{x+iy} \exp(t^2) dt \right) \quad (25)$$

and is related to the error function [Abramowitz and Stegun, 1972] according to

$$w(x + iy) = \exp(-(x + iy)^2) \left(1 + \operatorname{erf}(i(x + iy)) \right). \quad (26)$$

The analytic expression for the propagation factor for isovelocity case can be written in terms of the function $\Phi[Z, R, \theta_c]$ as

$$\begin{aligned}
 F_0(z_r, z_s) = & r^{-\frac{3}{2}} \sqrt{\frac{\pi}{\eta h}} \operatorname{erf}\left(\sqrt{\frac{\eta r}{h}} \theta_c\right) \\
 & - \left\{ \frac{2}{rh} \left[\Phi\left[2k_1 z_s, \frac{\eta r}{h}, \theta_c\right] + \Phi\left[2k_1 z_r, \frac{\eta r}{h}, \theta_c\right] \right. \right. \\
 & \left. \left. - \frac{\Phi\left[2k_1(z_s - z_r), \frac{\eta r}{h}, \theta_c\right] + \Phi\left[2k_1(z_s + z_r), \frac{\eta r}{h}, \theta_c\right]}{2} \right] \right\} \quad (27)
 \end{aligned}$$

where the first term is the error function based solution of the classic flux integral [Ainslie,2010a; Macpherson and Daintith,1967]. The term in curly parentheses describes the depth dependence for an isovelocity waveguide. In Figure 1, $\Phi[Z, R, \theta_c]$ is plotted as a function of R , a dimensionless range variable equal to $\frac{\eta r}{h}$, and a dimensionless depth variable Z that can be any one of $2k_1 z_r$, $2k_1 z_s$, $2k_1(z_r + z_s)$ and $2k_1(z_r - z_s)$. Specifically, the graph on the left shows the depth dependence of $\Phi[Z, R, \theta_c]$ for selected constant values of R , as stated in the figure legend. Similarly, the lower graph shows the range dependence of $\Phi[Z, R, \theta_c]$ for selected values of Z . The 2D contour plot (upper right panel) shows the combined R and Z dependence in a single graph. In all three graphs, the value of $\theta_c = \arccos(1500/1700) = 0.489957$ rad is used for consistency with the parameters of the selected scenario (A2.I) from Weston Memorial Workshop 2010. More detailed description of the test cases are given in the comparisons section.

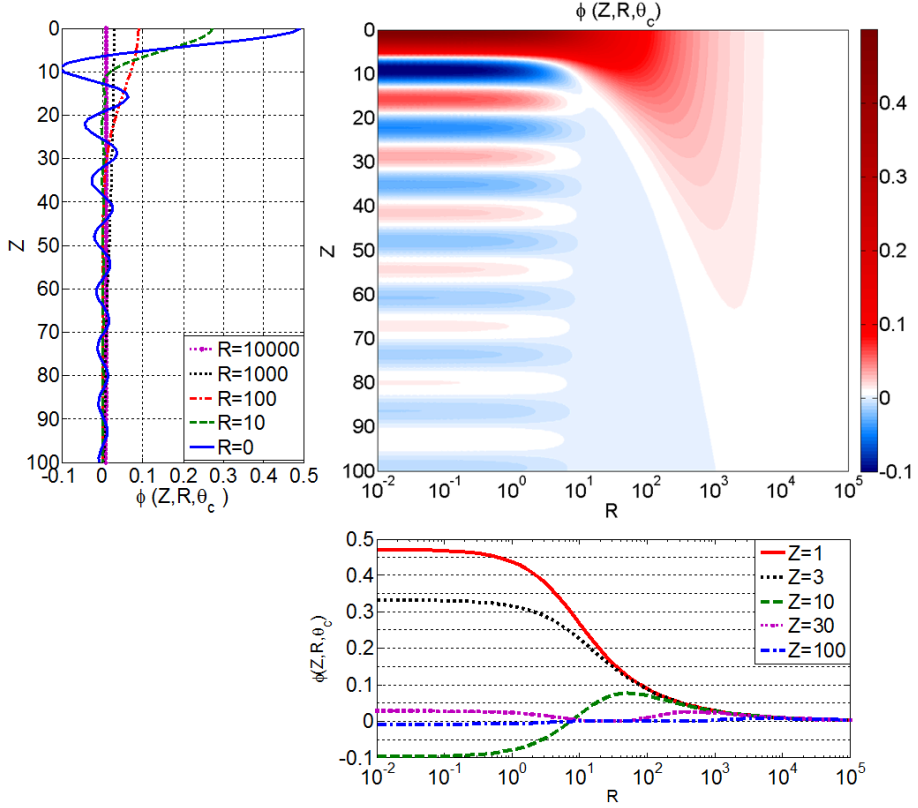


Figure 1. $\Phi[Z, R, \theta_c]$ function is plotted versus χ (on the upper left) and versus R (on the bottom right) for critical angle $\theta_c = 0.489957$ rad, corresponding to the scenario described in Sec. 2.2.3.

2D representation of $\Phi[Z, R, \theta_c]$ versus Z and R (on the upper right)

According to these figures, we expect more significant variations at low values of Z (low frequencies) and R (at small ranges or deeper water). The function $\Phi[Z, R, \theta_c]$ asymptotically approaches $\frac{1}{2} \sqrt{\frac{\pi}{R}} \exp\left(-\frac{Z^2}{4R}\right)$ for large R (by using Eq.(36)). For small R , $\lim_{R \rightarrow 0} \Phi[Z, R, \theta_c] = \frac{\sin(Z\theta_c)}{Z}$. For large Z , the asymptotic form is $\lim_{Z \rightarrow \infty} \Phi[Z, R, \theta_c] = 0$. For small Z , $\lim_{Z \rightarrow 0} \Phi[Z, R, \theta_c] = \sqrt{\pi} \frac{\text{erf}(\sqrt{R}\theta_c)}{2\sqrt{R}}$. When they are both small, $\lim_{Z, R \rightarrow 0} \Phi[Z, R, \theta_c] \approx \theta_c$. These approximate formulas can be helpful for simplifying the prediction of and increasing understanding of the dependence of the propagation on range, water depth and critical angle

B. *Harrison's approximation to Rayleigh reflection coefficient*

Use of an exponential reflection coefficient, as shown in the previous section, provides an analytical solution. This analytical solution (Eq.(27)) is based on a linear approximation to the seabed reflection loss. As it will be shown in Figure 2, the Rayleigh reflection coefficient can provide a better approximation for the decay rate [Harrison,2010]. Expressing the Rayleigh reflection coefficient in an exponential form can be computationally more efficient because of having less complicated equations in the final form. This exponential form also enables to facilitate comparisons with the previous derivations. A useful approximation to the Rayleigh reflection coefficient[Harrison,2010] that also leads to an analytical expression in a similar form to Eq.(18) is

$$|V| = \exp\left(-\frac{\eta \sin\theta}{\sqrt{1-v}\left(1 + \left(\left(\frac{\rho_2}{\rho_1}\right)^2 - 1\right)v\right)}\right) \quad (28)$$

where $v = \left(\frac{\sin\theta}{\sin\theta_c}\right)^2$, ρ_1 and ρ_2 are the densities of water and sediment. Thus, the propagation factor can be written as

$$F_0(z_r, z_s) = \frac{2}{r} \int_0^{\theta_c} \frac{(1 - W(z_r, z_s, \theta))}{(h + \Delta_B)} \exp\left(-\frac{\eta g r}{(h + \Delta_B)} \sin\theta \tan\theta\right) d\theta \quad (29)$$

where $g = \left(\sqrt{1-v}\left(1 + \left(\left(\frac{\rho_2}{\rho_1}\right)^2 - 1\right)v\right)\right)^{-1}$. In Section 2.2.3, propagation factors based on exponential and Rayleigh reflection coefficients are compared in Figure.2.

C. Symmetry of Depth Dependent Solution

The approximation F_0 is based on a continuous angle assumption for the eigenvalues as $\gamma_{1n} = k_w \sin(\theta)$. For the continuous angle approximation, the symmetry properties of propagation loss are not satisfied (See Eq.(19) and Appendix B). Therefore, the derived solution can be used to model the features at the sea surface and source depth. This derivation gives poor results for the features at sea bottom and complementary source depth as it could be seen in Figure 2. By using these symmetry properties from Eq.(A4) and Eq.(A5), the features at sea bottom and complementary source depth can be obtained from the features at sea surface and source depth as

$$F(z_r, z_s) = \begin{cases} F_-(z_r, z_s), & z_s < D/2 \\ F_+(z_r, z_s), & z_s > D/2 \end{cases} \quad (30)$$

where F_- and F_+ are defined as

$$F_-(z_r, z_s) = \begin{cases} F_0(z_r, z_s), & z_r < D/2 \\ F_0(D - z_r, z_s), & z_r > D/2 \end{cases} \quad (31)$$

and

$$F_+(z_r, z_s) = \begin{cases} F_0(z_r, D - z_s), & z_r < D/2 \\ F_0(D - z_r, D - z_s), & z_r > D/2 \end{cases} \quad (32)$$

These terms give the propagation factor (F) by using the symmetry property of source, receiver, complementary source and complementary receiver depths.

2.2.3. Comparisons

In this section, results obtained using the methods described in Sec. 2.2.2 are compared with KrakenC. In these comparisons, a range independent test case (Scenario A2.1) from the Weston Memorial Workshop [Zampolli et al,2010;Weston,1960] is used, based on Problem XI from the 2006 Reverberation Modeling Workshop at Un.Texas at Austin [Thorsos and Perkins,2007]. For Scenario A2.1, the water depth (h) is 100 m, source depth (z_s) is 30 m, sound speed in water (c_1) and sediment (c_2) are respectively are 1500 m/s and 1700 m/s, corresponding to a critical angle $\theta_c = 0.489957$ rad. The sediment-seawater density ratio (ρ_2/ρ_1) is 2 and resulting reflection loss gradient (η) is 0.273777 Np/rad, evaluated using Eq.(8.86) of [Ainslie,2010a].

[Weston,1980] derived the depth dependence for a number of specified distributions of energy with angle. For each angular distribution, which must be known in advance, four correction factors to the depth-averaged propagation factor are given of the form $[1 - f(x_0)]$ (sea surface and seabed) and $[1 + \frac{1}{2}f(x_0)]$ (source depth and complementary source depth), where $x_0 = k_1 d \phi_0$, d is the distance to the depth in question and ϕ_0 is an angle that characterises the distribution, equal to the critical angle for Weston's Case 2 ('low pass') and to the effective propagation angle $\phi_0 \approx \sqrt{\frac{h}{2\eta r}}$ for Cases 5 (Weston's 'Gaussian') and 6 ('dipole Gaussian'). In each case, the functional form $f(x_0)$ is given by Weston's Table I. In contrast to Weston's approach, use of Eq. (23) in terms of the Faddeeva function permits direct computation of the depth-dependent propagation factor without the need for prior knowledge of the angular distribution of energy. Instead, Eq.(23) and Eq.(29) automatically take into account all possible angular distribution cases for a Pekeris waveguide, dealing with transitions between different cases and combinations of multiple cases in a natural way, and permitting evaluation of all possible combinations of source or receiver depth. In Appendix C, relevant cases from Weston's table (Gaussian and dipole Gaussian) are derived from Eq.(23).

Figure 2 compares the result of evaluating expressions for Cases 2 ('low pass') and 5 ('Gaussian'). In the cylindrical spreading region (e.g., 0.5 km), the low pass solution is applicable, whereas for mode stripping (e.g., 25 km), one expects a Gaussian distribution with angle, and these expectations are confirmed by Figure 2. Less obvious is what happens for intermediate ranges (e.g., 2 km) at which it is necessary to make a choice between the low pass and Gaussian distributions. By contrast, Eq. (23) from the present section is applicable to both cylindrical spreading and mode stripping regions, including any intermediate range. Further, if greater

accuracy is required, this can be achieved by means of Harrison's approximation to the Rayleigh reflection coefficient, as implemented here in the form of our Eq. (29). For the purpose of Figure 2 and Figure 3, to combine the effects of multiple depth correction factors from Weston's paper, we have multiplied these together in the form (denoted $F_{2,5}$ for Weston's cases 2 and 5, applicable when the source is not close to the sea surface)

$$F_{2,5} = F_{\text{ref}} \left[\left(1 + \frac{f(x_{0,z_s})}{2} \right) \left(1 + \frac{f(x_{0,z_{cs}})}{2} \right) (1 - f(x_{0,0})) (1 - f(x_{0,D})) \right] \quad (33)$$

where the second subscript of the variable x_0 indicates the depth relative to which d is measured, such that $x_{0,\zeta} = k_1(z_r - \zeta)\phi_0$. Here F_{ref} is the analytical solution of Eq.(23) for $W(z_s, z_r, \theta) = 0$ as

$$F_{\text{ref}} = r^{-\frac{3}{2}} \sqrt{\frac{\pi}{\eta h}} \text{erf} \left(\sqrt{\frac{\eta r}{h}} \theta_c \right) \quad (34)$$

In Eq. (3) of [Weston, 1980], the low pass and Gaussian cases correspond to an assumption that $\sin^2(\gamma_{1n} z_s)$ may be replaced by its average value of 1/2. Consequently, Eq.(33) is not valid for source depths close to the sea surface or seabed on a wavelength scale. For small source depths, the depth corrections can be combined as (denoted F_6 , for Weston's case 6, 'dipole Gaussian' – as used in Figure 3)

$$F_6 = 2(k_1 z_s \phi_0)^2 F_{\text{ref}} \left[(1 - f(x_{0,0})) (1 - f(x_{0,D})) \right] \quad (35)$$

A similar form of Eq. (35) for the large receiver depth is also shown by [Denham,1986].

In Figure 2, the propagation loss results obtained with Eq.(23), Eq.(29), Weston's cases (Eq.(33)) and KrakenC are compared at different ranges. For these comparisons, Eq.(23) and Eq.(29) are evaluated numerically without applying the symmetry relations of Eqs. (30) to (32). The beam

shift is ignored in Figure 2. The classic form of the flux integral without depth dependent properties [Ainslie,2010a; Macpherson and Daintith,1967] is also plotted, as obtained by substituting $W(z_r, z_s, \theta_s) = 0$ in Eq.(23) gives this classical form of flux equation (Eq.(34)).

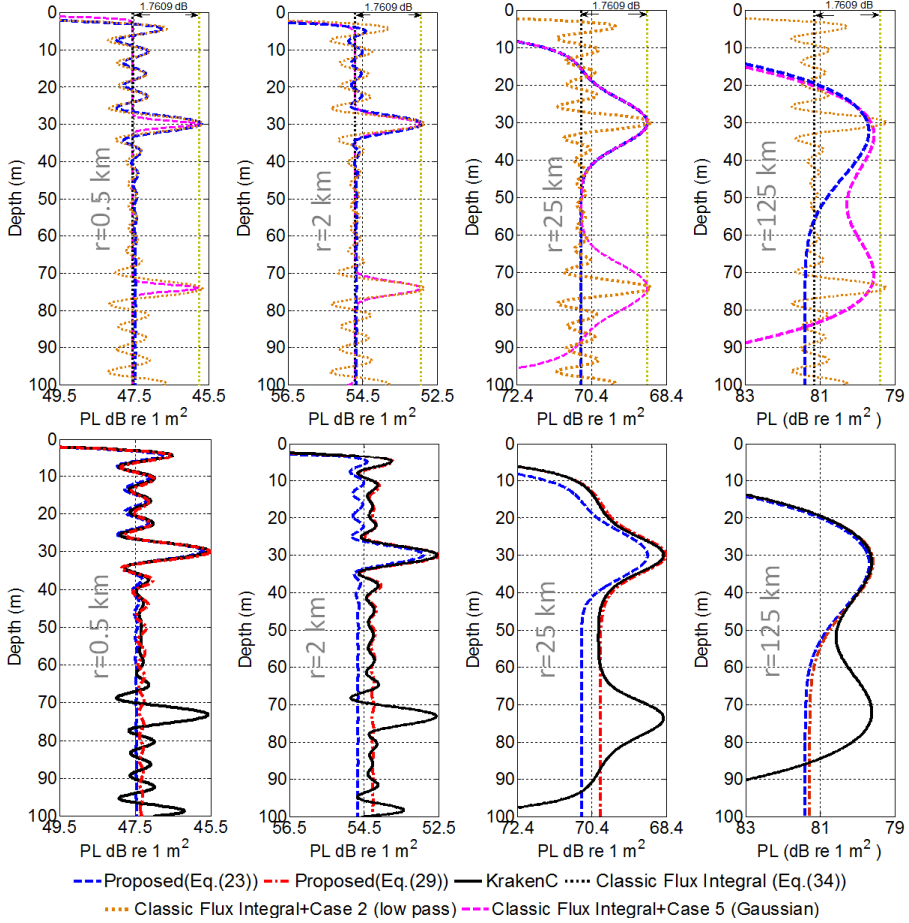


Figure 2. PL vs receiver depth calculated by Eq.(23), Weston's approach (Eq.(33)) for the various energy distributions with angle(low pass and Gaussian) and Flux integral (Eq.(34)) for 250 Hz at 0.5 km, 2 km, 25 km and 125 km.(upper graphs).PL vs receiver depth calculated by KrakenC, Eq. (23) and Eq.(29) for 250 Hz at 1 km, 5 km, 25 km and 125 km. Beam shift is neglected in these comparisons. For the dashed and dash-dotted lines, PL is approximated using $F \approx F_0$. (lower graphs) The source depth is 30 m.

The features at the complementary depth and seabed are not visible in the graphs of proposed solutions by Eq.(23) and Eq.(29) because the symmetry property of Eq.(30), Sec II.C, is not applied. They can be obtained, if desired, by applying the symmetry property described in Section 2.2.2.2.C. In Figure 3, Eq.(33) and Eq.(35) are evaluated for the different angle distributions (Gaussian and dipole Gaussian) for different source depths at 250 Hz and 25 km. In these comparisons, the same parameters of Scenario A2.I (described above) are used. The benefit of the Faddeeva function is that it includes all relevant limiting cases in one formula. To illustrate this benefit, consider the large R limit $\left(\frac{Z}{2\sqrt{R}} \ll \sqrt{R} \theta_c\right)$ in Eq.(26). In this limit, $\Phi[Z, R, \theta_c]$ simplifies to

$$\begin{aligned} \Phi[Z, R, \theta_c] &\approx \sqrt{\frac{\pi}{R}} \frac{\exp\left(-\frac{Z^2}{4R}\right)}{4} \left[(1 + \operatorname{erf}(\sqrt{R} \theta_c)) - (1 - \operatorname{erf}(\sqrt{R} \theta_c)) \right] \\ &\approx \frac{1}{2} \sqrt{\frac{\pi}{R}} \exp\left(-\frac{Z^2}{4R}\right) \end{aligned} \quad (36)$$

where $\operatorname{erf}(\sqrt{R} \theta_c) \approx 1$ for large R . When Eq. (36) is substituted in Eq.(23), we obtain the following general-purpose formula for the mode stripping region (generalising Weston's case 5 and 6)

$$F_0(z_r, z_s) = F_{\text{ref}} (1 - \exp(-2(k_1 z_r \phi_0)^2) - \exp(-2(k_1 z_s \phi_0)^2) [1 - \exp(-2(k_1 z_r \phi_0)^2)],$$

where $\phi_0 = \sqrt{\frac{h}{2\eta r}}$. The transition between Cases 5 and 6 is illustrated in Figure 3 by showing transition from 1 m (Case 6) to 30 m (Case 5) at 250 Hz. At the intermediate source depth of 10 m, neither Case 1 nor Case 5 predicts the correct solution.

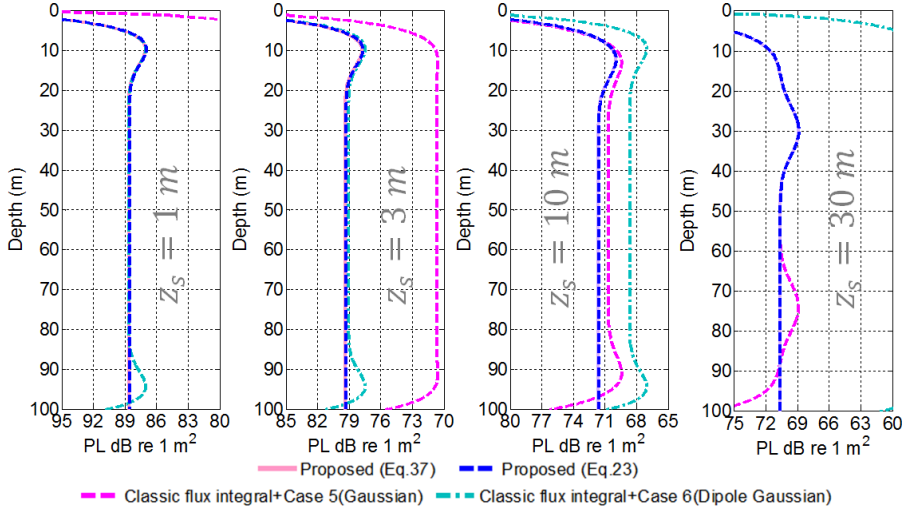


Figure 3. Propagation loss (PL) vs depth calculated by Eq.(23), Eq.(37) Weston's approach (Eq.(33)) for the different energy distribution with angle (Gaussian dipole Gaussian,) for different source depths (1 m, 3 m, 10 m and 30 m), Range is 25 km. Frequency is 250 Hz.

Eq.(33) and Eq.(35) each satisfy the reciprocity principle for their respective regime of applicability. For instance, Eq.(33) satisfies reciprocity for large receiver depths because of the use of $\sin^2(\gamma_{1n}z_s) \approx 1/2$ approximation. Eq.(35) satisfies reciprocity for sufficiently small source and receiver depth.

We apply Eq. (23) next (Figure 4) to investigate the depth dependence for Scenario A2.1 from the Weston Memorial Workshop, for frequencies in the range 50 Hz to 3500 Hz, at a range of 5 km. The symmetry approach described by Eq.(30) is used to obtain features close to the complementary depth and the seabed. The expressions for F_- and F_+ from Eq.(31) and Eq.(32) are evaluated numerically by the Rayleigh reflection coefficient based solution from Eq.(29), with and without beam shifts. There is good agreement with KrakenC, especially when the source or receiver is close to the sea surface. Although the results with the effect of beam shift are closer to KrakenC predictions than without beam shift, the difference is small. The beam shift can lead to larger differences especially for low frequencies. The proposed solution (Eq.(29)) can provide an accurate approximation to the incoherent normal mode sum, without the need to compute discrete eigenvalues.

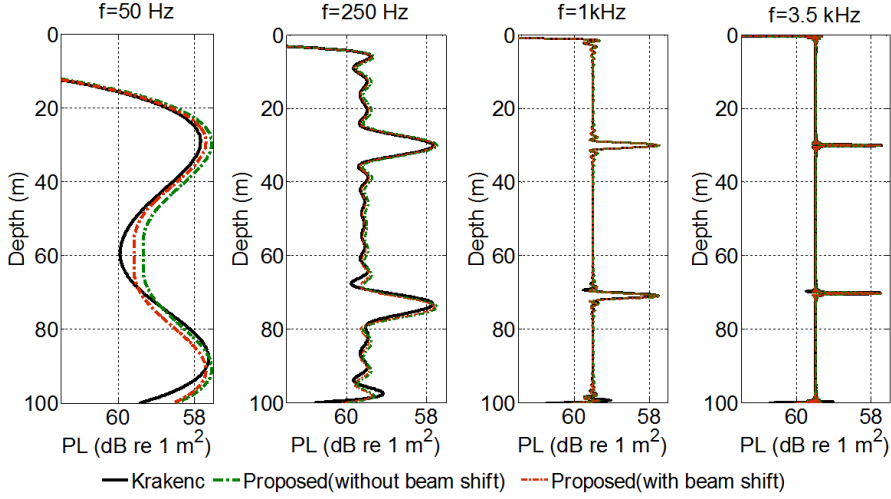


Figure 4. PL vs receiver depth by KrakenC and Eq. (30) (F_0 is calculated using Eq. (29)) for 50 Hz, 250 Hz, 1 kHz and 3.5 kHz at a range of 5 km from the source. The source depth is 30 m.

The classic flux integral without depth dependent properties (Eq. (34)) is selected as a reference PL ($PL_{\text{ref}} = 10 \log_{10} \frac{F_{\text{ref}}^{-1}}{1 \text{ m}^2} \text{ dB}$), with $h = 100 \text{ m}$, $\eta \cong 0.273777 \text{ Np/rad}$ and $\theta_c = 0.489957 \text{ rad}$. The relative PL ($PL_{\text{relative}} = PL - PL_{\text{ref}}$) is shown in Figure 5. PL is calculated using Eq.(30) (with the Rayleigh reflection coefficient, without beam shift) and KrakenC. In Figure 5, the range variation of the relative PL versus range at receiver depths 1 m, 30 m and 50 m is shown for 250 Hz. Good agreement between Kraken and Eq.(30) is observed. The largest differences between the proposed solution and Kraken at the different receiver depths considered are 0.19 dB (at 1 m), 0.07 dB at (30 m) and 0.15 dB (at 50 m). Figure 5 also shows the contribution of the proposed solution to Weston's classical flux integral. For example, we see large effects due to the surface decoupling at 1 m receiver depth.

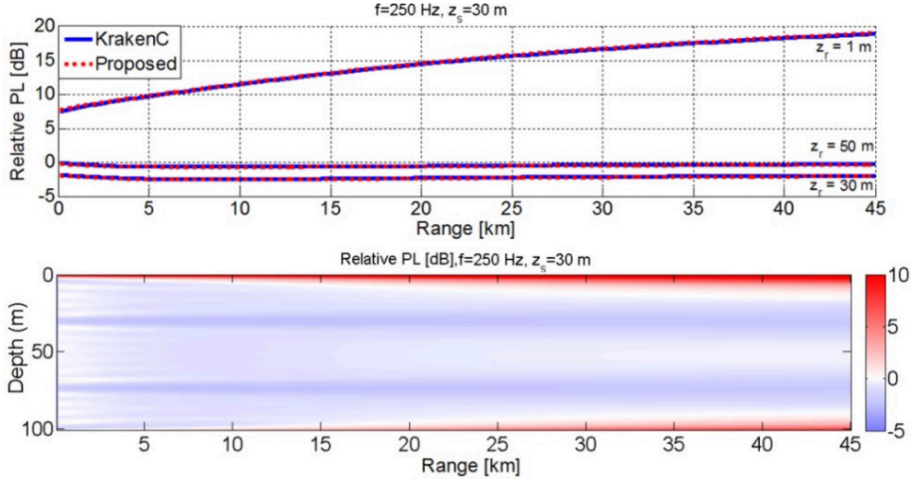


Figure 5. Relative Propagation loss ($PL_{relative} = PL - PL_{ref}$) versus range at different receiver depths (1 m, 30 m and 50 m) for 250 Hz (upper graph). Relative Propagation loss versus depth and range for 250 Hz (lower graph). PL is calculated using Eq.(30) (without beam shift) and KrakenC (incoherent mode sum). PL_{ref} is the reference PL from Eq. (34).

2.2.4. Conclusions

In this section, the depth dependence of propagation loss (PL) is investigated by deriving a depth-dependent correction term (as given by Eq.(19)) to the error function associated with the classical flux solution(Eq.(34)). This equation is derived from an incoherent normal mode sum, and provides a depth-dependent solution for a lossy Pekeris waveguide without the need for (computationally expensive) calculation of eigenvalues. Eq. (23) provides an analytical solution which includes all relevant depth corrections (Weston's low pass, Gaussian, and dipole Gaussian cases) in one formula. the depth dependence of PL for long ranges can be estimated by a simpler formula Eq.(37). If it is desired, a numerical solution based on Rayleigh reflection coefficient (Eq.(29)) including beam shifts can be also used in order to increase the accuracy. The explicit form of the result provides insight into the behaviour of the sound field close to the source depth, complementary source depth, sea surface and seabed.

APPENDIX A: THE SYMMETRY OF PROPAGATION FACTOR BY MODE SUM

The purpose of this appendix is to demonstrate that, if Weston's vertical wave shift is assumed to be independent of angle, the propagation factor for a source at the complementary source depth is equal to that for a source at the true source depth, and similarly for the receiver (for the isovelocity and isodensity case). Substituting $\gamma_{1n} = \frac{n\pi}{D}$ into

$$F(z_s, z_r) = \frac{2\pi}{r} \sum_{n=1}^{\infty} \frac{A_n^4 \sin^2(\gamma_{1n} z_r) \sin^2(\gamma_{1n} z_s)}{\kappa} \exp(-2\delta_n r) \quad (A.1)$$

the propagation factor becomes

$$F(z_s, z_r) = \frac{2\pi}{r} \sum_{n=1}^{\infty} \frac{A_n^4 \sin^2\left(n\pi \frac{z_s}{D}\right) \sin^2\left(n\pi \frac{z_r}{D}\right)}{\kappa_n} \exp(-2\delta_n r) \quad (A.2)$$

By using the periodicity property of trigonometric functions as $\sin^2\left(n\pi \frac{D-z_r}{D}\right) = \sin^2\left(n\pi \frac{z_r}{D}\right)$, the equation

$$F(z_s, D - z_r) = \frac{2\pi}{r} \sum_{n=1}^{\infty} \frac{A_n^4 \sin^2\left(n\pi \frac{z_s}{D}\right) \sin^2\left(n\pi \frac{z_r}{D}\right)}{\kappa_n} \exp(-2\delta_n r) \quad (A.3)$$

is obtained for the complementary receiver depth . The right hand side of this equation is equal to the propagation factor for z_r thus proving that the propagation factors at receiver and complementary receiver depths are equal. By repeating the same steps for the complementary source depth as $D - z_s$, a similar identity can be obtained. The resulting identities can be written

$$F(z_s, z_r) = F(z_s, D - z_r) \quad (A.4)$$

$$F(z_s, z_r) = F(D - z_s, z_r) \quad (A5)$$

and therefore

$$F(z_s, z_r) = F(D - z_s, D - z_r) \quad (A6)$$

These symmetry properties can be exploited to avoid the need to calculate PL for all receiver and source depth combinations separately. For computational efficiency, PL for all receiver depths can be calculated by Eq.(30) which based on these properties.

APPENDIX B: THE ASYMMETRY OF PROPAGATION FACTOR BY INTEGRAL SOLUTION

In this section, the symmetry of the integral representation is investigated. Figure 2 demonstrates that the integral over a continuum of modes fails to exhibit the symmetry property of the discrete mode sum characterised by Eq.(A4)-Eq.(A5). the purposes of this Appendix are to describe the conditions for which the integral solution breaks down and explain the reason for this failure. The differences between the discrete mode summand and continuous angle integrand are also shown. the $W(z_r, z_s, \theta)$ term in the integral solution is derived from eigenfunctions, which lead to the symmetrical propagation factor as described in Appendix A. First, the symmetry of $W(z_r, z_s, \theta)$ is investigated by replacing z_r with $-z_r$:

$$\begin{aligned} & W(D - z_r, z_s, \theta) \\ &= \cos(2z_s k_1 \sin \theta) + \cos(2Dk_1 \sin \theta - 2z_r k_1 \sin \theta) \\ &= \frac{\cos(2(z_s + z_r)k_1 \sin \theta - 2Dk_1 \sin \theta) + \cos(2(z_s - z_r)k_1 \sin \theta + 2Dk_1 \sin \theta)}{2} \end{aligned} \quad (B1)$$

The symmetry property shown by Eq.(A5) and Eq.(A6) comes from the periodicity of trigonometric functions. Thus, in order to ensure the symmetry property, $2Dk_1 \sin \theta$ must be equal to $2n\pi$, which holds only for the discrete angles corresponding to the eigenvalues. However, this relation is not valid for the non-integer values of n (continuous angles). Thus, having continuous angles in the integration can cause an asymmetric solution. The following equality can only be written for the discrete angles (θ_n),

$$\gamma_n = k_1 \sin(\theta_n) = \frac{n\pi}{D}, n = 1, 2, 3, \dots \quad (B2)$$

Eq.(B1) and Eq.(18) for continuous angles are different. This means the symmetry relations formulated by Eq.(A4) to Eq.(A6) are not satisfied for the continuous angle approximation. For an illustration of symmetry properties for discrete and continuous angles, the argument of $\sin^2(\gamma_n z_r) \sin^2(\gamma_n z_s)$ is plotted for discrete eigenvalues ($\gamma_n = \frac{n\pi}{D}$) and continuous angles ($\gamma_n = k_1 \sin \theta$) in Figure 6. The same comparison is also repeated for the complementary receiver depth as $\sin^2(\gamma_n (D - z_r)) \sin^2(\gamma_n z_s)$. The symmetry property for the receiver (Eq.(A4)) requires $\sin^2(\gamma_n z_r) \sin^2(\gamma_n z_s) = \sin^2(\gamma_n (D - z_r)) \sin^2(\gamma_n z_s)$. The validity of the continuous angle approach is investigated by the comparisons in Figure 6. For this comparison, $f = 250$ Hz, $z_r = 10$ m, $D = 104.06$ m and $\theta_c = 0.49$ rad.

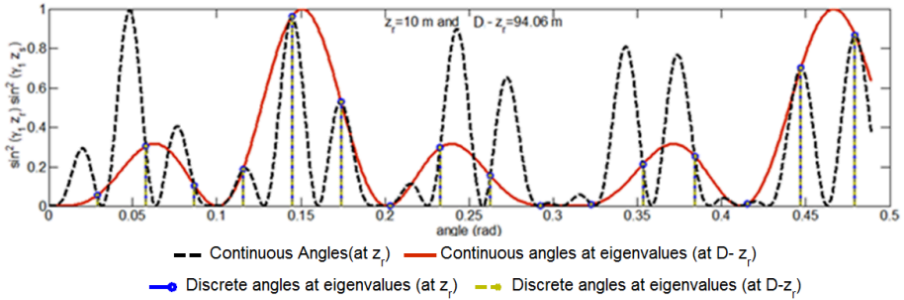


Figure 6. Variation of $\sin^2(\gamma_n z_r) \sin^2(\gamma_n z_s)$ for discrete angles at eigenvalues (vertical bars) and continuous angles (solid and dashed lines). the source depth is 30 m.

This comparison shows that the discrete mode solutions at receiver depth and complementary receiver depth are identical when calculated using Weston's wave shift concept, if the vertical wave shift is assumed independent of grazing angle. According to Eq. (B2), the discrete angles are calculated as $\theta_n = \arcsin\left(\frac{nc_1}{2Df}\right)$. The continuous angles can be any value between zero and θ_c , irrespective of the eigenvalues. In order for the continuous angle integral to approximate the discrete mode sum, the area under the curves in Figure 6 must be equal to the sum of contributions from discrete eigenvalues, which is the case if the curve contains no energy above

the Nyquist frequency corresponding to the rate at which the curves are sampled by the series of eigenvalues. Writing

$$\sin\left(\frac{n\pi}{D}z_s\right)\sin\left(\frac{n\pi}{D}z_r\right) = \frac{1}{2i}\left(\exp\left(i\frac{n\pi}{D}z_s\right) - \exp\left(-i\frac{n\pi}{D}z_s\right)\right)\frac{1}{2i}\left(\exp\left(i\frac{n\pi}{D}z_r\right) - \exp\left(-i\frac{n\pi}{D}z_r\right)\right),$$

the highest frequency component is the term proportional to $\exp(\pm i2n\pi F)$, where the highest frequency, F , is equal to $\frac{z_s+z_r}{2D}$. According to the Nyquist-Shannon theorem, the continuous function is well sampled, in the sense that it can be reconstructed from these samples, by the discrete modes if F is less than the Nyquist frequency (half the sampling rate), which is equal to 0.5. While it does not follow directly from this theorem, it seems reasonable to assume that the integral of a continuous function will be a good approximation to a discrete sum if the maximum frequency is below the Nyquist frequency corresponding to the sampling rate, and not otherwise. If the continuous function is sufficiently well sampled in the same sense, one can therefore expect the integral to exhibit the same symmetry property as the discrete sum. Given that the maximum frequency is $F = \frac{z_s+z_r}{2D}$ and the Nyquist frequency is 0.5, it follows that the condition for symmetry is $z_s+z_r < D$. This condition shows that the proposed solution is valid up to the complementary source depth ($z_r < z_{cs}$). Thus, the proposed solution by the continuum approach is valid for $z_r < z_{cs} - 2\sigma$, where σ is the width of the peak at the complementary source depth. In the mode stripping, this width is given by the simple formula as $\sigma = \frac{1}{2k_1\phi_0}$. In the cylindrical spreading region, the width is less well defined.

Even though the symmetry properties are not satisfied for the integral representation at the complementary source and receiver depths, the correct propagation factor can be obtained by exploiting the symmetry of Eq.(30) for $D/2 < z_r < D$.

APPENDIX C: DERIVATIONS OF WESTON'S CASES 5 AND 6 FROM THE PROPOSED SOLUTION

In this Appendix, Weston's Case 5 (Gaussian) and Case 6 (dipole Gaussian) are derived from Eq.(37).

Derivation of Case 5

When z_s is large enough and far from the waveguide's boundaries ($k_1 z_s \phi_0 \gg 1$, such that $\exp(-2(k_1 z_s \phi_0)^2)$) may be neglected, the propagation factor can be written as

$$F_0(z_r, z_s) \approx F_{\text{ref}}(1 - \exp(-2(k_1 z_r \phi_0)^2)) \quad (C1)$$

consistent with Weston's Case 5. Eq.(C1) can also be derived from [Denham,1986] by applying the reciprocity principle to Eq. (25) from that paper.

Derivation of Case 6

When z_s is small and close to sea surface, the propagation factor can be written as

$$F_0(z_r, z_s) = F_{\text{ref}}(1 - \exp(-2\varepsilon^2) - \exp(-2(k_1 z_r \phi_0)^2) [1 - \exp(-2\varepsilon^2) \cosh(4k_1 z_r \phi_0 \varepsilon)]) \quad (C2)$$

Where $\varepsilon = k_1 z_s \phi_0$. For small ε , the exponential and hyperbolic cosine function can be replaced with $\exp(-2\varepsilon^2) \approx 1 - 2\varepsilon^2$ and $\cosh(4\varepsilon k_1 z_r \phi_0) \approx 1 + \frac{(4\varepsilon k_1 z_r \phi_0)^2}{2} = 1 + 8(\varepsilon k_1 z_r \phi_0)^2$,

$$F_0(z_r, z_s) = F_{\text{ref}}(2\varepsilon^2 - \exp(-2(k_1 z_r \phi_0)^2)[1 - (1 - 2\varepsilon^2)(1 + 8(\varepsilon k_1 z_r \phi_0)^2)]) \quad (C3)$$

Then, neglecting terms of order ε^4 or higher

$$F_0(z_r, z_s) = 2\varepsilon^2(1 - (1 - 4(k_1 z_r \phi_0)^2)\exp(-2(k_1 z_r \phi_0)^2))F_{\text{ref}} \quad (C4)$$

consistent with Weston's Case 6. For large receiver depths, this expression may be approximated using $\exp(-2(k_1 z_r \phi_0)^2) \approx 0$, in which case Eq. (27) from [Denham,1986] is recovered.

2.3 SOPRANO HYBRID PROPAGATION MODEL: RANGE-DEPENDENT PROPAGATION EQUATIONS AND RESULTS FOR THE SHALLOW WATER WAVEGUIDES

This section is a modified version of [H.Ö Sertlek, M.A. Ainslie and K.L. Heaney, Range Dependent propagation equations and results for shallow water waveguides, under review by Journal of Acoustical Society of America]

Abstract: *The estimation of propagation loss for a range dependent shallow water waveguide is considered. Specifically, an analytical formulation for the calculation of the depth dependent propagation loss in isovelocity water with a gradually range dependent seabed is introduced. The range dependent bathymetry is handled with Weston's ray invariant approach. The depth dependence of propagation loss is formulated using a transformation from an incoherent mode sum to an integral over angle, in the adiabatic approximation, and the results obtained in this way are tested by comparison with a full adiabatic normal mode sum. The validity of the adiabatic approximation itself is then investigated by means of a comparison with parabolic equation and coupled normal mode results for selected test cases from the Weston Memorial Workshop held at the University of Cambridge in April 2010. The proposed approach provides practical, fast and accurate results.*

2.3.1. INTRODUCTION

The estimation of propagation loss (PL) [Ainslie,2010a; ISO/DIS 18405] for a range dependent shallow water isovelocity waveguide is relevant to various applications of underwater acoustics such as environmental impact assessment, underwater communications and sonar performance modelling. The present section introduces a method that combines the accuracy of an incoherent adiabatic normal mode sum with the speed of Weston's flux integral approach. To solve range dependent propagation problems, normal mode methods apply various approaches such as mode coupling, mode-matching or adiabatic approaches [Jensen et al, 1994]. These approaches are based on a stair-step approximation for the bathymetry and the calculation of normal mode eigenvalues for each stair step. Range dependent normal mode solutions can be computationally expensive for high frequencies or deep water where many modes propagate, and analytical solutions offer a practical alternative that avoids long computational times [Harrison,2005 ; Harrison,2013; Holland,2010]. Weston introduced the flux integral method for evaluation of PL for a variable water depth and arbitrary sound speed profile [Weston,1959]. By using the effective depth approach, Weston [Weston,1976] provided analytical expressions for the depth-averaged propagation factor (F) for various depth profiles. An arbitrary bathymetry can be constructed as a combination of these depth profiles. However, the dependence of the propagation factor on receiver and source depths is not visible in this approach.

In the present section, the method of [Weston,1976] is combined with the depth dependent propagation formula of [Sertlek and Ainslie,2013] to derive a formulation for depth-dependent propagation loss in a range dependent waveguide. Discrete and leaky mode effects are also considered, increasing the accuracy of this approach at low frequencies and long ranges. This proposed solution can provide fast and accurate propagation loss predictions for range dependent water depth and sediment type across a wide range of frequencies without summing a large number of normal modes. The results obtained in this way are validated with adiabatic mode theory. Then, the accuracy of the adiabatic mode theory is tested by comparison with coupled mode and parabolic equation model's results. Selected cases from the 2010 Weston Memorial Workshop [Ainslie,2010b] are used, providing insights into the performance of widely used propagation models in a shallow water environment.

This work is motivated by the need for sound mapping across a wide frequency range, namely 10 Hz to 100 kHz, roughly corresponding to the hearing range of marine animals. The proposed

approach enables the calculation of shallow water sound maps in an efficient way without requiring long computation times or advanced computer systems.

2.3.2. DEPTH DEPENDENCE OF PROPAGATION LOSS IN RANGE DEPENDENT WAVEGUIDE

A. Derivation

Propagation loss can be defined in terms of the propagation factor, F , as $PL = 10 \log_{10} \frac{F^{-1}}{1 \text{ m}^2}$ dB where F is the propagation factor [Ainslie, 2010a; ISO/DIS 18405]. For range independent waveguides, Weston's flux integral can be modified to take into account the depth dependence of the propagation factor [See Section 2.2]. This approach is generalised here for range dependent media. The derivation starts by applying the adiabatic approximation to the incoherent mode sum

$$F(r, z_r; z_0) = \sum_{n=1}^{\infty} \psi_n^2(z_0, 0) \psi_n^2(z_r, r) R_n^2(r) \quad (1)$$

where the eigenfunction (for isovelocity water) is $\psi_n(z, r) = A_n \sin(\gamma_n(r)z)$ and $R_n(r) = \frac{2\pi}{r \kappa_n(r)} \exp(-2 \int_0^r \delta(r') dr')$. Here A_n is the amplitude of the n th eigenfunction, γ_n is the vertical wavenumber, and κ_n the horizontal wavenumber. The mode decay rate $\delta(r') = -\frac{\ln(|V(\theta_n)|)}{r_{\text{CM}}}$ is the mode attenuation term in the horizontal direction which adds a small imaginary part to κ_n , $r_{\text{CM}} = 2h \cot \theta$ is the modal cycle distance for isovelocity water, and $V(\theta_n)$ is the reflection coefficient of the seabed. The integral in the exponential term for $R_n(r)$ can be written

$$\int_0^r \delta_n(r') dr' = -D^2(0) \sin^2 \theta_0 \int_0^r \frac{\ln(|V(\theta')|)}{2h(r') \cot \theta' D^2(r') \sin^2 \theta'} dr' \quad (2)$$

where

$$D(r) = h(r) + \Delta_W \quad (3)$$

is the wave-shifted water depth, $\Delta_W = \frac{\rho_2/\rho_1}{k_1 \sin \theta_c}$ is the corresponding vertical wave shift [Weston, 1994; Weston, 1960] and θ_c is the critical angle. Eigenvalues for the discrete sum can be approximated using $\gamma_n(r) = \frac{n\pi}{D(r)}$, and $D(0)$ and $D(r)$ are wave-shifted water depths at source and receiver range. Thus, the propagation factor becomes

$$F(r, z_r; z_0) = \frac{2\pi}{r} \sum_{n=1}^{\infty} \frac{A_{0n}^2 A_{rn}^2 \sin^2(\gamma_n(r) z_0) \sin^2(\gamma_n(r) z_r)}{k_{rn}(r)} \exp \left(D^2(0) \sin^2 \theta_0 \int_0^r \frac{\ln(|V(\theta')|)}{h(r') D^2(r') \cos \theta' \sin \theta'} dr' \right) \quad (4)$$

where $A_{0n, rn}^2 = \frac{4}{r_{cM}(\theta_{0,r}) \tan \theta_{0,r}}$. Further, $\theta_{0,r}$ shows the mode grazing angles at source and receiver ranges and θ' denotes the grazing angle at range r' . Using the trigonometric identity $\sin^2(\gamma_n(r) z) = \frac{1}{2} - \frac{1}{2} \cos(2\gamma_n(r) z)$, and approximating the discrete sum by a continuous angle integral [Sertlek and Ainslie, 2014a] it follows that

$$F_0(r, z_r; z_0) = \frac{2}{r} \int_0^{\theta_{\text{lim}}} \frac{D(0) \cos \theta_0}{h(0) D(r) \cos \theta_r} (1 - W(z_r, z_0, \theta_0)) \exp \left(D^2(0) \sin^2 \theta_0 \int_0^r \frac{\ln(|V(\theta')|)}{h(r') D^2(r') \cos \theta' \sin \theta'} dr' \right) d\theta_0 \quad (5)$$

where $\theta_{\text{lim}} = \arcsin \left(\frac{\min\{D(0), D(r)\} \sin \theta_c}{D(0)} \right)$. The function $W(z_r, z_0, \theta_0)$ is

$$W(z_r, z_0, \theta_0) = \cos(2k_w z_0 \sin \theta_0) + \cos \left(2k_w z_r \frac{D(0)}{D(r)} \sin \theta_0 \right) - \frac{\cos(2k_w \zeta_- \sin \theta_0) + \cos(2k_w \zeta_+ \sin \theta_0)}{2} \quad (6)$$

where $\zeta_{\pm} = z_0 \pm z_r \frac{D(0)}{D(r)}$, and Weston's ray invariant relation [Weston,1994]

$$D(r')\sin\theta' = D(0)\sin\theta_0 = D(r)\sin\theta_r \quad (7)$$

is used to relate angles at the source and receiver ranges. Eq.(5) can provide an analytical formulation for range dependent propagation problems. The factor $(1 - W(z_r, z_0, \theta_0))$ results from the product of the source and receiver eigenfunctions. A more detailed physical description of the range independent version of this term and its relation with Weston's solution in [Weston,1980] are provided in Section 2.2.

B. Analytical solution for exponential reflection coefficient

In Eq.(5), different forms for the reflection coefficient can be used. For an exponential reflection coefficient in the form

$$|V_B| = \exp\left(-\eta(r) \frac{\sin(2\theta)}{2}\right) \quad (8)$$

the propagation factor can be written

$$F_0 = \frac{2}{r} \int_0^{\theta_{lim}} \frac{D(0)\cos\theta_0}{h(0)D(r)\cos\theta_r} (1 - W(z_r, z_0, \theta_0)) \exp\left(-D^2(0)\sin^2\theta_0 \int_0^r \frac{\eta(r')}{h(r')D^2(r')} dr'\right) d\theta_s \quad (9)$$

This integral gives the propagation factor for range dependent media. If one ignores the wave and beam [Sertlek and Ainslie, 2014a; Weston,1994] shifts for high-order modes and assumes $\cos\theta_{0,r} \approx 1$ (consistent with the small angle approximation), it follows that

$$F_0 = \frac{2}{rh(r)} \int_0^{\theta_{\text{lim}}} (1 - W(z_r, z_0, \theta_0)) \exp\left(-h^2(0) \theta_0^2 \left\langle \frac{\eta}{h^3} \right\rangle r\right) d\theta_0 \quad (10)$$

where $\left\langle \frac{\eta}{h^3} \right\rangle$ is the average value of $\frac{\eta}{h^3}$ from the source (at range zero) to range r . In Appendix A this quantity is evaluated analytically using Weston's effective depth approach [Weston,1976]. Eq.(10) can be solved analytically in the terms of Faddeeva functions as described by SA-25 (using SA- n here and throughout to denote Eq. (n) from Section 2.2.). In this way, the analytical solution for Eq.(10) can be obtained as

$$\begin{aligned} & F_0(r, z_r; z_0) \\ &= r^{-\frac{3}{2}} \sqrt{\frac{\pi}{\eta h_{\text{eff}}}} \operatorname{erf}\left(\sqrt{h^2(0) \left\langle \frac{\eta}{h^3} \right\rangle r} \theta_{\text{lim}}\right) \\ & - \left\{ \frac{2}{rh_r} \left[\Phi\left[2k_w z_0, h^2(0) \left\langle \frac{\eta}{h^3} \right\rangle r, \theta_{\text{lim}}\right] + \Phi\left[2 \frac{D(0)}{D(r)} k_w z_r, h^2(0) \left\langle \frac{\eta}{h^3} \right\rangle r, \theta_{\text{lim}}\right] \right. \right. \\ & \left. \left. - \frac{\Phi\left[2k_w \zeta_-, h^2(0) \left\langle \frac{\eta}{h^3} \right\rangle r, \theta_{\text{lim}}\right] + \Phi\left[2k_w \zeta_+, h^2(0) \left\langle \frac{\eta}{h^3} \right\rangle r, \theta_{\text{lim}}\right]}{2} \right] \right\} \quad (11) \end{aligned}$$

where

$$\begin{aligned} \Phi[Z, R, \theta_{\text{lim}}] &= \int_0^{\theta_{\text{lim}}} \cos(Z\theta) \exp(-R\theta^2) d\theta \\ &= \sqrt{\frac{\pi}{R}} \frac{\exp\left(-\frac{Z^2}{4R}\right)}{4} \left[w\left(\frac{Z}{2\sqrt{R}} - i\sqrt{R}\theta_{\text{lim}}\right) \exp\left(\left(\frac{Z}{2\sqrt{R}} - i\sqrt{R}\theta_{\text{lim}}\right)^2\right) \right. \\ & \left. - w\left(\frac{Z}{2\sqrt{R}} + i\sqrt{R}\theta_{\text{lim}}\right) \exp\left(\left(\frac{Z}{2\sqrt{R}} + i\sqrt{R}\theta_{\text{lim}}\right)^2\right) \right] \quad (12) \end{aligned}$$

and $w(x + iy)$ is the Faddeeva function [Abramowitz and Stegun, 1972]. For the large R limit $\left(\frac{z}{2\sqrt{R}} \ll \sqrt{R} \theta_{\text{lim}}\right)$, $\Phi[Z, R, \theta_c] \approx \frac{1}{2} \sqrt{\frac{\pi}{R}} \exp\left(-\frac{z^2}{4R}\right)$ and $\text{erf}\left(\sqrt{h^2(0) \left\langle \frac{\eta}{h^3} \right\rangle r} \theta_{\text{lim}}\right) \approx 1$. In this limit, the solution simplifies to

$$F_0(r, z_r; z_0) = r^{-\frac{3}{2}} \sqrt{\frac{\pi}{\eta h_{\text{eff}}}} \left(1 - \exp(-2\phi_0^2 k_w^2 z_0^2) - \exp\left(-2\phi_0^2 k_w^2 z_r^2 \frac{D^2(0)}{D^2(r)}\right) + \frac{\exp(-2\phi_0^2 k_w^2 (\zeta_-)^2) + \exp(-2\phi_0^2 k_w^2 (\zeta_+)^2)}{2} \right) \quad (13)$$

where $\phi_0 = \sqrt{\frac{1}{2 h^2(0) H_\eta}}$, $\left\langle \frac{\eta}{h^3} \right\rangle = \frac{\eta h_{\text{eff}}}{h^2(0) h^2(r)}$ for a constant η , and Eq.(13) is a generalisation of SA-37 to the range dependent situation (SA-37 is identical to Eq (9) of [Weston, 1991], which was not cited by [Sertlek and Ainslie, 2014a] because they were unaware of the existence of [Weston, 1991] at that time). Equation (13) is valid for constant η and in the limit of large R .

2.3.3. DISCRETE MODE EFFECTS FOR RANGE DEPENDENT MEDIA

At short ranges, where many modes are present, the discrete mode sum may be approximated by an integral over a continuum of modes [Harrison and Ainslie, 2010]. In the mode stripping region, the number of modes that contribute to the sound pressure field decreases with increasing range, until at some point there remains only a handful, so that the integral ceases to provide a good approximation to the discrete sum. This point is the end of the mode stripping region and the beginning of a region in which the discreteness of the mode sum becomes important [Ainslie, 2010a]. In order to retain accuracy in this discrete mode region, a few low-order modes can be separated from the integral solution. In other words

$$F = \underbrace{\sum_{n=1}^M \psi_n^2(z_0) \psi_n^2(z_r, r) R_n^2(r)}_{F_M} + \underbrace{\sum_{n=M+1}^{\infty} \psi_n^2(z_0) \psi_n^2(z_r, r) R_n^2(r)}_{G_M} \quad (14)$$

Replacing G_M by an integral approximation for a continuum of modes, and applying the symmetry property identified by SA-30, we obtain

$$G_M(z_r, z_0) = \begin{cases} F_-(z_r, z_0), & z_0 < D/2 \\ F_+(z_r, z_0), & z_0 > D/2 \end{cases} \quad (15)$$

$$\text{where } F_- = \begin{cases} G_{M0}(z_r, z_0), & z_r < D/2 \\ G_{M0}(D - z_r, z_0), & z_r > D/2 \end{cases} \text{ and } F_+ = \begin{cases} G_{M0}(z_r, D - z_0), & z_r < D/2 \\ G_{M0}(D - z_r, D - z_0), & z_r > D/2 \end{cases}.$$

G_{M0} is the continuous angle representation of the propagation factor

$$G_{M0} = \frac{2}{r} \int_{\theta_{M+1/2}}^{\theta_{\text{lim}}} \frac{D(0) \cos \theta_0}{h(0) D(r) \cos \theta_r} (1 - W(z_r, z_0, \theta_0)) \exp \left(\left(D^2(0) \sin^2 \theta_0 \int_0^r \frac{\ln(|V(\theta')|)}{h(r') D^2(r') \cos \theta' \sin \theta'} dr' \right) \right) d\theta_0 \quad (16)$$

The lower integration limit is $\theta_{M+1/2} \equiv \frac{\theta_M + \theta_{M+1}}{2}$ because the first M modes are summed separately. Eq.(15) helps to obtain the properties at the sea surface (or seabed) and source (or complementary source) depths. The mode attenuation is calculated with the Kornhauser and Raney approximation [Kornhauser and Raney, 1955] and adiabatic approach. The resulting modal decay rate [Ainslie et al, 1993] is

$$\beta_n(r') = \frac{\epsilon \gamma_n^2 (\rho_{\text{sed}} / \rho_w) \cot^3 \theta_c \sec \theta_c}{h k_w \sqrt{k_w^2 - \gamma_n^2} \left(\left(1 - \frac{\gamma_n^2}{k_w^2 \sin^2 \theta_c} \right)^{1/2} + \frac{\rho_{\text{sed}}^2 \gamma_n^2}{\rho_w^2 k_w^2 \sin^2 \theta_c} + \frac{\rho_{\text{sed}}}{\rho_w k_w h \sin \theta_c} \right)} \quad (17)$$

where ρ_{sed} and ρ_w are the densities of seawater and sediment, respectively, and ϵ is the fractional imaginary part of the sediment wavenumber. This equation was derived from mode theory formulas that implicitly take into account wave and beam shifts [Weston, 1994]. In Eq. (17) we choose not to neglect such wave and beam shifts because the presence of these terms in the exponent leads to important corrections that are needed to maintain accuracy at long range. The contribution to the propagation factor from the first M discrete modes can be written as

$$F_M = \frac{8\pi}{rD(0)D(r)} \sum_{n=1}^M \frac{\sin^2(\gamma_n z_0) \sin^2(\gamma_n z_r)}{\sqrt{k_w^2 - \gamma_n^2}} \exp\left(-2 \int_0^r \beta(r') dr'\right) \quad (18)$$

Finally, the hybrid formulation of the propagation factor in range dependent media can be written analytically by ignoring the wave shifts for high-order of modes and using the small angle approximation (by assuming $\cos\theta_{0,r} \approx 1$),

$$\begin{aligned} F &= F_M \\ &+ \frac{2}{rh(r)} \int_{\theta_{M+1/2}}^{\pi/2} (1 - W(z_r, z_0, \theta_0)) \exp\left(\left(h^2(0) \sin^2 \theta_0 \int_0^r \frac{\ln(|V(\theta)|)}{h^3(r') \sin \theta} dr'\right)\right) d\theta_0 \end{aligned} \quad (19)$$

Any form for the reflection coefficient, including both exact or approximate forms of the Rayleigh reflection coefficient [Harrison,2010] can be used for $V(\theta)$, depending on the desired accuracy. Use of the exact form in the numerical solutions increases accuracy and permits calculations above the critical angle [Harrison,2010], by extending the upper integration limit to $\frac{\pi}{2}$, thus taking into account the contribution from leaky modes. Including leaky mode terms in the integrand of the adiabatic approach (exponential term in Eq.(18)) provides a smoother transition in the upslope region in the examples that follow, in which ray paths are continually steepened, and the corresponding modes pass from the discrete spectrum to the continuous spectrum. In the downslope region after the ridge, the same effect happens in reverse, with the discrete mode spectrum continually re-populated by a process of downslope conversion.

2.3.4. COMPARISONS

A. Comparison Procedure:

Description of Test Cases

In these comparisons, test cases derived from Scenarios A2.I and A2.IV from the Weston Memorial Workshop (WMW) are used [Zampolli et al,2010]. The purpose of the WMW, held at the University of Cambridge in April 2010[Ainslie,2010b], was to improve understanding of signal to noise ratio and signal to reverberation ratio for simple sonar performance problems based on the 2006 ONR workshop[Thorsos and Perkins,2007]. Following [Sertlek and Ainslie,2013] and [Ainslie et al,2013], the selected test cases are referred to as “Case 1”, “Case 4” and “Case 9”. Cases 1 and 4 are identical to Scenarios A2.I and A2.IV, respectively, except that absorption in water and seabed roughness are both set to zero. Case 9 is a modified form of Case 4 suggested by Preston[Preston and Ellis,2012; Ellis and Pecknold,2012]. In all comparisons, the source depth (z_s) is 30 m, sound speed in water (c_w) and sediment (c_s) are, respectively, 1500 m/s and 1700 m/s. The sediment-seawater density ratio is 2 and the sediment absorption coefficient (β), in units of decibels per wavelength, is 0.5, corresponding to an absorption coefficient per unit frequency of 0.294118 dB/(m kHz). (The sediment absorption coefficient is related to fractional imaginary part of complex sediment wavenumber by means of $\epsilon = \beta \ln(10) / 40\pi$). The comparisons start with the range independent case (Case 1), which has 100 m water depth. More detailed comparisons were done for this range-independent case in [Section 2.2]. Case 4 has 100 m water depth up to 5 km from the source. Then, it features an upslope region from 5 km to 7 km up to water depth 30 m, with uniform water depth thereafter. Case 9 follows Case 4 to 8 km. The shallow water region (depth 30 m) is then followed by a downslope region from 8 km to 10 km down to water depth 100 m, and uniform depth thereafter (Fig. 1). Case 9 is identical to Case 4 in all respects other than these differences in bathymetry.

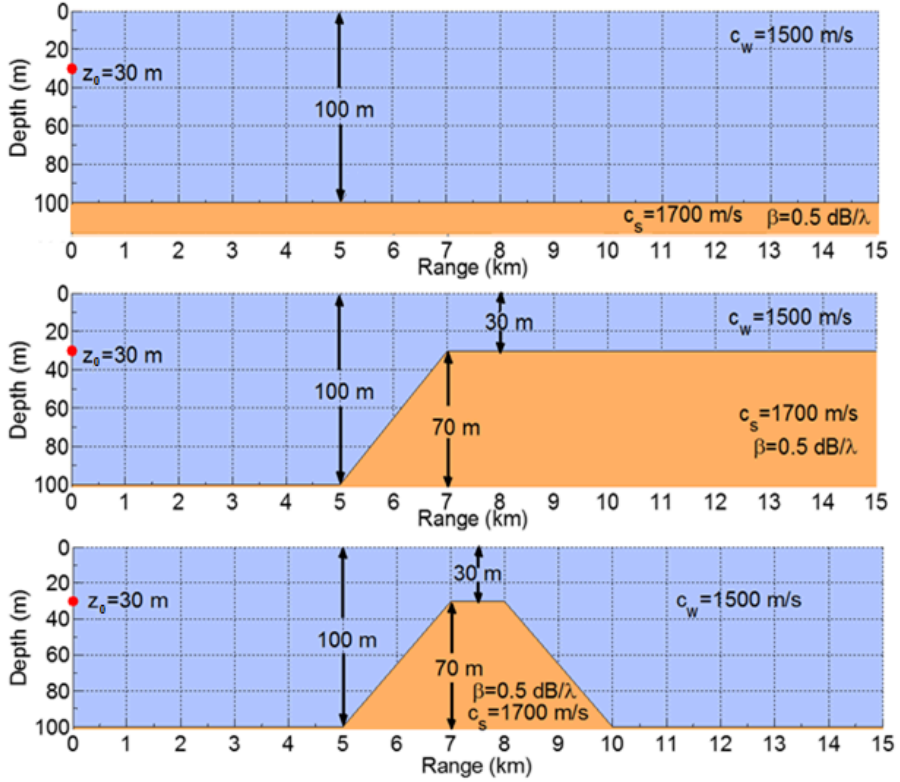


Figure 1. The bathymetry of Cases 1,4 and 9

Comparisons are made for the frequencies 250 Hz, 1 kHz and 3.5 kHz. For normal mode solutions, KrakenC and Couple are used. KrakenC is a normal mode algorithm that can handle range dependent problems with adiabatic and coupled mode approaches [Porter,1990]. For KrakenC's solution, we select the incoherent adiabatic option, which is based on complex eigenvalues and a stair-step approximation of the bathymetry. Couple is also a normal mode program, developed for obtaining normal mode solutions with various coupled mode approaches [Evans,1983]. Couple's solution (a coherent mode sum) is also based on a stair-step approximation. The proposed equations ((Eq.(11) ,Eq.(13) and Eq.(19))) in this section (incoherent mode sums) are based on a piecewise-linear bathymetry. For range dependent solutions, Δr_n equals 10 m as a stair-step length (in the mode theory solution) and piecewise-linear segment size (in the proposed integral solution) to have comparisons with the same resolution. Peregrine[Heaney and Campbell,2015] is an in-house version of RAM[Collins,1993] for parabolic equation calculations.

Reference and Relative PL

The challenge addressed here is that of magnifying small differences in PL predictions, when the individual PL curves exhibit a large dynamic range. In this situation, the use of a reference propagation loss curve and plotting the relative propagation loss as

$$PL_{\text{relative}}(r) = PL(r) - PL_{\text{ref}}(r) \quad (20)$$

can help to zoom in on detailed features. If the reference $PL_{\text{ref}}(r)$ is chosen to describe the general PL trend, PL_{relative} then describes the departure from that trend. In the following, Weston's flux integral [Weston, 1976] is chosen as the reference propagation factor

$$F_{\text{ref}} = \frac{2}{rh(r)} \int_0^{\theta_{\text{lim}}} \exp\left(-\frac{\theta_s^2 h_{\text{eff}}}{h^2(r)} r\right) d\theta_s = r^{-\frac{3}{2}} \frac{\pi}{\eta h_{\text{eff}}} \operatorname{erf}\left(\sqrt{\frac{\eta r h_{\text{eff}}}{h^2(r)}} \theta_{\text{lim}}\right) \quad (21)$$

such that the reference propagation loss is $PL_{\text{ref}} = 10 \log_{10} \frac{F_{\text{ref}}^{-1}}{1 \text{ m}^2}$ dB. The value chosen for the reflection loss gradient (η) is 0.273777 Np/rad [from page 454 of Ref.1], and the effective water depth is $h_{\text{eff}} = \frac{h^2(0)h^2(r)}{r} \int_0^r \frac{1}{h(r')^3} dr'$, which is evaluated analytically by using piecewise linear approximation for the bathymetry, as described in the Appendix. Equation (21) also follows from Eq.(9) for a uniform sediment type and with $W(z_r, z_s, \theta_s) = 0$. In Fig. 2, PL_{ref} versus range is shown for Cases 4 and 9. The PL_{relative} curves plotted in subsequent graphs quantify the departures from the corresponding curves in Fig 2.

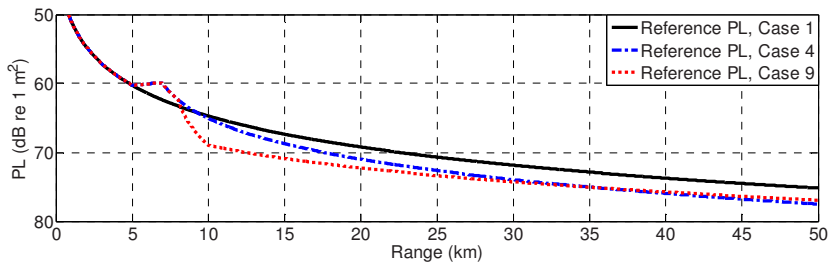


Figure 2. Reference PL for the test cases (Eq. 21 is used)

B. Validations: Comparisons with adiabatic mode theory

Leaky mode contributions

Eq. (19) and KrakenC results can be evaluated with or without the leaky mode contribution. In order to include the contribution from leaky modes, the continuum integral in Eq.(19) is extended to $\pi/2$, thus taking into account the eigenvalues whose grazing angles are beyond the critical angle. The contribution from leaky modes to the depth-averaged PL is shown in Fig. 3 for Cases 1, 4 and 9 at 250 Hz. All three are identical up to 5 km, after which the influence of the upslope region can be seen for Cases 4 and 9. First, Fig. 3 shows the effect of leaky (supercritical) modes on relative PL at short range (up to 2 km) Most of the initially generated leaky modes lose their energy within a few kilometres of the source, thus explaining the rapid initial decay of the leaky mode contributions in Fig.3, especially during the first kilometre. The range-dependent test cases (4 and 9) are identical up to 8 km. In these, ray paths are steepened by the upslope propagation between 5 km and 7 km, resulting in the conversion of discrete (trapped) modes into leaky ones that then decay quickly at the top of the slope, from 7k m to 8 km. Beyond 8 km, the curves for Cases 4 and 9 differ because of the different bathymetry, but no new leaky modes are generated beyond this point. This figure also shows the agreement between KrakenC and Eq.(19) with and without leaky mode contribution.

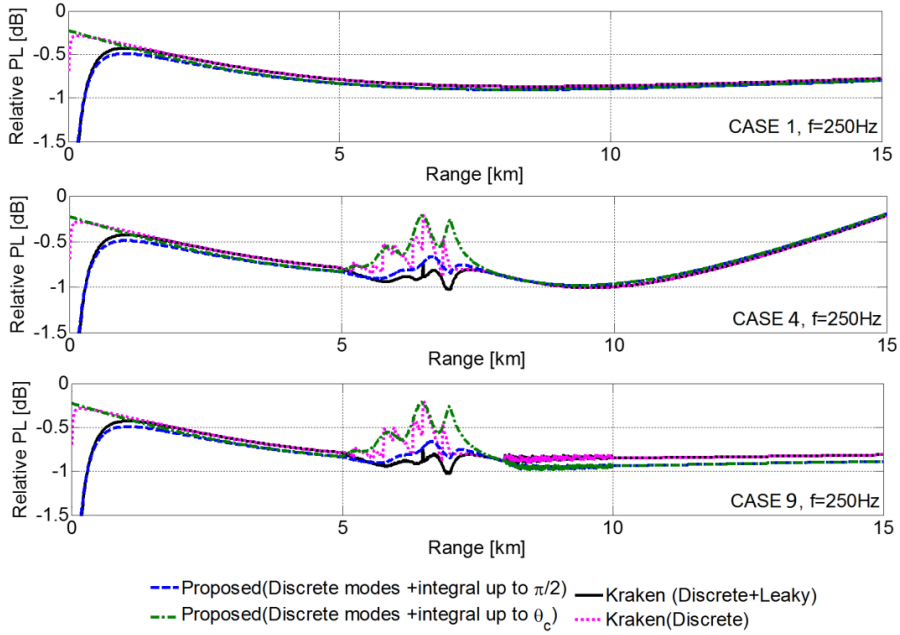


Figure 3. Eq.(19) is integrated up to critical angle and $\pi/2$ (with 5 discrete modes) to exclude and include leaky modes. Solutions of Eq.19 are compared with KrakenC without (with) leaky mode contribution. The exact Rayleigh reflection coefficient is used for the seabed reflection coefficient in Eq.(19).

Up to 500 m, the contribution of the leaky modes exceeds 1.2 dB. Then, the leaky mode contribution becomes less than 0.01 dB between 2 km and 5 km. The contribution from leaky modes is about 0.6 dB between 5 km and 8 km for the depth averaged PL, and is negligible at all other distances beyond 1 km. The proposed method agrees with the KrakenC adiabatic mode sum to within 0.2 dB when the upper limit of the angle integral is extended to $\frac{\pi}{2}$. Eq.(19) can be implemented easily and generates a fast solution without requiring the estimation of eigenvalues, which is computationally expensive, especially for high frequencies.

Validations for the relative PL field

In this section, the relative PL field (i.e., PL relative to PL_{ref}) is investigated. Results for Cases 4 and 9 are shown in Figs. 4 and 5, calculated using Eq.(19) and Eq.(13). The solutions based on Eq.(19) (left hand graphs), which include the contribution from leaky modes, replicate the

adiabatic form of KrakenC's results (not shown). The contribution from leaky modes can be significant over the slopes (as shown in Fig.4), and at low frequency Eq. (13) fails to capture the discrete nature of the mode sum. The solutions based on Eq.(13) (right hand graphs) use the exponential reflection coefficient and asymptotic form of $\Phi[Z, R, \theta_{lim}]$ for large R , which is described by Eq.(12).

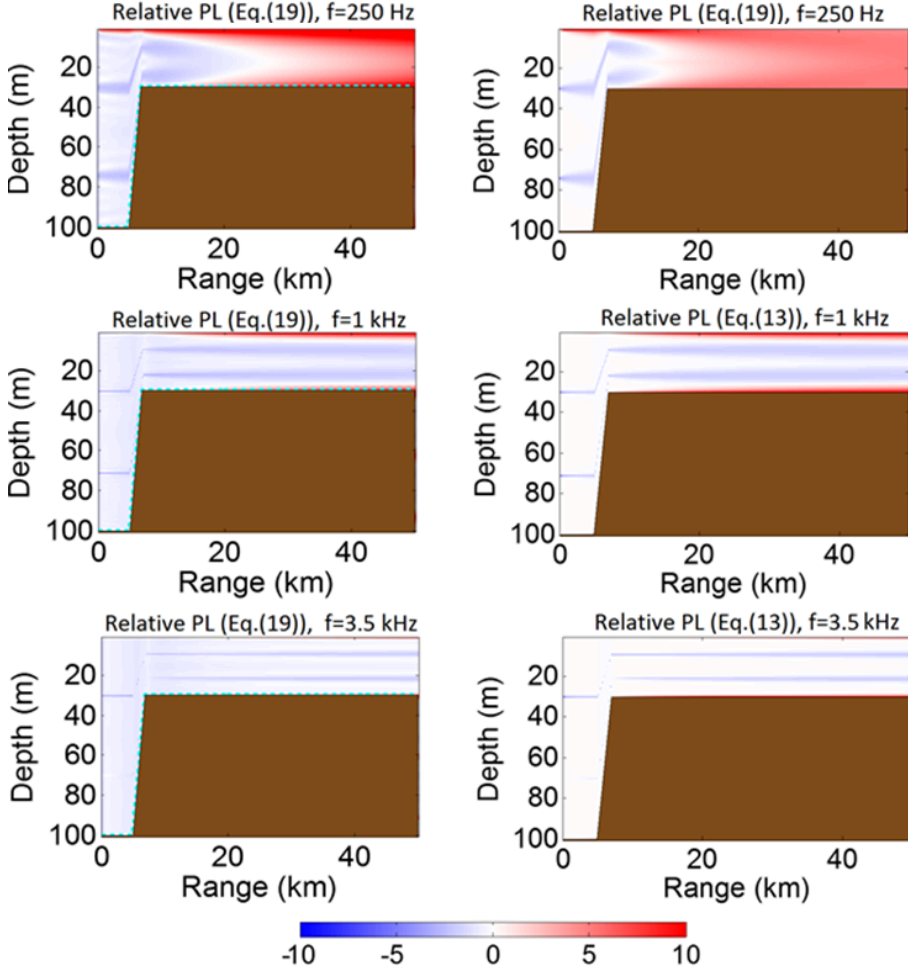


Figure 4. the relative propagation loss $PL - PL_{ref} [dB]$ field for Case 4 at 250 Hz, 1 kHz and 3.5 kHz using Eq.(19) (left) and Eq.(13) (right). Eq.(19) is evaluated using the exact Rayleigh reflection coefficient for $M = 5$, and including leaky modes; Eq.(13) is an approximate continuous integral solution and excludes leaky modes. The source depth is 30 m.

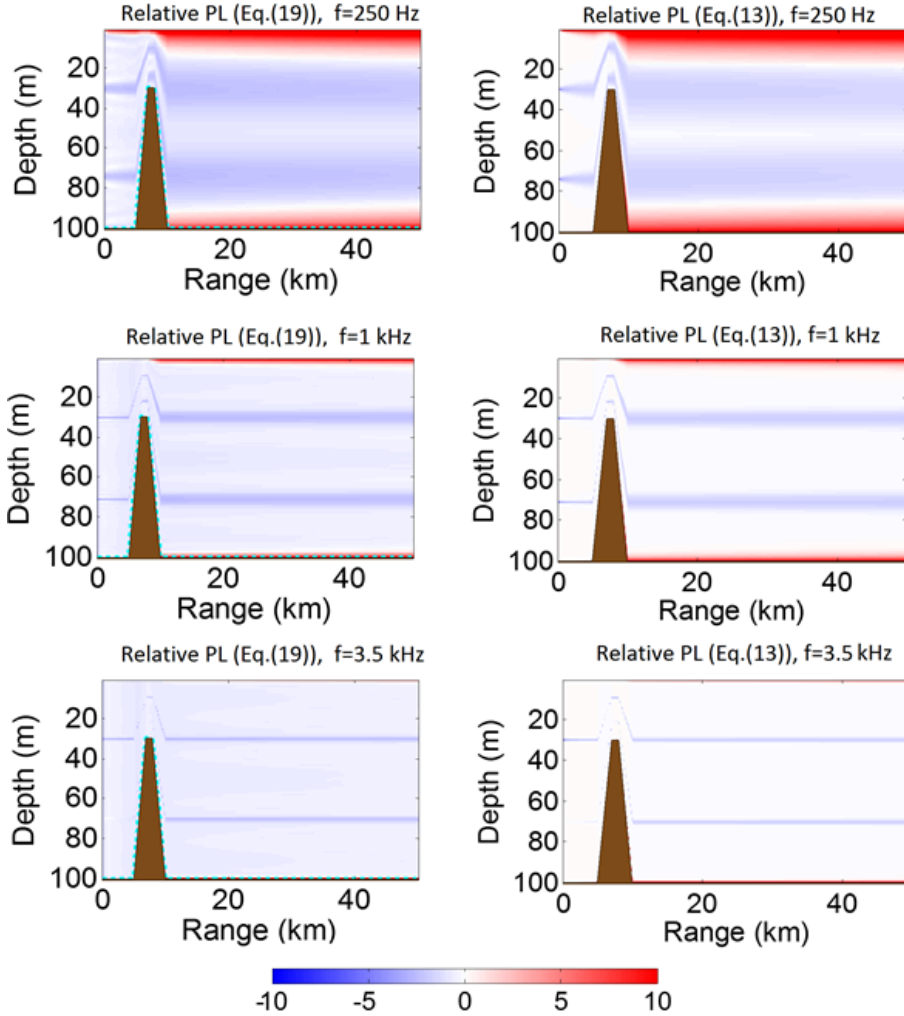


Figure 5. The relative propagation loss $PL - PL_{\text{ref}}$ [dB] field for Case 9 at 250 Hz, 1 kHz and 3.5 kHz using Eq.(19) (left) and Eq.(13) (right). Eq.(19) is evaluated by the exact Rayleigh reflection coefficient for $M = 5$, and including leaky modes; Eq.(13) is an approximate continuous integral solution and excludes leaky modes. The source depth is 30 m.

Wave theory features of two kinds are visible in these graphs: near the boundaries, surface decoupling effects cause the reference PL function, given by Weston's original flux integral (Eq.(21)) underestimates the propagation loss, and this region appears in red; and at the source and complementary depths there exist coherent enhancements [Weston,1980] that appear as

parallel blue streaks. In the adiabatic approximation, these streaks follow the slopes in the bathymetry. Considering its simplicity, Eq.(13) provides a surprisingly accurate analytical formulation for PL, especially for long ranges.

Comparisons between Proposed Approach and incoherent mode sum: PL_{Relative} vs depth

In Fig.6, PL vs depth comparisons are shown. Cases 4 and 9 have the same bathymetry up to 8 km from the source. Thus, the first and second comparisons are valid for both cases. The third comparison is for Case 4. The last comparison is for Case 9.

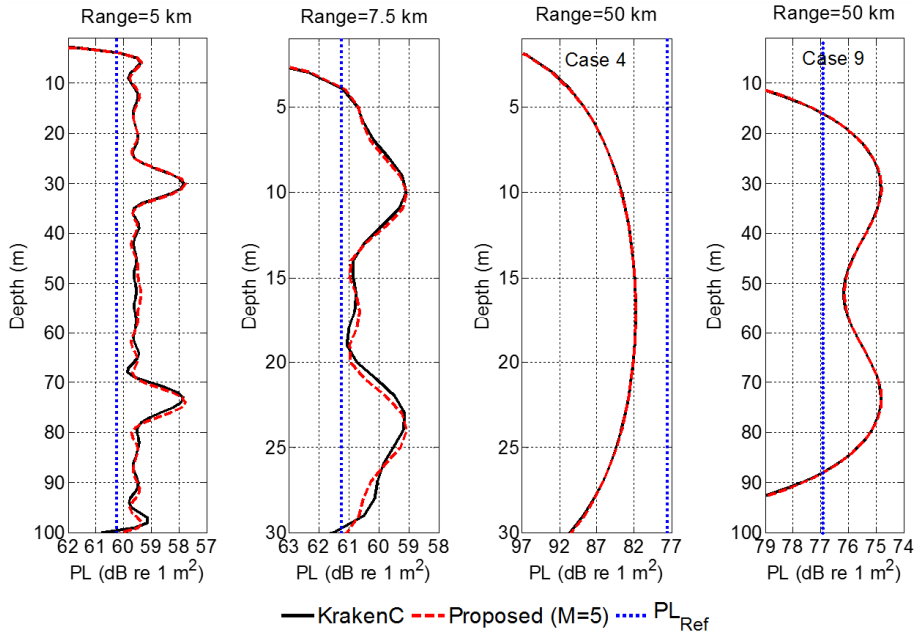


Figure 6. Relative PL vs depth comparisons with discrete mode region effects ($M=5$, no leaky modes) for 250 Hz at 5 km, 7.5 km and 45 km. The Rayleigh reflection coefficient is used for Eq.(19). The source depth is 30 m. The bathymetries for Cases 4 and 9 are the same until 8 km. Thus, the first depth vs PL graph is the same for Cases 1, 4 and 9; similarly, the first two depth vs PL graphs are the same for Cases 4 and 9; The third graph (note the different y axis scale) is for Case 4. The last one is for Case 9, The reference solution is evaluated using Eq.(21).

Good agreement is obtained between Eq.(19) and KrakenC (adiabatic) for the depth dependent propagation loss. At low frequencies for which only a few modes propagate, the mode region effects must be considered when estimating PL especially at long ranges. Eq.(19) can provide a solution as accurate as that of KrakenC(Adiabatic), without requiring complex root finding algorithms.

Comparisons for different number of discrete modes

In principle, the accuracy of Eq.(19) at long range and low frequency can be improved by adding more modes, and eventually one can expect the result to converge. In practice it converges for a surprisingly small number of discrete modes, as shown below. In Fig. 7, the relative PL for Case 4 is shown for different numbers of mode contributions at three frequencies.

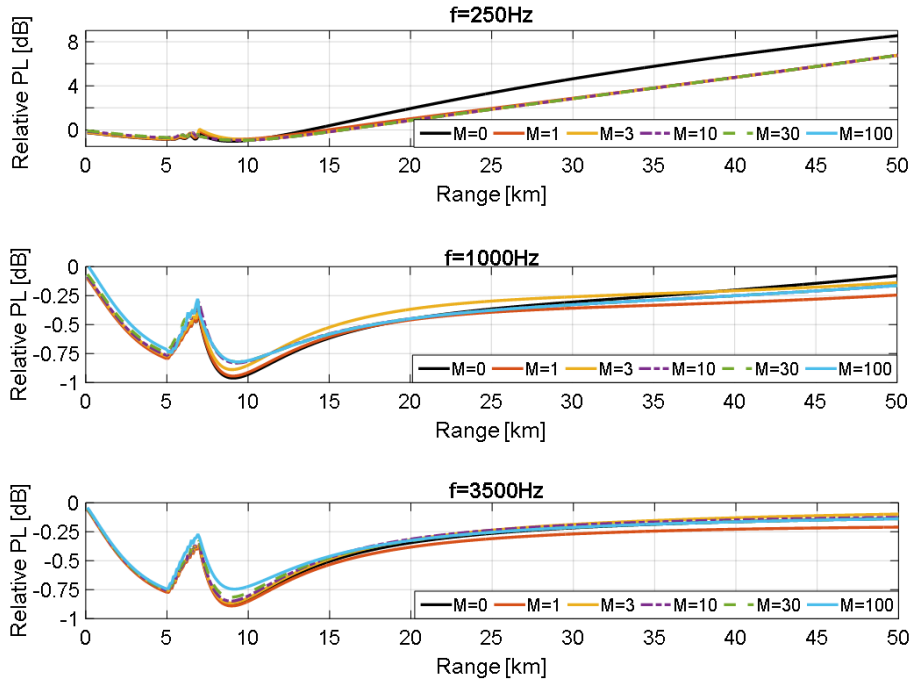


Figure 7. The effect of the number of discrete modes on the convergence of propagation loss. The mode sum includes only discrete modes, thus excluding paths steeper than the critical angle. The range step size is chosen to be 100 m for these comparisons. Note the different y axis scale at 250

Hz.

Convergence tests can provide insight into how many modes (M) can be enough. This therefore demonstrates that using $M = 3$ provides sufficient accuracy to provide a mode solution at low frequencies and long ranges (compared with $M = 5$ actually used). For low frequencies, the contribution from the integral part decreases. For high frequencies, such that many modes propagate, the continuum approach is more efficient than a discrete sum. Thus, adding more modes at high frequencies (1 and 3.5 kHz) does not make a significant contribution. Adding even only one mode at low frequency (250 Hz) helps convergence.

Comparisons for the computation time

In Fig 8, the running times of KrakenC and Eq.(19) are compared for Cases 1 and 9. For Case 9, the PL is calculated at every 50 m up to 45 km for frequencies between 30 Hz to 10 kHz. The adiabatic mode sum option is used in KrakenC. This comparison shows that similar accuracy with adiabatic mode theory can be obtained without requiring long calculation times. Eq.(19) is more than 1000 times faster than KrakenC at 10 kHz for Case 9 because it does not require any numerical algorithms for the estimation of eigenvalues. For the range independent case, which only requires the calculation of one set of eigenvalues by KrakenC, Eq.(19) is still more than 100 times faster than KrakenC at frequencies above 3 kHz.

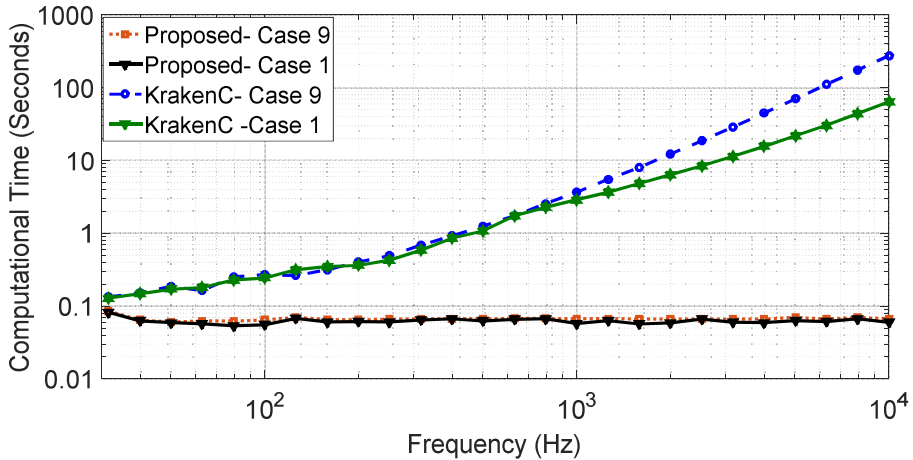


Figure 8. The computation times for KrakenC and Eq.(19) ("Proposed"). The stair-step size is 50 m for KrakenC.

C. Multiple Model Comparisons for Depth Averaged PL

In this section, depth-averaged PL_{relative} vs range results (obtained by averaging mean-square sound pressure over receiver depth between the sea surface and seabed) are compared for Cases 1, 4 and 9, with the purpose of quantifying the accuracy of the solutions from different models. To achieve this we first establish a “baseline” solution that is trusted withing a specified tolerance. Specifically, a baseline for the depth-averaged propagation loss is established when the maximum difference of the solutions predicted by Peregrine and Couple, for Cases 4 and 9, is less than 0.5 dB. For Case 1, the same criterion applies except that KrakenC replaces Couple for this range-independent environment. The baseline is equal to the average in decibels of the two (equivalent to taking the geometric mean of the depth-averaged propagation factors) at each range. These two models are chosen because they rely on different approaches for solving the Helmholtz equation[Jensen et al, 1994], one applying a marching solution with the paraxial approximation[Collins,1993] and the other applying a discrete normal mode expansion, including leaky modes. Because of the radically different nature of the nature of the approximations made, if, for any specific test case, these different approaches result in essentially the same solution, we consider it reasonable to infer from this agreement that the errors are small for both models. While this approach falls short of providing proof of accuracy (see, e.g.[Collins and Evans,1992] and [Porter et al,1991] for counter-examples), it provides a strong indication that errors are small, and we argue, in the sense of Reference 3 that the burden of proof is on others to identify and correct any errors in the baseline solution. In the following paragraphs, we investigate the difference between the baseline solution and the adiabatic approximation for Cases 4 and 9. In Table 1, the differences between Peregrine and Couple solutions are shown, providing a measure of the uncertainty in the baseline solutions. The 0.5 dB criterion for establishing a baseline is met for all combinations except for Case 4 at 3.5 kHz. Cases 1, 4 and 9 are now considered in turn.

Table 1. Maximum difference between Peregrine and normal mode (Couple or Kraken) solutions (magnitude of difference, in dB). A baseline is established for all combinations except Case 4 at 3.5 kHz, for which the maximum error exceeds 0.5 dB.

	250 Hz	1 kHz	3.5 kHz
Case 1 (Peregrine cf KrakenC)	0.1 dB	0.1 dB	0.1 dB
Case 4 (Peregrine cf Couple)	0.2 dB	0.1 dB	0.7 dB
Case 9 (Peregrine cf Couple)	0.2 dB	0.2 dB	0.3 dB

For Case 1 (Fig 9), at short range, Eq.(19) agrees with the baseline solution because of taking into account leaky mode effects. At long range, the differences between Eq.(19) and the baseline solution less than 0.15 dB for all three frequencies.

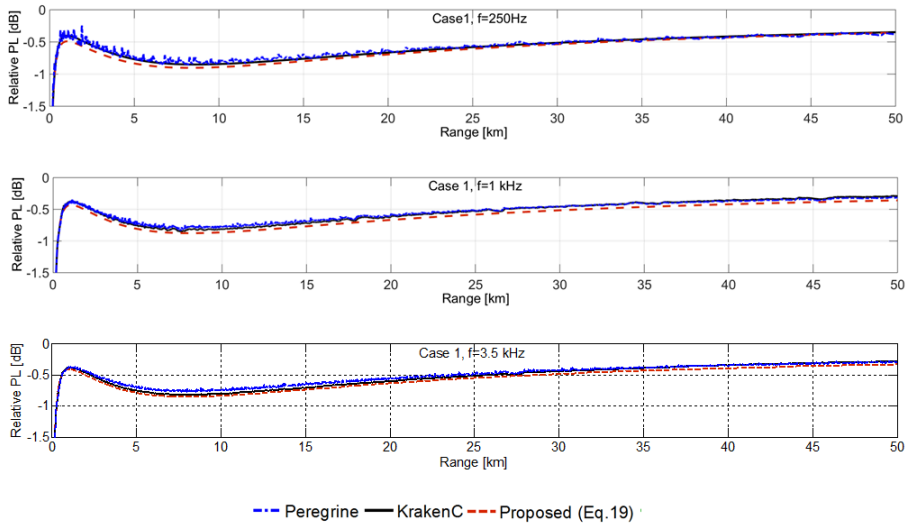


Figure 9. Comparisons for Case 1. Relative PL ($PL(\text{depth averaged}) - PL_{ref}$) results of KrakenC, Peregrine and Eq.(19). The exact Rayleigh reflection coefficient is used for Eq.(19). The source depth is 30 m. The squared sound pressure is averaged over receiver depths with 1 m resolution.

Results for Case 4 (Fig 10) and Case 9 (Fig 11) are identical to Case 1 up to 5 km and are not shown. For 250 Hz, the adiabatic approximation (KrakenC and Eq. (19)) replicate the baseline solution within 0.15 dB between 5 km and 10 km. At longer range, the adiabatic approximation overestimates the depth-averaged PL by up to 0.35 dB.

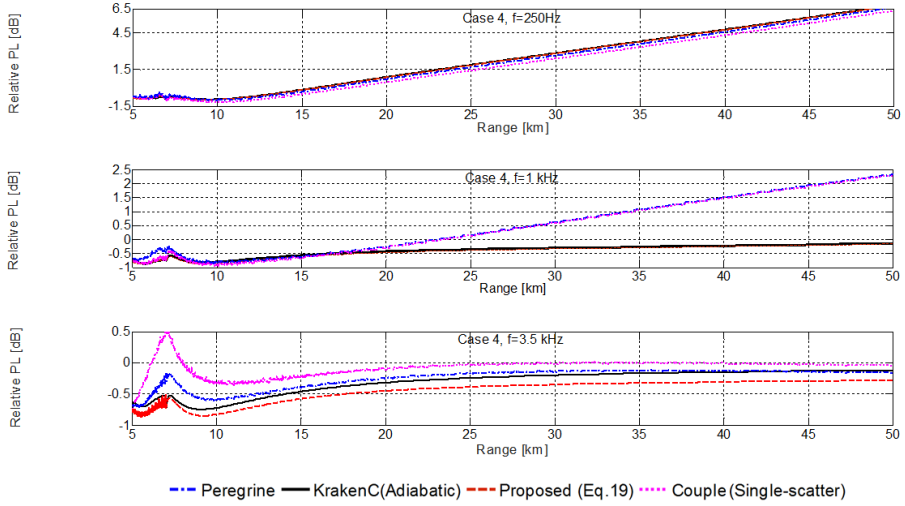


Figure 10. Comparisons for Case 4. Relative PL (PL (depth averaged) $- PL_{ref}$) results of KrakenC-Adiabatic(incoherent), Couple(Coherent), Peregrine(coherent) and Eq.(19)(incoherent). Exact Rayleigh Reflection coefficient is used for Eq.(19). The source depth is 30 m. The squared sound pressure is averaged over receiver depths with 1 m resolution. Note the different y axis scales for these comparisons.

For 1 kHz, the adiabatic approximation underestimates PL by an amount that increases with increasing range beyond 17 km. The difference between KrakenC and the baseline solution becomes 2.3 dB at 50 km. These comparisons show that the adiabatic approximation can replicate Peregrine solutions for 250 Hz and 3.5 kHz. At 250 Hz there is only one mode in the shallow water part, which is travelling at a steep angle, so there is no reason to expect a problem with the adiabatic approximation. Specifically, the steep ray path ensures a short cycle distance, and hence small changes in water depth for each ray cycle. At 1 kHz there is a region in which there is only one mode left, and this mode is not steep. In turn this implies a long cycle distance, and the potential for large changes in water depth per ray cycle in the sloping regions. This probably

causes the larger difference between adiabatic approximation and baseline solution at this frequency.

For Case 9 (Fig 11), the differences between KrakenC and the baseline solution are less than 0.6 dB for 250 Hz, 0.2 dB for 1 kHz and 0.4 dB for 3.5 kHz.

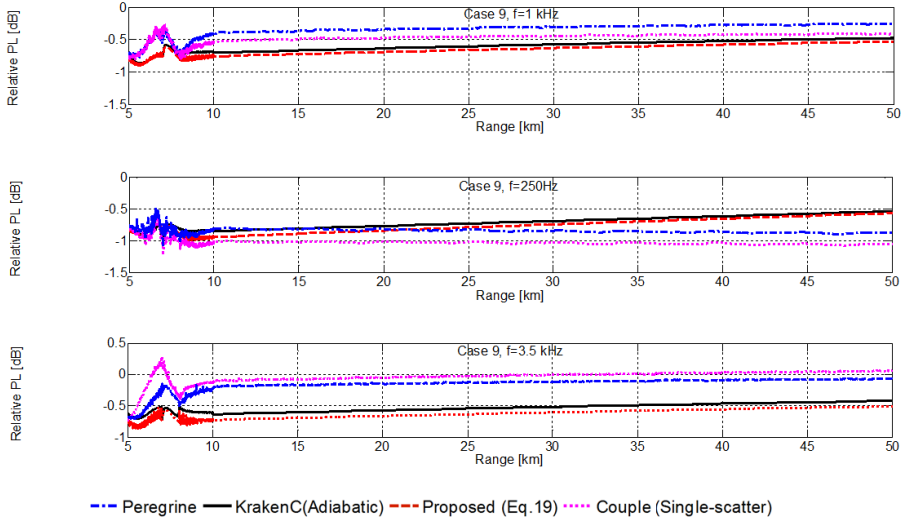


Figure 11 . Comparisons for CASE 9. Relative PL (PL (depth averaged) $- PL_{ref}$) results of KrakenC-Adiabatic(incoherent), Couple(coherent), Peregrine (coherent) and Eq.(19)(incoherent).

The exact Rayleigh Reflection coefficient is used for Eq.(19). The source depth is 30 m. The squared sound pressure is averaged over receiver depths with 1 m resolution.

The differences between the baseline solution and adiabatic model solutions are summarized in the Table 2.

Table 2. Summary of multimodel comparisons for range dependent cases (*magnitude of difference, in dB*).

	Method	250 Hz	1 kHz	3.5 kHz
		Maximum difference between baseline solution and adiabatic models	Maximum difference between baseline solution and adiabatic models	Maximum difference between baseline solution and adiabatic models
Case 4	KrakenC	0.35 dB	2.3 dB	n/a
	Eq.(19)	0.25 dB	2.2 dB	n/a
Case 9	KrakenC	0.6 dB	0.2 dB	0.4 dB
	Eq.(19)	0.4 dB	0.3 dB	0.6 dB

A final comparison is made between KrakenC and Eq.(19) to test the accuracy of the approximations made by Eq (19), as summarized in Table 3.

Table 3. Maximum difference between KrakenC and Eq.(19) (*magnitude of difference, in dB*).

	250 Hz	1 kHz	3.5 kHz
Case 1	0.1 dB	0.1 dB	0.1 dB
Case 4	0.1 dB	0.1 dB	0.2 dB
Case 9	0.1 dB	0.1 dB	0.1 dB

These comparisons and tables give an insight into the maximum average error of Eq.(19) for the three selected test cases.

2.3.5. SUMMARY AND CONCLUSIONS

In this section, practical approaches (Eq.(11) ,Eq.(13) and Eq.(19)) to calculate the propagation loss (PL) in range dependent waveguides are introduced. Eq.(11) is an analytical solution based on linear variation of reflection loss with angle. For long ranges, Eq.(11) asymptotically approaches to Eq.(13), which can be implemented without requiring a costly search for complex eigenvalues. Eq.(19) is a general form of solution which can be evaluated numerically by using the exact form of the Rayleigh reflection coefficient. The solutions based on Eq.(19) and exact Rayleigh reflection coefficient can take into account the leaky mode region. For selected test cases from the Weston Memorial Workshop, Eq.(19) achieves a similar accuracy to the adiabatic mode theory results (KrakenC) and is orders of magnitude faster at high frequency. The comparison with KrakenC results shows that Eq.(19) reproduces the depth and range dependent properties of incoherent mode theory without requiring long computational times.

The accuracy of adiabatic mode theory is investigated for selected test cases. PL is calculated with the propagation models KrakenC (adiabatic modes), Couple (coupled modes with single scatter option) and Peregrine (parabolic equation). The performance of each model for the selected test cases is tested.

For the range independent waveguide scenario (Case 1), the depth-averaged PL results of these models are very similar (the maximum difference is less than 0.15 dB). Given the entirely different nature of these methods[Ainslie,2010a], we interpret this difference as evidence that all models are providing the correct solution to Case 1, with an uncertainty of ± 0.15 dB.

For the range dependent cases (Case 4 and 9), the performance of the each algorithm is different. Eq.(19) replicates KrakenC (adiabatic mode theory) results to within 0.2 dB without requiring long computational times. However, the agreement between Couple and Peregrine and disagreement between Couple and KrakenC show the adiabatic approximation is not valid for Case 4 at 1 kHz after 19 km. The difference between Eq.(19) and the baseline solution is less than 0.6 dB for the selected test cases except 1 kHz result of Case 4.

APPENDIX A. EFFECTIVE DEPTH CONCEPT FOR THE RANGE DEPENDENT WAVEGUIDES

This section shows analytical implementation of the effective depth solution. The effective water depth is defined as [Weston, 1976]

$$h_{\text{eff}} = \frac{h^2(0)h^2(r)}{r} \int_0^r \frac{1}{h^3(r')} dr' \quad (A1)$$

where $h(0)$ and $h(r)$ are the water depths at source and receiver ranges. An arbitrary depth profile can be separated into smaller segments as shown in Fig. A.1

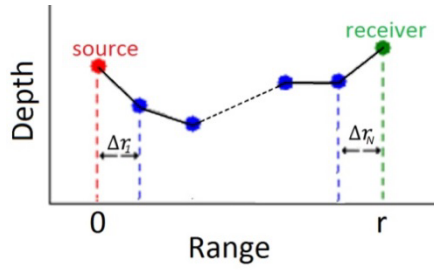


Figure A.1. Piecewise linear representation of bathymetry

where Δr_j is the horizontal length of j th segment as shown in Fig. A.1. Each segment can have different length. An analytical solution can be obtained by solving and summing the integrals for each segment. Weston's solution [Weston, 1976] for upslope or downslope bathymetry can be generalized for arbitrary set of piecewise linear segments as

$$h_{\text{eff}} = \frac{h^2(0)h^2(r)}{r} \sum_{j=1}^N \Delta r_j \frac{h_j + h_{j+1}}{2(h_j h_{j+1})^2} \quad (A4)$$

where h_j is the water depth at the end of j th segment, Δr_j is the length of j th segment and N is the number of segments. In our calculation, a uniform segment length $\Delta r_j = \Delta r$ is used. For a range dependent sediment type, the integral can be evaluated as

$$\begin{aligned} \left\langle \frac{\eta}{h^3} \right\rangle &= \frac{1}{r} \int_0^r \frac{\eta(r')}{h^3(r')} dr' = \frac{1}{r} \left(\int_0^{\Delta r} \frac{\eta_1}{h^3} dr' + \int_{\Delta r}^{2\Delta r} \frac{\eta_2}{h^3} dr' + \dots + \int_{(N-1)\Delta r}^{N\Delta r} \frac{\eta_N}{h^3} dr' \right) \\ &= \frac{1}{r} \sum_{j=1}^N \eta_j \Delta r_j \frac{h_j + h_{j+1}}{2(h_j h_{j+1})^2} \end{aligned} \quad (A5)$$

where η is assumed constant for each segment. [Holland,2010] has derived a similar equation to solve range dependent sediment problems. Specifically, Eq. (A5) above is closely related to Holland's Eq. (4), which can be written $|\hat{R}| = \exp\left(-h^2(0)\theta_0^2 \left\langle \frac{\eta}{h^3} \right\rangle \frac{\tilde{r}_c}{2}\right)$ for isovelocity water. Where \tilde{r}_c corresponds to weighted cycle distance (see Eq.(5) of Reference 6) and $|\hat{R}|$ is the geometric mean of the range dependent reflection coefficient.

Chapter 3 SOURCE MODELS AND SOUND MAPS

In this chapter, the approaches for sound mapping are explained with the description of source models and the underwater acoustic environment. First, the effect of the sound speed profile on shallow water shipping sound maps is investigated in Section 3.1. The error caused by neglecting the sound speed gradient is calculated for the selected sound speed profiles for the Dutch North Sea. Then, the accuracy of the shipping sound mapping approach is tested by the comparisons between shallow water measurements and sound pressure level calculations which is based on SOPRANO model in Section 3.2. It is shown that the approach used can generate very similar results to the measurements, especially for the low frequencies. This comparison also shows that the neglect of surface scattering can lead errors at high frequencies. In Section 3.3, the airgun array source model which is used for the seismic survey sound maps is described. The calculated results are compared with the measurements. Finally, sound maps (averaged over two years) of the Dutch North Sea are introduced in Section 3.4. The annual and weekly energies of shipping, explosion, seismic survey and wind sounds are compared in order to understand which source is making the largest contribution at various time scales.

3.1. EFFECT ON SOUND SPEED PROFILE ON SHIPPING SOUND MAPS

This section is submitted as [H.Ö Sertlek , B. Binnerts and M.A. Ainslie, The effect of sound speed profile on shallow water shipping sound maps, under review by JASA Express Letters]

Abstract: Sound mapping over large areas can be computationally expensive because of the large number of sources and large source-receiver separations involved. In order to facilitate computation, a simplifying assumption sometimes made is to neglect the sound speed gradient in shallow water. The accuracy of this assumption is investigated for ship generated sound in the Dutch North Sea, for realistic ship and wind distributions. Sound maps are generated for zero, negative and positive gradients for selected frequency bands (56 Hz to 3.6 kHz). The effect of sound speed profile for the decidecade centred at 125 Hz is less than 1.7 dB.

3.1.1. INTRODUCTION

Regulations in the USA [Marine Mammal Protection Act, 1972; Endangered Species Act of 1973] the European Union (EU) [Directive 2008/56/EC of the European Parliament and of the Council of 17 June 2008; Commission Decision of 1 September 2010], and worldwide [Lucke et al, 2013] aim to protect and preserve the marine environment. The EU's Marine Strategy Framework Directive (MSFD) requires member states to achieve or maintain Good Environmental Status (GES) by the year 2020. Specifically, the wording of Descriptor 11 of GES requires underwater noise to be at levels that do not adversely affect the marine environment. The MSFD further requires monitoring of trends in the ambient noise within the 1/3 octave bands 63 and 125 Hz (centre frequency) [Commission Decision of 1 September 2010; Dekeling et al, 2014]. These regulations increase the interest in understanding both local and global soundscapes [Anon et al, 2014]. The EU's expert group (TSG Noise) recommends the use of sound maps as a tool to monitor GES [Dekeling et al, 2014]. While there is no standard procedure for sound mapping, the isovelocity assumption is sometimes used in shallow water simulations for simplicity. The errors resulting from neglecting the sound speed gradient are not self-evident. This paper focuses on assessing the validity of the isovelocity assumption for a realistic distribution of ships in shallow water. The aim of the present paper is to quantify the maximum relative error caused by the use of isovelocity assumption instead of realistic sound speed profile (SSP) for different frequencies for different locations with representative shipping density. In order to simulate a realistic distribution of ships in the North Sea, an Automatic Identification System (AIS) snapshot from January 2014 is used. The Wales and Heitmeyer formula is used for the monopole source level of the ships [Wales and Heitmeyer, 2002]. The sound pressure level (SPL) is calculated for isovelocity, negative and positive sound speed profile gradients. SPL maps are shown for decidecade frequency bands (a decidecade is a logarithmic frequency interval equal to one tenth of a decade [ISO/DIS 18405]. This frequency interval is sometimes referred to as a "one-third octave" because it is approximately equal to one third of an octave) and compared with the isovelocity case results. The effect of the SSP for dense and sparse shipping is analysed.

3.1.2. METHOD

The effect of the SSP is quantified by comparing SPL relative to that for an isovelocity profile. The sound map for the isovelocity case is referred to henceforth as the "baseline map". Next, the

relative difference between the baseline maps and the selected SSP cases are compared by calculating the relative SPL as $SPL_{Relative}(x, y) \equiv SPL_{SSP}(x, y) - SPL_{ISO}(x, y)$, where SPL_{ISO} (the isovelocity baseline) and SPL_{SSP} (SPL for a specified SSP) both include contributions from wind and shipping, and no other sources. At each location, the mean-square sound pressure is computed at 15 receiver depths and averaged over these receiver depths

For shipping, SPL is calculated as $SPL = SL - PL$, where SL is calculated from Wales and Heitmeyer, extrapolated to higher frequencies by following the trend measured by [Arveson & Vendittis, 2000], as illustrated by Figure 8.16 from [Ainslie, 2010]. The PL is calculated using adiabatic normal mode theory [Jensen et al, 1994]. The eigenvalues are pre-calculated using KrakenC [Porter, 1990] for each sound speed profile. The assumed source depth is 5 m for all ships. The sea surface is assumed flat, neglecting the effect of surface losses and scattering. The resolution of the receiver grid is 0.02 degrees. The propagation loss (PL) is calculated between each source and receiver separately. The contributions from each ship are then summed incoherently.

The wind generated sound is computed using the method of [Ainslie et al, 2011], which assumes an isovelocity water column and locally uniform water depth. The chosen wind speed corresponds to the lowest mean monthly value (around 5 m/s at 10 m height) in the Dutch North Sea [ERA40 database from www.knmi.nl].

3.1.3. SOURCE DISTRIBUTION AND ENVIRONMENT

To investigate the effect of the SSP, a realistic ship distribution is used based on AIS data (available online at <http://www.marinetraffic.com>). The original AIS data had some gaps because of not receiving AIS signals for the northern part of the Dutch North Sea. The Maritime Mobile Service Identity (MMSI) number of each ship was tracked and the ship locations were interpolated over time for each ship separately. Next, a single time snapshot of AIS data is used in the simulation. In Figure 1 (right plot), a snapshot in time showing the shipping distribution as obtained from AIS data is shown. In the background of AIS distribution, the shipping density of the same day is plotted. The shipping density is plotted in gray tones, with the brightest tones (white) corresponding to the highest density. This shipping density graph suggests that the used points represent a representative ship distribution. The corresponding bathymetry (available online at <http://www.emodnet-hydrography.eu>) is plotted on the left. The two black markers in the bathymetry figure illustrate two locations, one southern and one northern, with dense and sparse

shipping activity, respectively. These locations are used later in the simulations to study the effect of the SSP in detail. The sediment type is assumed to be medium sand for the region considered.

Fig. 2 gives an insight into choice of the sound speed profile for the comparisons. In this section, sound speed gradients of ± 0.03 , ± 0.125 , $\pm 1 \text{ s}^{-1}$ are used. The simulation is also repeated for a summer sound speed profile, representative for the deepest part of the Dutch North Sea to study the effect of this specific profile on propagation.

3.1.4. COMPARISONS

The baseline (isovelocity) maps are shown in Figure 3. Next, the sound maps for the relative SPL are generated for the different sound speed gradients. In Fig.4, the relative SPL maps for the negative and positive gradients are shown for two decade bands and a broadband map from 56 Hz to 3.6 kHz.

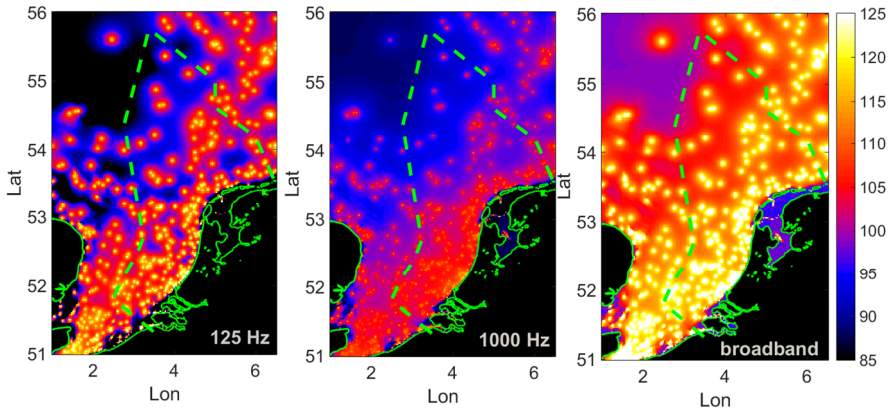


Figure 3. The sound maps for the isovelocity case (SPL_{ISO} dB re $1 \mu\text{Pa}^2$). The squared sound pressure is depth-averaged over 15 receiver depths. Ship source depth is 5 m. The sound maps are generated for 125 Hz, 1 kHz decade bands and broadband (56 Hz to 3.6 kHz). The wind generated sound is added to all maps (wind speed is 5 m/s at 10 m above sea surface).

Fig. 4 shows that the effect of the sound speed profile is decreasing for nearby ranges (corresponding to dense shipping) and increasing when there is a larger relative contribution from distant sources (sparse shipping). Where the shipping density increases, the effect of SSP decreases, because the distance to the nearest ship decreases. In order to illustrate this effect, two locations are chosen on sound maps in regions of high and low shipping density. The receiver points' latitude and longitude coordinates are $(52.76^\circ \text{ N}, 4.14^\circ \text{ E})$ for dense shipping and $(55.22^\circ \text{ N}, 3.24^\circ \text{ E})$ for sparse shipping. Then, relative SPL is plotted versus frequency for each sound speed gradient. The variation of relative SPL versus frequency is shown by Fig. 5.

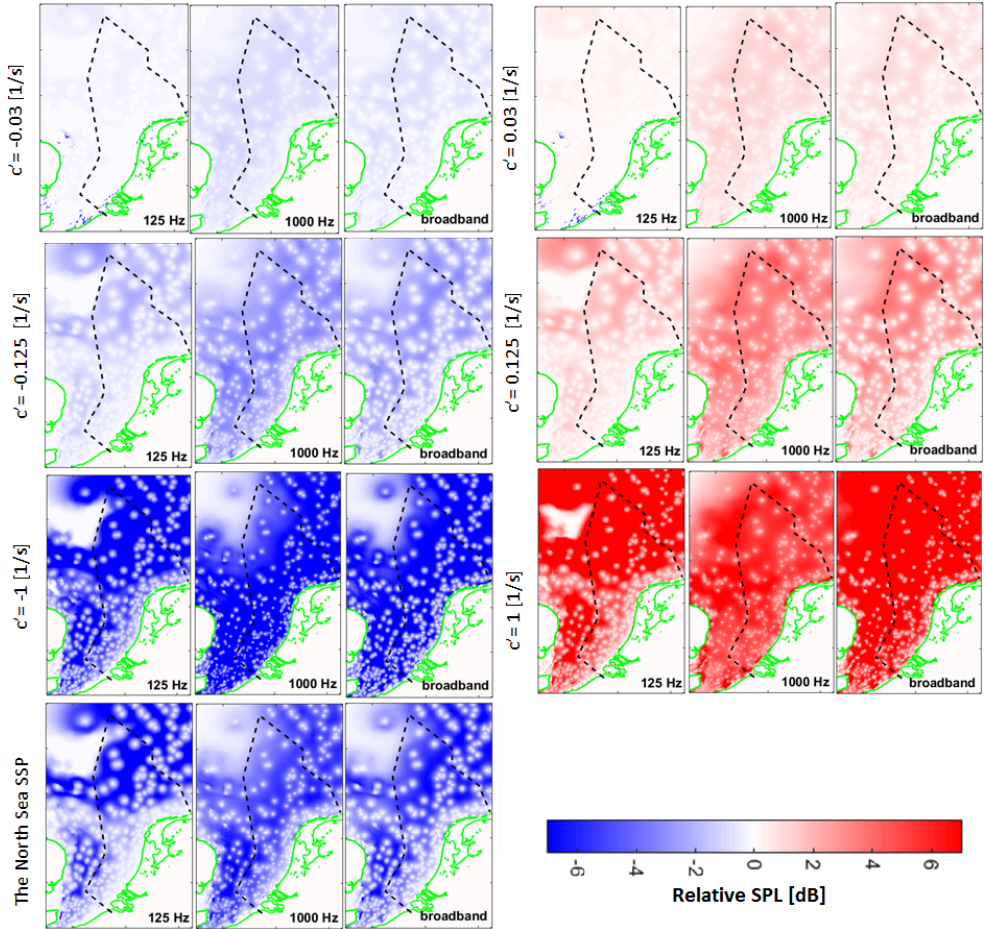


Figure 4. Relative SPL ($SPL_{\text{Relative}} = SPL_{\text{SSP}} - SPL_{\text{ISO}}$) for negative(left) and positive (right) gradients (0.03 s^{-1} , 0.125 s^{-1} , 1 s^{-1} and the North Sea SSP). The sound maps are generated for 125 Hz and 1 kHz decade bands and a broadband map for the frequency range 56 Hz to 3.6 kHz (all decade bands from 63 Hz to 3.2 kHz).

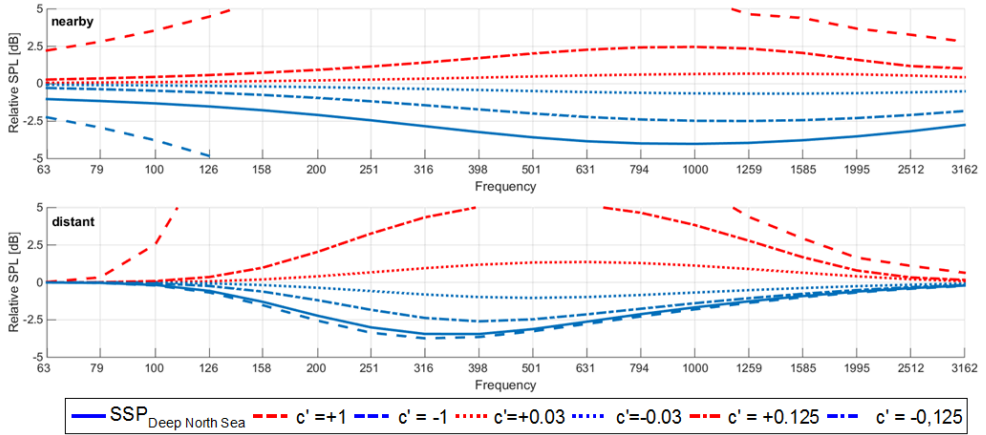


Figure 5. Relative SPL in decidecade bands from 63 Hz to 3.2 kHz (with the wind noise contribution) is plotted versus decidecade centre frequency for each sound speed gradient at the receiver for the dense (upper figure – “nearby”) and sparse (lower figure – “distant”) shipping. The receiver points’ latitude and longitude coordinates are) (52.76°N, 4.14°E) for dense shipping and (55.22°N, 3.24°E) for sparse shipping.

These comparisons show that the relative SPL increases with increasing frequency at low frequencies because the effect of the SSP is enhanced if the associated surface duct (if the sound speed gradient is positive) or bottom duct (if it is negative) is cut on[Ainslie,2010a]. The effect of SSP starts to decrease at higher frequencies, as can be expected by the increasingly important influence of volume absorption and wind-related surface loss, both of which reduce the importance of long range propagation paths (See Chapter 3.2). The frequency of maximum effect is between 300 Hz and 1 kHz. The largest effect for the 125 Hz decidecade band, for the North Sea SSP, is -1.7 dB as seen from Fig.5 for the deep water SSP of the North Sea at nearby receiver (we exclude $\pm 1 \text{ s}^{-1}$ case as this gradient is unrealistically large).

3.1.5. SUMMARY AND CONCLUSIONS

Sound maps are generated for the decidecade frequencies between 63 Hz and 3.2 kHz. The spatially averaged SPL is used to estimate the average error due to the neglect of sound speed profile in the entire maps. Squared pressure is averaged over depth and area to calculate the spatially averaged SPL. These relative differences in the spatially averaged SPL are summarized in

Table 1 for the 125 Hz decade and 56 Hz-3.6 kHz bands. This table shows that the effect of the SSP on the spatially averaged SPL is less than 1.5 dB except 1 s^{-1} which is one of the extreme cases. This relative SPL is less than 1.2 dB for the 125 Hz decade band.

Table 1. The relative differences in the spatially averaged SPL for the broadband and 125 Hz.

SSP gradient [$1/\text{s}$]	Relative Spatially averaged SPL for broadband (63 Hz to 3 kHz) [dB]	Relative spatially averaged SPL for 125Hz [dB]
-1	1.5 dB	-0.3 dB
-0.125	0.3 dB	0.1 dB
-0.03	0.2 dB	-1.1 dB
0.03	-0.1 dB	-0.3 dB
0.125	-0.4 dB	-0.8 dB
1	-3.4 dB	-1.0 dB
The North Sea SSP	0.7 dB	0.7 dB

The comparisons for the dense and sparse shipping receiver locations help to understand effects of local shipping density. The effect of the sound speed profile on the shipping sound is larger for the distant receiver location than for the nearby receiver location. The relative SPL for the North Sea SSP becomes lower when the wind contribution is added to SPL. The realistic values should be similar to results obtained for 0.03 s^{-1} and 0.125 s^{-1} gradients which are much more similar to sound speed gradient of the shallow water according to Figure 2. The sound speed gradients are more similar to 0.03 s^{-1} and 0.125 s^{-1} . The maximum error is around 5 dB at 500 Hz decade band for the sound speed gradient of 0.125 s^{-1} . The increase in the wind speed decreases this error. For these gradients, the relative SPL is less than 2.5 dB for a winter profile and up to 5 dB for a summer profile.

3.2. VALIDATION STUDY: COMPARISON OF SHIPPING SOUND MAP WITH THE MEASUREMENTS

This section is a modified version of the Sections 2 and 3 of [M.A. Ainslie, K.L. Heaney, B. Binnerts, H.Ö. Sertlek, P.D. Theobald and T. Pangerc, Use of sound maps for monitoring GES: Examples and way ahead, TNO Report 2014 R11167, 2014]

Abstract: *The use of sound propagation models for generating sound maps has been the theme of three recent sound mapping workshops: The Cetaceans and Sound ('Cetsound') workshop in Washington, USA [cetsound (Washington)], a collaboration between the two EU-funded projects [AQUO] and [SONIC] in Madrid, Spain [AQUO-SONIC (Madrid)], and an international workshop held in Leiden, Netherlands, [Anon et al, 2014]. Application of sound propagation models was also discussed during the Noise Impact Workshop held in Brussels [Borsani, 2014]. This section first presents a range of sound maps. These have been generated with the aim of showing the predicted contribution from shipping on the Dutch North Sea, and were derived using the Aquarius sound mapping framework (which uses the propagation model described in Chapters 2.2 and 2.3). Further, a comparison of model predictions with measurements is presented.*

3.2.1. INTRODUCTION

In this section, maps are presented of annually averaged sound pressure level (SPL) due to shipping (using annually averaged shipping density from Automatic Identification System (AIS) data) in one decidecade band (a decidecade is a frequency ratio equal to one tenth of a decade). This quantity is referred to as a “one-third octave”, following widespread common practice, because it is approximately equal to one third of an octave [ISO 266, 1997], [IEC 61260, 1995]. In the remainder of this section, the more precise term decidecade is used [ISO/DIS 18405].

3.2.2. METHODOLOGY

The sound maps presented in this section are based on an average distribution of ships in the exclusive economic zone (EEZ) of the Netherlands. The average shipping density map (see Figure 1) shows the average number of ships of a certain class within a grid cell for a specified time interval. This makes it possible to approximate the temporally averaged SPL in a computationally efficient way. The Aquarius sound mapping framework, originally developed using Weston’s flux theory [Weston, 1976] for a review of North Sea underwater sound sources in 2009 [Ainslie et al, 2009], has recently being enhanced to incorporate depth-dependent wave theory corrections using a hybrid propagation algorithm based on mode and flux theories [see Chapter 2.2 and 2.3]. It was used to compute the propagation loss. See [Wang et al, 2014] for an up-to-date review of propagation models for sound mapping. The number of discrete modes is chosen to provide accuracy at low frequency without a large computational overhead. This modelling approach is fast and accurate for broadband calculations in iso-velocity water. We do not expect large errors due to the neglect of sound speed gradient as investigated in Chapter 2.3. It also takes into account range dependent water-depth and sediment type. It calculates the incoherent propagation loss, including the depth dependent properties, using wave theory. Various other acoustic propagation models are included in the sound mapping framework. This makes it possible to compare different propagation models and numerically validate the selected modelling approach. This approach also allows the use of different models for different frequencies, optimizing both accuracy and computation time. As the propagation loss is calculated 2D (range versus depth), it is only possible to approximate a 3D distribution of the SPL by means of interpolation from 2D slices, referred to as the “N×2D” approach.

The modular character of the sound mapping tool allows fast computation of sound maps for a wide range of frequencies and on a large spatial scale, while maintaining the flexibility to study more complex, computationally expensive scenarios.

Inputs

Various inputs are required for the computation of the annual average shipping sound maps. Ships are modelled as point sources at a specified depth below the sea surface and a specified source level. The source level of each ship is calculated using the model by [Wales and Heitmeyer, 2002]. For the case study from the Dutch North sea presented here, the source depth consistent with use of the Wales-Heitmeyer source level was estimated as 5 m below the sea surface, based on information from [Gray & Greeley, 1980] and [Arveson & Vendittis, 2000]. The spatial distribution of the shipping traffic was computed using a density map for the year 2007 (generated by MARIN and provided via IMARES). Ships outside of the Dutch EEZ were not taken into account because the associated AIS data were not available. The density grid with a resolution of 5 km by 5 km was used, obtained from a sequence of AIS snapshots separated by 2 minutes in time. An 'AIS snapshot' is a map displaying all locations of ships fitted with AIS transponders for an instant in time.) AIS is an automatic tracking system used on ships and by vessel traffic services for identifying and locating vessels by electronically exchanging data with other nearby ships, AIS base stations, and satellites. The International Maritime Organization's International Convention for the Safety of Life at Sea requires AIS to be fitted aboard international voyaging ships with gross tonnage of 300 or more, and all passenger ships regardless of size. All EU fishing boats over 16 m length are required to have AIS. Hence, an AIS snapshot gives a good, though not necessarily complete, indication of the instantaneous shipping density. Figure 1 illustrates the annually averaged shipping density map for the EEZ in 2007.

SOURCE MODELS AND SOUND MAPS

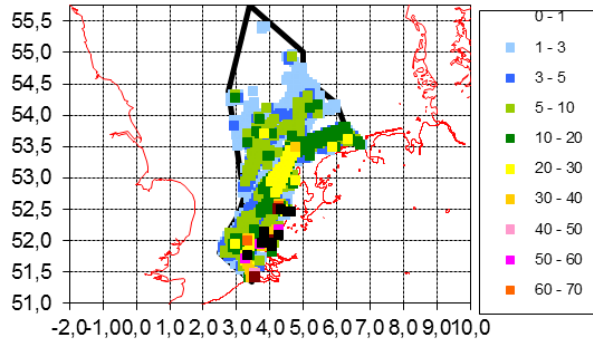


Figure 1: Shipping density map with a resolution of 5 km x 5 km for the year 2007. The values in the legend indicate the annual average shipping density in ships/1000 km². The axes represent latitude and longitude (WGS84).

The environment is defined by the bathymetry, the physical properties of the seabed and water, and the roughness of the sea surface. The bathymetry was obtained from the EMODnet portal for Bathymetry [EMODnet, 2014]. This dataset contains data from the local hydrography offices, improving the base GEBCO dataset with a resolution of 1/8 min. The effects of surface scattering and bubbles on sea surface reflection loss have been modelled using Eq. 8.22 of [Ainslie, 2010] and the fourth power averaged local wind speed, i.e., $(\overline{v_{10}^4})^{\frac{1}{4}}$. The fourth power is used because reflection loss scales with the fourth power of wind speed [Weston & Ching, 1989, Ainslie 2005]. The water was modelled using a uniform sound speed of $c_0=1500$ m/s and a density of 1000 kg/m³. The absorption loss α in dB/km was modelled using the equation of Thorp [Thorp, 1967]. The seabed was modelled as medium sand with a compressional sound speed $c_1=1797$ m/s and density $\rho_1=2086$ kg/m³ with an absorption given by $\alpha_b=0.88$ dB/λ [Ainslie, 2010].

Sound maps

Maps are shown (see Figure 2) for SPL in decibels with nominal centre frequencies 125 Hz, 1 kHz and 8 kHz and for broadband SPL. Precise centre frequencies follow [IEC 61260, 1995]. Broadband SPL maps (all decibels with centre frequencies between 32 Hz and 80 kHz) are given with and without M-weighting, for pinnipeds in water and cetaceans [Southall et al, 2007] (see Figure 3). In all cases the receiver depth is 2 m above the seabed. This information can be used, for example, to determine the M-weighted sound exposure level, and hence whether an animal at a given location is at risk of a temporary permanent hearing threshold shift according to the criteria of Southall et al, 2007 (see Ainslie 2010, p562).

SOURCE MODELS AND SOUND MAPS

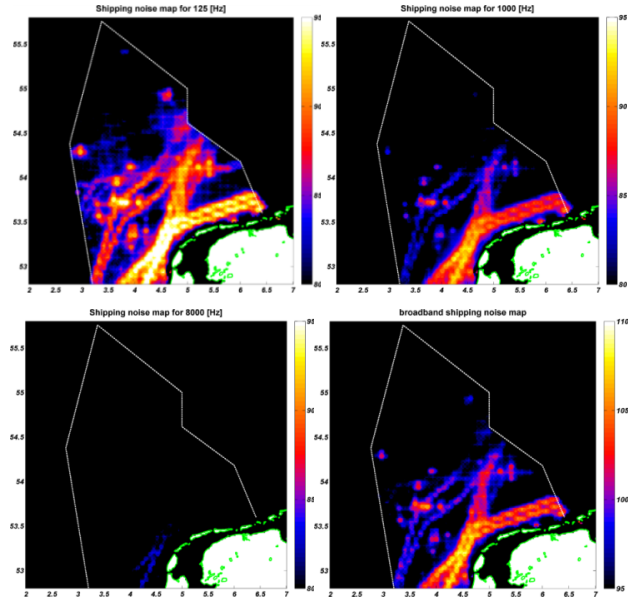


Figure 2: Shipping sound maps: unweighted SPL [dB re 1 μ Pa] in decibels centred at 125 Hz (upper left), 1 kHz (upper right), and 8 kHz (lower left); unweighted broadband SPL (lower right). The green border indicates the land boundary and the white border the Exclusive Economic Zone (EEZ) of the Netherlands.

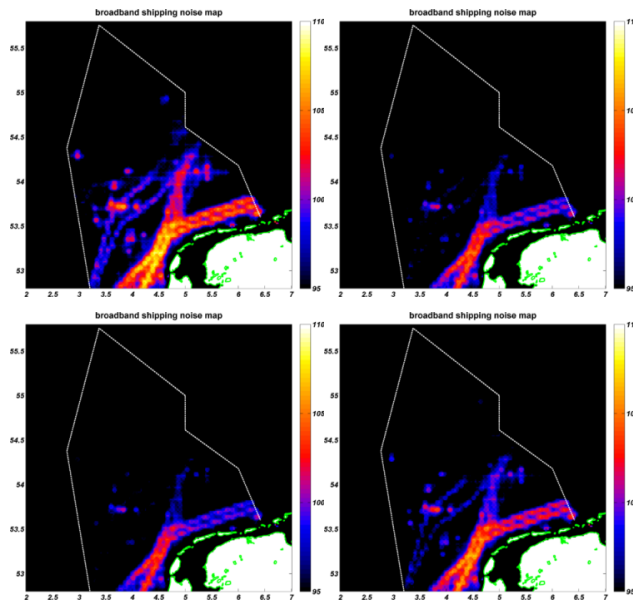


Figure 3: Shipping sound maps. Broadband M-weighted SPL [dB re 1 μ Pa]: for low-frequency (LF) cetaceans (upper left), mid-frequency (MF) cetaceans (upper right), high-frequency (HF) cetaceans

(lower left), and pinnipeds in water (lower right). The green border indicates the land boundary and the white border the Exclusive Economic Zone (EEZ) of the Netherlands.

3.2.3. VALIDATION

Background

Section 3.2.3 presents the work undertaken to quantify the accuracy of Aquarius (uses the same propagation model of SOPRANO as described in Chapter 2.3), and its sensitivity to uncertainties of the environment and the source models. This model validation was done using the underwater sound measurements done in 2009 by TNO for the construction of the “Tweede Maasvlakte”, (Second Maasvlakte, or ‘Maasvlakte 2’ [Maasvlakte2, 2014]) an expansion of the Port of Rotterdam port. Sound pressure was recorded by TNO’s autonomous acoustic measurement system ‘SESAME’ at a fixed location for a period of two weeks (26 September to 6 October 2009), at two depths (2 and 7 m above the seabed) [Ainslie et al, 2012b]. Also, for the duration of this measurement, the wind speed and spatial distribution of the shipping traffic were logged. Source levels of the dredgers were taken from a separate set of measurements designed for that purpose [de Jong et al, 2010]. See also [Heinis et al, 2013(risk assessment during Port of Rotterdam construction)] for more information. Measurements presented are for 29 September 2009 between 6:32:08 and 17:40:19 Rotterdam Local time (UTC +01:00), for the receiver at height 2 m from the seabed.

Methodology

In contrast to the shipping density maps used for Section 3.2.2, snapshots were computed for the validation. The advantage of using snapshots is that this allows studying the temporal variability and statistics of the sound, allowing the direct validation of the propagation loss if the source level is known. The disadvantage of introducing the temporal variability is the increased computational effort. The computational effort can be reduced by pre-computing the propagation loss (PL) in a lookup table. However, in order to keep the data size of the PL lookup table within bounds, compromises are required in the number of dimensions. The preferred modelling approach is therefore dependent on the application.

Inputs

Various inputs are required for the computation of the snapshots. The source level spectra of the dredgers were reported in [de Jong et al, 2010]. Levels were measured for passing, dredging, direct sand dumping, rainbowning and pumping. Depending on the speed and location of the dredgers (in combination with a log describing the activities of the dredgers), the most appropriate source level was estimated. For ships for which no measured source level was available, the [Wales and Heitmeyer, 2002] spectrum was assumed. The chosen source depth is 4 m below the sea surface for all ships and dredgers [de Jong et al, 2010]. The choice of depth here is driven not by any consideration of the “depth” of a ship, or of any sound source within a ship, but of consistency with the choice of depth for the nominal point source chosen for the original measurement of source level, which in this case was 4 m [de Jong et al, 2010]. The spatial distribution of the shipping traffic was available from AIS data logged during the measurement campaign. Based on the AIS data it was possible to estimate the speed of the ships. The Wales and Heitmeyer source level model is independent of ship speed, but applies for ships at their regular cruising speed. At that speed the radiated sound is generally dominated by propeller cavitation noise. This sound is absent for stationary ships, unless they are operating propellers or thrusters to maintain their position. For lack of a general model for the radiated machinery noise of stationary ships, ships were assumed to be silent when moving slower than 2 knots.

The environment is defined by the bathymetry, the physical properties of the seabed and water, and the roughness of the sea surface. The bathymetry was obtained from local survey data with a very high resolution. This allows to model blocking of acoustic energy from the sources disappearing behind the long thin curved island shaped like a boomerang (see Figure 4) [Ainslie et al, 2012b], which would not be represented in the coarser resolution bathymetry data, and which in any case predates the Maasvlakte 2 construction period. The water was modelled with a uniform sound speed of $c_0=1500$ m/s and a density of 1000 kg/m³. The absorption loss in the water was modelled using the equation of Thorp [Thorp, 1967]. The seabed was modelled as medium sand $c_1=1797$ m/s, $\rho_1=2086$ kg/m³ with an absorption given by $\alpha_b=0.88$ dB/ λ [Ainslie, 2010]. The effects of surface scattering and bubbles were modelled using Eq. 8.22 of [Ainslie, 2010], using the local wind speed from a nearby measurement station [Ainslie et al, 2012b]. Figure 4 illustrates the bathymetry and photographic images of the considered area. Wind generated sound was modelled using the areic dipole source factor spectrum from Eq. 8.206 of [Ainslie, 2010].

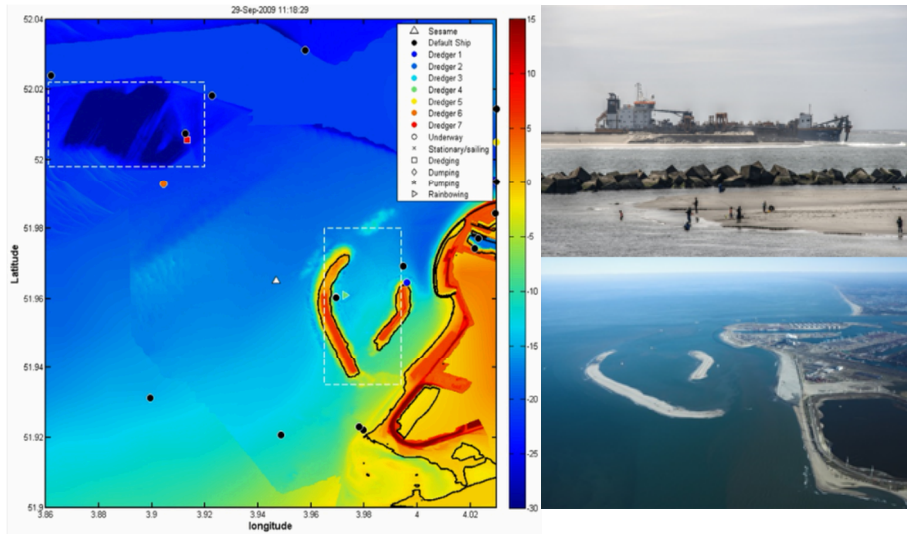


Figure 4: Bathymetry (depth in metres) and distribution of sources and corresponding activities. The white boxes (dashed line) indicate the dredging (top left) and dumping (between the curved sand dunes) regions. The marker symbols indicate the dredger activity and the colour the dredger ID. The black colour indicates unknown ships for which the Wales and Heitmeyer spectrum was used. The white triangle indicated the location of the acoustic measurement system SESAME). The right figures are photographs of the area.

Model data comparison

Measurements were made at two heights (2 m and 7 m) above the seabed at the Sesame location illustrated in Figure 6. As the measured levels are very similar, the model predictions are only given for 2 m above the seabed, across the entire region, and for decade bands between 32 Hz and 80 kHz. Figure 6 illustrates the modelled broadband SPL at 2 m above the seabed. The discontinuities result from the assumption that sound travels in straight horizontal lines, with no refraction or diffraction in the horizontal planes (the so-called “Nx2D” approximation). While computing snapshots helps understand the behaviour of the model, the direct model data comparison allows a more detailed understanding of the accuracy. Figure 7 and Figure 8 directly compare the modelled and measured decade bands SPLs at the measurement location.

SOURCE MODELS AND SOUND MAPS

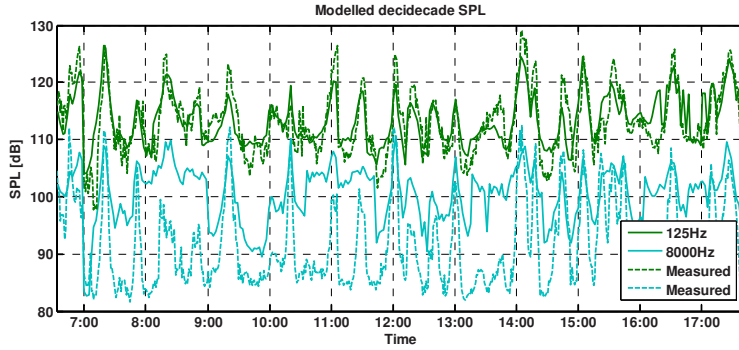


Figure 5: Modelled (solid) and measured (dashed) SPL [dB re $1 \mu\text{a}$] at 2 m above the seabed for the 125 and 8000 Hz decidecade bands at the Sesame location illustrated in Figure 4. Model predictions are for ship-generated sound only. Date is 29 September 2009 Rotterdam local time (UTC +01:00).

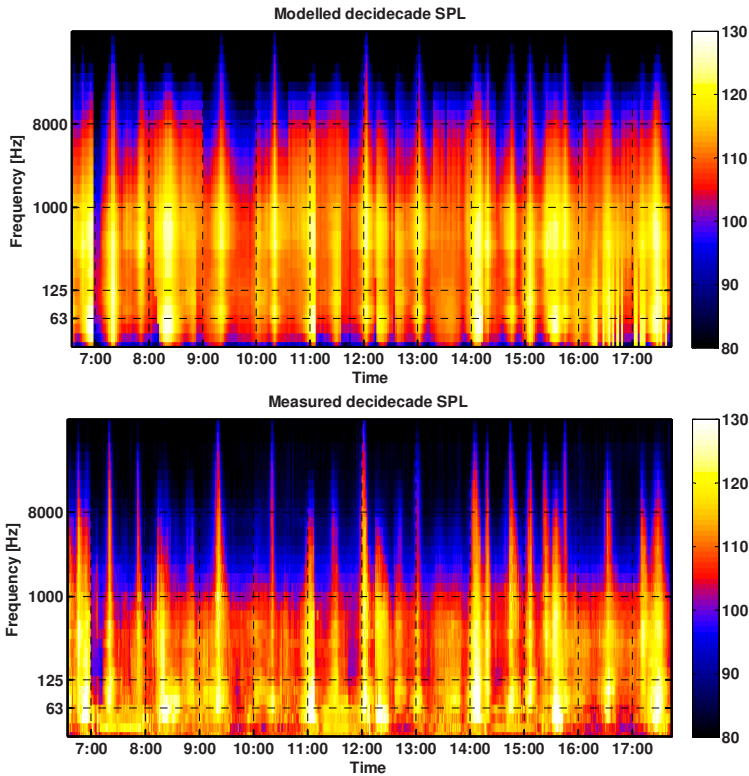


Figure 6: Modelled (top) and measured (bottom) SPL [dB re $1 \mu\text{Pa}$] at 2 m above the seabed for all decidecade bands (32 Hz up to 80 kHz) at the Sesame location illustrated in Figure 4. Model predictions are for ship-generated sound only. Date is 29 September 2009 Rotterdam local time (UTC +01:00).

Comparison with other model(s)

During the Madrid sound mapping workshop [Aquo-Sonic (Madrid)], comparisons were made between the depth average broadband SPL computed with the hybrid method of [Sertlek and Ainslie, 2014a] and other methods, such as the parabolic equation model RAM, for a synthetic shipping distribution in the Skagerrak Sea, north of Denmark for a set of synthetic scenarios with a defined set of environmental parameters. These comparisons will be reported on in the SONIC project. The computation time for generating the sound maps using the hybrid propagation algorithm was in the order of tens of minutes, while the computation time for the RAM model was in the order of days. For examples demonstrating the accuracy of the propagation model on some synthetic test cases designed to test sonar equation, see [Sertlek and Ainslie, 2013, 2014a, 2014b].

Accuracy

When computing sound maps, many parameters are uncertain. Uncertainties and assumptions in the snapshot modelling presented in Figures 6 and 7 result in a discrepancy between modelled and measured levels. This section discusses accuracy of the modelling approach.

Sound generated by shipping

For the Maasvlakte 2 simulation, the source level of seven dredgers was measured for transit, dredging, direct sand dumping, rainbowing and pumping activities [de Jong et al, 2010]. Levels were extrapolated for frequencies where levels were not available using the trends of other dredgers if available. The source level (SL) for frequencies between 8 kHz and 80 kHz were extrapolated linearly in log (frequency) by assuming a constant gradient above 6.3 kHz. For some of the dredgers, the low frequency SL was estimated using the trend from other measured dredgers. The source level of the other ships was approximated using the model by Wales and Heitmeyer at all frequencies. Above 1 kHz, such an extrapolation leads to higher source level than an extrapolation based on the measurements of Arveson and Vendittis [Ainslie, 2010 (p423)]. The directional behaviour of the ship radiated sound was not taken into account, and the ships were all modelled as point sources at 4 m depth. Besides the uncertainty in the source level, also the activity of the ships was estimated based on AIS data. Some useful information can be extracted from AIS data, although the reliability of, for example, the navigation status parameter is dependent on the crew and may not always be accurate.

Hence, the uncertainty in the source level estimation for the individual ships in each snapshot is rather large. Concerning the ‘type A’ [ISO GUM] statistical uncertainty, [Wales & Heitmeyer, 2002] indicate that ‘the standard deviation of the measured spectra on which their model is based varies about a nominal value of about 5.3 dB for frequencies below about 150 Hz and then decreases to a nominal value of about 3.1 dB for frequencies greater than 400 Hz’. The standard deviation of the estimated dredger source levels [de Jong et al, 2010] is about 5 dB. No attempt has been made to quantify the additional ‘type B’ uncertainty associated with, for example, assumptions about the navigation status of the ships, the lack of speed dependence in the source level model and the extrapolation of the measured source level spectra to higher frequencies.

Environment

The acoustical parameters describing the environment were chosen as realistic as possible based on the available data. No adjustment was made to reduce the difference between the modelled and the measured levels. The surface loss was estimated using the measured local wind speed. The sediment was modelled as a fluid approximating a medium sand seabed, typical for this region [Ainslie et al, 2012b].

Model applicability

For frequency-depth combinations very close to cut off where just one mode propagates, it becomes more complicated to predict the propagation loss. At frequencies above 4 kHz, the dependence of propagation loss on surface roughness and wind-generated bubble population is not well understood and requires further investigation [Ainslie, 2005]. Besides the propagation loss applicability, a cause of bias is the absence of other sound sources (e.g., wind [Dreschler et al, 2009]) in the model that contribute to the underwater sound in the measured data. There is evidence in Figure 7 that wind generated sound becomes important above about 10 kHz, especially for the 90 % exceedance level and the median. The effect of ship speed on radiated sound (presently approximated by a sharp cut off for an arbitrary ship speed of 2 knots) needs further investigation.

Quantification of error

Studying the differences between the model and the measurements, it is observed that the adopted modelling approach can accurately predict the sound pressure level at the hydrophone for the lower frequencies. Especially individual passages of dredgers for which the source level was

measured are accurately represented. Figure 7 shows the statistics of the measured and modelled levels illustrated earlier in Figure 5 and Figure 6 for an 11 hour period on 29 September 2009. The model tends to underestimate SPL by about 5 dB at low frequency (up to ca. 100 Hz) and overestimate SPL by a similar amount at frequencies above ca. 500 Hz. At higher frequencies still (above 30 kHz) the model underestimates SPL again, by an amount that increases with increasing frequency. The most likely reason for these high frequency errors is the omission of the contribution from wind, the likely magnitude of which is shown by the black line of Figure 7.

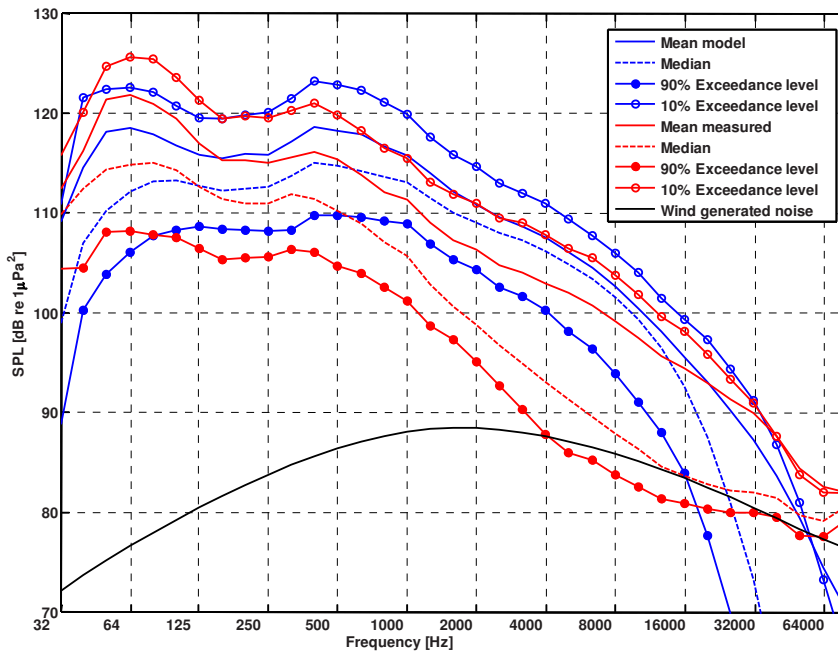


Figure 7: Mean, median and exceedance levels for both the measured and modelled receiver SPL [dB re 1 μPa^2]. The black curve is the temporally averaged wind generated sound. The modelled results include ship generated sound only. Statistics are for 6 s snapshots, once per minute. The statistics are computed for the distribution of mean-square sound pressure in each 6-second time window.

The most likely explanation for the overestimation of the SPL between 1 kHz and 10 kHz is the treatment of surface reflection loss, which includes the effect of rough surface scattering enhanced by the presence of near-surface bubble clouds [Ainslie, 2005], but neglects the effect of absorption by the bubbles, which at 8000 Hz and above is expected to dominate [APL 1994, Ainslie 2010]

3.2.4. SUMMARY AND DISCUSSION

In this section, an application of a propagation model (see Chapter 2.3) is applied to shipping sound maps for the annual ship distribution and AIS snapshots. The accuracy of sound maps are tested by comparison with actual measurements. Model results give similar accuracy as measurements at the MSFD indicator frequency of 125 Hz. However, the neglect of surface scattering seems to cause errors above 1 kHz. Consequently, the agreement between model and measurement results can probably still improve by adding a surface reflection term to the propagation model.

3.3. AGORA: AIRGUN SOURCE SIGNATURE MODEL

This section is published as “H.Ö.Sertlek and M.A. Ainslie, AGORA: Airgun source signature model: its application for the Dutch seismic surveys, Conference Proceedings of UAC 2015, Crete, Greece.”

Abstract: *Seismic exploration has the potential to make a significant contribution to the soundscape of the North Sea. An airgun works by rapid release of air into water, forming a large bubble, which then pulsates, radiating sound as the bubble successively compresses and rarefies the surrounding water. An airgun array source signature model is described, following Gilmore’s equation of motion, incorporating liquid compressibility, mass diffusion, and thermal effects, and gas pressure laws. Predicted airgun signatures are compared with measurements. The proposed source model, coupled with a propagation model, can be used to generate anthropogenic and natural sound maps for. In this study we focus specifically on sound maps associated with seismic surveys in the Dutch North Sea.*

3.3.1. INTRODUCTION

Sound maps can provide a useful insight about the distribution of sound over large regions. Model predictions offer a practical means to fill gaps left where measurements are unavailable [Mennitt et al,2014]. Sound maps based on model predictions rely on the solution to two key problems: the reliable modelling of sound propagation and of source characteristics. For sound mapping, the solution of large scale broadband propagation problems is required. The modelling of source properties requires an additional effort by understanding its working principles and supporting the source level estimations by measurements. The sound generated by airguns can be estimated by the solution of bubble motion problems by including the effect of liquid compressibility, mass diffusion, thermal effects and momentum. This results in a set of differential equations from various branches of physics. In this section, the calculation of airgun array signatures is investigated. A simulation tool (AGORA) is developed. The calculated source signatures can be used to generate seismic survey sound maps for anthropogenic and natural sources in the Dutch North Sea. The model is an implementation of Ziolkowski's approach [Ziolkowski,1970 ; Ziolkowski et al, 1982] including mass and heat transfer as described by [Laws et al,1990] and [MacGillivray,2006]. It solves a differential equation system iteratively. First, the bubble radius, bubble wall velocity, temperature and mass of the bubble are calculated. These quantities are then used for the estimation of the radiated pressure from the airguns. The signature of airgun array can be calculated as a sum of contributions from each single airgun, with bubble interactions treated as a perturbation [Ziolkowski et al, 1982]. Results so obtained are compared with measurements made available by the E&P Sound and Marine Life JIP (henceforth abbreviated "JIP"). After the validation of the source model, the calculated source signatures can be used as an input for seismic sound.

3.3.2. CALCULATION OF PRESSURE FROM SINGLE AIRGUN

The equation of motion can be represented by different equations from various approaches. Gilmore's equation which is based on the Kirkwood-Bethe approximation is investigated in this section [MacGillivray,2006],

$$\frac{du}{dt} = \frac{\left(1 + \frac{u}{c}\right)H + \frac{a}{c}\left(1 - \frac{u}{c}\right)\frac{dH}{dt} - \frac{3}{2}u^2\left(1 - \frac{u}{3c}\right)}{a\left(1 - \frac{u}{c}\right)}$$

where a is the bubble radius, $u = da/dt$ is the bubble wall velocity, c is the sound speed in the disturbed liquid, which can be calculated from the equation of state as $c = c_\infty \left(\frac{p_a+B}{p_\infty+B}\right)^{(n-1)/2n}$. Further, c_∞ is the sound speed in water, and B and n are experimental constants: $n = 7$ and $B = 304$ MPa for water. The parameter H is the specific enthalpy at the bubble wall, which can be calculated similarly by using the equation of state [Ziolkowski,1970] as $H = \int_{p_\infty}^{p_a} \frac{dp_a}{\rho} = \frac{p_a - p_\infty}{\rho} = \frac{n(p_\infty+B)}{(n-1)\rho_\infty} \left[\left(\frac{p_a+B}{p_\infty+B}\right)^{(n-1)/n} - 1 \right]$, where p_∞ is the undisturbed hydrostatic pressure $p_\infty = p_{\text{atm}} + \rho_\infty g z_{\text{gun}}$, g is the acceleration due to gravity, and z_{gun} is the depth of airgun. The pressure p_a is that at the bubble wall, which can be estimated using the polytropic relation, ignoring the surface tension and the liquid viscosity, i.e., $p_a = p_{a0} \left(\frac{a_0}{a}\right)^{3\gamma}$, where γ is the experimentally determined polytropic index. However, the calculation of the pressure at bubble wall by a polytropic relation has several limitations for nonlinear oscillations [Prosperetti,1984; Prosperetti et al, 1988]. Instead of using the polytropic relation, p_a can be written as $p_a = \frac{3m_b R_G T_b}{4\pi a^3} - \frac{2\sigma}{a} - 4\mu \frac{u}{a}$ where σ is the surface tension and μ is the liquid's shear viscosity, R_G is the specific gas constant, T_b is the temperature of the air in the gas bubble, m_b is the mass of gas contained in the bubble and V_b is the volume of the gas bubble. The time derivative of H can be written

$$\frac{dH}{dt} = \frac{1}{\rho} \left(R_G \left(\frac{V_b \left(T_b \frac{dm_b}{dt} + m_b \frac{dT_b}{dt} \right) - m_b T_b \frac{dV_b}{dt}}{V_b^2} \right) + \frac{2\sigma}{a^2} - 4\mu \left(\frac{au' - u}{a^2} \right) \right)$$

where $\frac{dm_b}{dt}$, $\frac{dV_b}{dt}$ and $\frac{dT_b}{dt}$ should be found to include mass and heat transfer [Laws et al,1990; MacGillivray,2006]. The derivative of volume can be simply written as $\frac{dV_b}{dt} = 4\pi u a^2$. The efficiency of the airgun can be estimated by an empirical parameter (η), which characterises the remaining

air in the gun chamber after the airgun has fired [Li Guo-fa et al,2010]. The maximum value of the mass in the bubble can be ηm_{gun} . The time derivative of mass can

$$\frac{dm_b}{dt} = \begin{cases} \tau \sqrt{\frac{(m_{\text{gun}} - m_b)}{V_{\text{gun}}}} (p_{\text{gun}} - p_a), & m_b \leq \eta m_{\text{gun}} \\ 0, & \end{cases}$$

where $\tau = \tau_0 (V_{\text{gun}})^\beta$ is the port-throttling constant which is related to the airgun-port area (with dimension $[L^2]$), τ_0 is the volume independent port-throttling constant (dimension $[L^{2-3\beta}]$), β is a dimensionless power law exponent which is empirically determined from the experiments, and p_{gun} , m_{gun} and V_{gun} are the pressure, mass and volume of remaining air in the gun chamber. The time derivative of temperature

$$\frac{dT_b}{dt} = \frac{R_G T_b \frac{dm_b}{dt} - \frac{dQ}{dt} - p_a \frac{dV_b}{dt}}{m_b c_v}$$

where $\frac{dQ}{dt}$ is the rate of heat transfer into the air bubble [Laws et al, 1990; MacGillivray,2006]. This rate can be written as $\frac{dQ}{dt} = \kappa(4\pi a^2 \Delta T)$ where $\Delta T = T_b - T_w$ is the temperature difference between the bubble and surrounding water. The parameter κ is also an experimentally determined constant. The buoyancy of the air bubbles changes the hydrostatic pressure because of the rise of the sea surface. This affects the bubble period [MacGillivray,2006] and can be described by $\frac{dz_{\text{gun}}}{dt} = \frac{2g}{a^3} \int_0^t a^3 dt$. The ideal gas law is not valid when the pressure in the gun chamber very high. For this situation, a modified form of temperature can be used [Laws et al,1990] to describe an effective temperature in the air-gun chamber, $T_{\text{gun}}' = T_{\text{gun}} \left(1 + \frac{p_{\text{gun}}}{p_c}\right)$, where $p_c = 139$ MPa for air. The relevant equations for the bubble motion, mass and heat transfer can be written as a differential equation system, which can be solved by iterative methods [MacGillivray,2006; Li Guo-Fa et al,2010] with the initial conditions: $m_0 = \frac{P_\infty V_{\text{gun}}}{R_G T_{\text{water}}}$, $T_0 = T_{\text{gun}}$, $a_0 = \left(\frac{3V_{\text{gun}}}{4\pi}\right)^{1/3}$ and $u_0 = 0$. The optimized empirical parameters from [MacGillivray,2006] are used for the mass and heat transfer

coefficients ($\beta = 0.52, \eta = 0.8317, \kappa = 22230 \text{ J m}^{-2} \text{ s}$ and $\tau_0 = 0.5355 \text{ m}^{2-3\beta} = 0.5355 \text{ m}^{0.44}$). These parameters should be selected carefully to increase the accuracy of the model results depending on the environment and airgun properties. Then, the radiated pressure can be expressed as a function of enthalpy, bubble wall velocity and bubble radius [Laws et al, 1990] as $s_0(t) = \lim_{R_0 \rightarrow \infty} R_0(p_a - p_\infty) = \rho_\infty a \left(H + \frac{u^2}{2} \right)$. Where R_0 is the distance from the bubble centre to the far field point. Pressure can be estimated by various approaches [Ziolkowski, 1970]. This equation is a first order approximation, in which higher order terms in $1/r$ are neglected by assuming r is large. Thus, this equation gives the pressure in the free field and is called the “notional signature”, without the surface reflection, or “ghost” [Ziolkowski, 1970]. The reflections from sea surface and seabed can be added from propagation theories separately. The sound pressure, including the contribution from the surface ghost, is calculated using image theory as

$$p_{\text{airgun}}(r, t) = \frac{a\rho_\infty \left(H(r, t) + \frac{u^2(r, t)}{2} \right)}{D_1} + R_S \frac{a\rho_\infty \left(H(r, t + t_0) + \frac{u^2(r, t + t_0)}{2} \right)}{D_2}$$

where $R_S = -1$ is the sea surface reflection coefficient, D_1 is the distance between gun and receiver, D_2 is the distance between the surface image and receiver as shown by Fig.1, and t_0 is time delay, calculated as $t_0 = \frac{D_2 - D_1}{c_\infty}$. The time domain source signature, $s(t; \varphi)$, is calculated as $s(t; \varphi) = \lim_{R_0 \rightarrow \infty} R_0 p_{\text{airgun}}(R_0, t; \varphi)$ where φ is the dip angle. For a single airgun, the source signature only varies with dip (φ) angle and does not vary with the azimuth angle (ψ). However, the airgun array pattern may also vary with azimuth angle depending on the array geometry. The mean-square sound pressure spectral density level is

$$L_f = 10 \log_{10} \left(\frac{2 |P_{\text{airgun}}(r, f)|^2}{1 \frac{\mu\text{Pa}^2 \text{s}}{\text{Hz}}} \right) \text{ dB}$$

and energy source spectral density level is

$$L_s = 10 \log_{10} \left(\frac{2 |S(f, \varphi)|^2}{1 \frac{\mu\text{Pa}^2 \text{m}^2 \text{s}}{\text{Hz}}} \right) \text{ dB}$$

where $P_{\text{airgun}}(r, f) = \int_{-\infty}^{\infty} p_{\text{airgun}}(r, t) \exp(-i2\pi ft) df$ is the Fourier transform of the sound pressure and $S(f, \psi) = \int_{-\infty}^{\infty} s(t, \psi) \exp(-i2\pi ft) df$ is the frequency domain source signature.

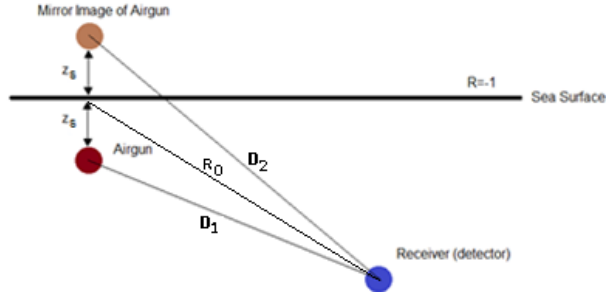


Figure 1. The contribution of surface ghost

3.3.3. SOURCE SIGNATURE OF AIRGUN ARRAYS

During a seismic survey, multiple airguns are used in an array to amplify the sound. Airguns arrays have horizontal and vertical directivity patterns. The effect of interference with the ghost is to direct the source energy more towards the seabed than in the horizontal direction. Before modelling the directivity, the interaction between the different airguns should also be taking into account. This can be done by adding a time dependent perturbation term to the source signature of each individual airgun[Ziolkowski et al,1982; MacGillivray,2006]. Hence, the bubble interactions can be estimated by an effective hydrostatic pressure for the m th airgun as

$$p_m^{eff}(t) = p_{\infty} + \sum_{k \neq 1} \Delta p_{mk}(t)$$

where $\Delta p_{mk}(t) = \frac{\rho a_k(t')}{D_{mk}} \left(H_k(t') + \frac{u_k(t')^2}{2} \right)$ and t' is the retarded time. This equation affects the enthalpy according to Tail's equation. Thus, the bubble motion characteristic will be changed. In the next steps of derivation, perturbed airgun signatures are used for the calculation of directivity.

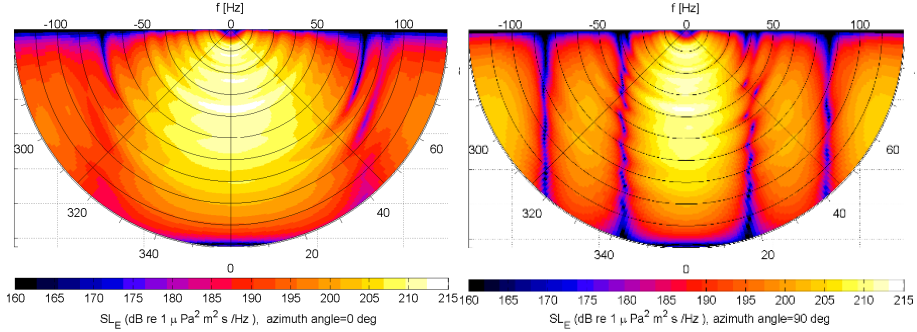


Figure 2. Vertical variation of energy source spectral density level vs dip angle (angle from the vertical direction) at 0 degree (left) and 90 degree(right) azimuth angles. The frequency axis varies from 0 Hz to 150 Hz.

For each individual airgun signature, the time delays between airgun location and centre point of array (described as origin point $x = 0, y = 0, z = 0$) are calculated. The distances between the gun and the ghosts are $D_{1m} = |\hat{\mathbf{r}} \cdot \hat{\mathbf{r}}_{\text{gun}_m}| = x_m \cos \psi \cos \theta + y_m \sin \psi \cos \theta + z_m \sin \theta$ and $D_{2m} = |\hat{\mathbf{r}} \cdot \hat{\mathbf{r}}_{\text{ghost}_m}| = x_{m-N} \cos \psi \cos \theta + y_{m-N} \sin \psi \cos \theta - z_{m-N} \sin \theta$, where $\hat{\mathbf{r}} = (\cos \psi \cos \theta, \sin \psi \cos \theta, \sin \theta)$ is a unit vector, and ψ and θ are the azimuth and grazing angles ($\varphi = \frac{\pi}{2} - \theta$). The positions of airguns and their surface images are $\hat{\mathbf{r}}_{\text{gun}_m} = (x_m, y_m, z_m)$ and $\hat{\mathbf{r}}_{\text{ghost}_m} = (x_m, y_m, -z_m)$. The time delays are summed to obtain the frequency domain pressure with 3D directivity as [Duren,1988]

$$P(r, f, \psi, \theta) = \sum_{m=1}^N S_{0m}(f) \left[\frac{\exp(ik_w D_{1m})}{D_{1m}} - \frac{\exp(ik_w D_{2m})}{D_{2m}} \right]$$

where N is the number of airguns in the airgun array, and $S_{0m}(f)$ is the frequency domain notional source signature of the m th airgun. The exponential phase terms represent the time

delays in the horizontal plane In Figure 2, the vertical variation of energy source spectral density level is shown at different dip angles.

3.3.4. COMPARISONS

Some comparisons are done for JIP measurements for Svein Vaage broadband airgun study measurements. One selected as representative of the 30 available airgun shots is used in these comparisons. The positions of receivers and airgun are shown in Figure 3. Three receiver locations are (0 m, 0 m, 30 m), (0 m, 0 m, 100 m) and (10.8 m, 9.8 m, 15 m). The airgun location is nominally (0 m, 0 m, 6 m). In the original measurement set-up, there are many receiver points. However, these three positions are chosen for the comparisons. The model is sensitive to small changes in the source depth. To estimate the location of the source depth during the shot, the nulls in Lloyd mirror pattern are used as $z_g \approx \frac{2N_{lobes}\lambda}{4} = 6.36 \text{ m}$.

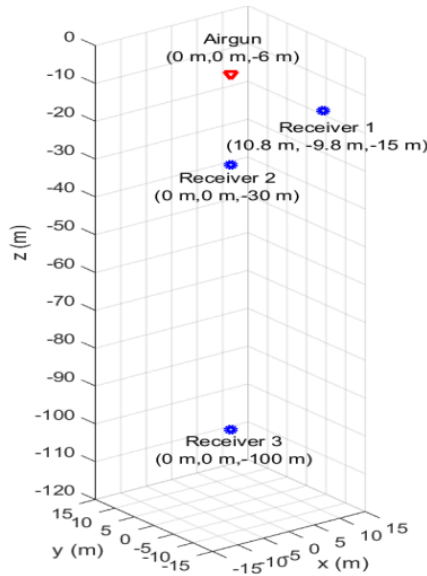


Figure 3. The geometry of the measurements

In Figure 4, the comparisons between AGORA and JIP measurements are shown for $V_{gun} = 1.31 \text{ L}$ (80 in^3) and firing pressure 13.8 MPa (2000 psi).

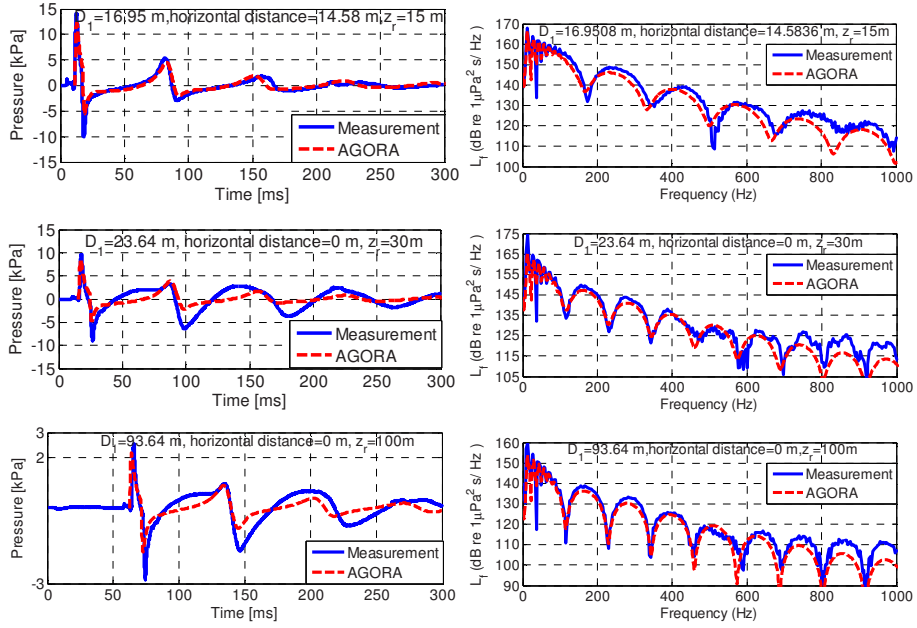


Figure 4. Comparisons of sound pressure (left panels) and mean-square sound pressure spectral density level (L_f) of 1.31 L (80 in^3) airgun at different distances (the distances between airgun and receiver location is 16.9 m, 23.6 m and 93.6 m) and elevations. The source depth is 6.36 m and the firing pressure is 13.8 MPa (2000 psi).

On the other hand, the source signatures can be calculated from different long ranges. R_0 denotes the distance between dipole centre (0 m, 0 m, 0 m) and measurement location. For these calculations, the measurements at (0 m, 0 m, 100 m) and (10.8 m, 9.8 m, 15 m) coordinates are used. The first measurement is at 100 m beneath of the airgun with 0 degree dip angle. The distance of second measurement at $R_0 = 20.9$ m with 54.4 degree dip angle. The measurement and calculated results are shown in Figure 5.

SOURCE MODELS AND SOUND MAPS

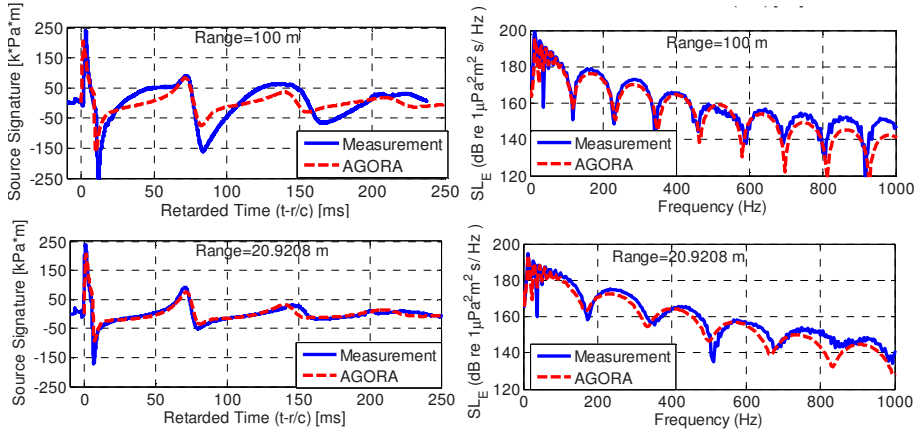


Figure 5. The comparisons for the source signature and energy source spectral density level (L_s).

The measured and calculated source signatures for $R_0=20.92$ m (dip angle is 54.4 degree) and $R_0=100$ m (dip angle is 0 degree)

The empirical calibration coefficients of mass and heat transfer are not optimized for this dataset. Thus, better agreement may be obtained by optimizing these parameters for JIP dataset. AGORA assumes that the surface is flat. Realistically, the sea surface is not flat, resulting in rough surface scattering. All these uncertainties can lead to differences between the model and measurement results. By using calculated signatures the seismic survey maps are generated for the North Sea in Figure 6. Propagation loss is calculated by a hybrid method based on normal modes and flux theory [described in Chapters 2.2. and 2.3]

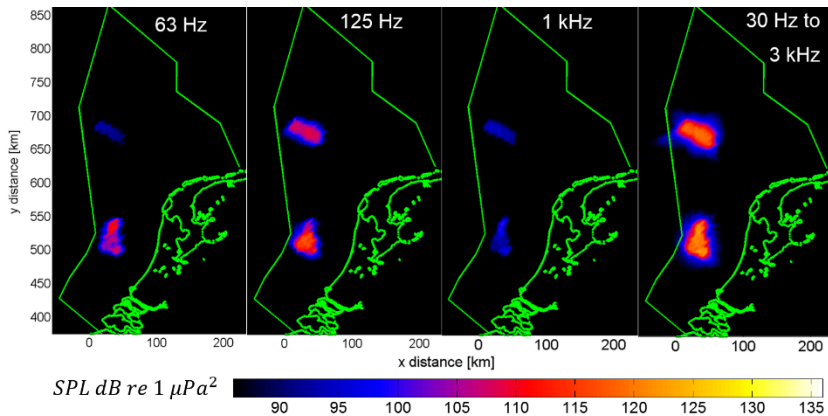


Figure 6. Annually averaged seismic survey sound maps of the North Sea for 2007. The receiver depth is 1 m. Frequency range for the broadband map is 30 Hz to 3 kHz. The green lines show the Dutch coastline and the Dutch EEZ outline

3.3.5. CONCLUSIONS

Calculation of airgun source signatures and their comparisons with E&P Sound and Marine Life JIP measurements are shown in this section. A Matlab script (AGORA) is developed to solve the set of differential equations for the bubble motion and visualize airgun array signatures. Good agreement is obtained between the JIP measurements and the airgun model described in the present section. The choice of exact source and receiver locations, environmental parameters, mass and heat transfer coefficients can affect the accuracy of the calculated results. Thus, these parameters should be selected carefully. After these validation tests, the calculated source energy spectral densities can be used for the calculation of seismic survey sound maps.

3.4. SOURCE SPECIFIC SOUND MAPPING: SPATIAL, TEMPORAL AND SPECTRAL DISTRIBUTION OF SOUND IN A HEAVILY EXPLOITED SEA

This section will be submitted as “H.Ö. Sertlek, H. Slabbekoorn, C. ten Cate and M.A. Ainslie, Source specific sound mapping: spatial, temporal and spectral distribution of sound in a heavily exploited sea ”

Abstract: *Effective measures for protecting and preserving the marine environment require an understanding of the potential effect of sound on marine life. This section focuses on modelling the spatial, temporal and spectral distribution of the sound from the main sound sources in the Dutch North Sea in various frequency bands between 100 Hz and 100 kHz. The selected sound sources (shipping, airguns, underwater explosions and wind) are ranked according to their contribution to the total acoustic energy in the Dutch North Sea. Of these sources, shipping is predicted to be responsible for the largest amount of acoustic energy, (~400 J), followed by seismic surveys (~90 J), explosions (~80 J), and wind (~20 J), in the 100 Hz to 100 kHz frequency band, averaged over a two year period. The potential impact of these sounds on aquatic animals depends not only on these temporally averaged and spatially integrated broadband energies, but also on the source-specific spatial, spectral and temporal variation. Shipping is dominant in the southern part and along the coast in the north, throughout the years and across the spectrum. Seismic surveys are relatively local and spatially and temporally dependent on exploration activities in any particular year and spectrally more biased to low frequencies than the other sources. Explosions occur mainly in the southern part of the North Sea and contribute energy across the spectrum, but for very short point events in time. Wind is ubiquitous and omnipresent, though more prominent in the winter months and in the high frequency range. This variation needs to be taken into account when assessing the sound impact on marine life.*

3.4.1. INTRODUCTION

Sound is likely to play a dominant role in the life of aquatic animals in deep and dark oceans or shallow and murky waters, as well as in the bright and colourful world around coral reefs, [Myrberg and Fuiman 2002; Montgomery et al. 2006; Slabbekoorn et al. 2010]. Visibility in water is less than 40 meters even in the most optimal conditions, depending on depth, time of day and water turbidity [Mobly 1994; Trees et al. 2005]. Typically, water transparency is not optimal and available light can be weak in the deep, in shadows, or at night. Dissolved odours can provide information about habitat, presence of predators and prey or food in general, and may also serve a role in communication among conspecifics [McLennan 2003; Huijbers et al. 2008]. However, independent of conditions for vision and smell, but dependent on species-specific sensory abilities, sound often provides critical information about the environment to an organism, either by itself or in concert with other stimuli [Stevens 2013; Halfwerk and Slabbekoorn 2015].

Many aquatic animals rely on sound for various functions that are vital to survival and reproduction. Reasons for this are that sound propagates extremely well through water and that perception is independent of light conditions (e.g. in dark murky water or at night) or directional attention. Animals are known to communicate acoustically underwater or exploit environmental sounds to find prey, avoid predators, or for orientation [Slabbekoorn and Bouton, 2008; Fay 2009]. However, biologically relevant sounds need to be extracted from a typically noisy background of many other sounds, which requires that animals are able to discriminate and recognize the relevant sounds. This ability will depend critically on suitable signal-to-noise ratios. Furthermore, the introduction of anthropogenic noise to the naturally present environmental sounds may not only increase the potential for masking problems, but also adds the possibly detrimental effects of distraction, disturbance, deterrence and injury [Popper and Hastings 2009; Slabbekoorn et al. 2010; Radford et al. 2014].

International concern about possible effects of anthropogenic sound sources on marine life has arisen due to increasing shipping traffic, exploitation of oil and gas reserves and the development of new offshore energy sources. This concern has led governments to introduce regulatory measures worldwide [Lucke et al 2014]. For example, the European Union's Marine Strategy Framework Directive (MSFD) [EU 2008] requires EU member states to achieve or maintain Good Environmental Status (GES) by 2020. Specifically, GES Descriptor 11 requires underwater noise to be "at levels that do not adversely affect the marine environment". The use of sound maps to

monitor and evaluate is the specific advice of a technical workgroup of the European Union on underwater noise (TSG Noise) [Dekeling et al,2014].

Sound maps can provide insight into the distribution of sound and the contribution to the energy budget from anthropogenic and natural sound sources. Many countries have an interest to identify the components of sound in their local seas [Dekeling et al 2014, Tyack et al,2015 ;Sutton et al, 2011; Folegot, 2012; Sertlek et al, 2015b, Cetsound; Hatch and Fristrup, 2009]. Sound maps can also provide insight and overview of the distribution and origins of sound for globally present sound sources such as shipping lanes [Porter and Henderson, 2013]. Erbe et al. (2012 and 2014) demonstrated the potential for applied value of sound maps by modelling shipping sound in Canada's Pacific Region and combining the acoustic distribution with density estimates for marine mammals that are of conservation concern [Borja et al, 2010]. However, the applied value of sound mapping and comparisons among sound sources relies on adequate acoustic processing and propagation formulas that vary per sound source type and environmental conditions such as water depth.

In the present section, we provide a case study that elucidates the state of the art and the potential for applications of marine sound maps worldwide. Sound maps are calculated for the shallow water environment of the Dutch Exclusive Economic Zone (henceforth abbreviated "Dutch North Sea"). This part of the North Sea is a heavily exploited area providing vessel entrance to the largest port in Europe (Rotterdam), and other activities adding to underwater acoustic load include: fisheries, several busy ferry lines between England and the Netherlands, the operation and construction of wind farms, seismic surveys and detonation of unexploded World War II ordnance. We here investigated the spatial, temporal (weekly) and spectral distribution (averaged over two years) of energy with a hybrid method [See sections 2.2 and 2.3], which enables the fast calculation of propagation loss across a wide range of frequencies. Because energy adds linearly, this approach permits the calculation of a sound energy budget per source. In this study, realistic source distributions are used to generate sound maps for each source and for the energy sum (incoherently) of all sources. Energy contributions of each sources are analysed for a wide frequency band 100 Hz to 100 kHz. The water depth in the Dutch part of the North Sea is mostly less than 50 m. This shallow water environment hosts various geophysical, biological and anthropogenic sources. Geophysical sources include wind, rain and lightning and can be prominent. Biological sources include communication and feeding sounds from invertebrates, crustaceans, fish and marine mammals, but are not thought to contribute significantly to the overall sound energy budget in the North Sea [Ainslie et al, 2009].

The purpose of our sound maps is to provide insight into the relative contribution of sound sources to the overall cumulative distribution of sound energy in space, time and spectrum. This will allow evaluation of potential environmental impact on different animal species living in the Dutch North Sea. The potential impact will vary per species depending on species-specific geographic distributions, the (seasonal) timing of critical activities and the absolute and spectral sensitivity to sound. Providing sound maps must be seen as a starting point for impact assessment and possible mitigation, as consequences of sound exposure are typically still unclear and there are more factors than source and propagation characteristics that will affect the sound exposure levels in marine animals. Pinnipeds are for example particularly common around the Wadden islands in the north, while many fish spawn in the southern part of the North Sea. The harbour porpoise is known to exhibit large fluctuations in density among different months of the year and some diving birds are present year-round, while others are only present in winter. Furthermore, the spectral range of auditory sensitivity varies per taxonomic group and can be broadly categorized: invertebrates (most likely < 300 Hz, some up to 3000 Hz) and fish (many < 500 Hz, most < 1000 Hz, all < 4000 Hz) and marine mammals: seals (0.3-60 kHz) and porpoises (1-125 kHz).

The starting point for constructing sound maps is the assessment of the acoustic energy generated by various sources. [Ainslie et al., 2009] introduced the concept of the “free-field energy” of a sound source, defined as the total acoustic energy that would exist in the water if the same source were placed in an infinitely deep ocean, of uniform impedance, no boundaries other than the sea surface, and with the same sound speed, density and absorption coefficient as seawater. This quantity is proportional to the source power and inversely proportional to the absorption coefficient of seawater, and provides a convenient way of ranking the contribution to the sound field from qualitatively different natural and anthropogenic sources. By adding the contributions from individual sources [Ainslie et al, 2009] made order of magnitude estimates of the contributions of different sound sources to the annually averaged free-field energy. We here follow up with more precise calculations and more extensive visualizations of variation in space, time and spectrum for the sound energy distribution in a real-world case study for the Dutch North Sea.

We calculate and compare the total energy contributions from four sound sources taking into account the environmental conditions in the Dutch North Sea. We do so by characterizing the spatial, temporal and spectral distributions of sound using previously developed source models [Weston 1960; Wales and Heitmeyer, 2002; Sertlek and Ainslie, 2015a; Kuperman and Ferla, 1985; APL-UW, 1994; Ainslie 2010; Arveson and Vendittis, 2000] and propagation models [Ainslie et al

2011; see Section 2.3]. We included three anthropogenic sources: ships, airguns and explosions, and one geophysical source: wind. While sophisticated pile driver source models exist [Reinhall and Dahl 2011; Zampolli et al 2013], the coupling of such source models with accurate propagation models is an active research topic in its own right [Schecklman et al 2015; Lippert et al, 2015; Hall, 2015] and is beyond the present scope. We have chosen to focus on wind as our geophysical sound source because of its ubiquitous nature, while rain and lightning can also contribute significantly to the acoustic energy budget.

The aims of the present section are:

- to quantify the contributions from ships, airguns, explosions and wind to the overall acoustic energy in the Dutch North Sea;
- to develop and apply quantification methods for providing insight into the spatial, temporal and spectral distribution of that energy;
- to provide an evaluation of the potential biological relevance.

In Section 3.4.2, we describe the inputs needed to generate the sound maps (source levels, bathymetry, sediment properties) and propagation method. In Section 3.4.3, two-year average sound maps are presented for the Dutch North Sea. We provide histograms and cumulative distribution functions derived from the spatial distribution of SPL (the squared sound pressure is averaged over two years), followed by the temporal distribution of sound energy contribution from each source in Section 3.4.4. In the final section, the proposed approach and results are summarized and discussed in the context of biological relevance and as a tool for policy makers, offshore industry, and conservationists.

3.4.2. TOWARDS SOUND MAPS

A. Source Level

We examined three anthropogenic sources (ships, seismic airguns and explosions) and one natural source (wind). These sound sources have a variety of different sound generation mechanisms. It is conventional to characterize underwater sound sources in terms of their “source level”. Unfortunately, this term has multiple different meanings, depending for example on the continuous [Wales and Heitmeyer, 2002] or impulsive [MacGillivray, 2006] nature of the source, or its proximity to the sea surface, whereby some sources are characterised in terms of the properties of the dipole formed in combination with their surface-reflected image, [Ziolowski, 1970; Arveson and Vendittis, 2000], while others are treated as a monopole regardless of their position relative to

the sea surface [Weston,1960; Wales and Heitmeyer,2002]. Finally, some sources, like wind and rain are more naturally described as sheet sources than as point sources. These multiple differences make it difficult to make meaningful comparisons between the source levels of different types of sources. Since each source has a different sound generation mechanism, there are different frequency-dependent patterns of amplitude fluctuations (Figure 1). Consequently, the comparison between any pair of sources is facilitated by first converting them to a common metric (as described in Appendix A).

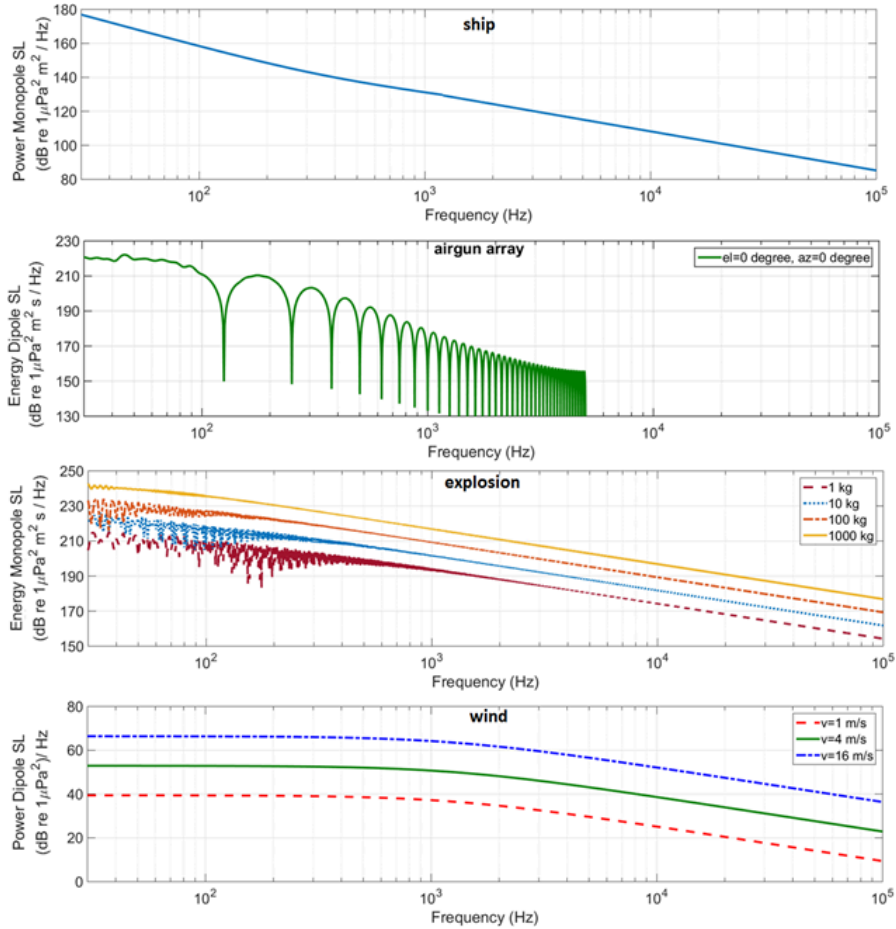


Figure 1. Spectral density source level for a monopole source of ship (extrapolated Wales and Heitmeyer formula) at 5 m source depth (based on information from [Gray & Greeley, 1980] and [Arveson & Vendittis, 2000]), for an energy dipole source level of an airgun array [Sertlek and Ainslie, 2015] at 6 m source depth, a monopole source of an explosion [Weston,1960], and an areic dipole spectral density level of wind (merged [Kuperman and Ferla,1985] and [APL-UW,1994]

models)

For ships, the source level is often characterised in terms of the radiated sound level [ISO 17208-1, Arveson and Vendittis]. The dipole source level description of ships is also possible although it is rarely used. We used the measurements of Wales and Heitmeyer, who measured the average *monopole* source level of different ships at different speeds [Wales and Heitmeyer,2002]. Their formula has been used here, extrapolated to high frequencies according to [Ainslie,2010 (p 423)]. An airgun operates by releasing a bubble of air under high pressure from the gun chamber into water. This creates a high pressure spherical pulse in the water that travels away from the bubble and is subsequently reflected from the sea surface. The oscillating bubble pulses are the main modulator of the spectrum. On the other hand, the interference between the airgun pulse and its surface reflection causes the oscillations in its energy source level. Depending on the positions of the airguns in the array, energy source level varies with elevation and azimuth angles. A numerical procedure has been used to quantify the airgun source signature based on bubble dynamics, mass and heat transfer and validated for frequencies up to 1 kHz [Sertlek and Ainslie,2015]. At higher frequencies, more advanced techniques are required to model nonlinear interactions between the bubbles. Consequently, we plotted the energy source level in Fig. 1 up to 5 kHz. The vertical variation in energy dipole source spectral density level for an airgun array is shown in Fig. 2.

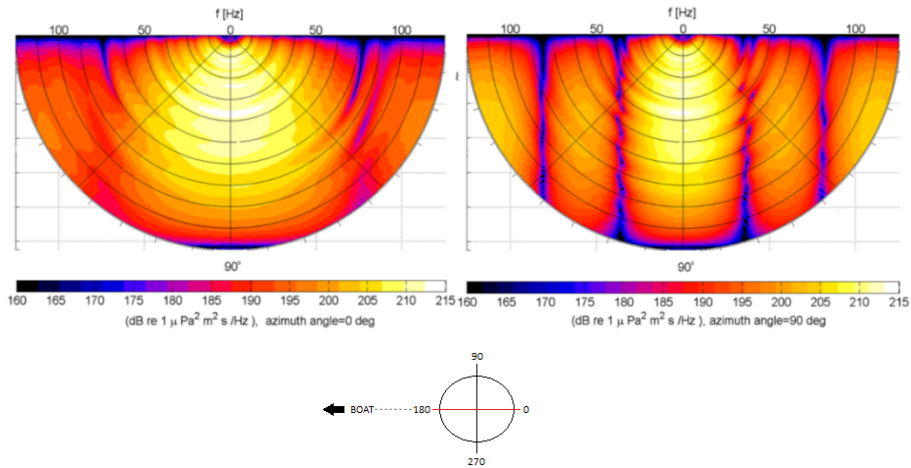


Figure 2. Vertical variation of energy dipole source spectral density level vs elevation angle (angle from the horizontal direction) of airgun array at azimuth angle=0 degree (left) and azimuth angle=90 degree (right). The source depth is 6 m.

The waveform resulting from an underwater explosion consists of a rapidly rising and decaying shock wave followed by a series of bubble pulses [Cole, 1965]. The interference between the shock

wave and bubble pulses results in the oscillations seen in Figure 1, especially at low frequency. For the acoustical characterisation of explosions, we adopted Weston's empirical formula [Weston,1960], which treats the explosion as a monopole source, without surface interaction. We convert Weston's characterisation to an equivalent monopole source level by assuming linear propagation from a distance of 5000 charge radii [Von Benda-Beckmann et al, 2014]. Von Benda-Beckmann et al, 2015] describes the uncertainty in the predictions of the energy source level of explosions in the shallow water and introduces a correction term which is based on the measurements. According to their paper, it was found that the use of the Weston/Cole formula for source level overestimates the sound exposure level, suggesting that the energy source level should be reduced by this amount to compensate. This correction term is added to results to increase the accuracy of calculated results in this paper. For the frequencies above 10 kHz, a flat variation of this correction factor is assumed (after a personal communication with Von Benda-Beckmann).

The variation of sea state or wind speed affects the source level of wind. Because wind produces sound over the entire sea surface, wind is usually characterized as a dipole sheet source [Kuperman and Ferla,1985; APL-UW,1994; Ainslie 2010], with the source level associated with a unit area of an infinite plane sheet. The properties of the four types of sources are described in turn, and summarised in Table 1.

Table 1. Source characteristics for the selected sources. The meaning of "source level" is different for each type of the sources.

Source	Quantity	ISO/DIS 18405	Temporal Pattern
ship	power monopole SL	source level ⁽¹⁾	Continuous
airgun	energy dipole SL	surface-affected energy source level ⁽²⁾	Impulsive
explosion	energy monopole SL	energy source level ⁽³⁾	Impulsive
wind	power dipole SL (areic)	surface-affected areic source level ⁽⁴⁾	Continuous

(1)level of the source factor, (2)level of the surface-affected energy source factor, (3) level of the energy source factor and

(4)level of the surface-affected areic source factor

B. Spatial and temporal Distribution of sources in the Dutch North Sea

Our aim is to gain insights in the distribution of sound across the Dutch North Sea, and to achieve this goal we analyzed the spatial, temporal and spectral distribution from various sources over a nominal two-year period. Due to limitations in availability of source data it has not been possible to select the same two-year period for all sources. Instead we constructed a fictional two-year period by combining the years 2007-2008 (seismic surveys [www.nlog.nl]) with 2010-2011 (explosions [KNMI] and wind [KNMI]) and 2013-2014 (shipping [www.marinetraffic.com]), (for shipping we have data for 2014 only, and these data are assumed representative for 2013 also). The resulting distributions of shipping, seismic surveys, explosions and wind speed are shown in Figure 3. The spatial distribution and timing of especially seismic surveys, and to a lesser extent explosions, will vary per year and depend on the particular localities and time periods of specific activities (more occurrence information can be found at the seismic survey data portal (see www.nlog.nl)).

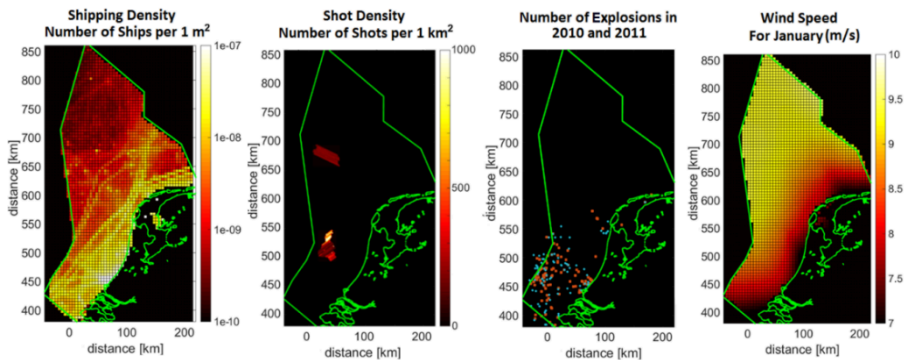


Figure 3. The distribution of areic shipping density (Number of ships per square kilometer) (left), seismic surveys (number of shots per square kilometer for 2007) (middle left), location of individual explosions between 2010 and 2011 (middle right) and Wind speed (m/s) for January (measured at 10 m above sea surface and extrapolated to the Dutch North Sea (right). Maps are based on the RD (Rijksdriehoek) coordinates

[<https://nl.wikipedia.org/wiki/Rijksdriehoekscoordinaten>]

Shipping density maps and airgun array shot density maps were calculated for 5 km x 5 km resolution. The source factor [described in Appendix A; Ainslie 2010; ISO/DIS 2015] was multiplied

by the number of ships or shots (by taking into account the directivity effects) in each source grid. The calculated notional signatures (far-field signatures of individual airguns, without the surface reflection) were coupled with a propagation model to estimate the horizontal and vertical directivity pattern [Eq.(4) from MacGillivray, 2012].

C. Environment : Spatial distribution of water depth and sediment properties

The underwater propagation of sound depends on various geophysical factors such as water depth and sediment type. The bathymetry and sediment grain size maps for the Dutch North Sea are shown in Figure 4. For the bathymetry, the EMOD-NET database is used [Emodnet, 2014]. The sediment maps are provided by the Geological Survey of the Netherlands project [<http://www.en.geologicalsurvey.nl/>]. Sediment data were not available outside the Dutch North Sea. These data are only required for the explosion maps, which include explosions outside the boundaries of the Dutch North Sea. For this case, it is assumed to consist of ‘medium sand’ [North Sea Atlas]. The sea surface is modelled as a flat pressure release surface (pi phase change in radians). The acoustic medium is assumed as two layered waveguide by neglecting the effects of sub-bottom material (even though this might be significant for the low frequency sound). The geoacoustic properties of the seabed material are inferred from the grain size using Table 4.17 of Ainslie 2010. The isovelocity approximation, which does not lead to large errors in the shallow water environment of the Dutch North Sea, is used [See Section 3.1]. Urlick’s equation for volume absorption [Urlick 1976, second edition; Fisher and Simmons,1977] is used, which includes the boric acid relaxation at low frequency [See Appendix A].

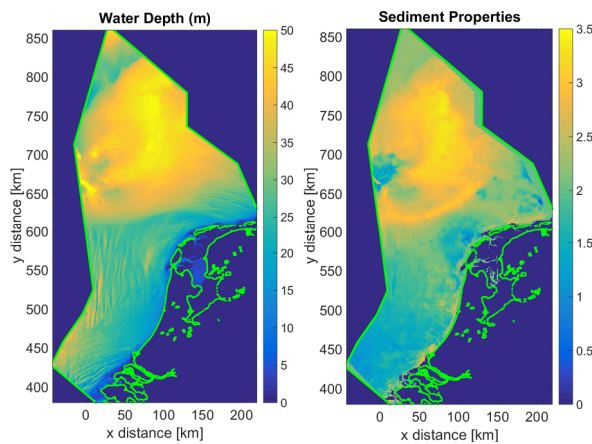


Figure 4. Bathymetry (water depth, in metres) (left) and sediment grain size ($-\log_2(\text{Grain diameter}/(1 \text{ mm}))$) (right) maps of the Dutch North Sea.

D. Underwater sound propagation

While [Erbe et al. 2012 and 2014] illustrate the potential application for sound maps in localizing acoustic conflicts at ecological hot spots, their sound propagation modelling approach leaves room for improvement. First they approximate the dipole source created by the ship and its surface image at low frequency with a monopole with the same power as the dipole (personal communication C. Erbe, 11 February 2016) Second, they assume the cylindrical spreading region extends indefinitely far from the source, which for a line source leads to an unphysical situation in which the sound pressure level becomes independent of distance from the source, a form of Olbers' paradox [Olbers, 1826]. An improved approximation could be obtained, with no extra effort, by applying the simple geometric spreading rules described by [Ainslie et al, 2014], comprising a modified cylindrical spreading region ($10 \log 10 R$) followed by a mode stripping region characterised by $25 \log 10 R$ [Denham, 1986] for a dipole source instead of the usual $15 \log 10 R$ for a monopole [Weston 1976].

In the current section, to simulate the propagation problem efficiently, we used a hybrid propagation model (called "SOPRANO") based on normal mode and flux theories [Sections 2.2 and 2.3]. The accuracy of this propagation model was investigated with multi-model comparisons [Sections 2.2 and 2.3]. SOPRANO can calculate the PL for a variable sediment type and bathymetry with an accuracy similar to the adiabatic mode theory (The differences between Soprano and KrakenC (adiabatic approximation) are less than 0.2 dB for the selected test cases in Section 2.3. The maximum difference is less than 2 dB for the realistic Dutch North Sea bathymetry (not shown).

PL is calculated over radial slices with 1 degree resolution. For ranges up to 1 km, small range steps are used (25 m). For longer ranges, PL is calculated for each 250 m intervals. Mean-square sound pressure (p_{kn}^2) is also spatially averaged over all receiver cells for the kth receiver depth as

$$p_{ijk}^2 = \frac{\sum_{n=1}^{N_{SPL}} r_n dr_n p_{kn}^2}{\sum_{n=1}^{N_{SPL}} r_n dr_n}$$

where dr_n is the range steps and N_{SPL} is the number of the discrete point in the receiver cell. Then, mean square sound pressure at each receiver cell (p_{ijk}^2) is averaged over receiver depths in order to take into account the variability of PL at the different receiver depths as

$$p_{ij}^2 = \frac{\sum_{k=1}^K p_{ijk}^2}{K}$$

where $K=10$ receiver depths which are equally spaced from 1 m below the sea surface to 1 m above the seabed.

For natural sources, the approximations used are slightly different than the modelling approach of anthropogenic sound sources. Wind sound sources are described as a sheet dipole source [Kuperman and Ferla, 1985; APL-UW, 1994; Ainslie, 2010]. The contribution from wind is calculated by an analytical approach [Ainslie et al, 2011], assuming a flat seabed. Thus, the calculations are done separately for each 5 km x 5 km grid cell by assuming a constant water depth in these source cells.

3.4.3. SOUND MAPS OF THE DUTCH NORTH SEA

Spatial, temporal and spectral analysis of the sound field

In this section, sound maps of the Dutch North Sea are shown (in Figure 6), with attention to the spatial distribution of SPL and the temporal distribution of total sound energy from the four selected sources, as well as for all sources together (all based on two-year averages). We seek a measure of sound with which we can make a like with like comparison between qualitatively very different sources (ships, airguns, explosives and wind). We wish to compare, for example, impulsive sounds with continuous ones, and sheet-like sources with point-like sources. One way of achieving this in principle is to look at their impact: how many animals are affected and in what way? In practice this would be a huge undertaking, partly because so little is known about the effects of underwater sound on most species, and partly because, even for the species for which such knowledge is partly available, it would require a multi-disciplinary activity involving acousticians, physiologists and ecologists that is beyond the scope of the present work. An exception is made for the case of an explosion [See Chapter 4], for which the impact is assessed by each explosion using SEL for that explosion, and then the cumulative impact for all explosions in a two-year time period is estimated. It is reasonable to assume that the effect increases with SEL per explosion and with the number of explosions. A natural physical measure that incorporates both is the total sound exposure accumulated over (say) a year, a quantity that is closely related to the

total energy, averaged over a year. While not a direct measure of impact, it is a useful metric that one can calculate for all 4 sources, and for which one can assert with some confidence that the risk associated with any one source will increase with increasing (annually averaged) energy [Ainslie & Dekeling 2011].

Visualizations for both spatial and temporal variation in energy distribution are provided for different frequency ranges: the 125 Hz deci-decade band and three single-decade bands 100 Hz to 1 kHz (referred to henceforth as the ‘low frequency’, or ‘LF’ band), 1 kHz to 10 kHz (‘mid-frequency’, or ‘MF’ band) and 10 kHz to 100 kHz (‘high frequency’, or ‘HF’ band). (A deci-decade is a logarithmic frequency interval equal to one tenth of a decade [ISO/DIS 18405]. This frequency interval is sometimes referred to as a “one-third octave” because it is approximately equal to one third of an octave). The EU’s MSFD requires its member states to monitor ambient sound in decidecade bands centred at 63 Hz and 125 Hz, the latter frequency being within the LF band considered in the present study. In the Dutch North Sea, average water depth is around 40 m-50 m, and 125 Hz sound is sufficiently above the cut-off frequency for the application of our propagation model. The frequency of 63 Hz is not included because as it is less than our minimum frequency (100 Hz).

SOURCE MODELS AND SOUND MAPS

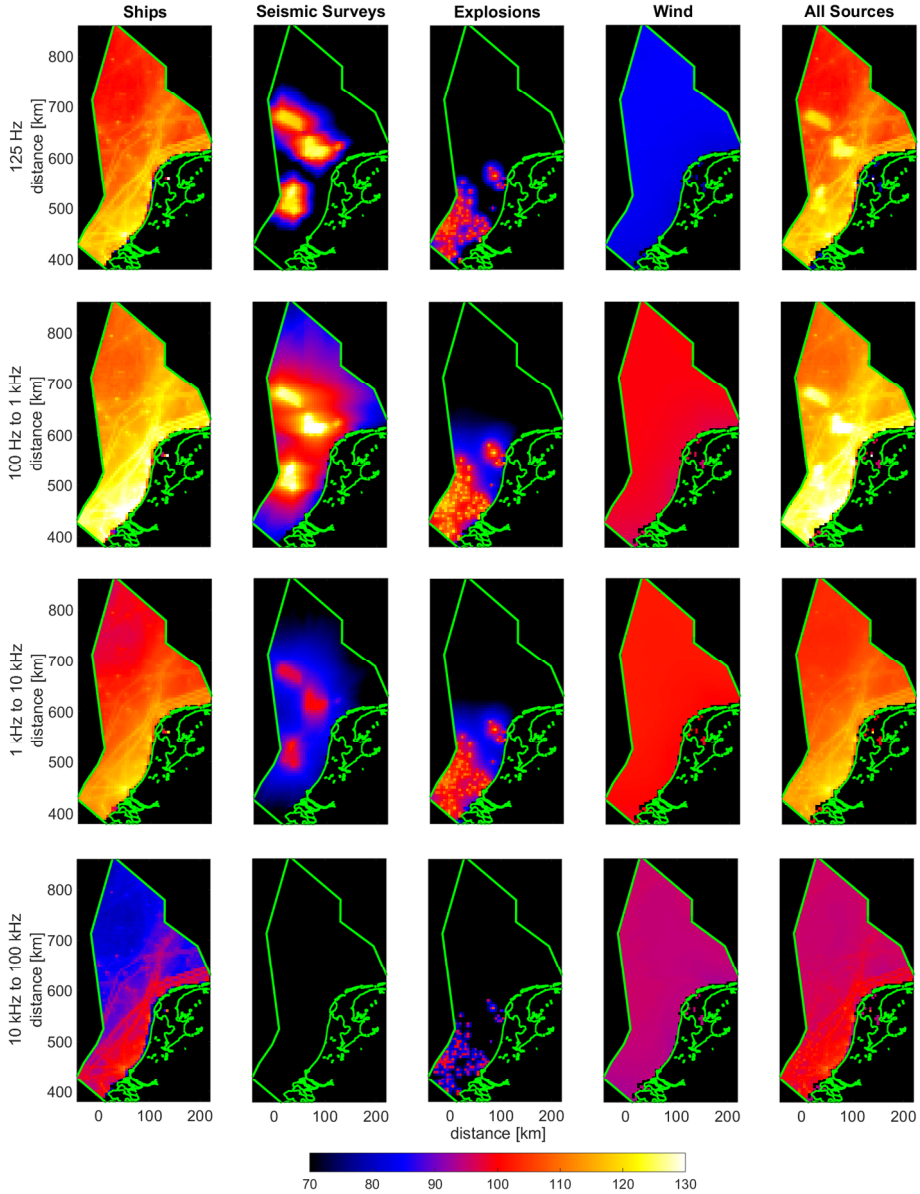


Figure 6. Two year average sound maps (SPL) for shipping, seismic survey, explosions, wind and sum of four sources. Squared sound pressure is averaged over receiver depth. The maps are generated for the 125 Hz decade frequency band, LF (100 Hz to 1 kHz), MF (1 kHz to 10 kHz) and HF (10 kHz to 100 kHz). The RD (Rijks-Driehoek) coordinate system used for the presented sound maps.

In Figure 7, we depicted spatial and temporal distribution of SPL (versus area) for LF, MF and HF bands. This histograms reflect the occurrence distribution of SPL over the Dutch North Sea. This figure provides a tool to assess the areas affected by different exceedance levels.

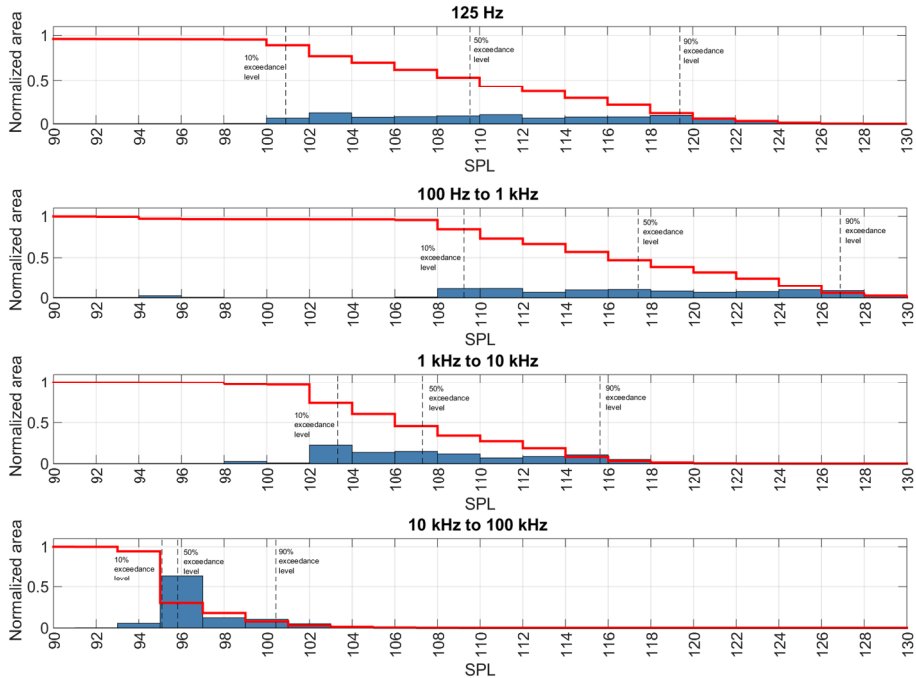


Figure 7. Histogram (blue bars) and cumulative distribution function (red lines) derived from the spatial distribution of the two-yearly averaged SPL for LF, MF, HF decade and 125 Hz decidecade bands in the Dutch North Sea. The area is divided by the total area of the Dutch North Sea (Normalized area). The 90%, 50% and 10% exceedance levels are indicated for each frequency band.

3.4.4. TEMPORAL AND SPECTRAL DISTRIBUTION OF SOUND ENERGY

Sound prediction tools can be used to estimate the contribution to the sound energy from each source. The benefit of quantifying contributions in terms of their energy is that the contributions can be added in a linear manner, making it possible to construct an energy-based sound budget. The total acoustic energy in the Dutch North Sea is calculated from spatial averages of the squared sound pressure which is based on the SPL sound maps in Figure 6 in order to understand what the

contribution is from each source to the total energy budget. The acoustic energies in the Dutch part of the North Sea are calculated at decade center frequencies by the following formula

$$E_{Total} = \frac{1}{\rho c_w^2} \int p^2(f, x, y, z) dV$$

This formula is approximated as

$$E_{Total} \approx \frac{1}{\rho c_w^2} \sum_{i=1}^{N_x} \sum_{j=1}^{N_y} p_{ij}^2 H_{ij} \Delta x \Delta y$$

where $\Delta x \Delta y$ are the dimensions of the receiver grid (the resolution of sound map), N_x and N_y are the number of receiver cells in x and y directions, H_{ij} is the water depth of the receiver cell, ρ is the density of the sea water, c_w is the sound speed in the water column and p_{ref} is the reference pressure.

The energy contributions from each source to the total acoustic energy are plotted in Fig. 8. The number of shots and the size of the weekly covered area by seismic surveys are estimated from the seismic survey reports. Then, the sound maps are scaled by this ratio. Figure 8 shows that shipping makes a dominant contribution in most weeks, with sporadic interruptions from explosions (e.g., week 8 for HF) and airgun surveys (e.g., week 51 for the 125 decade band and LF). Wind makes the largest contribution for HF.

SOURCE MODELS AND SOUND MAPS

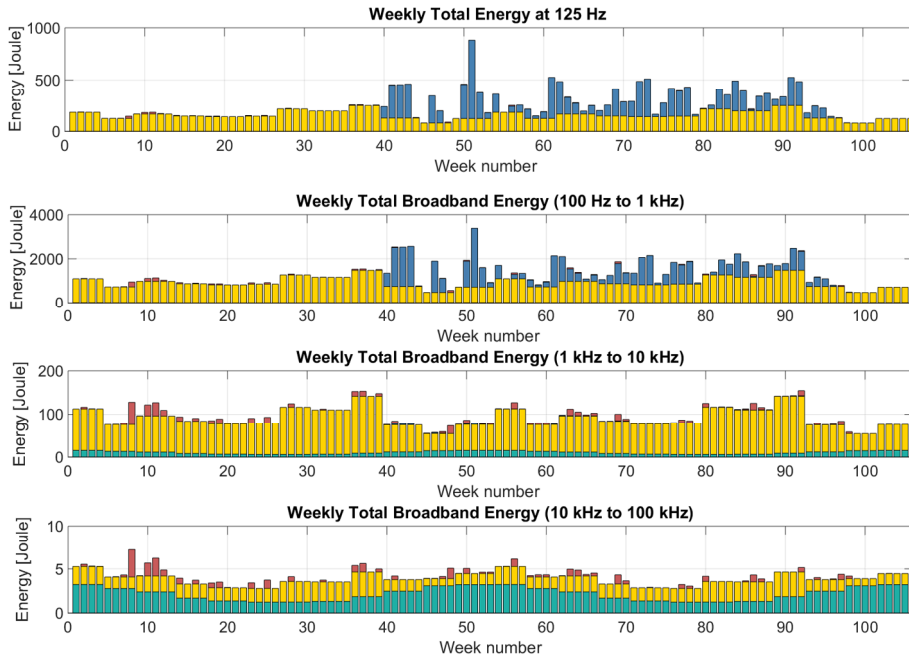


Figure 8. Weekly averaged total acoustic energy (in joules) vs time in LF, MF, HF decade bands and the 125 Hz decidecade band. The week numbers show time in weeks from 1 January of the first year

In any one week, activities of relatively short duration such as seismic surveys and (especially) explosions can make a larger contribution than shipping. For example, the explosions make a larger contribution than shipping in the 8th, 9th and 11th weeks in the HF band. The seismic surveys make a larger contribution than shipping in the 51st week as shown in Figure 8 in the LF band. The effect of averaging time for SPL is investigated in Appendix B.

Figure 9 shows the spectral distribution of two year averages of total energy in decidecade frequency bands. Having calculated the contribution to the total sound energy from each type of source it was also possible to construct an energy budget, showing the proportion of the total for each. These comparisons for the total acoustic energy provide insight into the ranking of the sources according to their contributions to the total acoustic energy during the two year time period. At the low and medium frequency band (LF and MF), shipping activities have the largest contributions (920 J and 80 J). For the mid-frequency range, the contribution from wind increases, and dominates the energy budget at frequencies exceeding 5 kHz (2 J for HF). For HF, the energies of shipping and explosions are very similar (about 0.2 J). The contribution from seismic surveys is very low above 1 kHz.

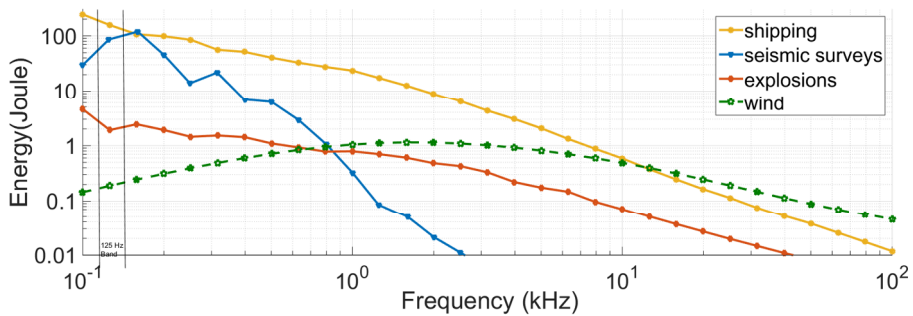


Figure 9. Two year average of total acoustic energy in the Dutch North Sea, in deci-decade bands. The shipping is making the largest contribution up to 5 kHz. Wind is the largest contributor above 5 kHz. The seismic surveys are contributing at the low frequencies (up to 1 kHz).

The relative energy budgets for the different sound sources are summarised in Table 2 for the various frequency bands (125 Hz, LF, MF and HF). This table is based on the long-term average (2 years) of the acoustic energy. The energy averaged over two years for 100 Hz to 100 kHz band is 1346 J, of which 72.8 % is from shipping, 24.4 % from seismic surveys and 1.6 % from explosions. The estimated contribution from wind is 1.2 %. The mean SPL is dB re 1 μPa^2 for 100 Hz to 100 kHz band. The total energy for 125 Hz band is 243 J, of which 64.3 % is from shipping, 34.8 % from seismic surveys and 0.8 % from explosions. The estimated contribution from wind is 0.1 %. The mean SPL is 114.2 dB re 1 μPa^2 for 125 Hz band.)

Table 2. The average sound energies for 125 Hz decade, and LF, MF and HF decade bands.

	Average sound energy in the Dutch North Sea				
	125 Hz decade	LF decade	MF decade	HF decade	100 Hz to 100 kHz
shipping	160 J	920 J	80 J	2 J	980 J
seismic surveys	85 J	330 J	0.4 J	-	330 J
explosions	2 J	19 J	4 J	0.25 J	22 J
wind	0.2 J	6 J	10 J	2 J	17 J

In Appendix A, the free-field energy associated with ships (3900 kJ), airguns (1000 kJ), explosions (110 kJ) and wind (15 kJ) are calculated for the same two-year period and for the same frequency band (100 Hz to 100 kHz) as the total sound energy in Table 2. It is expected to see larger energies in the free field because of the shallow water propagation leading to loss of energy into the seabed. This effect is especially pronounced for dipole-like sources (ships, airguns, wind), which direct their sound energy preferentially towards the seabed.

3.4.5. BIOLOGICAL RELEVANCE

The sound maps (shown in Figure 6), the information on spatial variation (Figure 7) and the energy distributions (Figure 8 and 9) can all be used for biological impact studies for different fish and marine mammal species [MacGillivray 2006; Erbe et al 2012 and 2014; Bouton et al, 2015]. The relationship between the frequency band categories and animal hearing ranges is depicted in Figure 10. Fish are sensitive to the low-end of the spectrum, while marine mammals are sensitive to broad ranges, with baleen whales going very low and overlapping with fishes, toothed whales and dolphins going very high into the ultrasonic, and pinnipeds somewhere in between.

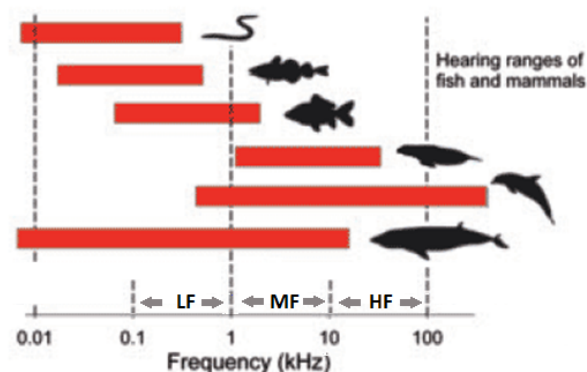


Figure 10. The hearing ranges of fish and mammals in LF, MF and HF bands (adapted from Slabbekoorn et al, 2010)

The geographical distribution of sound energy conveyed by the sound maps can provide information of relevance to the ecology of the Dutch North Sea by comparing this distribution with that of local marine life [CetSound, Sutton et al, 2011 ; Porter and Henderson, 2013]. After

combining Figure 7 with animal density maps or species-specific habitat-quality maps, one can add species specific disturbance thresholds to estimate how many animals or how badly a specific species is affected in the Dutch North Sea. For example, the CetSound Project investigates cetacean distribution in U.S. Exclusive Economic Zone (EEZ) and develops regional sound maps for low frequencies (50 Hz to 1 kHz) for multiple sources. The merger of these cetacean density and sound maps gives insight into the impact of sound on the animal distribution for different regions (for Beaufort and Chukchi Seas, Gulf of Mexico and Atlantic Coast). Similar studies are also done to investigate the impact of the underwater explosions on the distribution of harbour porpoises in the Dutch North Sea [see Sections 4.1 and 4.2].

The temporal distribution of sound is also relevant, but the current temporal resolution that we used (one week) seems unlikely to be sufficient to make meaningful statements in this regard, because it is expected that animals respond to sound on a shorter timescale (order of seconds, minutes or hours, rather than weeks). For this reason, the averaging time of sound maps is critical for the transients. Appendix B shows the impact of using different averaging times for assessing the SPL. The smaller the averaging time the higher the maximum SPL and the higher the spread in the temporal distribution. The impact assessment studies for each individual event will thus require a careful choice of the averaging time [Madsen, 2005; Sertlek et al, 2012]. Long averaging times lead to stable averages that make the results more comparable for different sources. The EU Noise expert group TSG Noise therefore recommends annually averaged sound maps for management purposes [Dekeling et al 2014], but it should be clear that assessing the biological impact of the various sources on specific communities or species requires to take the temporal dimension into account. Furthermore, it is important to realize that there are still a lot of uncertainties when it comes to acoustic thresholds for hearing across species and also little is known about impact of audible sounds on free-ranging animals in terms of individual fitness and population consequences [Popper et al. 2004; Slabbekoorn et al. 2010; Radford et al. 2014]. Sound maps may be helpful in guiding future research efforts towards most critical species or most critical areas as well as in site selection for sampling designs.

3.4.6. SUMMARY AND CONCLUSIONS

Our study aims to provide a calculation strategy for shallow water sound maps, which can be a useful tool for assessing the risks associated with anthropogenic sounds in the marine environment. This is achieved by developing a fast and accurate shallow water broadband

propagation method which enables the calculation of the results for a wide range of frequencies. The sound map analyses of the Dutch North Sea, based on realistic sound source levels and real events, revealed that most sound energy comes from ships, followed by airguns and explosions, with most energy at frequencies between 100 Hz and 1 kHz for all three anthropogenic sources. It should be noted, however, that this ranking is likely to vary from year to year depending on the agenda of human activities and will also be different for other marine areas. We therefore stress that our main message is not in the absolute values or specific source rankings or sound distribution details. We believe the main value of this work is the mapping approach using source specific and propagation-conditions dependent algorithms. Also interesting for extrapolation to other years or other areas is that all anthropogenic sources exhibited strong geographical signatures despite the relatively small scale of our case study.

The call from society for more information about the distribution and impact of sound levels underwater is growing, as we know sound is likely to play a dominant role in the life of many aquatic animals [Myrberg and Fuiman 2002; Montgomery et al. 2006; Slabbekoorn et al. 2010] and a variety of human activities add considerable amounts of sound to the naturally present levels. We typically do not know whether the elevation of sound levels undermines the “Good Environmental Status” of a particular waterbody [Dekeling et al 2014], but potential impact includes masking of critical sounds and other detrimental effects of distraction, disturbance, deterrence and injury [Popper and Hastings 2009; Slabbekoorn et al. 2010; Radford et al. 2014]. International concern about these possible effects has already found its way into regulatory measures worldwide [Lucke et al. 2014] and we believe our mapping methodology provides a useful toolbox for example to meet specific monitoring requirements on particular frequency bands in the Marine Strategy Framework Directive (MSFD) of the European Union [EU 2008].

Our approach of generating integrative maps for multiple sources can also give insight into the contribution of specific sources to an overall soundscape (acoustic footprint) and allows exploration of potential impact of individual sources or cumulative effects on specific areas, communities or species. Therefore, while sound may or may not turn out to significantly affect marine life in different cases, the current state of the art in underwater sound mapping allows us at least to adequately depict and investigate the temporal and spatial distribution of anthropogenic sound in the context of natural fluctuations in ambient noise. We hope our work will stimulate future applications and guide further impact studies with appropriate data on underwater acoustics.

APPENDIX A- CALCULATION OF FREE FIELD ENERGY

In this appendix, the calculation of free field energy is described. The “free-field energy” of a sound source is calculated by following the approach from Ref [Ainslie et al 2009] . E_f is not the true acoustic energy associated with the source, but the energy that would exist in the sound field produced if the same source were placed in free space (an infinitely deep ocean, of uniform impedance, no boundaries other than the sea surface, and with the same sound speed, density and absorption coefficient as seawater) and operated at the same source level. The spectral density of the free-field energies E_f of these sources can be calculated from the average power W_f [Ainslie et al, 2009]

$$E_f = \frac{W_f}{2\alpha c_w}$$

where ρ_w is density of water, c_w is sound speed in water and α (Np/m) is the volume absorption coefficient.

Here, free field energy is proportional to the source power and inversely proportional to the absorption coefficient of seawater, and provides a convenient way of ranking the contribution to the sound field from qualitatively different natural and anthropogenic sources. The source power spectra tell us how much sound is radiated by monopole, dipole and sheet sources, but it falls short of a complete picture because the source power does not tell us how far the sound propagates, and in particular takes no account of the efficient propagation (low absorption) of sound at low frequency.

The first step towards a quantitative comparison of free field energies is to estimate the source power spectra and compare those. To summarise, the average power spectral density, added over all sources of a given type, is shown in Table A1.

Table A1. The source powers for ship, explosions, airguns and wind.

Source Type	W_f (Source Power)	Description
Ship	$W_f = \frac{2\pi}{\rho c} \sum_i^{\text{Number of Sources}} \int_0^{\pi/2} S_{f,i}^{\text{dp}} \cos \theta \, d\theta$	For the ships the surface-affected (dipole) source factor is $S_f^{\text{dp}} = S_f^{\text{mp}} 4 \sin^2 k z_s \sin \theta$. The total number of ships in the monthly averaged density maps for 2014 varies between 500 and 950.
Explosion	$W_f = \frac{1}{T} \frac{2\pi}{\rho c} \sum_i^{\text{Number of Sources}} \int_{-\pi/2}^{\pi/2} S_{E,f,i}^{\text{mp}} \cos \theta \, d\theta$	$S_{E,f,i}^{\text{mp}} = (\rho c) r^2 E(\omega, r)$, $E(\omega, r)$ is the spectral density of the sound energy flux density (including the shock wave and the first two bubble pulses) and r is a distance beyond which the sound is assumed to behave linearly ($r \approx 5000 \times \text{radius of the explosive}$) [Ainslie, 2010]. t is the averaging time. Total number of explosions are 232.
Airgun	$W_f = \frac{1}{T} \frac{1}{\rho c} \sum_i^{\text{Number of Sources}} \int_0^{2\pi} \int_0^{\pi/2} S_{E,f,i}^{\text{dp}} \cos \theta \, d\theta \, d\phi$	$S_{E,f,i}^{\text{dp}} = 2 q(f, \theta, \phi) ^2$ and $q(f, \theta, \phi)$ is the frequency domain source signature as described in [Sertlek, Ainslie, 2015]. T is the averaging time.
Wind	$W_f = \frac{2\pi}{3\rho c} A K_f$	The areic source factor per unit area is described as [Ainslie et al, 2011] $K_f = \frac{10^{4.12} (v/(1 \text{ m/s}))^{2.24}}{1.5 + \left(\frac{f}{1000 \text{ Hz}}\right)^{1.59}} \mu\text{Pa}^2/\text{Hz}.$ The annually averaged wind speed is calculated as $\left((v)^{2.24}\right)^{\frac{1}{2.24}} = 6.78 \text{ m/s}$ from 12 months of wind speed data measured at 10 m above sea surface in the Dutch North Sea [KNMI]. where A is the total area.

By using the free field energy formulation, the comparison in Figure A1 can be done. The free field energies of all explosions, ships and seismic surveys in two year time period are shown. The calculation of energy is very sensitive to choice of absorption formula at low frequencies. The

volume absorption is calculated by Thorp formula which includes the low frequency effects [Fisher and Simmons,1977]

$$\frac{\alpha}{Np/m} = \frac{10^{-3}}{20 \log_{10} e} \left[\frac{0.1}{0.9144} \frac{(F)^2}{1 + (F)^2} + \frac{40}{0.9144} \frac{(F)^2}{4100^{0.5} + (F)^2} + \frac{2.7510^{-4}}{0.9144} (F)^2 \right]$$

where $F = \frac{f}{1000 \text{ Hz}}$.

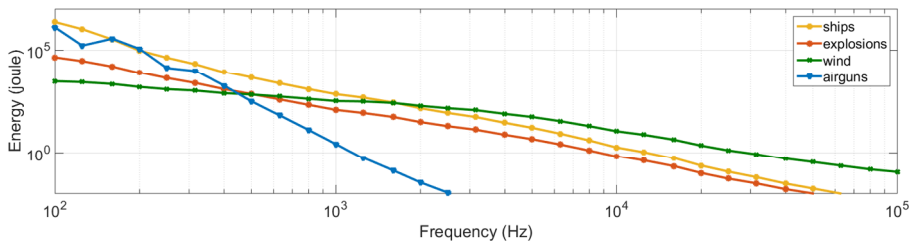


Figure A1. Total free field energies in decade bands of different sources averaged over year and Dutch North Sea. Source power is calculated for the total number of sources included. Although the source level cannot be directly compared, free-field energies (and source powers) can be compared between sources.

Table A2. Ranking of the sources for average radiated power per unit area and free-field energy.

The source power is divided by the total area of Dutch North Sea (63687 km²)

Source Type	average power per unit area		average free-field energy	
	125 Hz decade band	broadband (100 Hz to 100 kHz)	125 Hz decade band	broadband (100 Hz to 100 kHz)
shipping	10.6 nW/m ²	39.8 nW/m ²	1060 kJ	3920 kJ
seismic surveys	0.85 nW/m ²	10.1 nW/m ²	169 kJ	1960 kJ
explosions	0.3 nW/m ²	1.88 nW/m ²	18.8 kJ	107 kJ
wind	0.03 nW/m ²	2.26 nW/m ²	2.60 kJ	15.2 kJ

Appendix B- THE EFFECT OF AVERAGING TIME

The choice of averaging time is critical, especially for transient sounds [Madsen,2005]. In the main section, we focus on long term (two years) and weekly averaged quantities. However, some of the biological problems related with the sound maps may need higher time resolutions such as a day, hour or second. The shipping and wind are ubiquitous sources, the sound of which is present throughout the year. By contrast, the sounds from explosions and seismic surveys are focused in time over a period of a few weeks (seismic surveys) or seconds (explosions). For instance, for the weekly averaged sound maps, the contribution from each explosion during the time the sound takes to spread away from the source immediately after an explosion would be about $10\log_{10}(1 \text{ week}/100 \text{ s})$ dB, i.e., 38 dB higher than the levels shown in this section. A sound map of a single explosion, averaged over various time windows as 1 minute, 1 hour, 1 day, 1 week, 1 month and 1 year is compared in Figure A2 with the shipping sound map for January 2014. The purpose of this comparison is to demonstrate that the root mean squared (rms) sound pressure caused by the explosion, when averaged over a sufficiently short time window, exceeds that due to shipping over a large area. While the (monthly averaged) shipping sound map for January is not strictly comparable with the averages over durations of an hour or less, it provides a useful indication for the expectation value. It is immediately clear that when averaged over a short time window, the transient intensity exceeds that of continuous shipping over a large area, even in the presence of a high shipping density.

SOURCE MODELS AND SOUND MAPS

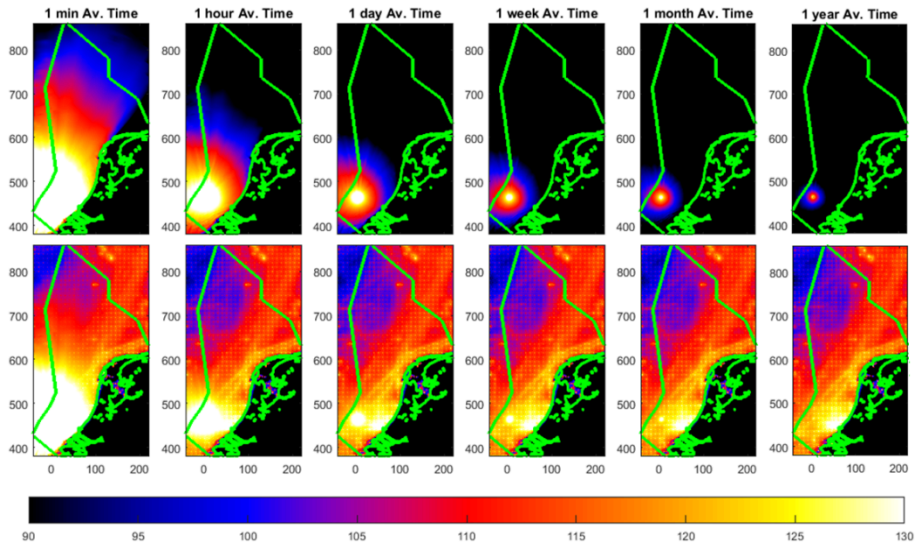


Figure A2. The effect of averaging time window is illustrated. In the upper maps, SPL maps of single explosion for the various time windows are shown. In the lower maps, these maps are summed with the shipping sound maps of January 2014.

Although we are aiming to find out what is the average contributions of each sound source to total energy which is averaged over two years, it is important to keep in mind that averaging may obscure the fact that such sudden events might potentially have a big impact at the moment they occur. We assume that transient sources can be represented as a continuous sounds (since the explosions and airgun shots were observed almost for each week at the various locations of the North Sea.) for the large time windows (over a week, month or year). They can be used to compare the annual contributions of each source to the total energy. However, the shorter time windows may be required for the transients depending on the type of the biological problems.

Chapter 4 BIOLOGICAL RELEVANCE OF SOUND MAPS

In this chapter, I included several examples of applications of sound maps to biological research. The sound maps for underwater explosions are integrated with biological models on animal distribution and behaviour. The impact of explosive clearance activities of historical unexploded ordnance (UXO) on harbour porpoises in the southern North Sea is assessed in Chapter 4.1. The uncertainty in the calculation of energy source level of explosions for shallow water is also investigated in the same chapter. Chapter 4.2 is the complementary part of Chapter 4.1 from a biological point of view. Chapter 4.2 shows that increased movement rate increases the cumulative number of individuals within a population that will be exposed to a repetitive anthropogenic sound. However, repeated exposure probability is reduced.

4.1. BIOLOGICAL RELEVANCE FOR MARINE MAMMALS: ASSESSING THE IMPACT OF UNDERWATER CLEARANCE OF UNEXPLODED ORDNANCE ON HARBOUR PORPOISES (*PHOCOENA PHOCOENA*) IN THE SOUTHERN NORTH SEA

*This section¹ is modified version of [A. M. von Benda-Beckmann, G. Aarts, H.Ö. Sertlek, K. Lucke, W. C. Verboom, R. A. Kastelein, D. R. Ketten, R. van Bemmelen, F.P. Lam, R.J. Kirkwood and M.A. Ainslie, Assessing the Impact of Underwater Clearance of Unexploded Ordnance on Harbour Porpoises (*Phocoena phocoena*) in the Southern North Sea, Aquatic Mammals, 2015, 41(4), 503-523, 2015]*

Abstract: Large amounts of legacy unexploded ordnance (UXO) are still present in the North Sea. UXO are frequently accidentally encountered by fishermen and dredging vessels. Out of concern for human safety and to avoid damage to equipment and infrastructure from uncontrolled explosions, most reported UXO found in the Dutch Continental Shelf (DCS) are detonated in a controlled way. These underwater detonations produce high amplitude shock waves that may adversely affect marine mammals. The most abundant marine mammal in the DCS is the harbour porpoise (*Phocoena phocoena*), a species demonstrated to be highly sensitive to sound. Therefore, an assessment of potential impacts of underwater explosions on harbour porpoises was undertaken. Information regarding UXO cleared in the DCS, provided by the Netherlands Ministry of Defence, was used in a propagation model to produce sound exposure maps. These were combined with estimates of exposure levels predicted to cause hearing loss in harbour porpoises and survey-based models of harbour porpoise seasonal distribution on the DCS. It was estimated that in a one-year period, the 88 explosions that occurred in the DCS very likely caused 1280, and possibly up to 5450, permanent hearing loss events, i.e. instances of a harbour porpoise predicted to have received

¹

My contribution to this section concerns providing sound maps and source model of the underwater explosions. This section is included as illustration of a biological application of the sound maps during my PhD project.

sufficient sound exposure to cause permanent hearing loss. This study is the first to address the impacts of underwater explosions on the population scale of a marine mammal species. The methodology is applicable to other studies on effects of underwater explosions on the marine environment.

4.1.1. Introduction

Large numbers of unexploded ordnance (UXO), such as aerial bombs, ammunition, mines and torpedoes, mostly legacies of WWII, remain in the North Sea. UXO are frequently accidentally encountered by fishermen and dredging vessels (OSPAR, 2010). There is a societal need for clearance of UXO, as they pose a risk to offshore activities such as fishing, dredging and pipe-laying. For example, in 2005 three Dutch fishermen were killed by a bomb that was caught in their net and exploded on deck (OSPAR, 2010). The Royal Netherlands Navy (RNLN) is tasked with clearing UXO from the Dutch Continental Shelf (DCS) and executes on average approximately 120 underwater detonations per year.

Underwater detonations of explosives produce some of the highest peak sound pressures of all underwater anthropogenic sound sources. The number of underwater detonations in the North Sea, and their high intensity shock waves and sound levels, have raised concerns about their impact on marine life (Nützel et al., 2008; Ainslie et al., 2009; Camphuysen & Siemensma, 2011; Koschinski, 2012). The high amplitude shock waves and the attendant sound wave produced by underwater detonations of UXO have the potential to cause injury or death to marine vertebrates and invertebrates (e.g., Ketten et al., 1993; Richardson et al., 1995; Lewis, 1996; Ketten, 2004, 2012; Danil & St. Leger, 2011).

The harbour porpoise (*Phocoena phocoena*) is the most abundant marine mammal species in the DCS and adjacent waters. In recent years, the harbour porpoise population has undergone a redistribution across its North Sea range resulting in an increase in abundance in Dutch waters (Camphuysen, 2011), with some 10000s of animals now present (Geelhoed et al, 2013).

Harbour porpoises have sensitive hearing, making them potentially exceptionally vulnerable to noise-induced effects from anthropogenic sound-producing activities at sea (Culik et al., 2001; Kastelein et al., 2002, 2010, 2012a-b, 2013, 2014a-b, 2015a-b; Ketten, 2004; Lucke et al., 2009; Tougaard et al., 2009). The main potential effects of concern of underwater explosions on an individual animal are: 1) trauma (from direct or indirect blast wave effect injury), such as crushing, fracturing, hemorrhages, and rupture of body tissues caused by the blast wave, resulting in immediate or eventual mortality; 2) auditory impairment (from exposure to the acoustic wave), resulting in a temporary or permanent hearing loss, such as temporary threshold shift (TTS) and permanent threshold shift (PTS); or 3) behavioural change, such as disturbance to feeding, mating, breeding and resting. Studies of blast effects on cetaceans indicate that smaller species are at greatest risk for shock wave or blast injuries (Ketten, 2004).

Underwater sound plays an important role in the lives of harbour porpoises. They use sound actively and passively for social interaction, communication, navigation, predator avoidance and foraging (Tyack, 2008, Clausen et al., 2010). Interference or impairment of their hearing ability as a result of underwater explosions may therefore directly or indirectly affect their reproduction and longevity. For instance, loss of important social bonds due to impaired communication (e.g. contact between mother and calf) or loss of prey could produce significant population level consequences (National Research Council, 2005).

The objective of this study was to assess the potential impact of underwater explosions due to clearance activities of UXO on North Sea harbour porpoises. Sound levels were estimated for explosions in shallow water, which were then compared to risk thresholds and distributions of harbour porpoises. It was decided to focus on explosion levels high enough to cause hearing loss in harbour porpoises, which are likely to occur at lower levels than possible direct traumatic injuries. Potential behavioural responses of harbour porpoises to single explosion events were not considered in this study. A paucity of observations of wild porpoise responses to explosions (single sound transients) made it impossible to address the severity of responses to single explosion events.

Because of a lack of acoustic measurements for large explosions (charge mass much larger than 1 kg TNT eq.) in shallow waters (bottom depths less than 50 m) (Weston, 1960; Chapman, 1984; Soloway & Dahl, 2014), measurements of sound produced by several large underwater explosives in shallow water environments were carried out. These measurements were used to correct deep water source models for explosions and were used in combination with a shallow water propagation model to generate maps of received sound exposure level (SEL) for the reported explosions in 2010 and 2011. Reported levels of impulsive sound that cause blast injury to harbour porpoises were reviewed (Ketten, 2004) to determine a range of onset thresholds at which explosions are expected to cause permanent hearing loss. Here, permanent hearing loss refers to a permanent reduction (at least partial) in hearing capability resulting from the blast wave or acoustic components of the explosion.

The sound propagation maps, available risk thresholds and aerial survey derived porpoise density estimates (Geelhoed et al., 2012; Aarts et al., in prep) were combined to obtain an estimate of the annual number of possible impact events, i.e., instances of a harbour porpoise receiving sufficient sound exposure to cause hearing loss. The estimated number of impact events were used to discuss the implications of UXO clearance for the North Sea harbour porpoise population.

4.1.2. Methods

Overview of clearance activities by the RNLN in the southern North Sea- Since 2005, the RNLN has recorded, for destroyed underwater ordnance, the approximate location, type of ordnance and date of detonation, but not always the charge mass. Because the detonations can interfere with geoseismic monitoring, all detonations exceeding 25 kg (TNT equivalent) were also reported to the Royal Netherlands Meteorological Institute (KNMI). These KNMI reports provided precise locations, times and charge masses of the explosions. For this study, activities over a 2-year period (2010 and 2011) were investigated using the combined RNLN and KNMI data sets. These lists were merged into a final list by removing the same detonations occurring in both lists; in such cases the information in the KNMI report was retained. In some cases small counter-charges used to detonate the main charge, were listed separately. In such cases only the the main charge mass (usually much larger) was considered. The final list comprised 210 explosions, of which 181 were within the DCS and 29 outside the DCS (a detailed list of explosions can be found in von Benda-Beckmann et al., 2015). Of the 210 explosion, 62 had unknown charge mass. These were most likely smaller explosions (e.g. of grenades and other small ammunition) that were below the 25 kg (TNT equivalent) that required reporting to the KNMI. An expert on explosives estimated the charge mass of these smaller explosives to be in the range of 5 – 20 kg (TNT equivalent) (R. van Wees, pers. comm.); therefore, for the purpose of this study, unknown charge masses were assumed to be 10 kg (TNT equivalent).

Pressure measurements of large explosions in shallow water- The acoustical properties of explosives are summarised by Weston (1960, 1962). The main feature is a short shock wave comprising a sharp – almost instantaneous – rise in pressure followed by an exponential decay with a time constant of a few hundred microseconds. The expanding shock-wave creates a large pulsating bubble with successive expansions and contractions that give rise to a series of weaker, more symmetrical bubble pulses, as happens also with an air-gun pulse (Weston, 1960; Cole, 1965). In shallow water, the multiple interactions of the shock and acoustic waves create a more complex time signal pattern. Because of a lack of published measurements for explosions in shallow water (see Soloway & Dahl, 2014), especially for charge mass much larger than 1 kg, a field experiment was carried out in 2010 to measure multiple detonations of aerial bombs at varying ranges up to approximately 2 km from the detonation site.

Measurements of underwater pulse duration (in s), sound exposure level (SEL in dB re 1 $\mu\text{Pa}^2\text{s}$) and peak overpressure (in kPa) were obtained in September 2010 for the underwater explosions of

seven aerial bombs (six 1000 lb and one 500 lb with TNT equivalent charge masses of 263 kg and 121 kg respectively). These bombs were found on land and detonated on the seafloor in an area with a water depth of 26-28 m and a sandy bottom. Measurements were obtained using a Hydrophone (B&K 8105) and ICP tourmaline pressure gauges (type W138A01/ M038CY060) measuring at a sampling rate of 50 kHz, set at depths of 4, 5, 13, 15, 23 and 25 m, and distances between 100 m and 2000 m from the source.

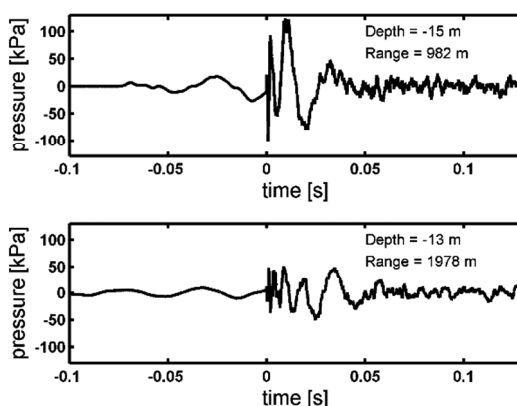


Figure 1. Examples of recorded sound pressure time-series of a detonation of a 263 kg TNT equivalent aerial bomb (measured at a sampling frequency of 50 kHz), recorded at a depth of 15 m at a distance of 982 m (upper) and at 13 m depth at a distance of 1978 m (lower) from the explosion site. An early arrival of the ground shock wave can be observed, followed by the water borne shock wave (at time = 0 s), and reflections and bubble oscillations.

Underwater explosions caused a series of typical pressure changes (see Figure 1). Following Madsen (2005), the pulse duration, T_{90} , was measured as the time containing 90% (5% - 95%) of the energy of the signal. The SEL within one tenth of a decade (decade)² bands as well as the broadband level was measured from each explosion within the pulse duration in a frequency band of 0 - 20 kHz. The peak overpressure (or peak compressional pressure, in kPa) of the shock wave, defined as the maximum value of the positive overpressure (pressure minus ambient pressure,

² a decade is one tenth of a decade, which is approximately one third of an octave, and for this reason sometimes referred to as a “third octave band” [ISO/DIS 18405:2015]]

when this quantity is positive), was measured within a set time interval (here taken to be 0.5 s to cover the full explosion event).

Risk thresholds for hearing loss for harbour porpoises exposed to explosions-This study focused mainly on the risk of explosions causing permanent hearing loss, as a result of direct blast injury caused by the shock wave close to the source or PTS from the acoustic wave of the blast incident farther away from the source. Permanent hearing loss estimated here may be partial (such as acoustically derived damage to some portion of the inner ear), occurring within a specific frequency range, or total (such as severe trauma to the auditory bulla or middle or inner ear tissues), depending on which components of the auditory system are affected, and how they are affected. More severe trauma was expected to occur at higher levels than those required to cause permanent hearing loss, and as such was considered as a lower limit.

Permanent and Temporary Threshold Shifts- Marine mammals exposed to intense underwater sounds may suffer hearing loss, resulting in hearing threshold shifts that may be temporary (TTS) or permanent (PTS). The extent of the hearing threshold shift and the frequency range affected may depend on the sound level, spectral content, temporal pattern, and exposure duration. TTS is defined as a threshold shift that recovers to normal sensitivity. The course and time of recovery depend on several factors: the individual's recovery ability, the sound an animal was exposed to and the amount of shift that incurred (Finneran & Schlundt, 2013, Kastelein et al., 2012a, 2014a, 2015a). TTS onset defined here is consistent with the criteria used in most studies on marine mammals; i.e., as a TTS of 6 dB or greater measured shortly (1-4 min) after cessation of the exposure, following Southall et al. (2007).

Different TTS onset SEL thresholds have been measured in harbour porpoises for a variety of pulse types (Lucke et al., 2009, Kastelein et al., 2012a, 2014a, 2015a, 2015b). Lucke et al. (2009) determined a masked TTS-onset SEL level for a porpoise subjected to single airgun transients, measuring auditory evoked potentials. As the sound stimuli of Lucke et al. (2009) resembled explosion sound better than other TTS studies currently available (Kastelein et al., 2012a, 2014a, 2015a, 2015b, Tougaard et al., 2015), our estimates for SEL thresholds for TTS and PTS were based on that study.

There is currently no experimental data available for predicting PTS onset levels in marine mammals. Observations for humans show that a TTS of 40 – 50 dB results in a significant risk of PTS (Kryter et al., 1966, Kryter, 1994). Southall et al. (2007) used reported TTS onset measurements for marine mammals to estimate the SEL required for a 40 dB TTS based on the TTS growth curve for

land mammals, which has a 2.3 dB increase in TTS per 1 dB increase in SEL (i.e., the TTS growth rate is 2.3 dB/dB). Based on this, PTS was predicted to occur for SEL values 15 dB above SEL causing TTS onset (Southall et al., 2007). Recent measurements for continuous noise exposure and sonar sound suggest that the growth rates may well exceed 2.3 dB/dB in some cases (Kastelein et al., 2013; 2014a). (dB/dB is a unit of “growth rate”, which is the rate of increase of threshold shift per unit increase in SEL.) Given the lack of data on growth rates in porpoises for impulsive sounds, let alone sound from explosions, the approach for extrapolating the TTS growth that is outlined by Southall et al. (2007) was used.

To account for the frequency selective sensitivity of the mammalian hearing system in sound exposure calculations, frequency-selective weighting functions are often used (Fletcher & Munson, 1933; Suzuki & Takeshima, 2004; Southall et al., 2007). Several weighting curves for harbour porpoises have been proposed in the literature (Verboom, 2005; Southall et al., 2007; Finneran & Jenkins, 2012; Wensveen et al., 2014; Tougaard et al., 2015). No frequency weighting study has been conducted for an explosive sound source. Because air-guns are an impulsive and low frequency source, and are fairly representative of an explosion sound at larger distances in shallow water, the data from an air-gun study (Lucke et al., 2009) were used to define TTS onset. Therefore, no frequency weighting was applied to the SEL when estimating the risk of TTS and PTS for explosions.

Lucke et al. (2009) concluded that the predefined TTS criterion (measured at 4 kHz) was exceeded at received SELs greater than 164 dB re 1 $\mu\text{Pa}^2\text{s}$. Based on this, it was therefore assumed that TTS-onset was very likely to occur for harbour porpoises exposed to explosion sounds at an (unweighted) SEL of 164 dB re 1 $\mu\text{Pa}^2\text{s}$. Following Southall et al. (2007), PTS-onset was then estimated by adding 15 dB to the TTS onset SEL. Given the uncertainties involved in this extrapolation this threshold should be considered as a lower limit, below which PTS is considered unlikely. The resulting lower limit for onset of PTS occurred at an unweighted SEL greater than 179 dB re 1 $\mu\text{Pa}^2\text{s}$. At higher SELs, the risk of PTS was considered to become increasingly likely. To denote a threshold where the onset of PTS was very likely to occur, the following section considers the observations of ear trauma observed in harbour porpoises exposed to underwater explosions.

Primary blast injury - A study on primary blast injury in marine mammals caused by shock waves was reported by Ketten (2004). In that study, fresh odontocete cadavers (including harbour porpoises) were exposed to explosions from varying charge masses in a controlled environment. In some cases the animals were tested within 24 hours postmortem after chilling. In others they were frozen within 4 hours postmortem and prepped by thawing under controlled conditions (chiller

and water bath). In all test specimens, the cadaver scanned on receipt when fresh and rescanned just prior to testing to assure that the lungs, brain, airways and other major organs had tissue appearances consistent with normal anatomy and no significant changes from their fresh condition. The specimens were then implanted with pressure gages for recording internal received PSI and again scanned to document the position of the gages. The necropsy and measurement of the blast effects was performed by a team consisting of experts on marine mammal physiology as well as experts on explosion-induced trauma. Trauma found included mild to severe and likely lethal injuries, particularly haemorrhages, as well as lung, esophageal, liver, brain, and ear injuries. At peak blast overpressures exceeding 172 kPa (25 psi) ear trauma was always observed, consistent with the ear being the most sensitive organ for blast related trauma. No effects were observed for peak overpressures below 69 – 83 kPa (10 – 12 psi).

Blast trauma to the porpoise middle and inner ear would likely result in a permanent, acute hearing loss, which could be broad spectrum, such as in the case of middle ear ossicular chain disarticulation (a probable 36 dB loss overall due to the dysfunction of the middle ear bones, Schuknecht, 1993) or elevated thresholds in only some frequencies depending upon the received acoustics impacting the inner ear. Observations of ear trauma and related peak overpressures could, therefore, serve as a proxy for moderate to severe permanent hearing loss.

Dose-response relationship for hearing loss- To delimit the range of SEL values at which onset of permanent hearing loss – either noise induced PTS or ear trauma caused by the blast wave – could occur, levels at which ear trauma resulting from primary blast injury was observed were considered. Peak overpressure was used by Ketten (2004) to predict the occurrence of primary blast injury. Here instead, the peak overpressure was empirically related to SEL for measured explosion sounds in shallow water, due to the difficulties of predicting peak overpressure in shallow water. From those measured data, an effective SEL that corresponded to peak overpressures resulting in ear trauma was estimated. A corresponding upper limit for the onset of PTS was estimated using the observations by Ketten (2004) in combination with measured SEL and peak overpressure for shallow water explosions (see Appendix A for full details). The expectation was that levels just below those required to cause minimal detectable ear trauma were very likely to be sufficient to cause PTS; i.e., the borderline between detectable blast injury and acoustic effects. Table 1 summarizes the SEL thresholds adopted in this study for the risk of temporary and permanent hearing loss for harbour porpoises, which were considered appropriate for harbour porpoises exposed to underwater explosions in shallow waters (less than 50 m depth).

Table 1. Thresholds related to temporary and permanent hearing loss caused by a single underwater explosion in shallow water (<50 m depth). Permanent hearing loss can be either noise induced permanent threshold shift (PTS) or be due to ear trauma caused by the blast wave. The right column indicates the best estimate for unweighted broadband (measured in 0 – 20 kHz) SEL risk thresholds for ‘permanent hearing loss’ induced by explosions. To indicate the chance of an effect to occur, the following terminology was adopted: ‘very likely’ indicates a probability exceeding 95%, and ‘unlikely’ a probability less than 5%. ‘Increasingly likely’ is then anything between 5% and 95% probability. The range of SEL thresholds for onset of permanent hearing loss was estimated to occur are indicated by arrows (see text and Appendix A for more detail).

SEL (unweighted) (dB re 1 μ Pa ² s)	Noise- induced TTS	Noise- induced PTS	Blast wave- induced ear trauma	Permanent hearing loss
> 203	Very likely	Very likely*	Very likely	Very likely
190-203			Increasingly likely	
179-190		Increasingly likely	Unlikely	Increasingly likely
164-179		Unlikely		Unlikely
< 164	Unlikely			

*Based on expert judgement

Modelling of sound exposure levels of explosions at large distances in shallow water- Although the measurements of the charges presented in the previous section are representative of typical UXO found in the North Sea, the inventories of the 2010 and 2011 detonations showed a wide range of explosive charge masses found in a range of water depths. The water depth affects the sound propagation characteristics, particularly of low frequency sound. A source model was therefore required to estimate the effect of underwater explosions for which there were no empirical data. The model used in this study for predicting the impact area for harbour porpoises consisted of two parts: a source model for underwater explosions and a sound propagation model for shallow water environments.

The source model was based on the empirical deep-water formula for explosion energy as a function of distance by Weston (1960). That model contained the energy contribution of both the shock wave as well as the first two bubble oscillations. From the Weston (1960) empirical relation, a linear source model was estimated by considering the energy spectrum at a distance of 5000 charge radii beyond which the sound wave is assumed to become linear (Ainslie, 2010) and back-computing this spectrum to a source energy level using spherical spreading. A spectral energy level was thus obtained for each decade frequency bin in a range from 10 Hz to 20 kHz.

The propagation model SOPRANO[See Sections 2.2 and 2.3], was used for calculating propagation loss in shallow water environments. SOPRANO is a hybrid model based on normal mode and flux theories. It is a fast analytical model which can estimate incoherent propagation loss with an accuracy similar to that of other propagation models (See Section 2.3). The SEL was then obtained by subtracting the propagation loss from the source energy level.

This model enabled the generation of sound maps (geographical distributions of SEL for each decade band) with high resolution and broad range frequencies, including range-dependent bathymetry (with adiabatic approximation) and sediment type effects. For bathymetric data, the EMODNET database was used, which has a grid size of 0.125 x 0.125 minutes (<http://www.emodnet-hydrography.eu/>). Information for describing the geoacoustical properties of the seabed was obtained from the DINO database (<http://www.en.geologicalsurvey.nl/>). Propagation loss was calculated with 25 m resolution, and the computed SEL was then mapped onto a sound map with resolution of 1 km x 1 km (Figure 2). Sea surface was assumed to be flat, and effects of non-constant sound speed profiles were neglected.

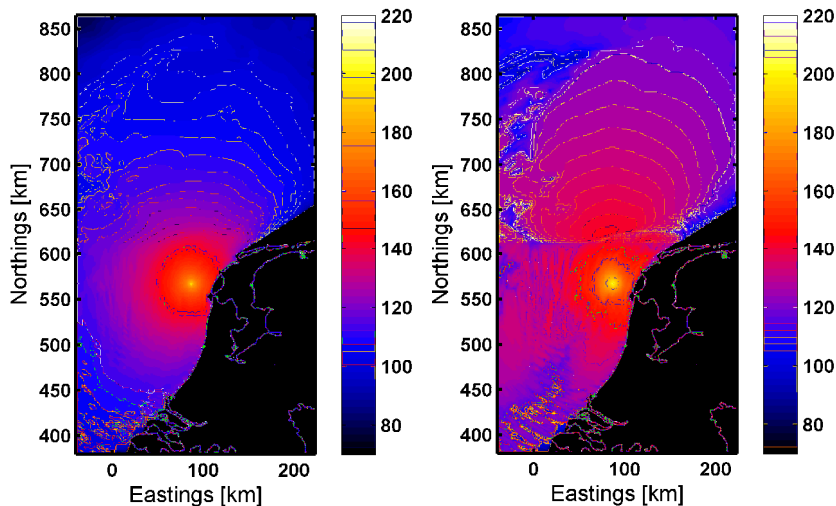


Figure 2. Examples of unweighted broadband SEL maps for a single explosion (263 TNT eq. charge mass) calculated for different receiver depths (at 1 m above the sea floor, left, and 1 m from the sea surface, right) computed with the model described in Section 2.3. The water depth at the detonation site is approximately 28 m.

In order to relate effects of explosions to the risk of hearing loss, an estimate for the peak overpressure was required. For deep water explosions, peak overpressure can be estimated using empirical models (Weston, 1960; Chapman, 1985). However, in shallow water, estimation of peak sound pressure is challenging, because the estimate is very sensitive to bandwidth and geometry (which is poorly known). Uncertainties in geometry lead to small phase uncertainties in arrivals of different sound paths, which can have a large effect on the predicted peak pressure. The estimate of peak sound pressure would therefore require a sensitivity study on top of the existing computation load for a single time series. As this was not possible here, peak overpressures, for which trauma from explosions were observed in harbour porpoises, were related instead to effective shallow water SEL thresholds. These were more easily calculated and robust to environmental uncertainties. The empirical relationship between the measured peak overpressure and SEL is described in Appendix A.

Harbour porpoise density estimates- Line transect surveys were carried out in the Dutch section of the North Sea during four seasons in 2010 and 2011 (i.e. in March, July and October/November 2010, and March 2011, Geelhoed et al., 2012, Scheidat et al., 2012), providing a large temporal

overlap with the occurrence of explosions. In order to estimate absolute abundance, one needs to correct for non-detectability (e.g. Hiby & Lovell 1998). To do so, the one-sided effective strip width (taking the detection probability or $g(0)$ -values into account) was calculated and defined as 76.5 m for good sighting conditions and 27 m for moderate sighting conditions (Scheidat et al., 2005, 2008, Gilles et al., 2009). Next, for each grid cell (10 km x 10 km), the number of porpoise sightings and the effective surveyed area were calculated. A Bayesian spatial model was fitted to the data, where the number of sightings in each grid cell was treated as a Negative Binomial distributed count, and the log of the area surveyed was treated as an offset. Spatial variability in sighting rate was modelled as a latent Gaussian random field using a two-dimensional autoregressive correlation function of order-1 (Rue et al., 2009). The final seasonal absolute porpoise density estimates (illustrated in Figure 4) were overlaid with the generated soundmaps. The number of affected animals receiving a SEL as defined by the risk thresholds was then estimated by summing the number of predicted animals for each grid cell within a contour on the sound exposure map (for more detail, see Aart et al., in prep). This resulted in an estimate of the number of harbour porpoise affected by each explosion.

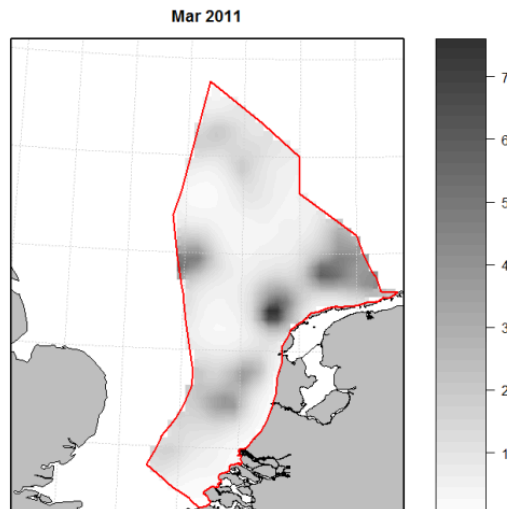


Figure 3. Example of the model-based estimates of porpoise density (grey scale: number of harbour porpoises/ km^2) within the Dutch continental shelf (DCS, red polygon) for March 2011, based on the aerial survey performed in that month.

4.1.3. Results

Overview of explosion activities by the RNLN in the Southern North Sea

In 2010 and 2011, detonations were located predominantly in the southern DCS (Figure 4). Reported charge masses range from 10 to 1000 kg, with most at 125 – 250 kg (Figure 4). Most detonations occurred in water depths between 20 and 30 m.

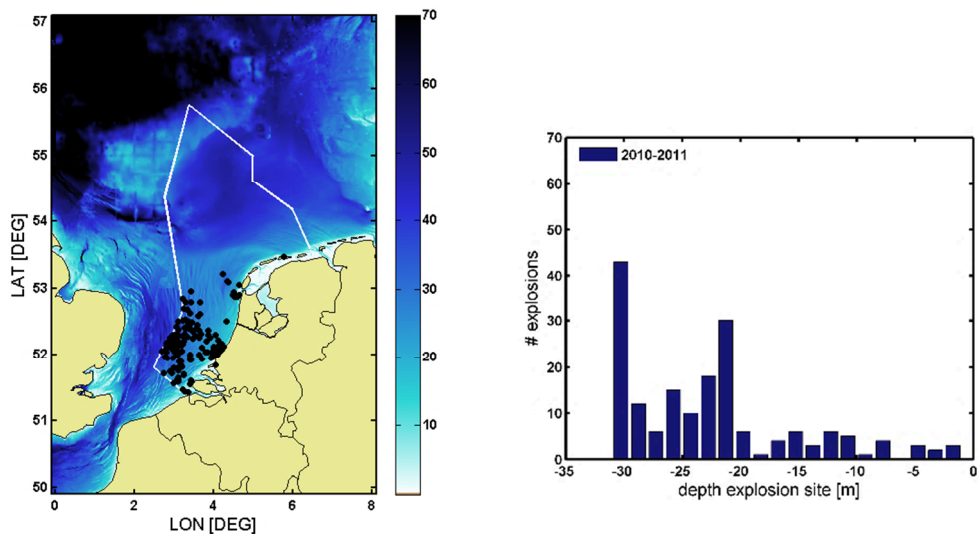


Figure 4. Geographical distribution of detonation events for the years 2010 and 2011 (left). Distribution of charge mass (TNT-equivalent) (top right) and depth (bottom right) at the charge detonation site for the years 2010 and 2011. The 62 explosions for which charge masses were not available are indicated by the magenta bar in the left plot. A charge mass of 10 kg TNT-eq. was assumed for these for the purpose of this study (see text for details).

There was a distinct seasonal pattern to the explosions, with a peak in March and smaller peaks in August and November (Figure 5). The March peak coincided with a peak of fishing activity and thus an increase in encounter rate of UXOs (OSPAR, 2010).

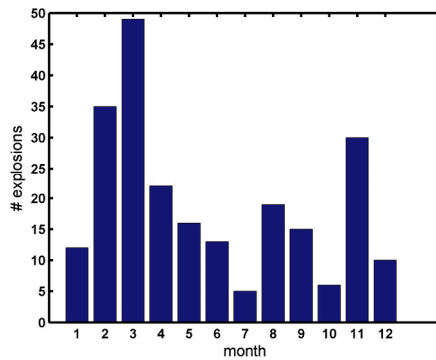


Figure 5. Number of explosion events per month in the North Sea for the years 2010 and 2011 based on the information provided by the Netherlands Ministry of Defence.

Measured SEL and peak overpressure of explosions in shallow water

In the measured explosions, large differences in received levels were noticeable. They were attributed to super-positioning of direct and surface reflected paths (Figure 6). Sound exposure levels were on average lower near the surface than near the bottom or in the middle of the water column. This suggested that the depth where the harbour porpoise was most likely to be located needed to be considered when discussing the impact of the sound.

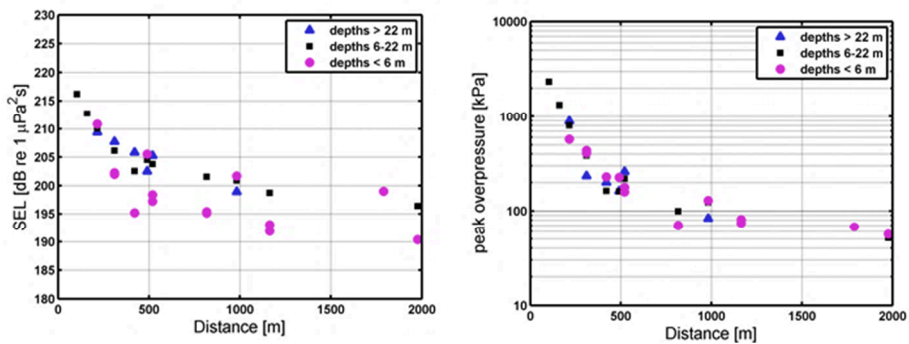


Figure 6. The 263 kg charge mass detonations measured in 2010: shown are SEL [dB re 1 $\mu\text{Pa}^2\text{s}$] (left), peak overpressure [kPa] (right) measured in a frequency band of 1 Hz - 20 kHz, at various distances from the detonation site, with recorders at varying depths (near surface = magenta, mid-water = blue, near bottom = black). SEL values for measurements close to the surface are lower due to pressure release of sound near the surface.

Comparison of measured and modelled sound levels of explosions in shallow water

Measured explosions were run through the propagation model to test its efficacy (Figure 7). The model was in agreement with the data at frequencies containing the peak energy in the spectrum between the cut-off frequency of ~ 20 Hz and 100 Hz, but systematically overestimated the measured SEL at frequencies above 100 Hz (right panel in Figure 7).

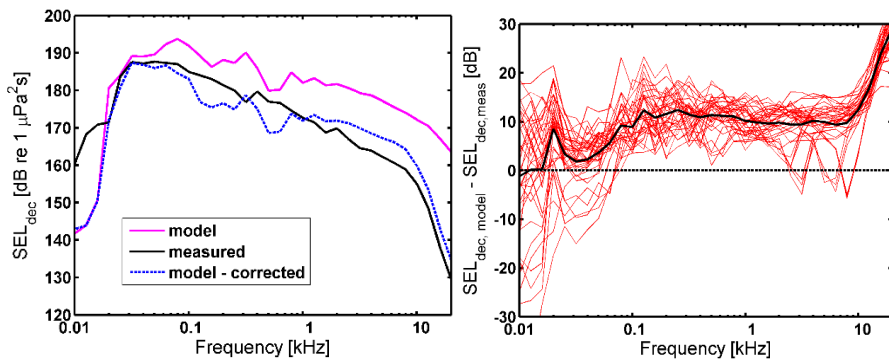


Figure 7. Left: Comparison of decadeband SEL levels as a function of frequency for a mid-water measurement at ~ 2 km distance (black) from an explosion, with model predictions (uncorrected: magenta; corrected: blue). Right: Comparison of all decadeband SEL levels difference between model and measurements (red lines), showing that the model tends to systematically over predict the measured SEL, particularly at higher frequencies. The black line indicates the power mean used as the empirical correction factor to the source level used to correct for the overestimation of the model.

The systematic overestimate of SEL by the model (likely causes are interpreted in the discussion) resulted in an overestimation of 8.1 dB (SD=3.6 dB) of the broadband SEL. Such an overestimate would lead to a systematic overestimation of the impact ranges and therefore required a correction factor. For this, the power mean over each decadeband was subtracted from the modelled SEL. After application of the correction factor, the modelled broadband SEL agreed within 0.1 dB (SD=3.7 dB) from the measured broadband SEL (see Figure 6) and was used to estimate impact distances and number of affected animals.

Effect distances for shallow water detonations based on field measurements

The largest distance at which the peak overpressure corresponded to risk of observed ear trauma was at approximately 500 m (Figure 8). Between 1200 and 1800 m the peak overpressures fell below the limit at which no ear trauma occurred. The minimum SEL measured within 2 km was 191 dB re $1 \mu\text{Pa}^2\text{s}$, which exceeded by 1 dB the SEL based risk threshold above which PTS was considered very likely (190 dB re $1 \mu\text{Pa}^2\text{s}$), and exceeded by 12 dB the lower limit of PTS onset (179 dB re $1 \mu\text{Pa}^2\text{s}$).

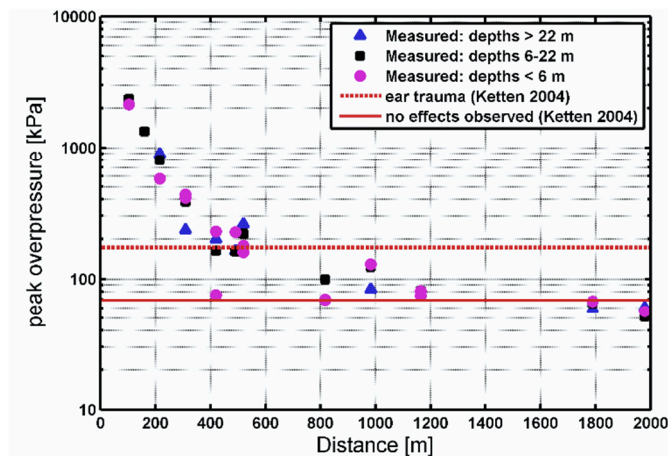


Figure 8. Effect distances based on measured peak overpressure for a charge mass of 263 kg, in water depth of 26 m. Superimposed in red are risk thresholds for blast injury from Ketten (2004).

Modelled effect distances for harbour porpoises exposed to explosions in 2010 and 2011

Model predictions of effect distances as a function of SEL threshold were made for all explosion events occurring in the DCS in the years 2010 and 2011 (Figure 9). Effect distances for the lower limit of PTS (179 dB re $1 \mu\text{Pa}^2\text{s}$) varied between hundreds of meters and 15 km, which were higher than the empirical relationship by Weston (1960) for deep water environments. There was a trend of increasing effect distances with increased charge mass, with substantial scatter due to variations in water depth in which explosives were detonated. This indicated that the water depth in which the explosion occurs has a significant influence on the effect range for a given charge mass (Fig. 10).

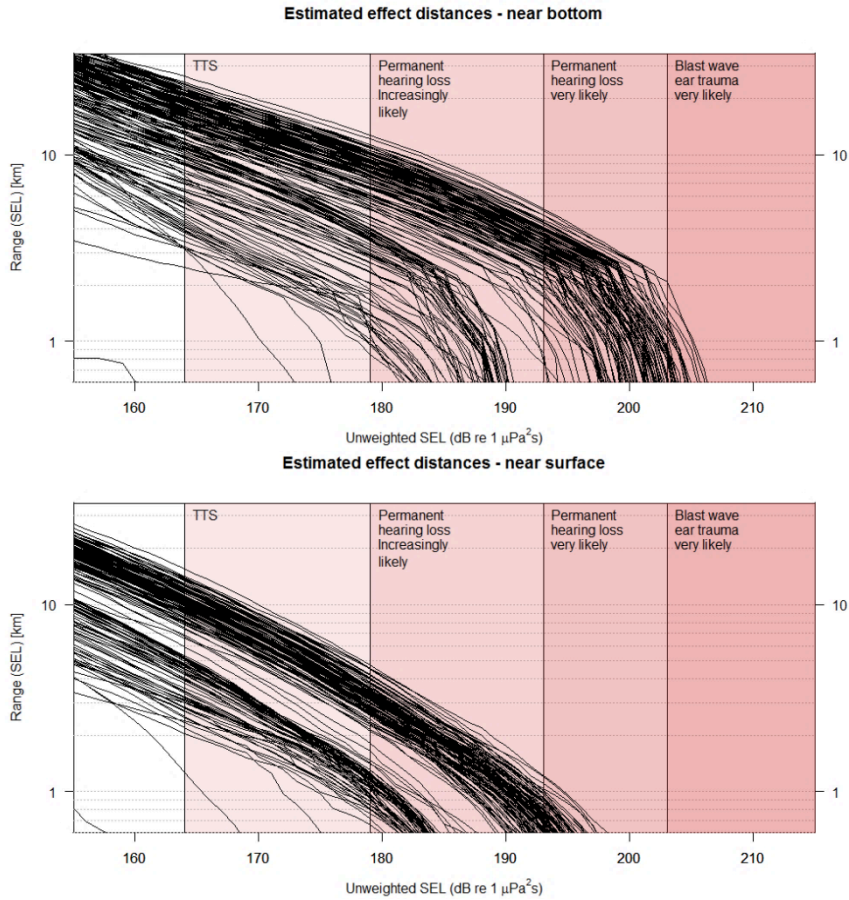


Figure 9. Modelled effect distances for a harbour porpoise at 1 m above the bottom (top) and 1 m below the surface (bottom), as a function of SEL threshold. Each black curve indicates a single explosion in the years 2010 and 2011. Vertical lines bordering the pink shaded areas represent the TTS, PTS and Ear Trauma onset threshold values (see Table 1).

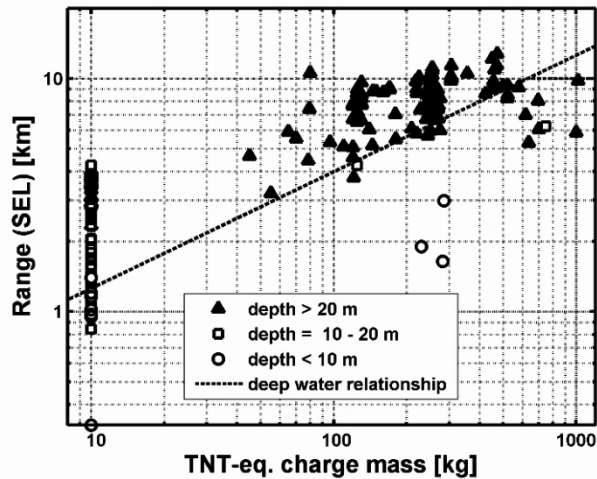


Figure 10. Modelled effect distances for a harbour porpoise at 1 m from the bottom, as a function of charge mass for the lower limit for PTS (179 dB re $1 \mu\text{Pa}^2\text{s}$). Symbols indicate different water depths at the location of explosion, showing lower effect distances for shallow water explosions. For comparison, the dashed line shows the deep-water prediction using the Weston (1960) model.

The density of harbour porpoises in the DCS in 2010 was dependent on season, varying between 1.34 animals/km² in early-spring to 0.60 animals/km² in summer (these model-based values are similar to the values reported by Geelhoed et al., 2012, and Scheidat et al., 2012, based on traditional distance analysis). Thus, a fixed impact distance would affect a different number of animals depending on the season of the event. Here, explosions occurring in the DCS between March 2010 and March 2011 were considered (88 in total), providing a maximal temporal overlap with the aerial line-transect surveys in the DCS. By comparing modeled effect areas to measured porpoise densities the mean number of affected animals and the total number of impact events as a function of SEL threshold per explosion were estimated (Figure 11, and Table 2).

Harbour porpoises were likely to receive lower SEL when near the surface than when at depth (see Figure 6). To account for this in the exposure determinations, it was assumed that harbour porpoises spent 50% of their time near the surface and 50% near the bottom (Table 2). This assumption was based on published data for normal harbour porpoise behaviour (Westgate et al., 1995; Akamatsu et al., 2007). The average number of animals affected by each underwater explosion was then estimated by taking the mean of the number of animals exposed at 1 m below the surface and 1 m above the bottom.

A typical underwater explosion was estimated to lead to PTS in multiple individuals, with a mean over all explosions ranging from 8 to 51 individuals, depending on the chosen SEL threshold level, and TTS in several hundreds of individuals (Figure 11). Although the impact area and corresponding number of harbour porpoises increased as a function of charge weight, the relationship was weakened by spatial and seasonal variability in porpoise density and location of the explosion relative to topography (i.e. shallower regions more strongly attenuate sound).

Between March 2010 and March 2011 (the period with temporal overlap between harbour porpoise surveys and explosions) a total of 88 UXO were detonated by the RNLN in the DCS. These would have resulted in a total of approximately 5450 impact events (i.e. instances in which the SEL at a harbour porpoise exceeded the estimated risk threshold) for the lower limit for permanent hearing loss and more than 28000 TTS-onset impact events (Table 2). This was possibly an overestimation of the number of individual animals affected, since some may have been affected on several occasions. The frequencies of multiple exposures depended on how individual animals move, but the probability of multiple exposures for high SEL thresholds that lead to PTS was small (See Section 4.2).

Based on the limited number of studies of actual explosion-induced ear trauma in fresh cadavers (Ketten, 2004), it was judged that a SEL >190 dB re $1\mu\text{Pa}^2\text{s}$ would very likely result in permanent hearing loss. The model estimated an annual total of approximately 1280 impact events in which animals were very likely to sustain permanent hearing loss (Table 2).

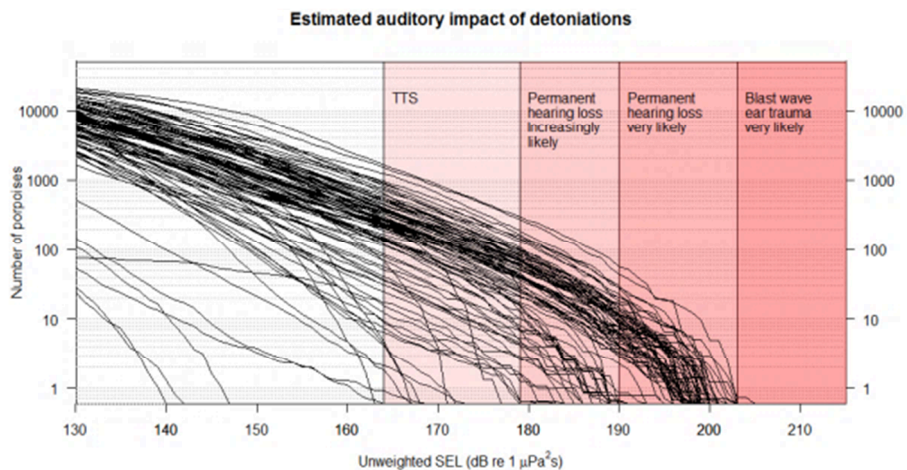


Figure 11. Estimated number of harbour porpoises affected by each explosion (black lines) as a function of received (unweighted) SEL for 88 explosions occurring in the DCS in the period between

March 2010 and March 2011, assuming animals are 50% at the surface and 50% near the bottom. Model SEL estimates were empirically corrected to match field acoustic measurements (see text in Methods section for details). Vertical lines bordering the pink shaded areas represent the TTS, PTS and Ear Trauma onset threshold values (see Table 1).

Table 2. The estimated average number of harbour porpoises impacted with a temporary or permanent hearing loss, by a single explosive clearance, and the total impact events (i.e. instances where a harbour porpoise was exposed to levels high enough to cause a specified effect) from the total of 88 explosions, in the Dutch continental shelf (DCS) waters between March 2010 and March 2011. The effects considered were temporary and permanent hearing loss by explosive. Estimates are made for near the sea surface (i.e. at 1 m depth), near the bottom (i.e. 1m above the bottom) and for the mean of these two, which assumed 50% of the porpoises were near the surface and 50% of the porpoises were near the bottom.

Type	Threshold unweighted SEL (dB re 1 μ Pa ² s)	# of harbour porpoises (single explosion – average)			# of impact events (88 explosions)		
		If all near surface	If all near bottom	If 50% near surface and 50% near bottom	If all near surface	If all near bottom	If 50% near surface and 50% near bottom
Blast wave ear trauma <i>Very likely</i>	203	0	1	1	1	119	60
Permanent hearing loss <i>Very likely</i>	190	2	27	15	205	2,362	1,283
Permanent hearing loss <i>Increasingly likely</i>	179	18	106	62	1,584	9,318	5,451
TTS <i>Very likely</i>	164	190	448	319	16,721	39,413	28,067

4.1.4. Discussion

Implication of underwater explosions for the North Sea harbour porpoise population

Risk of permanent hearing loss —This study aimed to quantify the potential impact on harbour porpoises of underwater ordnance explosions on the Dutch Continental Shelf, conducted by the RNLN. It was estimated that in a one-year period (March 2010 to March 2011), the 88 explosions that occurred in the DCS very likely caused 1280, and possibly up to 5450, permanent hearing loss events, with some animals potentially exposed multiple times.

The implication of a permanent hearing loss for a harbour porpoise depends on the severity of the hearing loss, and the frequency range that is affected. Because of the configuration and mapping of frequencies in the inner ear, the impulse from a blast results in a broad movement of the inner ear membranes that is not frequency specific. Since high frequencies are encoded shortly after the entry to the cochlea, they are subject to impulse-related effects even though the peak in the spectrum of the signal is lower. Such effects were also observed in Kastelein et al. (2014b), who reported TTS to occur at increasingly higher frequencies with increasing noise exposure. When received levels of an explosion impulse exceed the threshold for causing a permanent hearing loss to part of the harbour porpoises hearing range, a wider range of hearing is also likely to be negatively affected. Although the frequency range affected remains unknown, when explosion levels are high enough to cause primary blast injury resulting in ear trauma, exposures near those levels will very likely result in a large reduction in hearing ability over a broad frequency range.

Whilst the dominant parts of the sound energy from the explosion shock wave is contained in low frequencies (< 1 kHz), harbour porpoises are known to echolocate at frequencies above 100 kHz (Møhl & Andersen, 1973). They do produce low level sounds at frequencies below 1 kHz that have been attributed to communication (Verboom & Kastelein, 1997), while others argue that they communicate solely at frequencies > 100 kHz (Hansen et al., 2008; Clausen et al., 2010). Harbour porpoises rely on their echolocation ability on a daily basis to catch prey, navigate (Kastelein, 1997). Any impairment of their echolocation hearing abilities would likely lead to significant negative effects on their fitness. The implications of TTS are less clear. The estimated number of impact events for TTS by the model suggested that a large number of animals could have been exposed to one instance TTS, and some could have experienced multiple exposures each year (see Aarts et al., in prep). In principle, TTS is expected to recover quickly (within hours to days). Minor TTS shifts in a low frequency range outside the frequency regimes used for communication and echolocation is unlikely to significantly affect the animal's fitness. Repeated or severe TTS might

result in noticeable, even if transitory, damage to the inner ear at the submicroscopic level (Kujiwa & Liberman, 2009), which could have significant consequences for fitness and survival. It is unknown whether harbour porpoises would have responses similar to the species tested in Kijiwa & Liberman (2009).

The detonation activities in the DCS strongly peaked in March, when the harbour porpoise abundance also peaks (Geelhoed et al., 2012). The percentage of animals estimated to have suffered from permanent hearing loss per year due to exposure to underwater explosions in the DCS could be at least 1.3% and potentially up to 8.7% of the harbour porpoise population present in the DCS (based on the average population size in the DCS of the four survey estimates in Geelhoed et al., 2012).

Uncertainty in estimated impacts

The predicted impacts contained uncertainties, which were attributed to the following factors: 1) difficulty of predicting the generation and propagation of underwater shock waves in shallow water at large distances; 2) lack of data on sensitivity of harbour porpoises exposed to explosion shock waves and broadband impulsive sound; 3) a lack of knowledge on habitat use and movement patterns of harbour porpoises in the North Sea. The main uncertainties in the model predictions are discussed in the following sections. Uncertainties in habitat use are discussed in Section 4.2.

Sound exposure levels of explosions in shallow water — The impact assessment relied on the validity of the propagation model used to estimate SEL for different explosive charge mass and water depths. With the adopted deep water model for the explosion source energy level from Weston (1960), prior to correction the model systematically overestimated the observed broadband SEL (by approximately 8 dB), particularly at frequencies higher than 200 Hz.

Different mechanisms could be responsible for the overestimation of the (uncorrected) model. For example, interaction with the sea floor for an explosive detonated near or on the bottom, energy losses due to a blow-out as the shock wave first reaches the surface, energy loss by cavitation close to the surface, a lower effective charge mass due to degradation of the explosive charge, or propagation losses due to multiple interactions with wind-generated bubbles at larger distances could all lead to reductions in the estimated resulting SEL (Cole, 1965; Ainslie, 2010; Pfeiffer, 2014).

The explosion source model assumed that no blow-out at the surface occurred. Surface blow-out may lead to pressure release in the bubble, leading to lowered (horizontal) radiation efficiency. This may occur for large explosives in very shallow areas, however the effect on the radiated

energy in the shock wave at large horizontal distances is not well understood (Weston, 1960). No surface blow-out occurred during the measured explosions, which were both typical in charge mass and water depth (see Figure 4). The UXO were also assumed to detonate at full power, and possible degradation that may have occurred due to long contact with sea water (Pfeiffer, 2014) was not accounted for. Degradation occurs more strongly for some types of UXO (especially thin walled mines, or aluminium torpedoes), but other types of ammunition show less signs of strong deterioration (Pfeiffer, 2014). Since most of the larger UXO found at sea by the RNLN are aerial bombs, the assumption of full power detonation is likely a reasonable assumption for the majority of the UXO considered here (von Benda-Beckmann et al., 2015).

To adjust for the overprediction in SEL, the acoustic source model was corrected to match measured SEL levels at various depths. Because these experiments were representative of typical charges and water depths at which these detonations occur, the corrected model predictions were expected to give a realistic estimate of the impact distances for most of the explosions modelled.

Also for very small charges (~1 kg TNT equivalent charge mass), the uncorrected source model systematically overestimated broadband SEL measurements by Soloway and Dahl (2014) by ~7.6 dB (SD=2.1 dB) at distances up to 1 km. This overestimate also occurred for explosions in mid-water, and these explosives were calibrated charges. As a result, uncertainty in charge mass and effect of bottom interactions of a bottom explosion were unlikely causes for the model overestimating the SEL of an explosion. After applying the empirical correction factor proposed in this study, a better match was obtained for the Soloway and Dahl (2014) measurements. The corrected model slightly underestimated the Soloway and Dahl (2014) measurements by 1.5 dB (SD=2.3 dB) (1-sigma STD).

A plausible cause for the overestimation using the uncorrected model was the effect of the cavitation zone on the propagation of the generated shock wave. The cavitation zone created by the shock wave was likely to lead to energy loss and also could act as a bubble screen for the bottom-reflected paths, including the shock wave. In deep water, shielding by the cavitation zone is unlikely to have such a noticeable effect on the measured SEL because a large fraction of the bottom reflections would have travelled beyond the cavitation zone or would arrive much later than the direct blast. The size of the cavitation zone would be a function of the charge mass and depth of the explosion. The slight overestimation observed when comparing the model to the Soloway and Dahl (2014) datasets agreed with this interpretation, as a smaller charge mass would result in a smaller cavitation zone, and hence less absorption.

Another effect that becomes important at large distances is the attenuation by wind-generated bubbles. This is most noticeable at higher frequencies and longer distances. Attenuation by wind-generated bubbles could in part explain the large discrepancy between the modeled estimate and the measurements at frequencies above 10 kHz. Alternatively, this discrepancy could be caused by the low-pass filter on the measurement devices. However, since the energy above 10 kHz did not contribute significantly to the broad-band energy at a distance of 2 km, its impact on porpoises could be ignored.

It is concluded, therefore, that the corrected model provided a reasonable estimate of the SEL within the first 2 km around the explosion. This corresponded to the lower limit for effect distances for smaller charges (<25 kg). For larger explosions (>25 kg), where the effect distances for the lower limit of PTS onset (SEL >179 dB re $1\mu\text{Pa}^2\text{s}$) approached the 10 – 20 km, the model requires further validation.

Uncertainties in dose-response relationships for hearing loss

As there are no measurements of onset thresholds of permanent hearing loss in any marine mammal species, we considered a range of SEL thresholds at which permanent hearing loss could occur. A lower limit threshold, above which permanent hearing loss was considered increasingly likely to occur, was obtained by following the approach proposed by Southall et al. (2007). That study assumed that PTS occurs at a level of 15 dB above the TTS onset. Data from Kastelein et al. (2012a) suggests there could be a higher TTS/PTS exposure difference. Kastelein et al. (2014b) demonstrated a positive correlation between frequency and rate of TTS-increase. This would result in a wider offset between TTS and PTS than assumed in the present study and, consequently, a higher PTS threshold, especially for the low frequency range containing most of the propagated energy from an explosion. Therefore this SEL threshold of 179 dB re $1\mu\text{Pa}^2\text{s}$ might be conservative and lead to an overestimation of the number of animals that could be affected by permanent hearing loss.

In this study the effect of frequency weighting of the SEL was neglected when estimating the risk of TTS and PTS on the basis that our risk criterion was based on observation of TTS onset due to a single airgun exposure (Lucke et al., 2009), which was more representative of the explosion sound than other stimuli for which TTS measurements have been obtained in harbour porpoises.

Weighting of the received SEL would need to be compared to the corresponding weighted exposure levels at which TTS was measured by Lucke et al. (2009). Since the very low frequencies

propagate poorly in shallow waters, the frequency content was similar to that of an airgun, and hence the frequency weighting was unlikely to affect the results, as the risk threshold for TTS will be lowered by the same order as the predicted weighted sound exposure level. It was therefore expected that the lack of frequency weighting does not affect the estimated impact of temporary and permanent hearing loss.

Values of peak overpressure levels at which ear trauma was observed in eight cadaveric harbour porpoises exposed to underwater explosions (Ketten 2004) were used to put an upper limit to PTS SEL threshold. Ketten (2004) noted that other characteristics of the shock wave are likely to be important in determining the risk of injury and need to be considered, such as near field vs. far field loading effects, exponential vs. sinusoidal bursts, and synergistic effects of rate of pressure increase, peak sound pressure, waveform, duration and rise time, coupled with body mass (species with smaller average body mass have greater liability for shock-induced trauma, particularly in air-filled tissues and from bubble formation and oscillation, lesser body shadow protection, etc.). It is not obvious how to translate the experimental conditions employed by Ketten (2004) to large explosions at sea and with greater distances from the source, except in terms of received peak sound pressures. That is equivocal as well, however, because of the complex physics of propagating shock waves. Further, it is important to note that tissue and whole system responses are different in live versus post-mortem specimens. Even in the freshest material, the mechanical properties for some or all tissues may be altered due to death. In some cases, post-mortem material may be more responsive than living tissue; in others, less. Thus, cadaveric results are not definitive for live cases. However, they do provide insights into purely mechanical responses that may occur in marine mammals due to shock waves. For this reason, the Ketten (2004) study focused on the tissue changes that are essentially mechanical and should be robust even in cadavers, such as ossicular fracture and middle, fenestral and inner ear membrane responses and the minimal end and massive, distinct trauma in other tissues such as liver and brain.

4.1.5. Conclusion

In this study, the impact of explosive clearance activities of historical UXO on harbour porpoises in the Southern North Sea was assessed. This is the first study to address on a broad scale the potential impacts of underwater explosions on any marine mammal species. This assessment was based on actual explosion events carried out by the RNLN in 2010 and 2011 using information on

explosive type, location and timing of the detonations as made available by the Netherlands Ministry of Defense (NLMoD). While the data used in the analysis was site specific, the methodology used in this study is broadly applicable to other areas in which underwater explosions occur. For these explosion events, impact areas were modelled and compared to the aerial-survey based estimates of harbour porpoise distribution during the same period.

Within the period of 2010 and the 2011, a total of 210 explosions occurred, with charge masses ranging from several kilograms to one thousand kilograms TNT-equivalent. The model estimated that the 88 explosions that occurred in the DCS between March 2010 and March 2011 (the period of overlap between aerial surveys and reported explosion events) were very likely to have caused 1280, and possibly up to 5450, permanent hearing loss events, i.e. instances of a harbour porpoise predicted to have received sufficient sound exposure to cause permanent hearing loss. Distances to which there was a risk of permanent hearing loss were on the order of one to several kilometres, and possibly further for larger explosions.

The predicted impacts in this study contain uncertainties, which were attributed to the following factors:

- Lack of data on sensitivity of harbour porpoises to explosion shock waves and broadband impulsive sound.
- Difficulty in predicting the generation and propagation of underwater shock waves in shallow water at large distances.
- Lack of knowledge on movement patterns and habitat use of harbour porpoises.

This study confirms earlier concerns (Nützel et al., 2008; Ainslie et al., 2009; Koschinski, 2012; Camphuysen & Siemensma, 2011) that explosions in the North Sea pose a risk to harbour porpoises and has prompted the NLMoD to investigate and implement mitigation measures to reduce the adverse effects of underwater explosions. Even the most optimistic estimates presented in this study suggested that there was a significant risk that hundreds of individual harbour porpoises were negatively affected by the explosions, although the population level consequences could not be judged. Models are being developed to assess population level consequences of underwater sound on porpoises (Lusseau et al., 2012; Harwood et al., 2013; Nabe-Nielsen et al., 2014). The detonation activities by all nations active in the North Sea, as well as information on distribution of harbour porpoises, should be considered in order to judge the cumulative effect of all explosions on the harbour porpoise population in the North Sea. To enable

such assessment, it is recommended that reportings of detonations contain the necessary information (location, depth, time and estimated charge mass) to enable an impact assessment.

Appendix A

To delimit the effect range at which permanent hearing loss becomes ‘very likely’, levels at which ear trauma occurred in fresh animal cadavers resulting from primary blast injury were considered. Peak overpressure was used in Ketten (2004) to predict the occurrence of primary blast injury. Here instead, the peak overpressure was empirically related to SEL for measured explosion sound in shallow water, due to the difficulties of modelling peak overpressure in shallow water. Then an effective SEL that corresponded to peak overpressures resulting in ear trauma was estimated.

In order to indicate at what distances a risk of blast injury occurred, the measured peak overpressure was related to measured SEL using the data from the monitored explosions (Figure A1). Measured peak overpressure and broadband SEL showed a roughly log-linear relationship with a greater scatter for measurements close to the surface (depths smaller than 6 m).

Observations by Ketten (2004) showed that ear trauma occurred at peak overpressures exceeding 172 kPa (25 psi), indicated by the red dashed line in Figure A1, which corresponded to a range in SEL of 195 – 203 dB re $1\mu\text{Pa}^2\text{s}$, which suggests that ear trauma is very likely to occur at SEL >203 dB re $1\mu\text{Pa}^2\text{s}$. No ear trauma could be observed for peak overpressures of 69 kPa (10 psi), as indicated by the red solid line, suggesting that ear trauma due to primary blast injury is unlikely to occur at SEL <190 dB re $1\mu\text{Pa}^2\text{s}$. The probability of ear trauma to occur between SEL = 190 dB re $1\mu\text{Pa}^2\text{s}$ and 203 dB re $1\mu\text{Pa}^2\text{s}$ was considered to be increasingly likely.

It is expected that the acoustics of a blast event at a received level of SEL >190 dB re $1\mu\text{Pa}^2\text{s}$ is very likely (>95% probability) of causing PTS. The delimitation between the terms ‘unlikely’ (less than 5% probability), ‘increasingly likely’ (probability between 5% and 95%) and ‘very likely’ (greater than 95%) adopted in this study are not based on a statistical evaluation of the data; rather should be considered as indicative of the consensus opinion of the authors of the likelihood at which these effects occur.

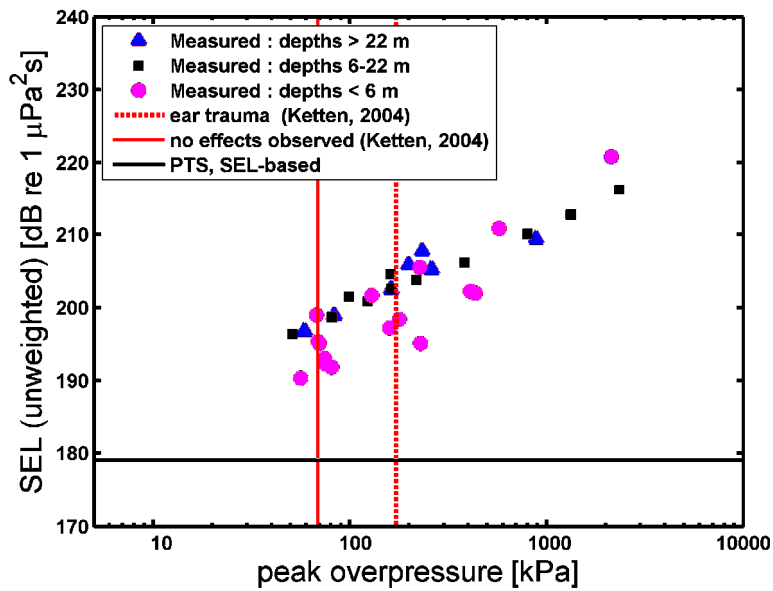


Figure A1. Empirical relation between un-weighted broadband SEL and peak overpressure for shallow water explosions of 263 kg TNT eq. charge mass, both measured at different distances (see Results for more details). Superimposed are risk thresholds for a lower limit for PTS onset (black line, based on the Lucke et al. (2009) TTS measurement and adding 15 dB following Southall et al. 2007) and observed pathological effects (red lines, observed by Ketten, 2004).

4.2. MOVEMENT BEHAVIOUR INFLUENCES POPULATION LEVEL EXPOSURE TO UNDERWATER SOUND: IMPACT OF EXPLOSIONS ON HARBOUR POPOISES

This section³ is submitted as [G. Aarts, A.M. von Benda-Beckmann, K. Lucke, H.Ö. Sertlek, R. van Bemmelen, S. Geelhoed, S. Brasseur, F.P. Lam, H. Slabbekoorn, R. Kirkwood, Movement behaviour influences population level exposure to underwater sound: Impact of explosions on harbor porpoises, under review by Journal of Animal Ecology]

Abstract: Anthropogenic sound in the marine environment can have negative population-level consequences for marine species. Estimating how many individuals are impacted by sound remains challenging though, as this is dependent on their mobility. The objective of this study is to reveal how animal movement influences how many and how often animals are impacted by sound. In a dedicated study we investigated the impact of sound from underwater detonations of recovered ordnance (mostly WWII aerial bombs) on harbour porpoise (*Phocoena phocoena*) in the Dutch North Sea. Geo-statistical distribution models were fitted to data from four marine mammal aerial line-transect surveys and used to simulate the distribution and movement of porpoises. Based on derived dose-response thresholds for temporary or permanent threshold shift (i.e. TTS and PTS), we estimated the number of animals affected was estimated. When individuals were free-roaming, 1200 and 24,000 unique individuals would suffer PTS and TTS, respectively. In contrast, when individuals were completely site-faithful, 1100 and 15,000 unique individuals would receive PTS and TTS, respectively. As explosions occurred more frequently in one region, the southern Dutch North Sea, high site-fidelity increased the probability of repeated exposures. Free-roaming

³

My contribution to this section concerns providing sound maps and source model of the underwater explosions. This section is included as illustration of a biological application of the sound maps during my PhD project.

movement, resulted in more individuals being exposed, but reduced the number of repeated exposures. Since most anthropogenic sound-producing activities operate continuous or are intermittent, snap-shot distribution estimates alone tend to underestimate the number of individuals exposed, particularly for mobile species. This study shows that an understanding of animal movement is needed to estimate the impact of underwater sound, or other human disturbance.

4.1.1 INTRODUCTION

Human activities in the marine environment such as offshore pile driving, seismic surveys, and detonation of explosives often produce impulsive sounds of high amplitude (Ainslie *et al.* 2009). Extreme levels of these anthropogenic sounds have the potential to disturb and/or damage marine mammals (Richardson *et al.* 1995, Southall *et al.* 2007, Nowacek *et al.* 2007). Particularly population-level consequences of sound are of great concern (National Research Council 2003). However, the first step of estimating the total number of individuals exposed to specific sound sources is challenging: Often only a fraction of the population is observed, and then, most marine mammals move large distances, changing the exposure probability, and consequently affecting the cumulative number of individuals exposed.

A general framework, labelled Population Consequences of Disturbance (PCoD) or Population Consequences of Acoustic Disturbance (PCAD) has been proposed to assess the impact of sound from anthropogenic activities at sea (e.g. offshore pile driving, seismic surveys, naval activities, shipping) at a population level (e.g. National Research Council 2003; Thompson *et al.* 2013b; New *et al.* 2014; King *et al.* 2015). The framework's first step in a chain of several steps requires an estimate of the number of individuals exposed to a level with detrimental impact. Frequency-specific sound source levels and sound propagation models are used to derive maps of sound exposure levels (SEL) or sound pressure levels (SPL). Published dose-response relationships describe the received level at which hearing impairment or behavioural responses are expected to occur (e.g. Southall *et al.* 2007; Lucke *et al.* 2009; Kastelein *et al.* 2012; Tougaard, Wright & Madsen 2014). The sound maps are then overlaid with marine mammal distribution estimates, to estimate the number of individuals exposed to sound levels above behavioural or auditory thresholds.

This method to estimate the number of individuals impacted can be used for single sound exposures, with the timescale of the exposure being small compared to the distance travelled by those individuals. However, it is deficient for the majority of situations, where continuous or intermittent sounds are produced over longer periods. These represent the majority of situations. With ongoing and intermittent sounds, individuals that are unaware of the event may (re-)enter an area of impact in-between the sound emission events. Consequently, a larger number of individuals could be exposed than would be expected based on 'snap-shot' density estimates. Moreover, individuals that have not vacated the area may receive multiple exposures during a sound production period.

Each type of anthropogenic sound-source has unique acoustic characteristics in terms of intensity, frequency range and repetition rate, and may change in location over time. Underwater explosions (e.g. controlled underwater detonations of recovered bombs, mines, and torpedoes from WWII) are unique as they represent single sound events, with the peak sound pressures of the blast wave being one of the highest anthropogenic noises produced in the marine environment (Ainslie et al. 2009, Koschinski 2011). Such detonations are conducted on the Dutch Continental Shelf (DCS) by the Royal Dutch Navy in a controlled manner, to reduce the risk of uncontrolled explosions, which could be dangerous to human life and infra-structure (Koschinski 2011, von Benda-Beckmann et al. 2015). Each year, approximately 100 detonations occur on the DCS. To marine mammals, the sound produced by these explosions could cause acute and chronic stress (Reeder & Kramer 2005), trigger behavioural reactions (Southall et al. 2007, Nowacek et al. 2007), and may lead to temporary or permanent hearing impairment or other physical injury (Ketten 2004, Lucke et al. 2009, Kastelein et al. 2012). Since the detonations appear to occur irregularly in time and space (von Benda-Beckmann et al. 2015), animals may be unable to anticipate and avoid them.

In the North Sea, the harbour porpoise (*Phocoena phocoena*) is the most abundant marine mammal, with approximately 230,000 individuals in 2005 (Hammond et al. 2013). In the southern North Sea, harbour porpoises were virtually absent for several decades but, since 1990, numbers have grown exponentially, presumably as a result of large-scale movement southwards (Camphuysen 2011, Hammond et al. 2013). Coastal sightings and aerial survey data suggest that most harbour porpoises reside in the southern North Sea in winter, and many migrate northwards along the Dutch and German coast in March and April (Scheidat et al. 2012). Due to their small size and a high metabolism in a cold environment, harbour porpoises require a higher daily food intake than most other Odontoceti (Kastelein 1997). Any impairment of their foraging efficiency, such as displacement in response to anthropogenic sound or impaired echolocation ability, could reduce the animal's fitness.

Benda-Beckmann *et al.* (2015) investigated potential impacts of naval explosive clearance activities on the harbour porpoise on the DCS and concluded that these likely resulted in hundreds to thousands of PTS *events* annually. However, the total number of individuals exposed could not be estimated.

Here, we extend the study of Benda-Beckmann *et al.* (2015) by applying individual-based models to investigate the effects of hypothetical movement strategies of harbour porpoise (random dispersal and site fidelity), and thereby deriving improved population-level estimates. We base our analyses on one year of distribution data of harbour porpoise in the North Sea, and the time-line

and amplitude levels of detonations in the same period. The first general question we aim to answer is ‘how does the interaction between the spacing and timing of explosions, and movement behaviour of the harbour porpoises, influence the exposure probability?’ And secondly, we attempt to estimate the total number of porpoises exposed to annual detonations of underwater explosions on the DCS. Although the study focusses on one species, one sound source and a finite region, the results are applicable to broader investigations of marine mammal (and potentially other marine fauna) responses to underwater anthropogenic sound.

4.1.2 METHODS

Pilot simulation: How does movement of the animal and the sound source influences the number of animals exposed?

Not only animals, but also sound sources tend to move through space, influencing how many and how often individual animals are exposed to sound. The sound source can be either fixed, moving randomly at high speed, or everything in-between. For illustrative purposes, we here adopt a simplified simulation to illustrate the extremes with respect to movement of the animal and the sound source, and how it affects the number of porpoises exposed, and exposure repeatability. A stationary sound source (e.g. underwater explosion or pile-driving event) was assumed to be either at a single location or at a different, randomly selected locations each day. It was active at one instance each day over a duration of 100 days. Porpoise movement was simulated on a 100 x 100 km grid, and those present within an arbitrarily chosen distance of 10 km from the source were assumed to be negatively impacted (e.g. auditory damage or severe panic response). The initial distribution of porpoises was randomly uniform, after which individuals moved according to different rules. One group of 1000 *site-faithful* porpoises remained at their initial location, and the other group of 1000 porpoises were *free-roaming*, making steps in random directions every 10 min., and moving at a high speed of 1.4 m/s (Otani et al. 2001). More realistic individual-based movement models for harbour porpoises that incorporate resource dynamics in space and time have been developed (Nabe-Nielsen et al. 2013). However, the necessary porpoise movement data and a representation of the food landscape were not available to parameterize this model for the southern North Sea. Another harbour porpoise movement model has been developed by Haelters *et al.* (2015), but this models applies to porpoises actively avoiding a pile-driving event. Here, we aim to simulate movement under more natural, undisturbed conditions.

Harbour porpoise aerial survey data

The defined one year study period was 15 March 2010 to 15 March 2011; data on explosions and harbour porpoise numbers on the DCS were analysed for this period. Here we use data from four aerial surveys of porpoise abundance, conducted in March, July and October-November 2010, and March 2011 on the DCS (Scheidat, Verdaat & Aarts 2012; Geelhoed *et al.* 2013). Surveys were conducted in weather conditions safe for flying and suitable for porpoise surveys, i.e. no heavy or freezing rain, visibility >3 km and expected sea state ≤ 3 bft. A high-winged, twin-engine aircraft (Partenavia 68) was used, flying at an altitude of ca. 183 m (600 feet) with a speed of 185 km/h (100 knots). Observers at bubble windows (allowing observations beneath the plane) on either side of the aircraft relayed details on environmental conditions (i.e. sea state, turbidity, cloud cover, precipitation and 'subjective' conditions) and sightings to a navigator. Conditions were reported at the beginning of each transect and whenever conditions changed. The subjective conditions (ranked as poor, moderate or good) represented the observer's perception of the likelihood of seeing a harbour porpoise should one be present, taking into account all environmental conditions. Only data collected under good and moderate conditions were used in the analysis. Sightings data included: species, inclination angle (to estimate distance), group size, presence of calves, behaviour, swimming direction and cue (e.g. body at surface, under water, splash).

Accounting for incomplete detection

To estimate absolute porpoise density, it is necessary to correct for the number of undetected porpoises (e.g. those well below the surface or not noticed by the observer). Here, detection probabilities were based on 'racetrack' calibrations and 'distance sampling' carried out in German and Danish waters using the same survey procedures and type of aircraft (Scheidat *et al.* 2008). The racetrack method estimates the proportion of animals re-sighted after flying a circle and resurveying part of the transect line (Hiby & Lovell 1998). The distance sampling method estimates the decrease in detection probability as a function of distance from the transect, using data on flight height and inclination of the porpoises from the aircraft (Buckland *et al.* 2004). The effective strip width (ESW) was calculated for each side of the aircraft. Published one-sided ESWs are 76.5 m (SE = 37.2 m) for good sighting conditions and 27 m (SE = 13.9) for moderate sighting conditions (Scheidat *et al.* 2008). The effective area surveyed is the distance travelled multiplied by the two-sided ESW.

Geo-statistical modelling of porpoise density

Estimating the number of individuals impacted by sound, requires species distribution estimates that can be overlaid with sound maps (e.g. McCarthy *et al.* 2011; Thompson *et al.* 2013). Not all types of species distribution models are suited for this purpose. For example, presence-absence models (e.g. Thompson *et al.* 2013; Bailey, Hammond & Thompson 2014) can yield biased estimates, because they do not differentiate between high and low density grid cells. In contrast, models based on count data provide estimates which are proportional to density (Aarts *et al.* 2012). To estimate the *absolute* number of individuals exposed, it is furthermore necessary to account for those individuals present, but not detected. This was achieved by incorporating the effective survey area, which accounts for the number of undetected individuals (see Hiby & Lovell 1998, Buckland *et al.* 2004).

In this study, porpoise density for the entire study area was derived from the survey data. First, a regular 10 km x 10 km grid was created, and the surveyed area and number of porpoise sightings within each grid cell were calculated. Grid cells with no survey effort resulted in missing values. Next a Bayesian spatial model was fitted to the data using Integrated Nested Laplace Approximation (INLA, Rue *et al.* 2009). The number of sightings (Y) in each grid cell ' i ' were treated as Negative Binomial distributed counts (with a dispersion parameter of τ) and the log of the effective area surveyed (A_i) was treated as an offset. A_i included the detection probability. Spatial correlation in the residuals (u) was treated as a latent Gaussian random field using a two-dimensional autoregressive correlation function of order-1:

$$Y_i \sim \text{NegBin}(\lambda_i, \tau)$$

$$\lambda_i = \exp(\beta_0 + \ln(A_i) + u_i) \quad (1)$$

where λ is the expected count and β_0 is the model intercept. Bayesian prior distributions for the parameters β_0 , τ and ρ_x and ρ_y (the correlation parameters in x and y direction, respectively) were defined as Gaussian distributed variables with mean 0 and precisions 0.0001. The model was used to estimate porpoise density for each grid cell within the DCS. We fitted models for each survey season to account for large seasonal differences in abundance and distribution. Linear interpolation between seasonal porpoise density estimates was used to estimate porpoise density at the date of each explosion.

Underwater sound field estimates

Information on the underwater explosions during 2010 and 2011, their location, timing, and sound propagation properties, are detailed in von Benda-Beckmann *et al.* (2015). We considered all 88 explosions on the DCS between 15 March 2010 and 15 March 2011, which concerned the period for which porpoise density estimates were available. Briefly, the acoustic property of the explosive is a short, expanding shock-wave comprising an almost instantaneous rise in pressure followed by an exponential decay, leaving behind expanding and contracting bubbles (Weston 1960), which then is transferred into a more complex waveform due to shallow water propagation (von Benda-Beckmann *et al.* 2015). Underwater sound propagation of the explosions was modelled using the software module SOPRANO (Sertlek *et al.*, Sertlek & Ainslie 2014), which takes into account frequency dependent reflection losses due to surface and bottom interactions, and attenuation by the water. Input data for estimating sound propagation includes spectral source level energy and depth of the explosion, bathymetry maps (resolution: 0.125 x 0.125 minutes longitude and latitude, respectively, source: EMODNET database, <http://www.emodnet-hydrography.eu/>), geo-acoustical properties of the seabed (source: DINO database, <http://www.en.geologicalsurvey.nl>), and wind speed. Broadband sound exposure levels were calculated for the near-surface layer (1 m from the surface), and the near-bottom layer (1 m from the bottom). It was assumed that 50% of the porpoises were near the surface (between 0-2m depth – Teilmann *et al.* 2013) and 50% near the sea floor at the time of the explosion.

Hearing loss thresholds

The (masked) TTS onset level (estimated based on measured auditory evoked potentials for a harbour porpoise exposed to single airgun transients) was at SEL of 164 dB re 1 $\mu\text{Pa}^2\text{s}$ (Lucke *et al.* 2009). Potential frequency dependent effects of underwater explosions on TTS were assumed to be similar to the airgun transients, and therefore, it was considered unnecessary to apply frequency weighting to the SEL when estimating TTS risk. No precise data are available on PTS-onset levels in marine mammals, instead, following (Southall *et al.* 2007), PTS-onset was defined as 164 dB re 1 $\mu\text{Pa}^2\text{s}$ + 15 dB = 179 dB re 1 $\mu\text{Pa}^2\text{s}$, and considered a lower limit below which PTS is unlikely to occur. Experimental exposure of fresh dead carcasses to underwater explosives (Ketten 2004) showed that ear trauma can occur at peak over-pressures between 10 – 25 psi (or 69 – 172 kPa), which approximately corresponds to SEL 190 – 203 dB re 1 $\mu\text{Pa}^2\text{s}$ for explosions in shallow water environment (von Benda-Beckmann *et al.* 2015). It was therefore assumed that explosion sound would very likely cause PTS at the lower limit at which ear trauma occurs (i.e. SEL >190 dB re 1 $\mu\text{Pa}^2\text{s}$), which is the PTS threshold used in this study.

Number of animals affected by single detonations

For single impulsive sound sources, the porpoise density estimates can be directly overlaid with SEL (or SPL) maps, to estimate the number of individuals exposed to sound levels above the previously defined TTS or PTS thresholds. For each explosion, we defined for which grid cells the SEL was above the defined auditory threshold, and used the porpoise density estimates to estimate the number of porpoises present in those cells.

The effect of animal movement on the exposure to underwater explosions

To estimate the total number of unique individual porpoises exposed, and how often each individual was exposed, we simulated their movement for two extreme scenarios.

1. *Site faithful*. Porpoise density estimates for each survey season were treated as a probability density surfaces from which independent realizations of individual points (i.e. porpoises) were generated (see e.g. Fig. 5). At the mid-point between two successive surveys, each simulated individual from one survey was linked to the nearest individual from the subsequent survey. Since the absolute abundance between seasons differed, some individuals could not be linked, and those were considered to be temporarily outside the study area. The SEL sound maps of each explosion were then linked to the realized distribution of individual animals derived from the aerial survey closest in time.

2. *Free roaming/high mobility*. Although in this simulation we only considered the impact of explosions on porpoises within the DCS, we allowed porpoises to move freely within the entire North Sea. The total North Sea population size was defined as the sum of the geographic areas B, H, J, L, M, T, U, V and Y of Hammond et al. (2013), which equates to 232,450 animals. Since no information was available on inter-annual changes in abundance, the population size was assumed to remain constant between 2010 and 2011. Although these 232,450 individual animals were allowed to move freely within the entire North Sea, the total abundance and distribution of animals within the DCS corresponded to our absolute, seasonal porpoise density estimate. This was achieved by assigning to each grid cell outside the DCS, but within the North Sea, a sampling probability of $(N_s - 232,450)/G$, where N_s is the total abundance within the DCS for season s , and G is the total number of grid cells in the entire study area.

For the first explosion, the simulated distribution of porpoises was based on the nearest survey in time, similar to scenario 1 above. Between the explosion at time t_1 and the subsequent explosion at time t_2 , the individual animal was allowed to move at an average cruising speed of $v = 1.4$ m/s over a maximum distance of $m = v(t_2 - t_1)$. Here v is the speed at which the energetic cost of

transportation is at its minimum (1.3 – 1.5 m/s), which lies in-between the mean (experimentally derived) swim speed (i.e. 0.76–0.91 m/s) and maximum observed swim speed (4.2 m/s) (Otani et al. 2001). For each individual porpoise at t_1 , the porpoise density map corresponding to the explosion at t_2 was used to generate a new point location, with the constraint that it was within the maximum travel distance m .

These two simulations allowed us to trace how individual animals (i.e. points) were exposed to multiple explosions in time. No data are available on how porpoises respond to exposure of underwater explosions, and it is even questionable whether they are capable of estimating the distance or direction of the source. Hence, no attempt was made to study in detail the effect of avoidance.

4.1.3 RESULTS

Pilot Simulation: The effect of movement on exposure probability of fixed and moving sound sources.

If the sound source remains at a fixed location and porpoises are site-faithful (Fig. 1d), only those individuals living directly within the impact zone (here <10 km from the source) will be negatively impacted (Fig. 2a), however, they will be exposed each time the sound source is active (Fig. 2b). In contrast, when porpoises are free roaming and not avoiding the impact area, nearly all individuals are exposed at least once (on average 937 of 1000 individuals), but on average each individual is only exposed 3 times within the 100 day study period. The total number of impact events remains the same, regardless of whether individuals are site-faithful or roam freely.

When simulating a sound source which is randomly moving in space (Fig. 1c, d), different movement behaviours have little effect on either numbers of individuals exposed or numbers of multiple exposures. Over time, approximately all individuals could be exposed at least once.

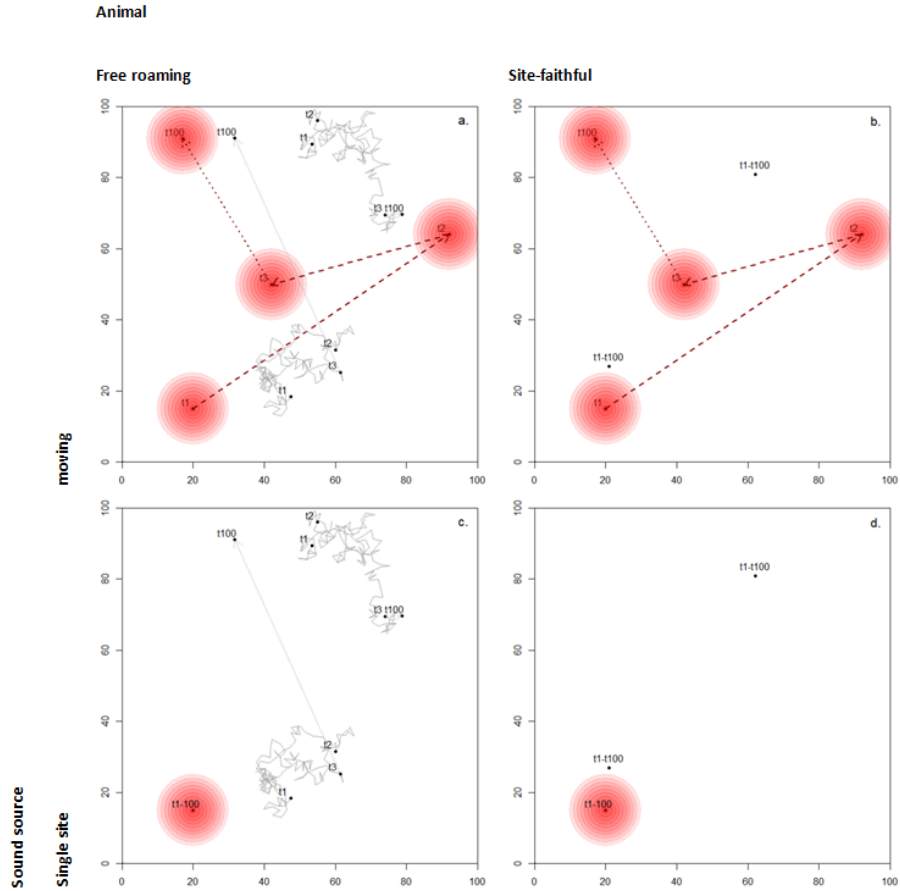


Figure 1. Illustrating the simulation of the movement by the animal and the sound source. The sound source (red circle) either moves randomly through space (a, b) or occurs at a single site (c, d). Animals (grey track and black dots) either move at a speed of 1.4 m/s randomly through space (a, c) or are site-faithful (b, d). t1-t100 represent day 1 through day 100. Only the track of the first three and final location of the animal and sound source are shown.

BIOLOGICAL RELEVANCE OF SOUND MAPS

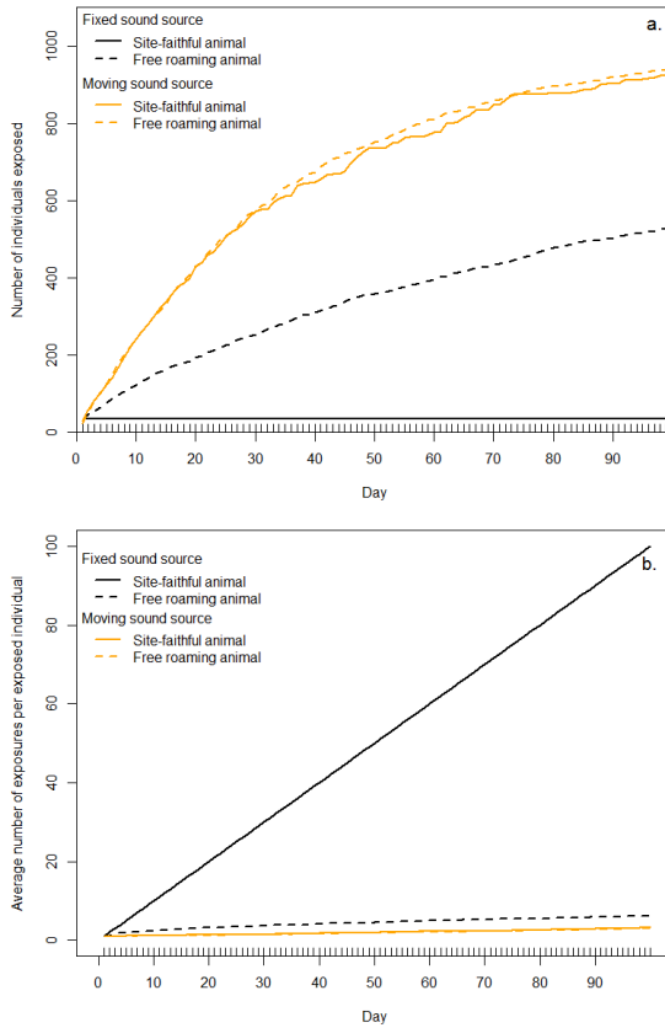


Figure 2. Simulation illustrating the effect of movement by the animal and the sound source on the exposure probability. When an organism is free roaming and the sound source is at a predictable (i.e. fixed) location, the cumulative number of individuals impacted is much larger than when the organism is site-faithful (a), however the number or repeated exposures is reduced (b). If the location of the source is completely unpredictable in space, movement does not reduce the number of individuals exposed (a) nor the average exposure probability (b).

Spatiotemporal distribution of underwater explosions in the DCS

Explosives were mostly detonated at their site of discovery, with the highest density in the southern part of the DCS (Fig. 3) as most of the explosives were dropped in this area during WWII (OSPAR Commission 2010). The detonations occurred in all months of the year, with a peak in March. There were 88 explosions on the DCS between 15 March 2010 and 15 March 2011.

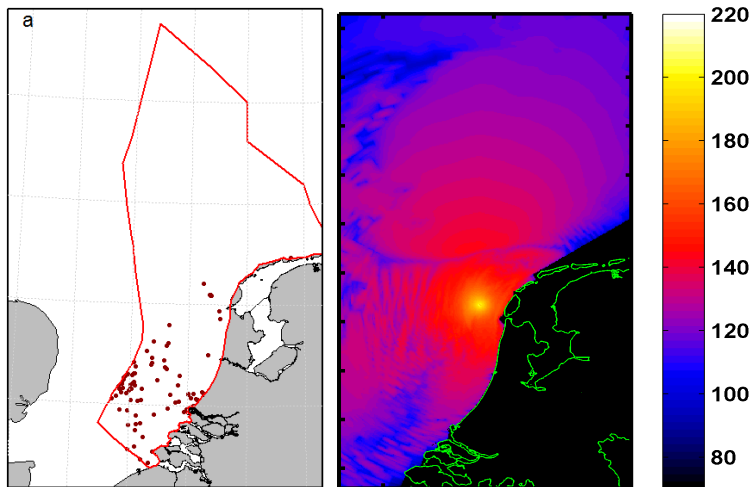


Figure 3. a. Distribution of explosives detonated by the Dutch Royal Navy for 1 year (15 March 2010 to 15 March 2011). b. Estimated unweighted broadband SEL of a single example explosion (263 TNT eq. charge mass) received at a depth of 1m above the sea floor. See Benda-Beckmann et al. (2016), Sertlek and Ainslie (2014) and Sertlek et al. (in prep.) for more details.

Spatiotemporal distribution of harbour porpoises in the DCS

Harbour porpoise distribution over the DCS changed between each survey (Fig. 4, see table S2 for summary of fitted models). In March 2010 (Fig. 4a), the average porpoise density was 1.09 km^{-2} , with the highest density in the central DCS, and the lowest density in the southern DCS. There was no survey effort in the most northern Dogger Bank region, so those density estimates were extrapolated from densities in the adjacent region B. In July 2010 (Fig. 4b), porpoises were present in low numbers, averaging 0.60 km^{-2} . In October/November 2010 (Fig. 4c), overall density was again low (0.63 km^{-2}). In March 2011 (Fig. 4d), the overall density was high again (i.e. 1.34 km^{-2}). The model-based estimates of harbour porpoise numbers on the DCS were 64,851 (March 2010),

35,754 (July 2010), 37,574 (Oct/Nov 2010) and 79,318 (March 2011). These estimates were within the 95% confidence intervals of the original stratified survey estimates of Geelhoed *et al.* (2013).

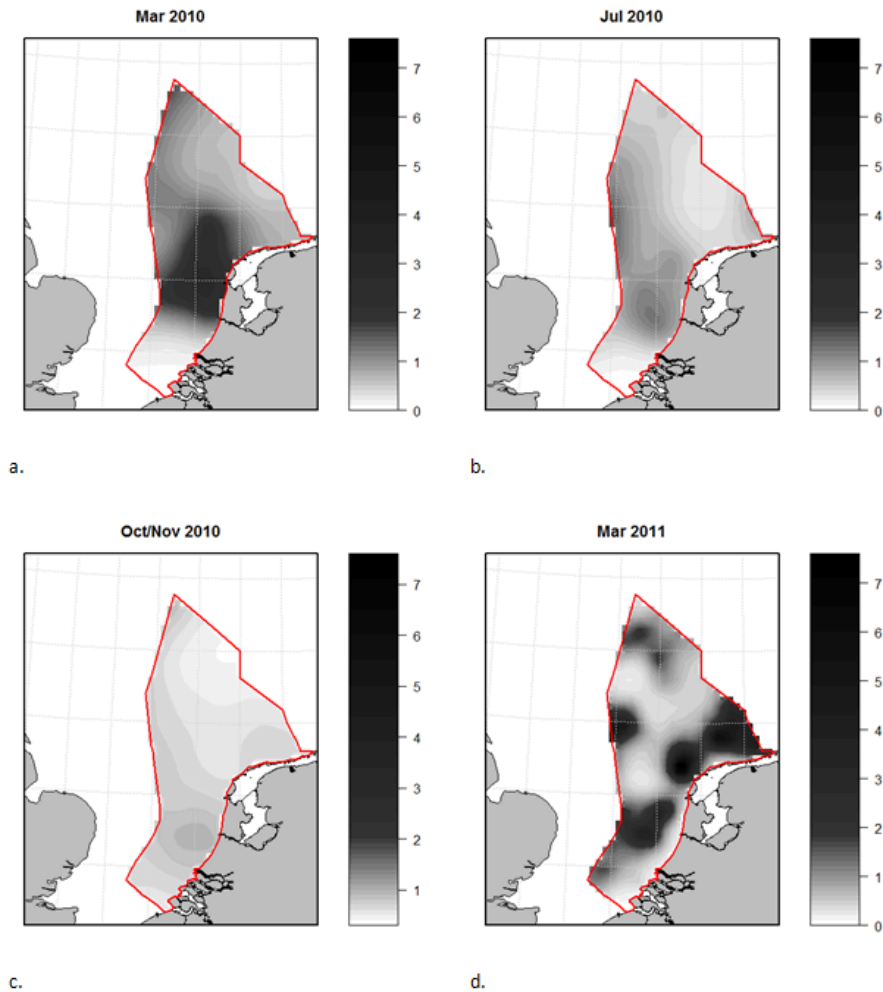


Figure 4. Seasonal model-based estimates of harbour porpoise density (grey scale) within the Dutch Continental Shelf (red polygon) for March (a), July (b) and October-November (c) 2010, and March 2011 (d).

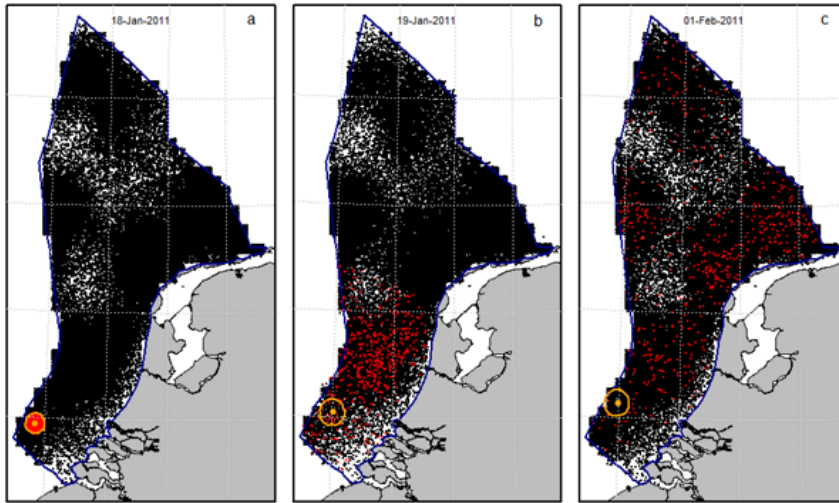
Estimated number of porpoises affected by single explosions

There was considerable variation in the number of harbour porpoises affected by each explosion. These estimates were influenced by the assumed position of harbour porpoises in the water column: if near the sea floor the exposure was approximately 8-times larger compared to near the surface (Table S1, Benda-Beckmann *et al.* 2015). On average, for each single explosion within the DCS during the survey period, 15 porpoises were estimated to be exposed to an SEL of ≥ 190 dB re $1\mu\text{Pa}^2\text{s}$ and hence, assumed to suffer PTS (Table S1). At the lower threshold limit of the range at which PTS becomes increasingly likely (i.e. $\text{SEL} \geq 179$ dB re $1\mu\text{Pa}^2\text{s}$), each explosion resulted in an average of 62 porpoises suffering PTS (Table S1). On average, following each explosion, 319 porpoises were estimated to have been exposed to a SEL of ≥ 164 dB re $1\mu\text{Pa}^2\text{s}$ and, therefore, to have suffered a TTS (Table S1).

Estimated number of porpoises affected by multiple explosions: The effect of movement

The average time between explosions was 3.8 days (median = 0.8, SD = 6.6), during which individuals were often able to redistribute. For the continuous roaming scenario, assuming a maximum average cruising speed of 1.4 m/s (Otani *et al.* 2001), individuals were theoretically capable of travelling 120 km within a single day (i.e. 24 hours). Assuming non-directional, random movement in-between successive explosions, some individuals remained in the proximity of the explosion site of the previous explosion, while others relocated to regions tens of kilometres away. If the time-window between successive explosions was sufficiently large, individuals were capable of relocating to any site within the DCS or even beyond (Fig. 5a-c). In contrast, site-faithful individuals (by definition) remain at their initial fixed location (Fig. 5d-f), and are exposed to successive explosions when the upcoming explosions were in the vicinity.

Free roaming



Site Faithful

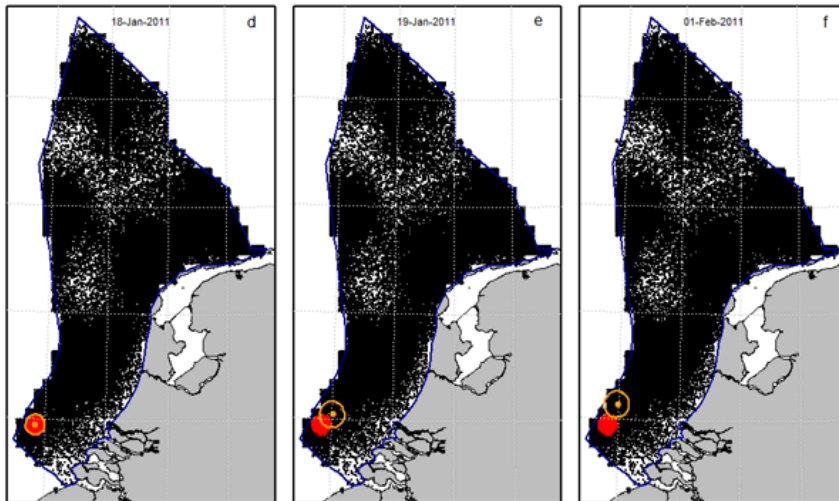


Figure 5. Example showing the effect of movement (a, b, c: free roaming, d, e, f: site-faithful) on repeated exposure probability to successive underwater explosions. The 79,000 black and red points represent all individual porpoises; their distributions are derived from the seasonal density surface estimates. Red points are those individuals exposed to an $SEL \geq 164$ dB re $1\mu Pa^2s$, i.e. received TTS (orange circle), from an explosion on 18 January 2011. Free-roaming individuals were capable of dispersing to other regions. With explosions occurring near to each other, amongst individuals affected by the first explosion, free-roaming individuals had less chance of multiple-exposures than did site-faithful individuals.

For a single year (March 2010 – 2011), there were 1283 estimated PTS events (i.e. PTS very likely, $SEL > 190$ dB re $1\mu Pa^2s$). When porpoises were free roaming throughout the North Sea, 0.5 % of the exposed individuals were exposed at least twice, while for site-faithful individuals it was 6 % (Fig. 6c,d, Table 1).

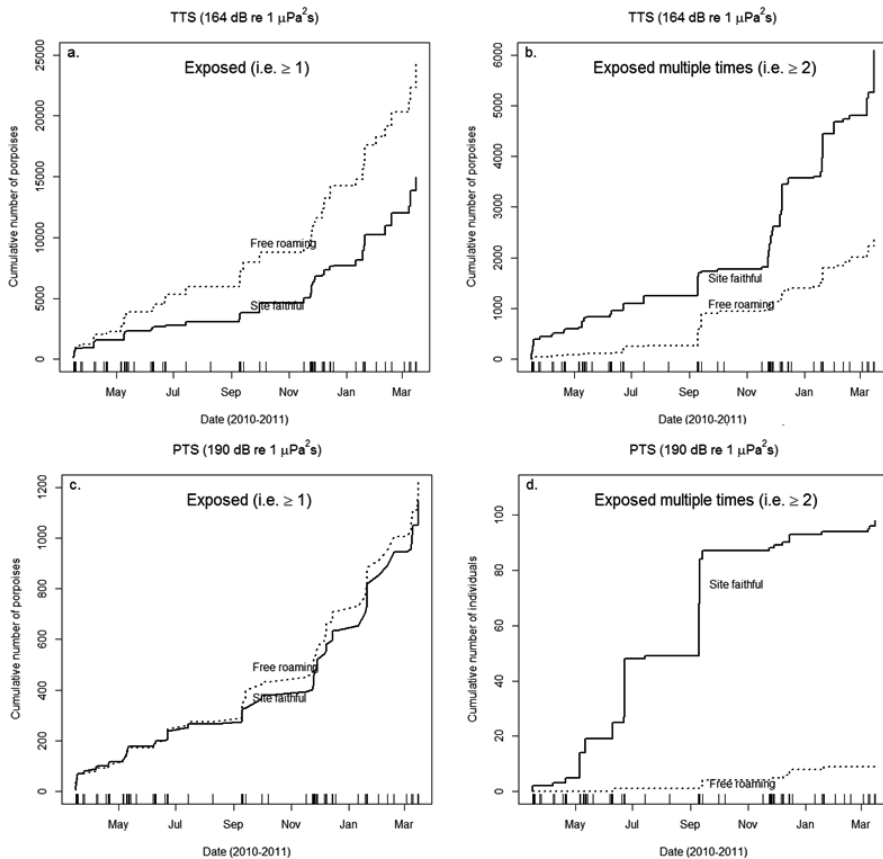


Figure 6. The effect of type of movement (high site-fidelity versus free roaming throughout North Sea) on the number of individuals expected to receive TTS ($SEL \geq 164$ dB re $1\mu Pa^2s$, a, b) or PTS onset very likely ($SEL \geq 190$ dB re $1\mu Pa^2s$, c, d) at least once (a, c) and at least twice (b, d). Free roaming movement will lead to more individuals being exposed to levels exceeding TTS (and PTS) thresholds, but high site fidelity leads to more individuals being exposed multiple times.

On average, 28,067 TTS events were estimated to occur on the DCS during the study period. If porpoises roamed freely within the entire North Sea, an estimated 24,272 unique individuals suffered TTS, and approx. 10 % of these suffered TTS on multiple occasions. In contrast, when individuals were site-faithful, only 14,963 suffered TTS, but doing so on multiple occasions (38%, Table 1 and Fig. 6a,b).

Table 1. The estimated number (and 95% confidence interval between brackets) of harbour porpoises suffering hearing loss due to the cumulative effect of 88 explosive clearances on the Dutch Continental Shelf (DCS) between 15 March 2010 and 15 March 2011. Porpoises were assumed to spend 50% of the time near the surface and 50% near the bottom.

Type	Threshold unweighted SEL [dB re 1µPa²s]	Number of unique porpoises	
		Free roaming	Site-faithful
Blast wave ear trauma 203 <i>Very likely</i>		59 (46-76)	50 (38-66)
Permanent hearing loss 190 <i>very likely</i>		1217 (1151-1287)	1145 (1081-1213)
Permanent hearing loss <i>increasingly likely</i>	179	5204 (5066-5346)	4275 (4152-4401)
TTS <i>very likely</i>	164	24,272 (23,985-24,562)	14,963 (14,748-15,180)

4.1.4 DISCUSSION

Effect of movement on the number of individuals exposed to sound from underwater explosions

This study shows that increased movement speed and dispersal rate increases the accumulative number of individuals within a population that will be exposed to a repetitive anthropogenic sound. However, repeated exposure probability is reduced. This effect is strongest if the sound source remains at a fixed location. Since most marine mammal species, including harbour porpoises, are highly mobile, incorporating the effect of movement is important for estimating impacts at the population-level.

Even for underwater explosions, which may appear unpredictable in space and time, the cumulative number of harbour porpoises exposed depends on how individuals move. We estimate that if all individuals were free-roaming and continuously on the move, in a single year on the DCS 1200 individuals were very likely to receive PTS and 24,000 individuals would receive TTS. In contrast, if harbour porpoises were site-faithful, less individuals would receive PTS or TTS (i.e. 1100 and 15,000, respectively), but more would be exposed on multiple occasions. These numbers are probably underestimated, since only porpoises on the DCS were considered here (given the available survey data), and many individuals outside the DCS might also be exposed. In addition, porpoises residing within the DCS might be affected by detonations outside the DCS, for which no complete data on detonation activities were available.

The effect of movement on the total number of animals experiencing PTS is small, because the PTS effect area is small (relatively to that for TTS), and few explosions occur exactly on the same spot. In contrast, the number of individuals exposed to SELs exceeding the TTS threshold in the free-roaming scenario was 1.6 times higher than in the site-faithful scenario. While movement alters the balance between the number of individuals exposed and the number of repeated exposures, it does not influence the number of impact events, at least assuming individuals do not actively avoid the region where they were previously exposed.

Site-fidelity increases repeated exposure probability: Avoid and redistribute?

The simulation study shows that if the location of the source is at a fixed location, remaining site-faithful increases the risk of being exposed again to following sound exposures. Conversely, if the location of the source is completely unpredictable, any type of movement, including active avoidance, has no effect on numbers exposed and repeated exposure probability. Even though the distribution of underwater explosions may appear unpredictable, this study shows that site-faithful individuals have an increased risk of suffering TTS or PTS on multiple occasions (Fig. 6). Hence, once exposed to underwater explosions, individual porpoises could reduce the risk of future PTS or TTS by avoiding the site of exposure. This suggests that the approximate location of explosions is to some extent predictable. Indeed, in this study explosions were more densely distributed in one region; the southern DCS (Fig. 3). Dense clustering of explosions (or other human sounds) is often likely as they could relate to either the biased distribution of ordnance, or a focus of human activity. For example prior to construction activities (e.g. wind farm development), an area is surveyed for the presence of unexploded ordnances, which are often detonated close in space and time. Such events are apparent in Fig 6, showing a sudden jump in the number of individuals exposed at least twice.

Although not explicitly explored in this study, the porpoise density in the southern DCS (i.e. the region with the highest density of detonations) is on average lower than the rest of the DCS (Fig. 4). This could be caused by natural processes (e.g. food availability) or other anthropogenic activities (e.g. shipping activity near the international harbour of Rotterdam). However, it may also be partly driven by large-scale redistribution resulting from avoidance of underwater explosions. If so, this has direct implications for our results. First, the March 2010 survey took place from 2 – 11 March. Explosions prior to the survey could have already reduced porpoise densities. Hence, the estimated number of exposed individuals might be underestimated for that period. Furthermore, although the possible influence of underwater explosions on porpoise distribution might be partly reflected in the observed porpoise density estimates, the movement simulation ignores direct avoidance and relocation. Avoidance could reduce the number of repeated exposures. However, for PTS the effect of avoidance will be small: Even if porpoises are completely site-faithful, less than 10% are exposed to PTS levels on multiple occasions, and hence relocation will have a minor influence on the total number of PTS events.

Several anthropogenic activities emit repetitive sounds separated by silent periods. During the silent periods, if sufficiently long, acoustically naive marine animals risk entering the area of high risk of auditory (or other physical) damage. This is more likely to occur for highly mobile organisms. Hence, although movement allows organisms to reach other regions with higher survival and reproduction potential, it increases the risk of individuals being exposed to repetitive sound sources.

Whether individuals should avoid an area once exposed to an intense sound source ultimately depends on how well the individual is capable of predicting when and where a new sound will be emitted. Even if the individual would have perfect knowledge of the spatial location and timing the sound event, it is questionable whether avoidance is the best decision. Avoidance may reduce future auditory damage, but it also reduces the time and the amount of habitat available in which to forage or reproduce. Clearly decisions about whether to move and/or avoid certain areas are complex and difficult to predict for species in which high levels of individual variability can be expected, such as for marine mammals.

The importance of movement data for assessing the impact of repetitive sound exposures

Given the importance of movement on the total number of individuals impacted, species distribution models producing a single distribution estimate (see e.g. Fig. 4) might be sufficient for a single event, such as a single explosion, but are insufficient for assessing the impact of longer

lasting human activities, including a series of explosions, seismic surveys, pile driving, and shipping operations. Particularly for highly mobile species, the time spent (or population density) at a specific location can be low. Nevertheless, when the sites are vital for the species' survival and reproduction, over time, the cumulative number of individuals using this site might be high (van Horne 1983). Hence, for longer-lasting disturbing activities (e.g. pile driving or seismic surveys), the cumulative number of individuals impacted might far exceed the instantaneous or average population density. The functional form of this accumulation depends on how individuals move. Such individual movement data is often unavailable for marine mammal species (including harbour porpoises in the southern North Sea). As an alternative, simulations can provide information on the magnitude of the effect of movement on the number of individuals exposed and exposure probability to specific anthropogenic sound sources.

The simulation in this study shows that for PTS, the type of movement has little impact on the estimated number of individuals exposed. In contrast, for more moderate exposure impacts with larger impact areas (e.g. TTS – Fig. 6), the type of movement behaviour has a substantial impact on the number exposed. As the initiation of behavioural response could be triggered at larger distances than the PTS and TTS threshold distances, movement behaviour is likely to have an even greater influence on total numbers impacted than suggested by our results. The availability of actual movement data and observations of responses at larger distances is critical to better understanding the magnitude of impacts from anthropogenic sounds.

Further research

Although the framework presented here illustrates how to make population level estimates, and suggests underwater explosions may impact a substantial part of the North Sea harbour porpoise population (Fig 6, Table 2), a number of improvements in the estimates can be made. First of all, various fundamental biological and especially auditory parameters, such as the level and frequencies at which PTS occurs (von Benda-Beckmann et al. 2015) are missing. Furthermore, although this study provides clues about how different movement regimes influence the total number of unique exposed individuals, there is currently no data on harbour porpoise movement within the southern North Sea. Studies in the Kattegat-Skagerrak suggest that porpoises mix local searching/site fidelity movements with larger scale movements (Nabe-Nielsen et al. 2013). Land- and ship-based surveys in coastal habitats, often reveal large tide-dependent variability in occurrence, which suggests that at least in these habitats, porpoises are not extremely site-faithful (Jones et al. 2014, IJsseldijk et al. 2015). In the North Sea, seasonal differences in coastal sighting rates (Camphuysen 2011) and absolute abundance estimates (Geelhoed *et al.* 2013, and this

study), suggest that long-distance migrations also occur seasonally. Several direct observations provide further detail on the flexibility in movement by harbour porpoises. In one example, an albino porpoise observed in Den Helder on 25 Feb. 2012 at 11:30, was re-sighted near Juist (Germany) on 28 Feb. 15:30, a distance of 187 km travelled in just 76 hours, implying a minimum average speed of 0.70 m/s (Cees Rebel and Kees Camphuysen pers. comm.). In contrast, a female porpoise with calf was observed to remain present near an offshore oil platform for at least 3-weeks (Camphuysen & Krop 2011), indicating a high level of temporal site-fidelity.

In addition to the lack of data on how porpoises move under 'natural' circumstances, it is unknown how porpoises respond to underwater explosions. Harbour porpoises do respond with avoidance behaviour to persistent sound (Dähne et al. 2013, Tougaard et al. 2014). Behavioural reactions to on-off explosions are unknown. They could involve brief startles, or periods of erratic, fast swimming, followed by directional swimming for long periods (minutes to hours – depending on the strength of the sound and previous experience). Although the animals are unlikely to be capable of determining the source direction for such a single, short duration, sound (Kastelein et al. 2007), persistent swimming over several kilometres by exposed harbour porpoises, may still lead to lower densities within the impact areas.

If porpoises in the southern North Sea move large distances on a daily basis and have no spatial knowledge regarding the location of upcoming detonations, impact areas may soon be replenished. Also the study by Thompson *et al.* (2013a) show that after short-term disturbance (by a seismic survey), porpoise density returned to initial values, and it was argued that therefore the activity did not lead to long-term displacement of porpoises. That study, however, was based on passive acoustic monitoring and visual aerial surveys. Without individual movement data, it is not possible to distinguish between a situation where displaced individuals returned, or whether the impacted area was replenished by acoustically naïve individuals. Such individual movement data is vital, particularly for assessing population level consequences of disturbance (PCOD – Rossington *et al.* 2013; King *et al.* 2015) on mobile marine organisms. Movement data reveals whether anthropogenic sound has long-term negative effects on individuals (e.g. reduction of available habitat and increased energetic costs), while observations on population density alone, can be obscured by the behaviour of previously unexposed individuals.

SUPPLEMENTARY MATERIAL

Table S1. The estimated average number of harbour porpoises suffering receiving hearing loss, caused by a single explosive clearance on the Dutch continental shelf (DCS) waters between 15 March 2010 and 15 March 2011. Estimates were made for near the sea surface at 1 m depth, near the bottom (i.e. 1 m above the bottom) and the average of these two. See also Benda-Beckmann et al. (2015) for more details.

Type	Threshold unweighted SEL [dB re 1µPa²s]	Number of porpoises					
		If all Surface	near If all Bottom	near If all and 50% bottom	near 50% bottom	near Surface	near Surface
Blast wave ear trauma 203 <i>Very likely</i>		0	1	1			
Permanent hearing loss <i>very likely</i>	190	2	27	15			
Permanent hearing loss <i>increasingly likely</i>	179	18	106	62			
TTS <i>very likely</i>	164	190	448	319			

Table S2. Summary of models to the four survey seasons: March, July and October-November 2010 and March 2011. The exponent of the fixed effects estimate of the intercept represents the mean density over the entire square study area. Since this also includes the areas on land and outside the DCS, the absolute value has no biological meaning. The overdispersion parameter represents the overdispersion in the residuals. When the estimate is large, this indicates clustering of individual sightings within the 10 x 10 km grid cells. The inverse of the “precision for node” reflects the variance of the latent Gaussian random field. The expected number of effective parameters is a measure of the complexity of the distribution surface. E.g. for the October-November 2010 survey, when the model estimates a relative homogeneous distribution (see Fig. 3c), the effective number of parameters is 3.1.

BIOLOGICAL RELEVANCE OF SOUND MAPS

March 2010

Fixed effects:

	<u>mean</u>	<u>sd</u>	0.025quant	0.5quant	0.975quant	<u>kld</u>
(Intercept)	-0.7973031	0.4607921	-1.792955	-0.7678689	0.04025625	0.003280844

Random effects:

Name	Model	Max KLD
<u>node</u>	<u>Random walk</u>	<u>2D</u>

node Random walk 2D

Model hyperparameters:

	<u>mean</u>	<u>sd</u>	0.025quant	0.5quant	0.975quant
size for the <u>nbino</u> mial observations (<u>overdispersion</u>)	0.6678	0.1330	0.4475	0.6537	0.9675
Precision for node	15.0235	11.9080	3.1429	11.7383	46.4856
Expected number of effective parameters(std dev): 12.47(3.387)					

July 2010

Fixed effects:

	<u>mean</u>	<u>sd</u>	0.025quant	0.5quant	0.975quant	<u>kld</u>
(Intercept)	-1.3294	0.6410484	-2.771558	-1.245625	-0.2874667	0.006136986

Random effects:

Name	Model	Max KLD
<u>node</u>	<u>Random walk</u>	<u>2D</u>

node Random walk 2D

Model hyperparameters:

	<u>mean</u>	<u>sd</u>	0.025quant	0.5quant	0.975quant
size for the <u>nbino</u> mial observations (<u>overdispersion</u>)	0.6179	0.1448	0.3798	0.6024	0.9460
Precision for node	6.0357	6.2653	1.0741	4.1593	22.2915

October-November 2010

Fixed effects:

	<u>mean</u>	<u>sd</u>	0.025quant	0.5quant	0.975quant	<u>kld</u>
(Intercept)	-0.5169351	0.1244001	-0.7647517	-0.5156758	-0.2762939	0.000400913

Random effects:

Name	Model	Max KLD
<u>node</u>	<u>Random walk</u>	<u>2D</u>

node Random walk 2D

Model hyperparameters:

	<u>mean</u>	<u>sd</u>	0.025quant	0.5quant	0.975quant
size for the <u>nbino</u> mial observations (<u>overdispersion</u>)	8.258e-01	2.419e-01	4.654e-01	7.871e-01	1.403e+00
Precision for node	1.854e+04	1.828e+04	1.264e+03	1.315e+04	6.656e+04
Expected number of effective parameters(std dev): 3.069(0.07673)					

Chapter 5 DISCUSSION AND SUMMARY

The aim of this thesis was to investigate the spatial, temporal and spectral distributions of sound that are generated by anthropogenic and natural sources in the Dutch North Sea. The acoustic insights and mathematical tool box that came out should help policy makers, legislators, biologists and conservationists and may serve in ecological monitoring and impact assessments, guide marine research efforts and may be used to determine potential regions or periods of acoustic conflict between human activities and aquatic life. The process by which I achieved this aim is reflected in the nature of the data chapters that address three distinct steps.

First, I explored, developed and combined mathematical models for specific sound sources and for underwater sound propagation dependent on the environmental conditions (Chapter 2). I was not only able to develop a model which enables fast calculations of propagation of sounds over a large frequency band, but also applied the detailed comparisons of the model to several test cases from the Weston Memorial Workshop, held in 2010. Another prominent step taken was to adjust the propagation model for shallow water application where we can use the isovelocity approximation. I was able to show that the isovelocity approximation for shallow water waveguides does not lead to large errors.

Second, I used the mathematical models to integrate measurements from the North Sea about anthropogenic and natural sound sources into a variety of maps and visualizations of sound distribution underwater (Chapter 3). I focussed on three anthropogenic sources (shipping, underwater explosions and seismic surveys) and one natural source (wind). However, in the future, similar sound mapping techniques can be applied to other sound sources such as pile driving, lightning and rain. The mapping and other visualizations were used to reveal the ranking of the selected sources in terms of their annual contribution of acoustic energy. Most of the sound energy (averaged over two years) in the Dutch North Sea was found to come from ships, followed by airguns and explosives for 100 Hz to 100 kHz frequency band, with most energy at frequencies between 100 Hz and 1 kHz for all three anthropogenic sources. However, I also show that some sources are characterized by brief bursts of very high energy and hence that this needs to be taken into account when assessing the biological impact of energy originating from various sources.

The sound mapping of the Dutch North Sea revealed strong geographical signatures for all anthropogenic sources. Shipping lanes formed fixed acoustic traces like highways on land, while seismic surveys and explosions were clustered in space and time, depending on the human

activities of the particular year. Wind was present throughout the Dutch North Sea but the relatively loud high-frequency component was particularly prominent in the northern half due to a combination of higher wind speeds, the absence there of major shipping lanes and the clustering of explosions in the south. As part of this chapter, I also checked and confirmed modelling accuracy with actual sound measurements. The precision of my simulations is inevitably limited by lack of detailed environmental data (time dependent variation of sea surface, seabed properties, sound speed profile etc.), source properties (the number of sources of each type and their geographical distribution, source spectrum and associated source depth), and simplifications in propagation and source models, all of which create uncertainties in the predictions. While I have demonstrated that the effect of the sound speed profile is small, many other uncertainties remain to be quantified, a task that I gratefully leave to a future project.

Third, I participated in a collaborative effort to show the biological relevance of advanced acoustic insights through the integration of acoustic and biological data to assess exposure levels of marine mammals (Chapter 4). Sound exposure levels, locations and event dates of explosions were combined with distribution data and swimming patterns of harbour porpoises to reveal exposure levels at the population level and the impact of animal behaviour on exposure risk at the individual level. The results clearly showed the applied value of sound mapping in combination with biological data and the potential is high for future applications to other marine mammals or fish species. The maps can for example be weighted for species specific swimming depth and hearing range, and thus applied to investigate possible impact on hearing. In order to do this in a meaningful way for fish, the modelling techniques may have to be extended in the future to model particle motion, as all fish are sensitive to particle motion, while just fish with swim bladders have added sensitivity to sound pressure.

In conclusion, the modelling and mapping efforts reported in this thesis reflect both the progress in our understanding of underwater acoustics and the distribution and level of anthropogenic underwater sounds. However, we should not take the brightness in maps for danger or damage. At least not yet at this stage and likely also in many cases not at a later stage. We typically do not know whether artificial elevation of sound levels through noisy human activities really affects aquatic life and whether the effects have detrimental consequences. Aquatic life that may be affected include marine mammals, fish and even invertebrates, which can play a critical role in the food chain or can be important for fisheries (shrimps, lobsters) and the impact may concern masking of critical sounds, distraction, disturbance, deterrence and injury. However, empirical evidence from field studies showing that anthropogenic sound undermines the “Good

DISCUSSION AND SUMMARY

Environmental Status” of a particular waterbody is still rare and often non-existing. I hope the acoustic insights and mathematical toolbox coming out of my thesis will raise awareness of these major gaps in our knowledge and stimulate future studies in order to be able to detect, avoid, and mitigate acoustic conflicts due to spatial and temporal overlap in human and animal activities.

DISCUSSION AND SUMMARY

Dutch Summary

Het doel van deze thesis is te onderzoeken wat de ruimtelijke, temporale en spectrale verdeling is van het onderwater geluid ten gevolge van antropogene en natuurlijke bronnen in het Nederlandse deel van de Noordzee, als onderdeel van een grootschaliger project waarbij in andere deelprojecten gekeken is naar de effecten van geluiden op vissen en zeezoogdieren. De akoestische inzichten en wiskundige tool die uit dit werk zijn voortgekomen kunnen door beleidsmakers, wetgevers, biologen en natuurbeschermers worden gebruikt voor milieu effect rapportages, het sturen van onderzoeksinspanningen en het vinden van potentiële gebieden of periodes waar er een "akoestisch conflict" kan ontstaan tussen menselijk handelen en het dierlijk leven onderwater. De hoofdstukken van dit rapport beschrijven hoe deze inzichten zijn verkrijgen en hoe dit heeft geleid tot de ontwikkelde tool. Er is hierbij een onderscheid gemaakt tussen de volgende drie fases:

In de eerste fase (hoofdstuk 2) heb ik in een literatuur studie een inventarisatie gemaakt van beschikbare modellen voor bronvermogen en geluidsvoortplanting. Ik heb de meest bruikbare modellen gecombineerd om tot een zo optimale oplossing te komen. Deze modellen hangen af van de omgevingsparameters. Naast dat de ontwikkelde modellen zijn geoptimaliseerd met betrekking tot de rekentijd, zijn ze ook numeriek gevalideerd voor een aantal rekenscenario's uit de Weston Memorial Workshop (2010). Tot slot heb aangetoond dat de voor het voortplantingsmodel aangenomen diepte- onafhankelijke geluidssnelheid niet leidt tot grote onnauwkeurigheden voor het Nederlands continentaal plat waar het water ondiep is.

In de tweede fase (hoofdstuk 3) heb ik de ontwikkelde modellen gebruikt om echte data van antropogene en natuurlijke bronnen voor de Noordzee om te zetten in verschillende kaarten en visualisaties die het onderwatergeluid in de Noordzee beschrijven. Ik heb me hierbij gericht op drie antropogene bronnen (Scheepsvaart, onderwaterexplosies, en seismische onderzoeken) en een natuurlijke bron (wind). De ontwikkelde methodiek kan in de toekomst echter ook worden ingezet voor andere geluidsbronnen zoals het heien van heipalen voor windparken, bliksem of regen. De gegenereerde geluidskaarten zijn gebruikt om de bronnen te sorteren op basis van hun totale bijdrage aan de akoestische energie onderwater (gemiddeld over een periode van twee jaar). Het is gebleken dat scheepsvaart de meest dominante bron van energie is (100Hz - 100kHz), gevolgd door seismisch bodem onderzoek (airguns) en daarna door explosies. Voor al deze bronnen bleek

de meeste energie zich te bevinden in de 100Hz tot 1kHz band. Wanneer er wordt gekeken naar de impact van het geluid op het zeeleven is het van belang om ook rekening te houden met de duur van de akoestische blootstelling.

De geluidskaarten onthulden duidelijke ruimtelijke kenmerken voor alle antropogene bronnen. Scheepsvaart routes resulteerden in akoestische paden met verhoogde geluidsniveaus zoals snelwegen op land. Het seismische bodemonderzoek en de explosies kenmerkten zich daarentegen door een meer gefragmenteerde karakteristiek; verbonden aan meer in de ruimte en tijd variabele planning van deze activiteiten. Als deel van dit hoofdstuk heb ik ook de modelnauwkeurigheid gevalideerd met echte metingen.

De nauwkeurigheid van mijn simulaties is gelimiteerd door het ontbreken van gedetailleerde informatie van de omgeving (het beweeglijke zee oppervlakte, de bodem, de geluidssnelheid etc.), bron beschrijving (het aantal bronnen van elk type, hun geografische verspreiding, bron spectrum en equivalente bron diepte) en de onderliggende aannames achter het propagatie model en de bron modellen, allen welke resulteren in onzekerheden in de berekeningen. Hoewel ik heb kunnen aantonen dat het effect van de geluidssnelheid klein is, verdienen de overige onzekerheden nog nader onderzoek, een taak die ik dankbaar achterlaat voor een toekomstig project.

In de derde fase (hoofdstuk 4) heb ik deelgenomen aan een gemeenschappelijke inspanning met als doel om de relevantie van akoestische inzichten aan te tonen. Hierbij zijn de geluidsniveaus, locaties en data van explosies gecorreleerd aan dierverspreiding en zwemgedrag van bruinvissen. Deze resultaten zijn gebruikt om een akoestische blootstelling om te zetten naar een populatie-effect en om het effect te bepalen van de blootstelling op diergedrag. De gevonden resultaten tonen duidelijk de meerwaarde aan van het gebruik van geluidskaarten in combinatie met biologische data. De gebruikte methodiek is ook toe te passen voor andere zoogdieren en vissoorten. De geluidskaarten kunnen ook worden gewogen voor de zwemdiepteverdeling en de gehoorgevoeligheid van dieren om tot een meer "dierspecifieke" akoestische blootstelling te komen. Om tot een realistische effect te komen voor vissen is het waarschijnlijk nodig om ook de deeltjessnelheid te berekenen, omdat alle vissen hiervoor gevoeliger zijn. Enkel vissen met een zwemblaas zijn gevoelig voor de akoestische druk.

Samengevat beschrijven de in deze thesis opgenomen berekeningen en geluidskaarten de huidige kennis over het onderwater geluid en de geluidsbelasting die lijkt plaats te vinden. De felle kleuren in de kaarten dienen echter niet per definitie als gevaarlijk te worden geïnterpreteerd. In ieder geval nog niet, en naar waarschijnlijkheid ook niet in een later stadium. Het is nog onbekend of de

door menselijke activiteit toegenomen onderwater geluid niveaus leiden tot schadelijke effecten op het zeeleven. Diersoorten in de zee die eventueel beïnvloed kunnen worden door het geluid zijn zoogdieren, vissen en zelfs ongewervelden, welke een kritische rol kunnen spelen in de voedselketen of voor de visserij (garnalen en kreeften). De impact kan gaan om het maskeren van belangrijke geluiden, afleiding, verstoring, weggagen en zelf gehoorschade. Echter. empirisch bewijs dat aantoont dat antropogeen geluid het leven onderwater beïnvloedt ("Good Environmental Status") is zeldzaam of niet beschikbaar. Ik hoop dat dit werk en de beschikbaar gemaakte tools helpen om bewustwording te creëren voor deze ontbrekende kennis, en dat mijn werk helpt om akoestische verstoring van het leven onderwater te detecteren, voorkomen of te mitigeren.

References

A

- [1] A Marine Strategy Directive to save Europe's seas and oceans, http://ec.europa.eu/environment/water/marine/index_en.htm, last accessed 03/11/2010.
- [2] Aarts G. et al, (2012), Comparative interpretation of count, presence-absence and point methods for species distribution models. *Methods in Ecology and Evolution*, 3, 177–187.
- [3] Aarts G. et al. (submitted on 23-11-2015), Movement behaviour influences population level exposure to underwater sound: Impact of explosions on harbor porpoises, *Journal of Animal Ecology*.
- [4] Abramowitz M. and Stegun I., (1972), *Handbook of Mathematical Functions with Formulas, Graphs, and Mathematical Tables*, New York: Dover Publications.
- [5] Ainslie, M. A. , (2005). "Effect of wind-generated bubbles on fixed range acoustic attenuation in shallow water at 1–4kHz". *J. Acoust. Soc. Am.* , 118(6), 3513-3523.
- [6] Ainslie, M. A. et al, (2009). "Assessment of natural and anthropogenic sound sources and acoustic propagation in the North Sea." TNO report TNO-DV, C085.
- [7] Ainslie M.A., (2010a), *Principles of Sonar Performance Modeling*, Praxis Publishing, Chichester, UK.
- [8] Ainslie M.A., (2010b), Editorial: Validation of Sonar Performance Assessment Tools, in *Validation of Sonar Performance Assessment Tools (workshop held in memory of D. E. Weston, 7-9 April 2010)*, *Proceedings of the IOA*, Vol.32, Pt.2, pp.1-8.
- [9] Ainslie et al, (2011), An analytical solution for signal, background and signal to background ratio for a low frequency active sonar in a Pekeris waveguide satisfying Lambert's rule, *Proc. 4th International Conf. and Exhibition on Underwater Acoustic Measurements: Technologies and Results*, pp 491-498.
- [10] Ainslie M. A., (2011), Ad hoc European working group on terminology for underwater sound, "Standard for measurement and monitoring of underwater noise, Part I: Physical Quantities and

References

- Their Units”, TNO Report, TNO-DV 2011 C235,.Ainslie M.A. et al, (2012a), “What is the Source Level of Pile-Driving Noise in Water?”, The Effects of Noise on Aquatic Life, pp.445-448, Springer Media.
- [11] Ainslie, M.A. et al, (2012b), Dredger noise during Maasvlakte 2 construction: Noise maps and risk assessment, TNO report 2012 R10818
- [12] Ainslie M.A. et al, (2013), Echo, reverberation and echo to reverberation ratio for isovelocity waveguides related to Weston Memorial workshop Scenarios A2.I AND A2.IV.
- [13] Ainslie M.A. et al, (2014), Practical spreading laws: the snakes and ladders of shallow water acoustics, Proceedings 2nd International Conference and Exhibition on Underwater Acoustics, UA2014, 22-27 June, Rhodes, Greece, 879-886.
- [14] Ainslie M.A., Ellis D.D. and Harrison C.H., (2015), Low frequency bottom reverberation in a Pekeris waveguide with Lambert’s rule, Journal of Computational Acoustics, Vol. 23, 1550022
- [15] Akamatsu t. et al, (2005). New stereo acoustic data logger for free-ranging dolphins and porpoises. Marine Technology Society Journal, 38, 6-12.
- [16] Anon et al, 2014, “Draft joint workshop report: predicting sound fields; global soundscape modelling to inform management of cetaceans and anthropogenic noise”. Available from: “<https://events.iwc.int/index.php/scientific/SC65B/paper/viewFile/802/870/SC-65b-Rep03rev.pdf>”
- [17] APL-UW, (1994), APL-UW high-frequency ocean environmental acoustic models handbook(APL-UW TR 9407, AEAS 9501 October), Applied physics Laboratory, University of Washington, Seattle, WA
- [18] [AQUO], Information on the “Achieve quieter oceans by shipping noise footprint reduction (AQUO)” European project can be found on: <http://www.aquo.eu/>
- [19] [Aquo-Sonic (Madrid)], Meeting report in preparation.
- [20] Arveson P. T. and Vendittis D. J. , (2000). “Radiated noise characteristics of a modern cargo ship”. J. Acoust. Soc. Am. , 107(1), 118-129

B

- [21] Bailey H. et al, (2010), Assessing underwater noise levels during pile-driving at an offshore

References

- wind farm and its potential effects on marine mammals”, *Mar. Pol. Bul.* ,60 (6), p.888-897.
- [22] Bailey H. et al, (2014) Modelling harbour seal habitat by combining data from multiple tracking systems. *Journal of Experimental Marine Biology and Ecology*, 450, 30–39.
- [23] Borja A. et al, (2010) Marine management – Towards an integrated implementation of the European Marine Strategy Framework and the Water Framework Directives. *Mar Poll Bull* 60:2175–2186.
- [24] Borsani J.F., (2014), Impacts of noise and use of propagation models to predict the recipient side of noise, Cefas project report C6082
- [25] Buckland, S.T. et al, (2004) *Advanced Distance Sampling*. Oxford University press, New York.
- [26] Bouton N. et al, (2015), Hearing and water column use in the North Sea fishes: a review to serve exploration of variation in exposure to vessel sounds among species and species group, Sonic project report (draft), (<http://www.sonic-project.eu/>)

C

- [27] Camphuysen C. J. and Siemensma M. L., (2011). Conservation plan for the Harbour Porpoise *Phocoena phocoena* in The Netherlands: towards a favourable conservation status. (NIOZ Report 2011-07), Royal Netherlands Institute for Sea Research, Texel.
- [28] Camphuysen C. J. (2011). Recent trends and spatial patterns in near-shore sightings of harbour porpoises (*Phocoena phocoena*) in the Netherlands (Southern Bight, North Sea), 1990-2010. *Lutra*, 54, 39–47.
- [29] Camphuysen C.J. and Krop A., (2011), Maternal care, calf-training and site fidelity in a wild harbour porpoise in the North Sea. *Lutra*, 54, 123–126.
- [30] [Cet sound], Cet sound workshop report available from : <http://cetsound.noaa.gov/report.html>
- [31] Chapman N. R. (1985), Measurement of the waveform parameters of shallow explosive charges. *J. Acoust. Soc. Am.*, 78, 672–681.
- [32] Clausen, K. T. et al , (2010), Click Communication In Harbour Porpoises *Phocoena Phocoena*. *The International Journal Of Animal Sound And Its Recording*, 20, 1–28.

References

- [33] Cole R. H., (1965). Underwater explosions. [Originally published in 1948 by Princeton University Press] (Dover, New York).
- [34] Collins M. D. and Evans R. B., (1992), A two-way parabolic equation for acoustic backscattering in the ocean, J. Acoust. Soc. Am. 91 ,1357–1368.
- [35] Collins M. D., (1999), RAM user guide, <http://ram.nrl.navy.mil/>
- [36] Collins M. D., (1993), A Split-Step Pade Solution for the Parabolic Equation Method, J. Acoust. Soc. Am. 93, 1736-1742,
- [37] Commission Decision No. 2010/477/EU on criteria and methodological standards on good environmental status of marine waters, (2010), O. J. L 232/14.
- [38] Culik B. et al, (2001). Reactions of harbor porpoises *Phocoena phocoena* and herring *Clupea harengus* to acoustic alarms. Mar. Ecol. Prog. Ser. 211, 255-260.

D

- [39] Dähne M. et al , (2013), Effects of pile-driving on harbour porpoises (*Phocoena phocoena*) at the first offshore wind farm in Germany, Environmental Research Letters, 8, 025002.
- [40] Daly JN and Harrison J., (2012),The Marine Mammal Protection Act: a regulatory approach to identifying and minimizing acoustic-related impacts on marine mammals, Adv. Exp. Med Biol. 730:537-9,
- [41] Danil K. and St. Leger J. A. , (2011). Seabird and dolphin mortality associated with underwater detonation exercises. Marine Technology Society Journal, 6, 89-95.
- [42] de Jong C.A.F. et al , (2010), “Underwater noise of Trailing Suction Hopper Dredgers at Maasvlakte 2: Analysis of source levels and background Noise”. TNO-DV report 2010 C335.
- [43] Denham R.N., Intensity decay laws for near-surface sound sources in the ocean, J. Acoust. Soc. Am. 79, 60 (1986)
- [44] Dekeling et al, (2014a), Monitoring Guidance for Underwater Noise in European Seas, Part I: Executive Summary, J.V. JRC Scientific and Policy Report EUR 26557 EN, Publications Office of the European Union, Luxembourg, (<http://publications.jrc.ec.europa.eu/repository/handle/111111111/30979>)

References

- [45] Dekeling et al, (2014b), Monitoring Guidance for Underwater Noise in European Seas, Part II: Monitoring Guidance Specifications, JRC Scientific and Policy Report EUR 26555 EN, Publications Office of the European Union, Luxembourg, <http://publications.jrc.ec.europa.eu/repository/handle/111111111/30973>)
- [46] Directive 2008/56/EC of the European Parliament and of the Council of 17 June 2008 establishing a framework for community action in the field of marine environmental policy (marine strategy framework directive), (2015), (<http://eur-lex.europa.eu/legal-content/en/txt/?uri=celex:32008l0056>”, accessed 18 september 2015).
- [47] Duren R E, 1988, A theory for marine source arrays, *Geophysics* 53 650–8
- [48] Dreschler J. et al ,(2009), “Measurements of underwater background noise Maasvlakte 2”, TNO-DV 2009 C212
- [49] Dragoset B., “Introduction to Air Guns and Air-Gun Arrays,” *The Leading Edge*, pp.892-897, (August 2000)

E

- [50] [EC, 2010] Commission Decision No. 2010/477/EU on criteria and methodological standards on good environmental status of marine waters, 2010 O. J. L 232/14.
- [51] Ellison, W. T. et al, (2012). A New Context-Based Approach to Assess Marine Mammal Behavioral Responses to Anthropogenic Sounds. *Conservation Biology*, 1, 21-28.
- [52] Endangered Species Act of 1973, “<http://www.fws.gov/laws/lawsdigest/ESACT.html>”, last accessed 25 April 2012.
- [53] Emodnet, 2014, public Bathymetry database available online at: <http://www.emodnet-hydrography.eu/>)
- [54] Erbe, C. and King, A. (2009), Modeling cumulative sound exposure around marine seismic surveys, *J. Acoust. Soc. Am.* ,125 (4): pp. 2443-2451.
- [55] Erbe C. et al, (2012), Mapping cumulative noise from shipping to inform marine spatial planning. , *J. Acoust. Soc. Am.* , 132 (5): pp. 432-428.
- [56] Erbe C. et al, (2014), Identifying Modeled Ship Noise Hotspots for Marine Mammals of Canada’s Pacific Region. *PLoS ONE*. 9 (3): e89820 .

References

[57] Etopo, 2014, public Bathymetry database available online:<http://www.ngdc.noaa.gov/mgg/global/global.html>

[58] Evans R.B., (1983), A coupled mode solution for acoustic propagation in a waveguide with stepwise depth variations of a penetrable bottom," J. Acoust. Soc. Am. 74, 188-195.

F

[59] Fay, R. R. (2009), Soundscapes and the sense of hearing of fishes. Integr. Zool. 4,26–32.

[60] Finneran J. J. and Schlundt C. E., (2011). Subjective loudness level measurements and equal loudness contours in a bottlenose dolphin (*Tursiops truncatus*). J. Acoust. Soc. Am., 130(5), 3124-3136.

[61] Finneran, J. J. and Jenkins A. K. ,(2012). Criteria and thresholds for U.S. Navy acoustic and 51 explosive effects analysis, San Diego, California: SPAWAR Systems Center Pacific, April 2012, pp. 64.

[62] Finneran J. J. and Schlundt C. E. (2013). Effects of fatiguing tone frequency on temporary threshold shift in bottlenose dolphins (*Tursiops truncatus*). J. Acoust. Soc. Am. , 133(3), 1819-1826.

[63] Fisher, F. H., and Simmons, V. P. (1977), Sound absorption in seawater. J. Acoust. Soc. Am. , 62(3): 558–564.

[64] Fisheries Hydroacoustic Working Group (FHWG),"Agreement in Principle for Interim Criteria for Injury to Fish from Pile Driving Activities",12 June 2008 (Vancouver, Canada, 2008), http://www.dot.ca.gov/hq/env/bio/fisheries_bioacoustics.htm, last accessed 22 April 2012.

[65] Fletcher H. and Munson W. A. ,(1933). Loudness, its definition, measurement and calculation. J. Acoust. Soc. Am. 5, 82-108. 10.1121/1.1915637.

[66] Folegot T, (2012), Ship traffic noise distribution in the Strait of Gibraltar: an exemplary case for monitoring global ocean noise using real-time technology now available for understanding the effects of noise on marine life, Adv Exp Med Biol. 2012;730:601-4.

G

[67] Gauss, R. C. et al, (2002). Broadband models for predicting bistatic bottom, surface, and

References

volume scattering strengths (No. NRL/FR/7100--02-10). NAVAL RESEARCH LAB WASHINGTON DC.

[68] Gebco(+), 2014, public Bathymetry database available online at: <http://www.gebco.net/>

[69] Geelhoed S. et al, (2012). Shortlist Masterplan Wind Aerial surveys of harbour porpoises on the Dutch Continental Shelf (IMARES Report number C103/11). Den Burg, Texel.

[70] Geelhoed, S.C.V. et al, (2013) Abundance of harbour porpoises (*Phocoena phocoena*) on the Dutch Continental Shelf, aerial surveys in July 2010-March 2011. *Lutra*, 56, 45–57.

[71] Geological Survey of the Netherlands , DINO database, (<http://www.geologicalsurvey.nl>)

[72] Gray L. M., and Greeley D. S. , (1980), Source level model for propeller blade rate radiation for the world's merchant fleet, *J. Acoust. Soc. Am.* , 67(2), 516-522.

[73] Groot-Hedlin C., (2004), Criteria for discretization of seafloor bathymetry when using a staircase approximation: application to computation of T-phase seismograms, *J. Acoust. Soc. Am.*, 115 (3), 1103-1113.

H

[74] Haelters J, Dulière V, Vigin L, Degraer S (2015) Towards a numerical model to simulate the observed displacement of harbour porpoises *Phocoena phocoena* due to pile driving in Belgian waters. *Hydrobiologia* 756:105–116

[75] Hall V.H, (2015), An analytical model for the underwater sound pressure waveforms radiated when an offshore pile is driven, *J. Acoust. Soc. Am.* , 138 (2): pp. 795-806.

[76] Hammond P.S. et al, (2013) Cetacean abundance and distribution in European Atlantic shelf waters to inform conservation and management. *Biological Conservation*, 164, 107–122.

[77] Hansen M. et al, (2008). Low-frequency components in harbour porpoise (*Phocoena phocoena*) clicks: communication signal, by-product, or artifacts? *J. Acoust. Soc. Am.* 124, 4059–4068.

[78] Harrison C.H., (2005), Closed form bistatic reverberation and target echoes with variable bathymetry and sound speed, *IEEE J. Oceanic Eng.* 30, 660–675.

[79] Harrison C.H. and Nielsen P.L. , (2007), "Multipath pulse shapes in shallow water: Theory and simulation", *J. Acoust. Soc. Am.*, 121 (3), p.1362-1373

References

- [80] Harrison C. H. and Ainslie M. A. ,(2010), Fixed time versus fixed range reverberation calculation: Analytical solution, *J. Acoust. Soc. Am.* 128,28–38
- [81] Harrison C.H. , (2010), An approximate form of the Rayleigh reflection loss and its phase: application to reverberation calculation. *J Acoust Soc Am.*, 128(1), 50-7
- [82] Harrison, C. H. ,(2013). Ray convergence in a flux-like propagation formulation. *J. Acoust. Soc. Am.* , 133(6), 3777-3789.
- [83] Harwood J. et al, (2013). A protocol for implementing the interim population consequences of disturbance (PCOD) approach: quantifying and assessing the effects of UK offshore renewable energy developments on marine mammal populations (report SMRUL-TCE-2013-014 Scottish Marine and Freshwater Science 5(2)).
- [84] Hatch LT and Fristrup KM, (2009), No barrier at the boundaries: implementing regional frameworks for noise management in protected natural areas, *Marine Ecology Progress Series* 395, 223-244
- [85] Heaney K. D. and Campbell R. L., (2015), Three-dimensional parabolic equation modelling of mesoscale eddy deflection, *J. Acoust. Soc. Am.*, submitted August 11 2015.
- [86] Heinis F. et al, (2013), “Monitoring programme for the Maasvlakte 2, part III—the effects of underwater sound”
- [87] Hiby L. and Lovell P. (1998) Using Aircraft in Tandem Formation to Estimate Abundance of Harbour Porpoise. *Biometrics*, 54, 1280–1289.
- [88] Hildebrand J.A., (2009), Anthropogenic and natural sources of ambient noise in the ocean”, *Mar. Ecol. Prog. Ser.*, 395: p.5–20.
- [89] Holland C. W., (2010), Propagation in a waveguide with range dependent seabed properties, *J. Acoust. Soc. Am.* 128 (5), 2596-2607.
- [90] Horne B van (1983) Density as a Misleading Indicator of Habitat Quality. *J Wildl Manage* 47:893–901
- [91] Huijbers CM et al, (2008) Shallow patch reefs as alternative habitats for early juveniles of some mangrove/seagrass-associated fish species in Bermuda. *Revista de Biologia Tropical* 56 (Suppl. 1): 161-169

I

- [92] IEC 1995 (EN 61260), Electroacoustics - Octave-band and fractional-octave-band filters, International Electrotechnical Commission, Geneva, Switzerland, 1996.
- [93] IEC 60050:1994, International Electrotechnical Vocabulary, part 801: Acoustics and Electroacoustics, (section 801-32 covers terms for underwater acoustics), International Electrotechnical Commission (IEC), Geneva.
- [94] IEC60565: 2006 Underwater acoustics-Hydrophones - Calibration in the frequency range 0.01 Hz to 1 MHz, IEC 60565 - 2006 (EN 60565: 2007, BS60565:2007), International Electrotechnical Commission, Geneva, 2006
- [95] IJsseldijk L.L. et al, (2015) Going with the flow: tidal influence on the occurrence of the harbour porpoise (*Phocoena phocoena*) in the Marsdiep area, The Netherlands. *Journal of Sea Research*, 103,129–137.
- [96] ISO/DIS 18405,Underwater acoustics terminology, International Organization for Standardization, Geneva, Switzerland
- [97] ISO/CD 18405 Underwater acoustics terminology, International Organization for Standardization, Geneva, Switzerland
- [98] [ISO - GUM], JCGM 100 series, Guides to the expression of uncertainty in measurement (GUM series). Available from: <http://www.iso.org/sites/JCGM/GUM-introduction.htm>
- [99] ISO 266:1997, Acoustics - Preferred frequencies (1997)
- [100] ISO 80000-8:2007, Quantities and units – part 8: Acoustics, International Organization for Standardisation (ISO), Geneva.

J

- [101] Jackson, D. R. (1994). APL-UW high-frequency ocean environmental acoustic models handbook, Applied Physics Laboratory, University of Washington, Technical Report, 9407.
- [102] Jensen F.B. and Ferla C.M.,(1990), Numerical solutions of range-dependent benchmark problems in ocean acoustics, *J. Acoust. Soc. Am*, 87 (4) , 1499-1510.
- [103] Jensen F.B. et al. ,(1994), *Computational Ocean Acoustics*, American Institute of Physics, New

References

York

[104] Jackson D.R., (1994). "APL-UW high-frequency ocean environmental acoustic models handbook". Applied Physics Laboratory, University of Washington, Technical Report, 9407.

[105] Jones AR et al, (2014) Fine-scale hydrodynamics influence the spatio-temporal distribution of harbour porpoises at a coastal hotspot. *Prog Oceanogr* 128:30–48

K

[106] Kastelein, R.A. (1997) Food Consumption and Growth of Marine Mammals. Landbouwniversiteit Wageningen, the Netherlands.

[107] Kastelein, R. A. et al, (2002). Audiogram of a harbor porpoise (*Phocoena phocoena*) measured with narrow-band frequency-modulated signals. *J. Acoust. Soc. Am.* , 112, 334-344.

[108] Kastelein, R.A. et al , (2007) The influence of signal parameters on the sound source localization ability of a harbor porpoise (*Phocoena phocoena*). *J. Acoust. Soc. Am.* , 122, 1238–1248.

[109] Kastelein, R. A. et al, (2012a). Temporary threshold shifts and recovery in a harbor porpoise (*Phocoena phocoena*) after octave-band noise at 4 kHz . *J. Acoust. Soc. Am.* 132 , 3525.

[110] Kastelein, R. A. et al, (2012b). The hearing threshold of a harbor porpoise (*Phocoena phocoena*) for impulsive sounds (L). *J. Acoust. Soc. Am.* , 132 (2), 607-610.

[111] Kastelein, R. A. et al, (2013). Hearing frequency thresholds of a harbour porpoise (*Phocoena phocoena*) temporarily affected by a continuous 1.5 kHz tone. *J. Acoust. Soc. Am.* , 134, 2286-2292.

[112] Kastelein, R. A. et al, (2014a). Effect of level, duration, and inter-pulse interval of 1-2 kHz sonar signal exposures on harbour porpoise hearing. *J. Acoust. Soc. Am.* , 136, 412-422.

[113] Kastelein, R. A. et al, (2014b). Frequency of greatest temporary hearing threshold shift in harbor porpoises (*Phocoena phocoena*) depends on the noise level. *J. Acoust. Soc. Am.* , 136, 1410-1418.

[114] Kastelein, R. A. et al, (2015a) Hearing frequencies of a harbor porpoise (*Phocoena phocoena*) temporarily affected by played back offshore pile-driving sounds. *J. Acoust. Soc. Am.* , 137, 556.

[115] Kastelein, R. A. et al, (2015b). Effects of exposure to intermittent and continuous 6–7 kHz sonar sweeps on harbor porpoise (*Phocoena phocoena*) hearing. *J. Acoust. Soc. Am.* , 137 (4),

References

1623–1633.

[116] Ketten D. R. et al, (1993). Blast injury in humpback whale ears: Evidence and implications. *J. Acoust. Soc. Am.* , 94(3/2), 1849-1850.

[117] Ketten D. R. (2004). Experimental Measures of Blast and Acoustic Trauma in Marine Mammals. (ONR Final Report: N000149711030).

[118] Ketten D. R. (2012). Marine Mammal Auditory System Noise Impacts: Evidence and Incidence. In A. N. Popper & A. Hawkins (Eds.) *The Effects of Noise on Aquatic Life*. New York: Springer.

[119] King, S.L. et al (2015) An interim framework for assessing the population consequences of disturbance (ed C Kurle). *Methods in Ecology and Evolution*, 6, n/a–n/a.

[120] Kornhauser E.T. and Raney W.P.,(1955) Attenuation in shallow-water propagation due to an absorbing bottom, *J. Acoust. Soc. Am*, 27(4), 689-692.

[121] Koschinski S. and Koch K. H., (2009), Underwater Unexploded Ordnance – Methods for a Cetacean-friendly Removal of Explosives as Alternatives to Blasting, IWC, Scientific Committee Paper SC/61 E:1-13.

[122] Koschinski S. (2011). Underwater noise pollution from munitions clearance and disposal, possible effects on marine vertebrates, and its mitigation. *Marine Technology Society Journal*, 45, 80-88.

[123] Kryter K. D. et al, (1966). Hazardous exposure to intermittent and steady state noise. *J. Acoust. Soc. Am.* , 39, 451-464.

[124] Kryter K. D., (1994). *The handbook of hearing and the effects of noise*. New York: Academic Press. 673

[125] Kujiwa S. G., and Liberman M. C. (2009). Adding insult to injury: cochlear nerve degeneration after “temporary” noise-induced hearing loss. *J. Neurosci.* 20, 14077-14085.

[126] Kuperman W.A. and Ferla M.C., (1985) ,A shallow water experiment to determine the source spectrum level of wind-generated noise, *J. Acoust. Soc. Am.* ,77: pp. 2067-2073.

[127] KNMI, The Royal Netherlands Meteorological Institute (KNMI) Databases <http://www.knmi.nl>

L

References

- [128] Laws R.M. et al.,1990,Computer modeling of clustered air guns: First Break, 18(9), 331–338
- [129] Lewis, J. A. (1996). Effects of underwater explosions on life in the sea. Melbourne, Victoria: Dept. of Defence, Defence Science and Technology Organisation, 38 pp.
- [130] Li Guo-Fa et al,2010, Modeling air gun signatures in marine seismic exploration considering multiple physical factors, Applied Geophysics, Vol.7, No.2 , P. 158 – 165
- [131] Lippert et al,2015, COMPILE - A Generic Benchmark Case for Predictions of Marine Pile Driving Noise", accepted for publication by IEEE J Oceanic Eng, December 2015.
- [132] Lucke K. et al (2009). Temporary shift in masked hearing thresholds in a harbor porpoise (*Phocoena phocoena*) after exposure to seismic airgun stimuli. J. Acoust. Soc. Am. , 125 (6), 4060-4070.
- [133] Lucke et al, (2014), Report of the Workshop on International Harmonisation of Approaches to Define Underwater Noise Exposure Criteria (Budapest, Hungary 17th August 2013)
- [134] Lurton, X. (2002). An introduction to underwater acoustics: principles and applications. springer.
- [135] Lusseau D. et al (2012). Assessing the risks to marine mammal populations from renewable energy devices – an interim approach. Final Workshop report, 29 pp.

M

- [136] [Maasvlakte 2, 2014], Website on the extension of the Rotterdam port <https://www.maasvlakte2.com/en/index/>
- [137] MacGillivray A.O., (2006), An acoustic study of seismic airgun noise in Queen Charlotte Basin, MSc Thesis.
- [138] MacGillivray A.O. and Chapman N.R., (2012), Modeling Underwater Sound propagation from an airgun array using the parabolic equation method, Canadian Acoustics, Vol.40, No.1, 19-25 .
- [139] Macpherson and Daintith, (1967) Practical model of shallow-water acoustic propagation, J. Acoust. Soc. Am., 41(4), 850-854.
- [140] Madsen, P. A, (2005). Marine mammals and noise: Problems with root mean square sound pressure levels for transients. J. Acoust. Soc. Am. , 117(6), 3952–3957.

References

- [141] Marine Mammal Protection Act (MMPA) of 1972, "<http://www.nmfs.noaa.gov/pr/laws/mmpa/>", last accessed 25 April 2012.
- [142] Malme C.I. et al, (1983), Investigations of the potential effects of underwater noise from petroleum industry activities on migrating gray whale behaviour. Bolt Beranek & Newman Report Number 5366, Cambridge, Massachusetts, Bolt Beranek and Newman Inc.
- [143] McCarthy E. et al, (2011) Changes in spatial and temporal distribution and vocal behavior of Blainville's beaked whales (*Mesoplodon densirostris*) during multiship exercises with mid-frequency sonar. *Marine Mammal Science*, 27, E206–E226.
- [144] Mennitt D. et al, (2014), A geospatial model of ambient sound pressure levels in the contiguous United States, *J. Acoust. Soc. Am.* 135 (5), 2746–2764
- [145] Møhl B and Andersen S. , (1973). Echolocation: high-frequency component in click of harbor porpoise (*Phocoena-Ph. L.*). *J. Acoust. Soc. Am.* 54, 1368–1372.
- [146] Mobley Curtis D., (1994), *Light and Water: Radiative Transfer in Natural Waters*, Academic Press; 0125027508
- [147] Montgomery et al. 2006; Sound as an orientation cue for the pelagic larvae of reef fishes and decapod crustaceans. *Adv. Mar. Biol.* 2006;51:143–96.
- [148] McLennan DA (2003), The importance of olfactory signals in the gasterosteid mating system: sticklebacks go multimodal, *Biol J Linnean Soc*, 80:555–572.
- [149] Myrberg AA Jr, Fuiman LA. 2002. The sensory world of reef fishes. *Coral reef fishes*. New York: Elsevier Science. p 123–160.

N

- [150] Nabe-Nielsen, J. et al, (2013) How a simple adaptive foraging strategy can lead to emergent home ranges and increased food intake. *Oikos*, 122, 1307–1316.
- [151] Nabe-Nielsen, J. et al, (2014). Effects of noise and by-catch on a Danish harbour porpoise population. *Ecological Modelling*, 272, 242–251
- [152] National Research Council, (2003), *Ocean noise and marine mammals*, Ocean Study Board,

References

Washington, DC: The National Academies Press.

[153] New, L. et al, (2014), Using short-term measures of behaviour to estimate long-term fitness of southern elephant seals. *Marine Ecology Progress Series*, 496, 99–108.

[154] Nowacek, D.P. et al, (2007), Responses of cetaceans to anthropogenic noise, *Mammal Review*, 37, 81-115.

[155] [NPL GPG 133 2014], Good Practice Guide for Underwater Noise Measurement, National Measurement Office, Marine Scotland, The Crown Estate, Robinson, S.P., Lepper, P. A. and Hazelwood, R.A., NPL Good Practice Guide No. 133, 2014.

[156] Nützel, B. (2008). Untersuchungen zum Schutz von Schweinswalen vor Schockwellen. (Forschungsanstalt der Bundeswehr für Wasserschall und geophysik (FWG), Technischer Bericht TB 2008-7).

O

[157] Ocean Acoustic Library (OALIB), (2013), <http://oalib.hlsresearch.com>, last accessed 31 March 2013

[158] Olbers H.W.M., 1826, Ueber die Durchsichtigkeit des Weltraums in Bode's Jahrbuch für 1826, pp. 110–121.

[159] OSPAR Commission (2010). Quality status report, Assessment of the impact of dumped conventional and chemical munitions. OSPAR Commission, London, U.K.

[160] Otani, S. et al, (2001) Oxygen consumption and swim speed of the harbor porpoise *Phocoena phocoena*. *Fisheries Science*, 67, 894–898.

P

[161] Parks SE et al, (2005), The gunshot sound produced by male north Atlantic right whales (*Eubalaena glacialis*) and its potential function in reproductive advertisement", *Marine Mammal Science* 21, 458-475

[162] Pfeiffer, F. (2014). Changes in Properties of Explosives Due to Prolonged Seawater Exposure.

References

Marine Technology Society Journal, 102-110.

[163] Poppe P. M. and Wijers C. M. J., ACM, (1990), Transactions on Mathematical Software 16, 38-46,

[164] Popper, A. N., and Hastings, M. C. (2009). The effects of anthropogenic sources of sound on fishes. *J. Fish Biol.* 75, 455–489.

[165] Porter M. B., (1990), The KRAKEN Normal Mode Program, SACLANT Undersea Research Centre Tech. Rep., 1990.

[166] Porter M.B., Jensen F.B. and Ferla C.M., (1991), The problem of energy conservation in one-way models, *J. Acoust. Soc. Am.* 89, 1058-1067.

[167] Porter M. B. and Henderson L. J., (2013), Global Ocean Soundscapes, Proceedings of the International Congress on Acoustics 2013, Vol. 19, 010050 (Proceedings of Meetings on Acoustics) Montreal, Canada.

[168] Porter M.B., (2013), Bellhop Manual and User Guide, <http://oalib.hlsresearch.com/Rays/>, last accessed 31.03.2013

[169] Preston J.R. and Ellis D.D., (2012), Adiabatic normal mode reverberation and clutter modelling. Proc. of 11th European Conference on Underwater Acoustics (ECUA), 239-246, Edinburgh, UK.

[170] Prosperetti A., (1984), Bubble phenomena in sound fields: Part one, *Ultrasonics* (22), 69-77

[171] Prosperetti A. et al, (1988), Nonlinear bubble dynamics, *J. Acoust. Soc. Am.* 83(2), 502-514

R

[172] Radford C.A. et al , (2011), Modelling a reef as an extended sound source increases the predicted range at which reef noise may be heard by fish larvae, *Mar. Ecol. Prog. Ser.* , Vol. 438, 167-174

[173] Radford, A. N., Kerridge, A., and Simpson, S. D. (2014). Acoustic communication in a noisy world: can fish compete with anthropogenic noise? *Behav. Ecol.* 25, 1022–1030.

[174] [RD Coordinates], <https://nl.wikipedia.org/wiki/Rijksdriehoekskoordinaten>

References

- [175] Reeder D.M. and Kramer K.M. (2005) ,Stress in free-ranging mammals: integrating physiology, ecology, and natural history. *Journal of Mammalogy*, 86, 225–235.
- [176] Reinhall P.G. and Dahl P.H., Underwater Mach wave radiation from impact pile driving: Theory and observation, *J. Acoust. Soc. Am.* , 130 (3), p.1209-1216 , (2011).
- [177] Richardson W. J et al, (1995). *Marine Mammals and Noise*. Academic Press, San Diego, CA, 576 pp.
- [178] Robertson J. S., (1999), Sound propagation over a large wedge a comparison between the geometrical theory of diffraction, *J. Acoust. Soc. Am.* 106 (1), 113-119.
- [179] Rossington, K. et al, (2013) Eco-hydro-acoustic modeling and its use as an EIA tool. *Marine pollution bulletin*, 75, 235–43.
- [180] Ryan K.L.,(2009), NATO Undersea Research Centre Marine Mammal Risk Mitigation Rules and Procedures, NURC-SP-2009-02

S

- [181] Scheidat, M. et al , (2008) Harbour porpoise *Phocoena phocoena* abundance in the southwestern Baltic Sea. *Endangered Species Research*, 5, 215–223.
- [182] Scheidat, M. et al ,(2012) Using aerial surveys to estimate density and distribution of harbour porpoises in Dutch waters. *Journal of Sea Research*, 69, 1-7.
- [183] Schecklman, S. et al, 2015, A computational method to predict and study underwater noise due to pile driving , *J. Acoust. Soc. Am.* , 138(1), 258-266.
- [184] Schuknecht, H.F. (1993). *Pathology of the Ear*, 2nd edn., Lea-Felbiger, Philadelphia.
- [185] [Scrimger & Heitmeyer, 1989], Scrimger, P., & Heitmeyer, R. M. (1991). Acoustic source-level measurements for a variety of merchant ships. *J. Acoust. Soc. Am.* , 89(2), 691-699.
- [186] Slabbekoorn H and Bouton N., (2008), Soundscape orientation: a new field in need of sound investigation. *Animal Behaviour* 76: e5-e8.
- [187] Slabbekoorn, H et al, 2010, A noisy spring: the impact of globally rising underwater sound levels on fish. *Trends Ecol. Evol.* 25, 419–427.

References

- [188] Sertlek H.O. and Aksoy S., (2010), An Alternative Approach for Treatment of Lossy Seabed In Fluid-Solid Waveguide Problems, ECUA 2010, Istanbul, Turkey.
- [189] Sertlek H.Ö, Aksoy S., (2012), Benchmarking Of Acoustic Pulse Propagation Problems In An Isovelocity Waveguide By An Analytical Time Domain Normal Mode Method, 11th European Conference on Underwater Acoustics (ECUA), Edinburgh, The Scotland, (2-6 July 2012)
- [190] Sertlek H.O., Ainslie M.A. (2013), "Propagation loss model comparisons on selected scenarios from the Weston memorial workshop." UA2013 1st international Conference and Exhibition on underwater acoustics.
- [191] Sertlek, H. Ö., & Ainslie, M. A. (2014a). A depth-dependent formula for shallow water propagation. J. Acoust. Soc. Am. , 136(2), 573-582.
- [192] Sertlek H.O., Ainslie M.A. (2014b), "A fast algorithm for the computation of incoherent propagation loss for variable water depth: a validation study" UA2014 2nd International Conference and Exhibition on underwater acoustics.
- [193] Sertlek, H. Ö. et al, (under review), Range-dependent propagation equations and results for Pekeris waveguide, under review in JASA.
- [194] Sertlek et al,(2015b), Mapping underwater sound in the Dutch part of the North Sea, Vol.875 , Chap.124, Advances in Experimental Medicine and Biology, pp 1001-100
- [195] Slabbekoorn H. et al, (2010)., "A noisy spring: the impact of globally rising underwater sound levels on fish", Trends Ecol Evol. , 25(7), 419-27
- [196] Soloway A. G. and Dahl P. H., (2014). Peak sound pressure and sound exposure level from underwater explosions in shallow water. J. Acoust. Soc. Am., 136, 3, EL219-EL223.
- [197] [SONIC], Information on the "Suppression Of underwater Noise Induced by Cavitation (SONIC)" European project can be found on: <http://www.sonic-project.eu/>
- [198] Southall B. L. et al, (2007), Marine Mammal Noise Exposure Criteria: Initial Scientific Recommendations, Aquatic Mammals, 33 (4), pp. 411-509.
- [199] Stevens, M. (2013),Sensory Ecology, Behaviour, and Evolution, Oxford University Press.
- [200] Sutton et al, (2011), Mapping the Spatio-temporal Distribution of Underwater Noise in Irish Waters, EPA STRIVE Report,2011-W-MS-7, (<http://erc.epa.ie/safer/reports>, last accessed on 09/12/2015)

References

[201] Suzuki, Y. and Takeshima, H. (2004). Equal loudness-level contours for pure tones. *J. Acoust. Soc. Am.* 116, 918-933.

T

[202] Teilmann, J. et al, (2013) Geographic, seasonal, and diurnal surface behavior of harbor porpoises. *Marine Mammal Science*, 29, E60–E76.

[203] Thompson, P.M. et al, (2013a) Short-term disturbance by a commercial two-dimensional seismic survey does not lead to long-term displacement of harbour porpoises. *Proceedings. Biological sciences / The Royal Society*, 280, 20132001.

[204] Thompson P.M. et al, (2013b) Framework for assessing impacts of pile-driving noise from offshore wind farm construction on a harbour seal population. *Environmental Impact Assessment Review*, 43, 73–85.

[205] Thorp, W. H. (1967). Analytic Description of the Low-Frequency Attenuation Coefficient. *J. Acoust. Soc. Am.* , 42(1), 270-270.

[206] Thorsos E.I. and Perkins J.S., (2007), Overview of the reverberation modeling workshops, *J. Acoust. Soc. Am.* Volume 122, Issue 5, pp. 3074-3074.

[207] Tindle C.T., (1979), The equivalence of bottom loss and mode attenuation per cycle in underwater acoustic, *J. Acoust. Soc. Am.*, 66(1) , 250-255.

[208] Tindle C.T. and Weston D.E., (1980), Connection of acoustic beam displacement, cycle distances and attenuations for rays and normal modes, *J. Acoust. Soc. Am.*, 67 , 1614-1622.

[209] Tougaard J et al, (2009), “Pile driving zone of responsiveness extends beyond 20 km for harbor porpoises (*Phocoena phocoena* (L.))”, *J. Acoust. Soc. Am.* 126, pp.11-14.

[210] Tougaard J. et al, (2009). Pile-driving zone of responsiveness extends beyond 20 km for harbour porpoises (*Phocoena phocoena*, (L.)). *J. Acoust. Soc. Am.* , 126(1), 11-14.

[211] Tougaard J. et al, (2014) Cetacean noise criteria revisited in the light of proposed exposure limits for harbour porpoises. *Marine Pollution Bulletin*, 90, 196–208.

[212] Tougaard J. et al, (2015). Cetacean noise criteria revisited in the light of proposed exposure limits for harbour porpoises. *Marine Pollution Bulletin*, 90, 1–2, 196-208.

[213] Trees et al. 2005, Monitoring water transparency and diver visibility in ports and harbors

References

using aircraft hyperspectral remote sensing , Proc. SPIE 5780, Photonics for Port and Harbor Security, 91 (May 25, 2005)

[214] Tyack, P. L. (2008). Implications for marine mammals of large-scale changes in the marine acoustic environment. *Journal of Mammalogy*, 89(3), 549–558.

[215] Tyack P. et al, (2015), International Quiet Ocean Experiment plan, (http://www.scor-int.org/IQOE/IQOE_Science_Plan-Final.pdf, Last accessed 09/12/2015)

U

[216] Urlick R.J., “Principles of underwater sound for engineers”, McGraw-Hill, New York, (1975).

V

[217] Van Horne B., (1983) Density as a Misleading Indicator of Habitat Quality. *The Journal of Wildlife Management*, 47, 893–901.

[218] Verboom W. C. and Kastelein R. A. (1997). Structure of harbour porpoise (*Phocoena phocoena*) click train signals. In: *The biology of the Harbour porpoise* (Eds. Read, A.J., Wiepkema, P.R. and Nachtigall, P.E.), De Spil Publishers, Woerden, The Netherlands, 343-362.

[219] Verboom, W. C. and Kastelein, R. A., (2005). Some examples of marine mammal discomfort thresholds in relation to man-made noise. *Proceedings UDT 2005*, Amsterdam, June 2005.

[220] Von Benda-Beckmann A.M. et al, (2014). Assessment of impact of underwater clearance of historical explosives by the Royal Netherlands Navy on harbour porpoises in the North Sea, TNO Report, TNO 2014 R10916.

[221] Von Benda-Beckmann A. M. et al, (2015), Assessing the Impact of Underwater Clearance of Unexploded Ordnance on Harbour Porpoises (*Phocoena phocoena*) in the Southern North Sea, *Aquatic Mammals*, 2015, 41(4), 503-523.

W

[222] Wales S.C. and Heitmeyer R.M.(2002), An ensemble source spectra model for merchant ship-

References

radiated noise , J. Acoust. Soc. Am., Vol 111, Issue 3: 1211-1231

[223] Wang L. et al, (2014), "review of underwater acoustic propagation models", NPL report AIR (RES) 086

[224] Wenz. G.M., (1962), Acoustic ambient noise in the ocean: Spectra and sources, J. Acoust. Soc. Am. vol. 34, p. 1936–1956.

[225] Weston D.E.,(1959), Guided propagation in a slowly varying medium, Proc.Phys.Soc., 73,365–384

[226] Weston, D. E. (1960), Underwater explosions as acoustic sources, Proc.Phys.Soc., 76, 233-249.

[227] Weston D.E., (1960), A Moiré fringe analog of sound propagation in shallow water, J. Acoust. Soc. Am. 32-6, 647-654.

[228] Weston, D. E. (1962), Explosive sources in Underwater Acoustics (Plenum Press, New York), pp 51-66.

[229] Weston D.E., (1971),Intensity-range relations in oceanographic acoustics, J. Sound Vib.,18, pp.271-287

[230] Weston D.E., (1976), Propagation in water with uniform sound velocity but variable-depth lossy bottom, J. Sound Vib., 47, pp.473-483.

[231] Weston D.E. and Tindle C.T., (1979),Reflection loss and mode attenuation in a Pekeris model, J. Acoust. Soc. Am., 66(3) , 872-879

[232] Weston D. E., (1980), Acoustic flux methods for oceanic waveguides, J.Acoust.Soc.Am.,68(1), 287-296.

[233] Weston D.E. ,(1980), Wave theory peaks in range averaged channels of uniform sound velocity, J. Acoust. Soc. Am. ,68 (1), 282 -286

[234] Weston D. E. and Ching P. A., (1989). Wind effects in shallow-water acoustic transmission. J. Acoust. Soc. Am. , 86(4), 1530-1545.

[235] Weston D.E., (1991), Diffusion-like growth of decoupling and enhancement depths in shallow-water acoustic propagation, Proc. I.O.A. 13 (3), 85-92.

[236] Weston D.E., (1994), Wave shifts, beam shifts, and their role in modal and adiabatic propagation, J. Acoust. Soc. Am. 96, 406-416

References

[237] World Ocean Atlas 2013 (WOA13) is a set of objectively analyzed (1° grid) climatological fields of in situ temperature, salinity, dissolved oxygen, Apparent Oxygen Utilization (AOU), percent oxygen saturation, phosphate, silicate, and nitrate at standard depth levels for annual, seasonal, and monthly compositing periods for the World Ocean. Available from: <http://www.nodc.noaa.gov/OC5/woa13/>

[238] Wensveen, P. J. et al, (2014), Equal latency contours and auditory weighting functions for the harbour porpoise (*Phocoena phocoena*). *The Journal of Experimental Biology*, 217, 359-369.

[239] Westgate, A. J. et al, (1995). Diving behaviour of harbour porpoises, *Phocoena phocoena*. *Canadian Journal of Fisheries and Aquatic Science*, 52, 1065-1073.

[240] Wouter H. and Slabbekoorn H, (2015) , Pollution going multimodal: the complex impact of the human-altered sensory environment on animal perception and performance *Biol. Lett.* 2015 11 20141051.

Y

Z

[241] Zampolli M. et al, Scenarios for benchmarking range-dependent active sonar performance models, *Proceedings of the IOA*, Vol. 32, Pt. 2, pp 53-63,2010.

[242] Zampolli et al, (2013) , Validation of finite element computations for the quantitative prediction of underwater noise from impact pile driving, *J Acoust Soc Am.*, 133(1):72-81.

[243] Ziolkowski, A., (1970), A method for calculating the output pressure waveform from an air-gun: *Geophys. J. R. Astr. Soc.*, 21, 137 – 161.

[244] Ziolkowski A. et al, (1982), The signature of an air-gun array: Computation from near-field measurements including interactions: *Geophysics*, 47(10), 1413- 1421.

References

Acknowledgements

My PhD project is supported by NWO-ZKO grant “Effects of underwater noise on fish and marine mammals in the North Sea”. First of all, I specially thanks to my family mother, father and brother who always supports my decisions for my entire life, including coming to the Netherlands from Turkey to make this research. I thank to my supervisors Michael A. Ainslie, Hans Slabbekoorn and Carel ten Cate for all their support, insightful suggestions and patience for my questions during this research. I thank to all participants of ZKO programme for their stimulating discussions and feedbacks during our meetings; Joint Industry Programme on Sound and Marine Life for the measurements of single airgun data and the NL Ministry of Defence and the KNMI for making available the reported explosion events used in this study; specially thanks to Lisanne Brouwer who designed my thesis cover with her great art.

I thank to Michael B. Porter for his help during the use of Acoustic Toolbox’s models; Alex MacGillivray for his willingness to answer our questions about his MSc thesis during the development of airgun source model; Robert Laws for many discussions about airgun source modelling; René Dekeling for his comments about this work and helps for providing the data; my TNO colleagues Bas Binnerts for his translation for the Dutch summary and many stimulating discussions about the sound maps and implementation of Soprano, Mathieu Colin and Henry Dol for stimulating discussions about the propagation models and environmental inputs; Stefania Giodini and Mark Prior for their detailed feedback for airgun source model; Sander von Benda Beckmann for his stimulating discussions and comments on all sound maps and source models (especially for explosions); Mario Zampolli who took my interest to the underwater acoustic group at TNO during our short chat at ECUA 2010 in Istanbul; Geert Aarts for the valuable comments on the biological relevance. I thank all IBL group members Errol, Katharina, Saeed, Fleur, Michelle, Pralle, Peter, Annabel, Jiani and many others.

Specialy thanks to Serkan Aksoy who conducted to start working on underwater acoustic problems, helped and taught me a lot during my academic career; H. Avni Serim for his encouragement and reference to start this PhD project; all of my valuable colleagues from TUBITAK, Mustafa Yağımlı, Umut, Ahmet Yılmaz, Ahmet Güneş, Onur, Esra, Hakan, Baki, Özge, Lalehan, Senem, Okan, Mustafa

References

Unal, Köksal Hoccoğlu, Alper, Sultan, Şamil, Osman and all project team members; my old managers Bülent Örencik, Deniz Bolükbaş and Sevgi Akgün for their help and understanding during my leave. I specially thanks to my friends Umutcan, Mehmet Can, Ulaş, Kadir, Arda, Okan, Yasin, Kürşat who encouraged me to make a decision on starting a new life in a new country. Finally, to readers of this thesis for their interest to my research.